UNIVERSITY OF CALIFORNIA,
IRVINE

ΛCDM and Beyond: Neutrinos and the Puzzle of Cosmological Tensions

DISSERTATION

submitted in partial satisfaction of the requirements
for the degree of

DOCTOR OF PHILOSOPHY

in Physics with Concentration in Astronomy and Astrophysics

by

Helena García Escudero

Dissertation Committee:
Professor Kevork N. Abazajian, Chair
Professor Manoj Kaplinghat
Professor Steph Sallum

2025

Chapter 2 © 2022 Phys. Rev. D
Chapter 3 © 2023 Phys. Rev. D
Chapter 4 © 2024 Phys. Rev. D
Chapter 5 © 2025 Phys. Rev. D
Chapter 6 © 2025 Apj L.
All other materials © 2025 Helena García Escudero

DEDICATION

To my parents, whose love, strength, and unwavering belief in me have been the quiet force behind every step of this journey, I especially dedicate this work to my mother, whose unconditional support has always felt close, like home, even across oceans, time zones, and distance, and to my father, whose resilience, encouragement, and constant faith have carried me through every challenge, as only we know the obstacles overcome and sacrifices made to arrive here. Every page of this thesis reflects your boundless love, enduring patience, and the dreams we have carried together across continents.

A mis padres, cuyo amor, fortaleza y fe inquebrantable en mí han sido la fuerza silenciosa detrás de cada paso de este camino, dedico especialmente este trabajo a mi madre, cuyo apoyo incondicional se ha sentido cercano, como un hogar, incluso a través de océanos, husos horarios y distancias, y a mi padre, cuya resiliencia, ánimo y constante confianza me han acompañado en cada desafío, como solo nosotros sabemos, con los obstáculos superados y los sacrificios realizados para llegar hasta aquí. Cada página de esta tesis refleja su amor sin límites, su paciencia inagotable y los sueños que hemos alcanzado y seguiremos haciendo realidad juntos a través de continentes.

Gracias por enseñarme a creer, luchar y nunca rendirme.

TABLE OF CONTENTS

Page

LIST OF FIGURES **vi**

LIST OF TABLES **xi**

ACKNOWLEDGMENTS **xiii**

VITA **xv**

ABSTRACT OF THE DISSERTATION **xvii**

1 Introduction **1**
- 1.1 The Expanding Universe: key equations in Cosmology . . . 2
- 1.2 Neutrinos in Cosmology . . . 9
- 1.3 Cosmological Observations . . . 12
- 1.4 Challenges to ΛCDM from Current Observational Data . . . 16
- 1.5 Bayesian Analysis Framework . . . 20
- 1.6 Scope and Structure of this Thesis . . . 22

2 Early or Phantom Dark Energy, Self-Interacting, Extra, or Massive Neutrinos, Primordial Magnetic Fields, or a Curved Universe: An Exploration of Possible Solutions to the H_0 and σ_8 Problems **25**
- 2.1 Introduction . . . 26
- 2.2 Beyond ΛCDM models . . . 28
- 2.3 Methodology . . . 31
  - 2.3.1 Data sets . . . 31
  - 2.3.2 Statistical and cosmological software . . . 34
- 2.4 Results . . . 36
  - 2.4.1 Alleviation of the H_0 tension . . . 36
  - 2.4.2 Alleviation of S_8 tension . . . 38
  - 2.4.3 Combined alleviation of the H_0 and S_8 tension . . . 41
- 2.5 Discussion . . . 42
  - 2.5.1 Cosmologies and Cosmological Parameters . . . 42
  - 2.5.2 The Level of the S_8 Tension . . . 44
- 2.6 Conclusion . . . 46
- 2.7 APPENDIX: Details of considered models . . . 49

2.7.1 Early dark energy . . . 49
2.7.2 Self-interacting neutrinos . . . 50
2.7.3 Primordial Magnetic Fields & Baryon Inhomogeneity . . . 52

3 Visible in the laboratory and invisible in cosmology: decaying sterile neutrinos 60
3.1 Introduction . . . 60
3.2 Neutrinos in a Low-Reheating Temperature Universe . . . 64
3.3 Current Constraints . . . 66
3.4 Dark Decay Model . . . 69
3.4.1 Evolution of the Abundance of Decaying Sterile Neutrinos in an LRT universe . . . 71
3.4.2 Decaying Sterile Neutrino Parameter Space in LRT Cosmologies . . . 75
3.5 Discussion & Conclusions . . . 78

4 Status of neutrino cosmology: Standard ΛCDM, extensions, and tensions 80
4.1 Introduction . . . 80
4.2 Cosmological Datasets . . . 86
4.2.1 Planck CMB . . . 87
4.2.2 CMB lensing . . . 89
4.2.3 BAO . . . 89
4.2.4 Type Ia SNe . . . 90
4.2.5 Tension Datasets . . . 91
4.3 Methodology . . . 92
4.4 ΛCDM and Neutrino cosmology . . . 97
4.4.1 Hierarchical Neutrino Mass Ordering . . . 98
4.4.2 Free Neutrino Mass . . . 100
4.5 Exploring Beyond ΛCDM Models . . . 104
4.5.1 ΛCDM+$N_{\rm eff}$ . . . 104
4.5.2 Sterile Neutrinos . . . 107
4.5.3 The S_8 Tension and Massive Active or Sterile Neutrinos . . . 110
4.5.4 Evolving Dark Energy, Massive Neutrinos, Extra Relativistic Energy Density, and Curvature . . . 112
4.6 Discussion & Conclusions . . . 115

5 Extra Radiation Cosmologies: Implications of the Hubble Tension for eV-scale Neutrinos 125
5.1 Introduction . . . 125
5.2 Neutrino Cosmology: $\boldsymbol{N_{\rm eff}}$ & $\boldsymbol{\Sigma m_\nu}$ from CMB, LSS, and BAO . . . 129
5.2.1 Suppression of LSS by $\boldsymbol{\Sigma m_\nu}$ & $\boldsymbol{N_{\rm eff}}$ . . . 130
5.2.2 BAO: Geometry and Anticorrelation . . . 131
5.3 Cosmological datasets & Methodology . . . 135
5.3.1 Baseline cosmological dataset . . . 135
5.3.2 Complementary Data: SDSS DR12 BAO & Full-Shape . . . 137
5.3.3 Methodology . . . 137

5.4 Results . . . 140
5.5 Discussion & Conclusions . . . 143
5.6 APPENDIX: Prior Dependence and Volume Effects . . . 145

6 Sound-Horizon-Agnostic Inference of the Hubble Constant and Neutrino Mass from BAO, CMB Lensing, and Galaxy Weak Lensing and Clustering 151
6.1 Introduction . . . 151
6.2 Constraining cosmology with the sound horizon as a free parameter . . . 154
6.2.1 BAO Observables . . . 154
6.2.2 CMB Lensing, Galaxy Lensing and Clustering . . . 156
6.2.3 The effect of massive neutrinos . . . 158
6.2.4 Parameter degeneracies . . . 159
6.3 Analysis details . . . 160
6.3.1 Datasets . . . 160
6.3.2 Model Parameters and Priors . . . 161
6.3.3 Forecasts . . . 164
6.4 Results . . . 167
6.4.1 Current data constraints with fixed Σm_ν . . . 171
6.4.2 Current data constraints with varying Σm_ν . . . 171
6.4.3 Forecasted parameter constraints . . . 173
6.5 Summary . . . 174

7 Conclusions and Future Directions 176

Bibliography 178

LIST OF FIGURES

Page

1.1 Summary of H_0 estimates from different cosmological probes with error bars smaller than 3.5 $\mathrm{km\,s^{-1}\,Mpc^{-1}}$. Figure taken from CosmoVerse White Paper [144]. 17

2.1 Shown here are the $-\Delta$AIC values of considered models (from left to right: wCDM, ΛCDM+$N_{\rm eff}$, non-trivial neutrino mass, non-zero curvature, primordial magnetic fields, self-interacting neutrinos and early dark energy) for relieving the H_0 tension for our baseline CMB, BAO and SNe data sets: P18+R21 (red), P18+BAO16+R21 (green) and P18+BAO16+SN+R21 (blue). The horizontal line is the threshold of stronger than "weak preference" on the Jeffreys' scale. 37

2.2 Comparison of H_0 posterior distributions from early dark energy 39

2.3 Shown here are the $-\Delta$AIC values of considered models (from left to right: wCDM, ΛCDM+$N_{\rm eff}$, non-trivial neutrino mass, non-zero curvature, primordial magnetic fields, self-interacting neutrinos and early dark energy) for relieving the S_8 tension for our baseline CMB, BAO and SNe data sets: P18+V09 (red), P18+BAO16+V09 (green) and P18+BAO16+SN+V09 (blue). The horizontal line is the "strong" threshold on the Jeffreys' scale. 40

2.4 We show 68% and 95% CL contours of (Σm_ν, σ_8) and their posterior distribution for the combination of P18 with our three cluster data sets: SZ13 (grey), SZ21 (red) and V09 (blue). Only P18+SZ13 has a likelihood that peaks at nonzero neutrino mass, with $\Sigma m_\nu = 0.28 \pm 0.14\,\mathrm{eV}$. 54

2.5 Shown here are the $-\Delta$AIC values of considered models (from left to right: wCDM, ΛCDM+$N_{\rm eff}$, non-trivial neutrino mass, non-zero curvature, primordial magnetic fields, self-interacting neutrinos and early dark energy) for relieving the H_0 and S_8 tensions simultaneously for our baseline CMB, BAO and SNe data sets: P18+R21+V09 (red), P18+BAO16+R21+V09 (green) and P18+BAO16+SN+R21+V09 (blue). The horizontal line crosses the threshold of "strong" on the Jeffreys' scale. 55

2.6 Comparison of 1σ and 2σ contours of ($\Omega_{\rm m}$, σ_8) from Planck (2015 and 2018) and measurements including X-ray clusters V09/SR17 (left panel), SZ clusters SZ13/SZ21 (middle panel) and lensing KiDS20/CHFTLenS/DES (pink/olive/light blue, right panel). 55

2.7 EDE v.s. ΛCDM: 68% and 95% CL contours of $\{\log(10^{10}A_s)$, n_s, $100\theta_{\rm MC}$, $\Omega_b h^2$, $\Omega_c h^2$, $\tau_{\rm reio}$, σ_8, $H_0\}$ of EDE (purple) v.s. ΛCDM (green) for our baseline cosmological data sets plus H_0, P18+BAO16+SN+R21. The grey dashed line denotes the best-fit value of $H_0 = 73.04\,{\rm km/s/Mpc}$ reported by R21. 56
2.8 wCDM v.s. ΛCDM: 68% and 95% CL contours of $\{\log(10^{10}A_s)$, n_s, $100\theta_{\rm MC}$, $\Omega_b h^2$, $\Omega_c h^2$, $\tau_{\rm reio}$, σ_8, $H_0\}$ of wCDM v.s. ΛCDM for our baseline cosmological data sets plus H_0, P18+BAO16+SN+R21. The grey dashed line denotes the best-fit value of $H_0 = 73.04\,{\rm km/s/Mpc}$ reported by R21. 57
2.9 ΛCDM+$N_{\rm eff}$ v.s. ΛCDM: 68% and 95% CL contours of $\{\log(10^{10}A_s)$, n_s, $100\theta_{\rm MC}$, $\Omega_b h^2$, $\Omega_c h^2$, $\tau_{\rm reio}$, σ_8, $H_0\}$ of ΛCDM+$N_{\rm eff}$ model (purple) v.s. ΛCDM (green) for our baseline cosmological data sets plus H_0, P18+BAO16+SN+R21. The grey dashed line denotes the best-fit value of $H_0 = 73.04\,{\rm km/s/Mpc}$ reported by R21. 58
2.10 PMF v.s. ΛCDM: 68% and 95% CL contours of $\{\log(10^{10}A_s)$, n_s, $100\theta_{\rm MC}$, $\Omega_b h^2$, $\Omega_c h^2$, $\tau_{\rm reio}$, σ_8, $H_0\}$ of PMF (purple) v.s. ΛCDM (green) for our baseline cosmological data sets plus H_0, P18+BAO16+SN+R21. The grey dashed line denotes the best-fit value of $H_0 = 73.04\,{\rm km/s/Mpc}$ reported by R21. 59

3.1 Shown here is the parameter space for a possible low reheating temperature universe with $T_{\rm RH} = 5\,{\rm MeV}$, for the case of $\nu_s \leftrightarrow \nu_e$ mixing. The regions of this figure are described in the beginning of Sect. 3.3. 64
3.2 Shown here is the calculated production and energy density evolution for massless standard neutrinos (black line) and an example of $m_s = 100\,{\rm keV}$ sterile neutrinos. We show five different $\sin^2 2\theta$ cases of sterile neutrino energy density evolution, ρ_{ν_s}. The sterile neutrinos decay at different times (temperatures) ranging from a case that matches the neutrino's mass $T_{\rm decay} = 0.1\,{\rm MeV}$ (red line) down to the temperature of matter radiation equality (green line). Note that sterile neutrinos with very different initial production densities can all match the same density relative to the active neutrinos at their decay. Therefore, a wide range of sterile neutrino masses and $\sin^2 2\theta$ can match a designated $N_{\rm eff}$, when combined with either a nearly fully thermalized or non-thermalized ρ_{ν_α} in LRT cosmologies. The reheating temperature in this example is chosen to be 5 MeV. The moments of $T = m_s$ and $T_{\rm rm}$ are shown with the dotted and dashed vertical lines, respectively. 72
3.3 Shown are the updated parameter spaces of dark decay in an LRT Universe for two cases, $T_{\rm RH} = 1.8\,{\rm MeV}$ and $7\,{\rm MeV}$, left and right, respectively. The diagonal reddish and blueish lines correspond to the cases when the decay happens at the temperature of matter-radiation equality, and match different $N_{\rm eff}$ values. For each pair, the darker color (lower) is associated with a value of $N_{\rm eff,Std} = 3.044$, and the lighter color one $N_{\rm eff,H0} = 3.48$ [173]. For the darker shaded region, $N_{\rm eff}$ ranges from the minimal provided by $N_{\rm eff,act}$ to the standard value with a contribution from sterile neutrino decay. In the lighter shaded region on the right panel, $N_{\rm eff}$ ranges from the standard value to that preferred to alleviate the Hubble tension, $N_{\rm eff,H0}$. Above the lighter diagonal, the parameter space can accommodate an alleviation of the Hubble tension with $N_{\rm eff,H0}$, or provide the standard density, $N_{\rm eff,Std}$. For the case of $T_{\rm RH} = 1.8\,{\rm MeV}$, the thermal nature of the CMB [235] constrains the red hatched portion. This constraint does not apply for $T_{\rm RH} = 7\,{\rm MeV}$ in this parameter space. 76

4.1 Comparison of 1D marginalized posterior distributions for Σm_ν [eV] for different data combinations. As seen above, there are three clusters of likelihoods that are stringent, moderate, and weakest. The stringent combination includes five likelihoods, with P18, DESI, & U3 being orange, P18, DESI, & PP being green, with CamSpec, DESI, & U3 being red, CamSpec, DESI, & PP being grey and the 11 parameter chain with our benchmark data in black. The moderate cluster combination includes four datasets' likelihoods, with P18, DESI, & DES Y5 being red, CamSpec, DESI, & DES Y5 being light blue, with P20, DESI, & U3 being dark blue, and P20, DESI, & PP being green. The weakest likelihood contour, in purple, is for P20, DESI, & DES Y5. All datasets include CMB lensing. 96
4.2 Shown is the comparison of our benchmark datasets, but with different choices of the CMB analyses (P18, CamSpec, P20), with their 68% and 95% CL likelihoods of ΛCDM parameters plus Σm_ν. Σm_ν is in units of eV and H_0 in units of $\mathrm{km\,s^1\,Mpc^1}$. 119
4.3 Shown is the comparison of our benchmark datasets, but with different choices of the SNe samples (PP, DES Y5, and U3), with their 68% and 95% CL likelihoods of ΛCDM parameters plus Σm_ν. Here, Σm_ν is in units of eV and H_0 in units of $\mathrm{km\,s^1\,Mpc^1}$. 120
4.4 Shown here are the same 1D marginalized posterior distributions for Σm_ν shown in Fig. 4.1 (dashed lines), together with their Gaussian fits (solid lines). The black colored lines represent the different cosmological dataset combinations for the 7-parameter model where Σm_ν can vary freely. The red lines correspond to the 11-parameter chain. Going from left to right in the peak of the black-colored likelihoods, the curves correspond to the cosmological likelihood combinations P18+DESI+U3; P18+DESI+PP; CamSpec+DESI+U3; CamSpec+DESI+PP; P20+DESI+U3; P18+DESI+DES Y5, P20+DESI+PP; CamSpec+CMB lensing+DESI+DES Y5; and lastly the P20+DESI+DES Y5. The centroid for each combination, respectively, is below 2σ from the normal-ordering minimal neutrino mass, for all of the cases. The centroid for the red 11 parameter chain likelihood of the benchmark data is at the 2.31σ level. All datasets include CMB lensing. 121
4.5 Shown here is a comparison of 1D marginalized posterior distributions for $N_{\rm eff}$ for different SNe data combinations when added to the P18, CMB lensing and DESI likelihoods. The solid dark blue, dashed light-blue, and black lines correspond to the PP, U3, DES Y5 SNe samples respectively, with all consistent with $N_\nu^{\rm SM}$. The green line is the resulting posterior distribution when the SH0ES H_0 measurement likelihood is added to the PP chain. finding $N_{\rm eff} = 3.45 \pm 0.12$. 122
4.6 Comparison of the one-dimensional marginalized posterior distributions for $m_{\nu_{\rm s}}$ is shown, for the case of a fully thermalized sterile neutrino ($N_{\rm eff} = 4.044$). The black curve represents the benchmark data alone, while the red curve includes the SH0ES H_0 measurement. 123

4.7 Shown are the 68% and 95% CL likelihood contours of the extension parameters in our 11-parameter case, using our benchmark data. Without the tension data, no significant shifts are seen in any extended parameters, except for $w_0 = 0.975^{+0.012}_{-0.024}$. As with more economical models, only $N_{\rm eff}$ deviates strongly from its standard value when including H_0. Here, Σm_ν is in units of eV and H_0 is in units of $\mathrm{km\,s^1\,Mpc^1}$. 124

5.1 **Left panel:** contours of the clustering amplitude σ_8 as a function of the total neutrino mass Σm_ν and the effective number of relativistic species $N_{\rm eff}$, computed while keeping the remaining ΛCDM parameters fixed at their standard values. Lowering Σm_ν and $N_{\rm eff}$ increases σ_8, while raising them decreases it. **Right panel:** contours of the BAO distance ratio $D_{\rm M}/r_{\rm d}$ at $z = 0.51$ for different Σm_ν and $N_{\rm eff}$ values when the total matter density is fixed. An increase in neutrino mass is compensated by a reduction in the cold dark matter fraction. These contours reveal the anticorrelated response of Σm_ν and $N_{\rm eff}$ through their opposite effects on the $D_{\rm M}/r_{\rm d}$ BAO observable. Together, these panels highlight the complementary ways in which neutrino properties imprint on growth and geometry. 131

5.2 **Top Panels:** $D_{\rm M}/r_{\rm d}$ shown along the horizontal axis and $D_{\rm H}/r_{\rm d}$ along the vertical axis, calculated from the parameters of the MCMC chains from the *Planck* 2018 CMB likelihoods alone, for two distinct models with free neutrino mass and $N_{\rm eff}$, separately. The left panel corresponds to a redshift of 0.51 and the right panel to a redshift of 2.33. The colors indicate the values of $N_{\rm eff}$ and Σm_ν specified in the color bar. A positive vertical offset has been applied to the Σm_ν chains in both panels to ensure clarity of the figure ($z = 0.51$ vertical offset of $+1$; $z = 2.33$ vertical offset of $+0.2$). The purple contours denote the 1σ and 2σ DESI DR2 BAO measurements of $D_{\rm M}/r_{\rm d}$ and $D_{\rm H}/r_{\rm d}$. **Bottom Panels:** To show their dependence on the neutrino parameters independent of $r_{\rm d}$, $D_{\rm M}$ is shown along the horizontal axis and $D_{\rm H}$ is along the vertical axis for models with free neutrino mass and $N_{\rm eff}$, including only the *Planck* 2018 CMB likelihoods. A positive vertical offset of $+100$ Mpc has been applied to the Σm_ν chain points at $z = 0.51$ to ensure clarity of the figure. 147

5.3 Variation of the transverse distance $D_{\rm M}$ (solid lines) and the radial distance $D_{\rm H}$ (dashed lines) is shown at two redshifts: $z = 0.51$ (blue) and $z = 2.33$ (red). These are plotted as the Hubble constant H_0 along the lower horizontal axis and the matter density Ω_m are varied along their linear degeneracy from the *Planck* 2018 CMB likelihoods, as described in the text. The left panel shows models where Σm_ν increases in correlation with Ω_m (to the left) and the right panel shows models where $N_{\rm eff}$ increases in anticorrelation to Ω_m, to the right. 148

5.4 We show the profile likelihood for the physical sterile neutrino mass m_s, with the effective number of neutrino species fixed to $N_{\rm eff} = 3.50$. The red points show the computed $\Delta\chi^2$ values at discrete mass points used in the fit, while the blue curve represents a parabolic interpolation through these points. Shaded bands indicate the 68% (black) and 95% (purple) confidence intervals, respectively. 149
5.5 Two-dimensional posterior distributions are shown for the physical sterile neutrino mass, $m_{\rm s}$ and the effective number of neutrino species, $N_{\rm eff}$, under three different prior choices using MCMC Bayesian methods and our baseline datasets. The black contours correspond to a prior set as $1/\sqrt{m_s}$, the light purple contours to a prior as $1/m_s$, and the pale green contours, which give the most relaxed bounds, correspond to a prior of $1/m_s^2$. This figure illustrates the impact of prior volume effects in Bayesian analyses of this cosmological model. 150

6.1 Relative difference in the CMB lensing convergence spectrum $C_\ell^{\kappa\kappa}$ for a modified recombination model with an r_d smaller by 2%, relative to the Planck best-fit ΛCDM model. Orange points, green stars, and red triangles with error bars show the $C_\ell^{\kappa\kappa}$ bandpowers from *ACT*, *Planck*, and *SPT-3G*, respectively. The figure illustrates that recombination changes capable of raising H_0 to ~ 72 km/s/Mpc have only a minor effect on the CMB lensing spectrum. . 156
6.2 Relative difference with respect to the Planck+DES Y3 best-fit ΛCDM prediction for galaxy clustering correlation functions $w_{ij}(\theta)$ and $\gamma_{t,ij}(\theta)$ in four redshift bins ($i = j = 1, \ldots, 4$). Points with error bars show the DES Y3 measurements, while solid lines show the residuals for the same modified recombination model as in Fig. 6.1. The figure shows that recombination changes leave the 3×2-pt observables essentially unaffected. 157
6.3 The 68% and 95% CL contours and the 1D marginalized posterior distributions for H_0, $\Omega_m h^2$, Ω_m, and Σm_ν from current data. The elongated 2D contours of H_0, $\Omega_m h^2$ and Σm_ν highlight the positive correlations between these parameters discussed in the text. The DESI2+Planck+DESY3+PP analysis uses the full Planck data, with r_d as a derived parameter computed using the standard recombination routine in CAMB. In the analyses of all other data combinations in this figure, r_d is a free parameter. 169
6.4 The 68% and 95% CL contours, along with the 1D marginalized posterior distributions for H_0, $\Omega_m h^2$, and Σm_ν from current data, comparing the results obtained with a uniform prior and a logarithmic prior on Σm_ν. This figure illustrates how using a logarithmic prior eliminates the apparent bias towards higher values of H_0 and $\Omega_m h^2$. 170
6.5 The forecasted 68% and 95% CL posterior distributions for H_0, $\Omega_m h^2$, Ω_m, and Σm_ν. For reference, the green dashed lines represent the fiducial values used in the forecast. 170

LIST OF TABLES

Page

1.1 Scaling of major cosmological components with scale factor a, their energy density evolution, and the corresponding time dependence of the scale factor $a(t)$. 5

2.1 We show the σ value of the residual tension of each model given our full baseline data set P18, BAO16, and SN, when including the SHOES collaboration (R21) H_0 measurement, X-ray clusters measurement of $\sigma_8(\Omega_{\rm m}/0.25)^{0.47}$ in V09, and the DES measurement of S_8. Though we use more data from V09 and DES in our full analysis, here we use only the tension data point for the residual, which is calculated using Eq. (2.3). 44

2.2 Best-fit values of the parameter σ_8 for the three combinations of our baseline data sets P18, P18+BAO16, and P18+BAO16+SN, when including the SHOES collaboration (R21) H_0 measurement for each of the analysed models. The conclusions from the values S_8 are the same. 44

2.3 Best-fit values and 68% intervals of parameters for the preferred candidate models from P18+BAO16+SN+R21. The first nine rows are baseline ΛCDM parameters, and the last row shows model-specific extra parameters. 48

4.1 Summary of the cosmological datasets we considered in this work, as introduced in Section 6.3.1. 87

4.2 We list our adopted ranges for the flat prior distributions imposed on the 6 ΛCDM, as well as the 5 additional extended-model cosmological parameters. 93

4.3 Best-fit values and 68% confidence intervals for the parameters are presented for the 7- and 11-parameter extended models are shown. Our benchmark data includes P18, CMB lensing, DESI, and PP likelihoods, both without external data and with the addition of H_0 and S_8 posteriors, considered individually and in combination. 111

6.1 Priors adopted for the parameters in the analysis of current data, and the fiducial values and priors used in the forecast. Uniform priors are indicated by square brackets, while Gaussian priors with mean μ and standard deviation σ are denoted as $\mathcal{N}(\mu, \sigma)$. 162

6.2 Constraints on cosmological parameters from current data, assuming fixed $\Sigma m_\nu = 0.06$ eV. The "Base" dataset denotes DESI2+$\theta_\star$+APS-L. Uncertainties are quoted at 68% CL. 168

6.3 Constraints on cosmological parameters from current data, allowing Σm_ν to vary. The "Base" dataset denotes DESI2+$\theta_\star$+APS-L. For Σm_ν, both 68% CL intervals and 95% CL upper bounds are shown. 168

ACKNOWLEDGMENTS

First and foremost, I would like to express my deepest gratitude to my parents, whose love, encouragement, and unwavering support have guided me across continents and time zones. Mom and Dad, your strength, determination, and belief in me have been my foundation. You have taught me to be persistent, to chase success with integrity, and to never give up, even in the most challenging moments. None of this would have been possible without your sacrifices and constant inspiration.

I am profoundly grateful to my Ph.D. advisor, Professor Kevork N. Abazajian, for his invaluable guidance, time, and support throughout my doctoral journey. Since we first met in 2017, when I took his quantum mechanics class as an undergraduate, his mentorship has profoundly shaped my academic and personal growth. Kevork has not only taught me how to think like a scientist but also how to be passionate about discovery. His advice, encouragement, and trust in me have been instrumental in shaping the researcher I have become. Beyond research, his mentorship has enriched my life in countless ways, and I will carry the lessons I have learned from him throughout my career and beyond.

I would also like to extend my heartfelt thanks to the members of my committee, Professors Steph Sallum and Manoj Kaplinghat. Their insightful feedback, mentorship, and genuine care have been invaluable throughout my Ph.D. journey. They have provided guidance not only in research but also during difficult moments inside and outside the classroom. Their example as outstanding scientists and mentors continues to inspire me.

My sincere gratitude goes to the entire Department of Physics and Astronomy at UC Irvine, including faculty, staff, and students, for creating a welcoming, collaborative, and intellectually stimulating environment. I am especially thankful to my fellow graduate students, who have been an incredible source of support, laughter, and friendship. I owe a special thanks to my cohort and close friends Ethan, Mackenzie, Lorraine, Chelsea, and César, whose companionship made the long days and nights of graduate school truly worthwhile. To the members of our research group, including Cannon Vogel and Ryan, thank you for your collaboration, patience, and for turning difficult days into productive and enjoyable ones. I am also grateful to former group members and colleagues who have already graduated but remain lifelong friends, including Anne Katherine, Max, Yahya, Maya, and Roshan, as well as the many others in the department whose friendship and support have meant so much to me.

I also wish to thank my collaborators and coauthors Jui-Lin, Ryan, Hamid, and Levon, whose scientific insight and enthusiasm have deeply enriched the work presented in this dissertation. Special thanks go to Hamid, Levon, and Gopi for inviting me to visit them at Simon Fraser University in Canada, where I learned, explored, and grew both personally and scientifically. Those visits were filled with inspiration, fun, and collaboration that I will always remember fondly.

I would like to acknowledge undergraduate friends Victor, Vicente, Amadeo, and Santiago, who shared with me the very first steps of my academic journey and with whom I built

lasting memories. I am sincerely thankful to my undergraduate advisor, Professor Ansemil, for introducing me to research and inspiring my curiosity in physics. My gratitude also goes to my master's advisor, Professor Jesús, and my mentor and professor during my master's studies, Dr. Benjamin Montesinos, whose guidance and encouragement strengthened my academic path and prepared me for the challenges of graduate research.

Beyond academia, I have been fortunate to share my life with many wonderful friends who have made this journey brighter. To my friends from other departments and beyond UC Irvine, including Edu, Brandon, and Carlos, thank you for your encouragement and for reminding me to enjoy the world outside academia. To my running mates from CalCoast, including Natalie, Jonas, Erick, and Kelly, thank you for the early mornings, long runs, and shared goals that kept me grounded and energized. To my fitness friends, especially Deora and Natasha, and to friends who became chosen family, such as Steph, Anna, and Adam, thank you for your laughter, warmth, and constant support.

Finally, to my family and friends in Spain, your love has transcended distance. Thank you, Uncle Ángel, for your unwavering optimism and positivity from Spain and my cousins, as well as my dearest friends Irene, Paloma, Adrián, Paula, María, and many others, for your encouragement and care throughout all these years. Though we have been far apart, your presence has always been felt and deeply appreciated.

I would also like to acknowledge the publishers of my previous work, including *Physical Review D* and the *Astrophysical Journal Letters*, for granting permission to incorporate that material into this dissertation, in accordance with Section 3.2 of the UCI Thesis and Dissertation Manual.

Lastly, I gratefully acknowledge the financial support during the first two years of my PhD program that made this research possible. I was supported by a fellowship from the "La Caixa" Foundation (ID 100010434). Their generous support enabled me to pursue this research with focus and independence.

To all who have surrounded and supported me through this journey, thank you. You have each left a mark on my life, and I will forever be grateful for your kindness, friendship, and belief in me.

VITA

Helena García Escudero

EDUCATION

Doctor of Philosophy in Physics (Astrophysics concentration) **2025**
University of California, Irvine *Irvine, CA*

Master in Theoretical Physics and Astrophysics **2020**
Universidad Autónoma de Madrid *Madrid, Spain*

Bachelor of Science in Physics **2019**
Universidad Complutense de Madrid *Madrid, Spain*

Bachelor of Science in Mathematics **2019**
Universidad Complutense de Madrid *Madrid, Spain*

RESEARCH EXPERIENCE

Graduate Research Assistant **2021–2025**
University of California, Irvine *Irvine, California*

Visitor Researcher **2021–2025**
Simon Fraser University, Burnaby *Vancouver, Canada*

TEACHING EXPERIENCE

Lead Instructor Physics 3B **2025**
University of California, Irvine *Irvine, California*

Teaching Assistant **2023–2024**
University of California, Irvine *Irvine, California*

REFEREED JOURNAL PUBLICATIONS

Extra Radiation Cosmologies: Implications of the Hubble Tension for eV-scale Neutrinos **2025**
Submitted to Phys. Rev. D

Sound-Horizon-Agnostic Inference of the Hubble Constant and Neutrino Mass from BAO, Supernovae, CMB Lensing, and Galaxy Weak Lensing and Clustering **2025**
Submitted to Astrophysical Journal Letters

Cosmic Structure Strikes Back: The Elimination of Vector-Mediated Nonstandard Interaction Models as a Mechanism for Sterile Neutrino Dark Matter Production **2025**
Submitted to Phys. Rev. D

Return of the Lepton number: Sterile neutrino dark matter production and the revival of the Shi-Fuller mechanism **2025**
Published in Phys. Rev. D

The Status of Neutrino Cosmology: Standard ΛCDM, Extensions, and Tensions **2024**
Published in Phys. Rev. D

Visible in the Lab and Invisible in Cosmology: Decaying Sterile Neutrinos **2023**
Published in Phys. Rev. D

Early or Phantom Dark Energy, Self-Interacting, Extra, or Massive Neutrinos, Primordial Magnetic Fields, or a Curved Universe: An Exploration of Possible Solutions to the H_0 and σ_8 Problems **2022**
Published in Phys. Rev. D

ABSTRACT OF THE DISSERTATION

ΛCDM and Beyond: Neutrinos and the Puzzle of Cosmological Tensions

By

Helena García Escudero

Doctor of Philosophy in Physics with Concentration in Astronomy and Astrophysics

University of California, Irvine, 2025

Professor Kevork N. Abazajian, Chair

Abstract

The Λ-Cold Dark Matter (ΛCDM) model successfully describes the evolution and large-scale structure of the Universe, supported by high-precision cosmological observations. Yet, it leaves key questions unresolved—most notably the nature of dark matter, dark energy, and neutrinos—and faces persistent "cosmological tensions," such as discrepancies in the local Hubble expansion rate and the amplitude of matter clustering. These challenges suggest that extensions to ΛCDM or new physics may be required to fully capture cosmic dynamics.

This dissertation investigates these issues through studies of extended cosmological models and their implications for neutrino physics and the early Universe. We examine a broad class of ΛCDM extensions—including phantom and early dark energy, spatial curvature, primordial magnetic fields, and additional or self-interacting neutrino species—in the context of the Hubble and structure growth tensions. We then explore sterile neutrinos as probes of the pre–Big-Bang-nucleosynthesis epoch, focusing on scenarios involving decays or new interactions and their relevance to current and upcoming laboratory searches. We then perform comprehensive analyses using cosmic microwave background, baryon acoustic oscillation, and supernova datasets to study the effects of neutrino mass hierarchies and extra relativistic species. We further test extra-radiation cosmologies with the latest DESI observations and develop a sound-horizon-independent framework for inferring the Hubble constant and neutrino mass from large-scale structure and lensing data.

Overall, this work draws connections between new physics in the neutrino sector and cosmological tensions, constraining Standard Model and beyond-Standard-Model neutrino properties, and advancing our understanding of the open challenges faced by ΛCDM in light of forthcoming precision data.

Chapter 1

Introduction

Cosmology studies the Universe's origin, composition, and evolution by integrating fundamental physical principles with astronomical observations across cosmic history. Over the past century, it has evolved into a precision science, guided by the framework of General Relativity and constrained by increasingly accurate measurements of the cosmic microwave background (CMB), large-scale structure (LSS), and and distance–redshift relations that trace cosmic expansion. These observations have enabled the construction of a coherent picture of cosmic evolution—from the earliest moments following the Big Bang to the present epoch dominated by dark energy.

Despite its remarkable success, modern cosmology faces profound open questions. The nature of dark matter and dark energy remains elusive, and the fundamental properties of neutrinos—such as their absolute mass scale, and mass hierarchy—are not yet fully understood. Neutrinos occupy a unique place within the Standard Model, standing as some of its most enigmatic constituents. Although light and weakly interacting, they play a central role in the dynamics of the early Universe and in the formation of cosmic structures. Experimental evidence from oscillation measurements has firmly established that at least two neutrino

species possess non-zero masses—a discovery that extends beyond the original framework of the Standard Model. Despite this progress, key aspects of their nature remain unknown. As cosmology enters an era of high-precision measurements, the demand for accurate theoretical modeling becomes ever more critical to interpret these subtle effects and to search for potential signatures of physics beyond the Standard Model. Understanding how neutrinos affect cosmological observables is therefore crucial for interpreting present data, constraining new physics, and constitutes one of the main goals of this work.

1.1 The Expanding Universe: key equations in Cosmology

The Standard Cosmological Model relies on two foundational pillars: first, that gravitation is accurately described by Einstein's theory of General Relativity; and second, that the Universe satisfies the cosmological principle, being statistically homogeneous and isotropic on sufficiently large scales. Under these assumptions, the evolution of the Universe is fully determined by its geometry and energy content, as governed by Einstein's field equations. These assumptions lead naturally to the Friedmann–Lemaître–Robertson–Walker (FLRW) metric and to the Friedmann equations, which govern the expansion of the Universe as a function of its energy content.

Einstein Equations

In natural units ($\hbar = c = k_B = 1$), these equations relate the curvature of spacetime to its energy–momentum content,

$$G_{\mu\nu} \equiv R_{\mu\nu} - \frac{1}{2} R g_{\mu\nu} = 8\pi G\, T_{\mu\nu}, \tag{1.1}$$

where $R_{\mu\nu}$ and R denote the Ricci tensor and scalar curvature, respectively, and $T_{\mu\nu}$ is the stress–energy tensor describing the distribution of matter and radiation. The Einstein tensor $G_{\mu\nu}$ encapsulates the curvature of spacetime by combining the Ricci tensor and scalar in a way that guarantees the conservation of energy and momentum. The left-hand side thus encodes the geometry of spacetime, while the right-hand side specifies its physical sources.

The left-hand side encodes the geometry of spacetime, while the right-hand side specifies its physical sources.

Assuming large-scale statistical homogeneity and isotropy, the geometry of the Universe is described by the *Friedmann–Lemaître–Robertson–Walker* (FLRW) metric. The spacetime interval, or line element, is defined as

$$ds^2 = g_{\mu\nu}\, dx^\mu\, dx^\nu, \tag{1.2}$$

where $g_{\mu\nu}$ is the metric tensor. In the FLRW case, this takes the form

$$ds^2 = -dt^2 + a^2(t)\left[\frac{dr^2}{1-kr^2} + r^2(d\theta^2 + \sin^2\theta\, d\phi^2)\right], \tag{1.3}$$

where $a(t)$ is the scale factor, t the cosmic time, (r, θ, ϕ) the comoving spatial coordinates, and $k = \{-1, 0, +1\}$ denotes open, flat, or closed spatial curvature, respectively.

The Friedmann Equations

Inserting the FLRW metric into Einstein's field equations, one obtains the *Friedmann equations*, which describe the large-scale dynamics of the Universe's expansion [165, 114]. These equations connect the geometry of spacetime with its energy–momentum content, forming the foundation of modern cosmology. The expansion of the Universe is quantified by the *scale factor* $a(t)$, whose fractional growth rate defines the *Hubble parameter*, $H(t) \equiv \dot{a}/a$, where a dot denotes a derivative with respect to cosmic time t.

The first Friedmann equation is derived from Einstein's 00 component and relates the expansion rate to the total energy density ρ, spatial curvature k, and the cosmological constant Λ:

$$H^2 + \frac{kc^2}{a^2} = \frac{8\pi G}{3}\rho + \frac{\Lambda c^2}{3}. \tag{1.4}$$

Here, $k = 0, +1, -1$ corresponds to flat, closed, and open spatial geometries, respectively; G is Newton's gravitational constant; c is the speed of light; and ρ is the total energy density of all cosmic components.

It is often convenient to include the cosmological constant Λ as part of the energy density and pressure, by defining:

$$\rho \to \rho_{\text{total}} = \rho + \rho_\Lambda, \quad \& \quad p \to p_{\text{total}} = p + p_\Lambda,$$

where $\rho_\Lambda = \frac{\Lambda c^2}{8\pi G}, \quad p_\Lambda = -\rho_\Lambda c^2$, and $\rho_\Lambda = \frac{\Lambda c^2}{8\pi G}, \quad p_\Lambda = -\rho_\Lambda c^2$.

Then, the first Friedmann equation takes the commonly expressed form:

$$H^2 = \left(\frac{\dot{a}}{a}\right)^2 = \frac{8\pi G}{3}\rho - \frac{kc^2}{a^2}, \tag{1.5}$$

The acceleration of the Universe's expansion is governed by the second Friedmann equation, which is derived from the trace of Einstein's field equations:

$$\frac{\ddot{a}}{a} = -\frac{4\pi G}{3}\left(\rho + \frac{3p}{c^2}\right) + \frac{\Lambda c^2}{3}, \tag{1.6}$$

where $\ddot{a}$ is the second derivative of the scale factor respect to cosmic time and p denotes the pressure of the cosmic fluid. This equation highlights the competing effects of the attractive gravitational pull of matter and radiation (through ρ and p) and the repulsive influence of

the cosmological constant Λ.

Conservation of energy and momentum, expressed by $\nabla_\mu T^{\mu\nu} = 0$, leads to the continuity equation, which specifies how the energy density of each component evolves with cosmic expansion,

$$\dot{\rho} + 3H(\rho + p) = 0. \tag{1.7}$$

For a perfect fluid with equation of state $p = w\rho$ and constant w, the solution is

$$\rho(a) \propto a^{-3(1+w)}. \tag{1.8}$$

Each dominant cosmic component is characterized by a specific w and dominates at different epochs, shaping the expansion history. The table below summarizes their properties.

Component	Eq. of State (w)	$\rho(a)$	$a(t)$
Radiation	$1/3$	$\propto a^{-4}$	$\propto t^{1/2}$
Matter (baryons, CDM)	0	$\propto a^{-3}$	$\propto t^{2/3}$
Dark Energy (Λ)	-1	$\propto$ const.	$\propto e^{H_0 t}$

Table 1.1: Scaling of major cosmological components with scale factor a, their energy density evolution, and the corresponding time dependence of the scale factor $a(t)$.

The *critical density* $\rho_c = 3H^2/(8\pi G)$ defines the energy density required for spatial flatness ($k = 0$), and the density parameter $\Omega_i = \rho_i/\rho_c$ quantifies each component's contribution. Values of $\Omega_{\text{tot}} = 1, > 1$, or < 1 correspond to flat, closed, and open Universes, respectively.

The Boltzmann Equations

While the Friedmann equations describe the homogeneous and isotropic background evolution of the Universe, understanding the formation of cosmic structures requires studying small deviations from this background. These perturbations in the metric, density, velocity, and temperature fields evolve under gravity and microscopic interactions, giving rise to the

anisotropies observed in the CMB and the LSS of the Universe.

In the early Universe, each particle species can be described statistically by a phase-space distribution function $f_i(\mathbf{x}, \mathbf{p}, t)$, where i labels the species, $\mathbf{x}$ denotes comoving position, and $\mathbf{p}$ is the comoving momentum. The evolution of f_i is governed by the *Boltzmann equation*,

$$\frac{df_i}{dt} = \frac{\partial f_i}{\partial t} + \frac{d\mathbf{x}}{dt} \cdot \nabla_{\mathbf{x}} f_i + \frac{d\mathbf{p}}{dt} \cdot \nabla_{\mathbf{p}} f_i = C[f_i], \tag{1.9}$$

where $C[f_i]$ represents the *collision term*, accounting for interactions such as scattering, annihilation, or decay. In the absence of collisions, the equation reduces to Liouville's theorem ($df_i/dt = 0$), describing free-streaming evolution along geodesics.

The distribution function can be decomposed into a background part $f_i^{(0)}(p, t)$ and a perturbation $\Psi_i(\mathbf{x}, \mathbf{p}, t)$:

$$f_i(\mathbf{x}, \mathbf{p}, t) = f_i^{(0)}(p, t) \left[1 + \Psi_i(\mathbf{x}, \mathbf{p}, t)\right]. \tag{1.10}$$

The background term governs the homogeneous evolution (as in the Friedmann equations), while the perturbation Ψ_i encodes spatial and temporal fluctuations that give rise to anisotropies and inhomogeneities.

The Boltzmann equations for different species (photons, baryons, neutrinos, and dark matter) are coupled to the perturbed Einstein equations through the metric perturbations. Solving this system provides the time evolution of density contrasts, velocity fields, and gravitational potentials, forming the basis of linear cosmological perturbation theory.

For photons, interactions with free electrons via Thomson scattering introduce a non-negligible collision term in the Boltzmann hierarchy, sourcing the characteristic temperature anisotropies and polarization patterns observed in the CMB. For collisionless species such as cold dark matter or neutrinos after decoupling, $C[f_i] = 0$, and their distribution functions evolve purely

under gravitational effects. In practice, solving the coupled Einstein–Boltzmann system requires numerical integration over time and wavenumber. This is achieved by Boltzmann solvers such as `CAMB` [281] and `CLASS` [274, 98], which compute key cosmological observables including the CMB temperature and polarization power spectra, the matter power spectrum $P(k)$, as well as several cosmological parameters and background quantities such as the Hubble parameter $H(z)$ and the densities of individual species.

These tools are essential in modern cosmology, enabling precise comparisons between theoretical models and high-precision observational data. Together with the Friedmann equations, the Boltzmann equations provide a comprehensive framework that describes both the Universe's background expansion and the evolution of linear perturbations, thereby shaping the LSS and CMB anisotropies we observe today.

In summary, Einstein's field equations lay the foundation for our understanding of gravity and spacetime geometry, from which the Friedmann equations describe the large-scale dynamics of the Universe's expansion. The Boltzmann equations complement this picture by tracking the evolution of matter and radiation perturbations on this expanding background. Together, these equations form the core theoretical framework of modern cosmology, linking fundamental physics with observations to reveal the history and composition of the cosmos.

The Standard Cosmological Model: ΛCDM

The Λ Cold Dark Matter (ΛCDM) model stands as the foundation of modern cosmology, celebrated for its elegant simplicity and remarkable ability to accurately describe a wide range of observations. Despite being defined by only six fundamental parameters, it provides an exceptionally precise fit to data spanning the anisotropies of the CMB, the LSS of the Universe, and the primordial element abundances predicted by BBN.

The minimal ΛCDM model is parametrized by six key quantities:

$$\begin{cases} \Omega_b h^2 & \text{Physical baryon density} \\ \Omega_c h^2 & \text{Physical cold dark matter density} \\ \theta_s & \text{Angular size of the sound horizon at recombination} \\ \tau & \text{Optical depth to reionization} \\ A_s & \text{Amplitude of the primordial scalar perturbations} \\ n_s & \text{Spectral index of the primordial scalar perturbations} \end{cases} \tag{1.11}$$

At its core, ΛCDM describes the Universe as composed of several energy components. Baryonic matter—which forms stars, planets, and gas—accounts for roughly $\Omega_b^0 \simeq 0.049$ of the total energy density and behaves as pressureless matter on cosmological scales. Radiation, dominated by photons, contributes a small fraction $\Omega_r^0 \sim 10^{-4}$, while neutrinos transition from relativistic to non-relativistic, affecting both radiation and matter densities depending on their masses.

The dominant components are cold dark matter (CDM), a non-baryonic, non-relativistic form of matter comprising about $\Omega_c^0 \simeq 0.265$ and driving structure formation, and dark energy, modeled as a cosmological constant Λ, which constitutes roughly $\Omega_\Lambda^0 \simeq 0.685$ and is responsible for the Universe's accelerated expansion.

Embedded within the framework of General Relativity and seeded by nearly scale-invariant primordial fluctuations generated during inflation, the ΛCDM model serves as the backbone of contemporary cosmology. Its enduring success lies in encapsulating the Universe's complexity within a simple and predictive theoretical framework, supported by an extensive body of high-quality observational data.

1.2 Neutrinos in Cosmology

In the early Universe, at temperatures much higher than the electron rest mass energy ($T \gg m_e c^2 \approx 0.511\,\mathrm{MeV}$), neutrinos were in thermal equilibrium with the primordial plasma through weak interactions. Their distribution followed Fermi-Dirac statistics,

$$f(E, T_\nu) = \frac{1}{\exp(E/T_\nu) + 1}, \tag{1.12}$$

and during this period neutrinos shared the same temperature as photons and electrons, i.e., $T_\nu = T_\gamma = T$.

The neutrino number density and energy density can be expressed as integrals over their momentum distribution:

$$n_\nu = \frac{g}{(2\pi)^3} \int f(E, T_\nu)\, d^3p, \quad \rho_\nu = \frac{g}{(2\pi)^3} \int E f(E, T_\nu)\, d^3p, \tag{1.13}$$

where g represents the degrees of freedom of neutrinos.

As the Universe expands and cools, the weak interaction rate, roughly $\Gamma_\nu \sim G_F^2 T^5$ (with G_F the Fermi coupling constant), falls below the Hubble expansion rate $H(T) \sim \sqrt{g_*}\, T^2 / M_{\mathrm{Pl}}$, where g_* is the effective number of relativistic degrees of freedom and M_{Pl} is the Planck mass. This causes neutrinos to decouple from the plasma.

Shortly after decoupling, electron-positron pairs annihilate, transferring their entropy to photons and increasing the photon temperature relative to that of neutrinos. This process yields the well-known relation:

$$\frac{T_\nu}{T_\gamma} = \left(\frac{4}{11}\right)^{1/3}. \tag{1.14}$$

Using this, the neutrino number density per species today relates to the photon number density by:

$$n_\nu = \frac{3}{4}\left(\frac{4}{11}\right) n_\gamma, \tag{1.15}$$

where the factor 3/4 accounts for the difference between Fermi-Dirac and Bose-Einstein statistics.

The energy density of relativistic neutrinos per species is similarly connected to the photon energy density:

$$\rho_\nu = \frac{7}{8}\left(\frac{4}{11}\right)^{4/3} \rho_\gamma, \tag{1.16}$$

where the factor 7/8 reflects neutrinos being fermions.

The total radiation energy density including neutrinos can be parameterized by the effective number of relativistic neutrino species $N_{\rm eff}$:

$$\rho_R = \left[1 + \frac{7}{8}\left(\frac{4}{11}\right)^{4/3} N_{\rm eff}\right] \rho_\gamma. \tag{1.17}$$

Neutrinos decouple before electron–positron annihilation is complete, causing partial energy transfer from the annihilating plasma to the neutrino sector, which raises the total radiation energy density above the value expected for three fully decoupled species. Standard cosmology therefore predicts $N_{\rm eff} \approx 3.044$, accounting for three active neutrino flavors plus small corrections from non-instantaneous decoupling [275, 139].

As neutrinos become non-relativistic at late times ($m_\nu \gg T_\nu$), their energy density evolves as $\rho_\nu = m_\nu n_\nu$, contributing to the matter content of the Universe. The neutrino mass sum Σm_ν is constrained by cosmology, with the present-day neutrino density parameter approximately

given by:

$$\Omega_\nu h^2 \approx \frac{\Sigma m_\nu}{93.14\,\mathrm{eV}}. \tag{1.18}$$

Due to their high thermal velocities, neutrinos free-stream and suppress structure formation below a characteristic scale, which depends on their mass and redshift.

Neutrino oscillation experiments have established that neutrinos change flavor as they propagate, requiring non-zero masses and mixing. The flavor eigenstates ν_α ($\alpha = e, \mu, \tau$) are quantum superpositions of mass eigenstates ν_i ($i = 1, 2, 3$), connected by the unitary Pontecorvo–Maki–Nakagawa–Sakata (PMNS) matrix U:

$$\nu_\alpha = \sum_i U_{\alpha i} \nu_i. \tag{1.19}$$

Oscillation experiments measure the squared mass differences Δm^2_{21} and Δm^2_{31}, but do not provide the absolute mass scale or mass ordering. In the simplest two-flavor approximation, the probability that a neutrino of flavor ν_α oscillates into another flavor ν_β after traveling a distance L in vacuum is given by

$$P_{\alpha\to\beta} = \sin^2(2\theta)\,\sin^2\left(\frac{\Delta m^2 L}{4E}\right), \tag{1.20}$$

where θ is the mixing angle, E is the neutrino energy, and $\Delta m^2 = m_2^2 - m_1^2$ is the mass-squared difference. This expression highlights the dependence of oscillations on Δm^2, which determines the characteristic oscillation length.

In realistic environments, however, oscillations are medium-dependent: thermal and matter effects modify the effective mixing parameters and mass-squared differences, altering the oscillation behavior in dense media such as the Sun or the early Universe plasma.

Neutrino oscillation experiments have determined that the neutrino mass-squared differences for solar and atmospheric oscillations differ by about two orders of magnitude:

$$\Delta m^2_{\rm solar} = (7.53 \pm 0.18) \times 10^{-5}\,{\rm eV}^2, \tag{1.21}$$

$$\Delta m^2_{\rm atm} = (2.455 \pm 0.028) \times 10^{-3}\,{\rm eV}^2\ [(-2.529 \pm 0.029) \times 10^{-3}\,{\rm eV}^2]. \tag{1.22}$$

for the normal [inverted] ordering [315]. Consequently, there is a minimum combined mass of the three active neutrinos, $\Sigma m_\nu = m_1 + m_2 + m_3$, which depends on the mass ordering:

$$\begin{aligned} \Sigma m_\nu^{\rm NO} &= m_1 + \sqrt{m_1^2 + \Delta m^2_{\rm solar}} + \sqrt{m_1^2 + |\Delta m^2_{\rm atm}|}, \\ \Sigma m_\nu^{\rm IO} &= m_3 + \sqrt{m_3^2 + |\Delta m^2_{\rm atm}|} + \sqrt{m_3^2 + |\Delta m^2_{\rm atm}| + \Delta m^2_{\rm solar}}, \end{aligned} \tag{1.23}$$

where the lightest eigenstate is m_1 for normal ordering (NO) and m_3 for inverted ordering (IO). Assuming minimal masses ($m_1 = 0$ for NO and $m_3 = 0$ for IO), the corresponding minimal total masses are $\Sigma m_\nu^{\rm NO} \approx 58\,{\rm meV}$ and $\Sigma m_\nu^{\rm IO} \approx 101\,{\rm meV}$.

Cosmological observations provide complementary constraints on the absolute neutrino mass scale through their effects on the expansion history and structure formation, making them essential probes of neutrino properties beyond the reach of laboratory experiments.

1.3 Cosmological Observations

Modern cosmology draws upon a diverse set of observational probes that collectively illuminate the evolution, composition, and geometry of the Universe. These observations cover a broad range of epochs and physical phenomena, from the primordial radiation emitted shortly after the Big Bang to the large-scale distribution of matter in the current Universe.

Cosmic Microwave Background (CMB)

In the early Universe, conditions were extremely hot and dense, with photons and baryons tightly coupled through frequent interactions, forming a plasma. As the Universe expanded, it cooled adiabatically. Around a temperature of approximately $T \approx 0.3\,\mathrm{eV}$ (corresponding to redshift $z \sim 1100$), electrons and protons combined to form neutral hydrogen in a process known as recombination. This event caused the free electron density to drop dramatically, allowing photons to decouple from the plasma and propagate freely. These photons constitute the Cosmic Microwave Background (CMB), observed today as nearly isotropic blackbody radiation at a temperature close to 2.7 K.

The CMB exhibits tiny anisotropies with temperature fluctuations at the level of $\sim 10^{-5}$ across the sky. These fluctuations contain crucial information about the early Universe and are conveniently analyzed through a spherical harmonic decomposition on the celestial sphere. The temperature fluctuations, $\delta T(\theta, \phi)/T$, are expanded as

$$\frac{\delta T}{T}(\theta, \phi) = \sum_{\ell=0}^{\infty} \sum_{m=-\ell}^{\ell} a_{\ell m} Y_\ell^m(\theta, \phi), \tag{1.24}$$

where Y_ℓ^m are the spherical harmonics. Statistical isotropy ensures that the angular power spectrum,

$$C_\ell = \frac{1}{2\ell + 1} \sum_{m=-\ell}^{\ell} \langle |a_{\ell m}|^2 \rangle, \tag{1.25}$$

fully characterizes the two-point statistics of the temperature anisotropies. Measurements of the Cosmic Microwave Background (CMB) power spectra by experiments such as COBE [372], WMAP [374], and Planck [42] have provided some of the tightest constraints on fundamental cosmological parameters to date. More recent ground-based experiments, including the Atacama Cosmology Telescope (ACT) [125, 109] and the South Pole Telescope (SPT) [111], have improved these measurements with higher resolution and sensitivity at smaller

angular scales.

Baryon Acoustic Oscillations (BAO)

Prior to recombination, the tightly coupled photon-baryon plasma experienced acoustic oscillations driven by the competition between gravitational forces and radiation pressure. These sound waves propagated through the primordial medium, imprinting a characteristic scale—the sound horizon—on the distribution of baryons. After photons decoupled from baryons, this acoustic scale remained encoded in the matter distribution, observable today as baryon acoustic oscillations (BAO) in the large-scale structure.

The comoving sound horizon at the baryon drag epoch is given by

$$r_d = \int_{z_d}^{\infty} \frac{c_s(z)}{H(z)}\, dz, \tag{1.26}$$

where $c_s(z)$ represents the sound speed in the photon-baryon fluid, $H(z)$ is the Hubble parameter, and z_d corresponds to the drag redshift when baryons effectively decoupled from photons. This scale acts as a robust standard ruler that can be measured through galaxy and quasar clustering in large redshift surveys.

By detecting the BAO feature at various redshifts, cosmologists extract the angular diameter distance,

$$D_A(z) = \frac{c}{1+z} \int_0^z \frac{dz'}{H(z')}, \tag{1.27}$$

as well as the expansion rate $H(z)$, thereby providing key constraints on the Universe's expansion history and fundamental cosmological parameters.

In addition to BAO, redshift surveys measure the growth of cosmic structure through the combination $f\sigma_8$, where $f(a)$ is the growth rate of matter perturbations and σ_8 quantifies the

root-mean-square fluctuation amplitude of the matter density field on scales of $8\,h^{-1}$Mpc. This quantity is defined as

$$f\sigma_8(a) = a\frac{d\ln\delta_m}{da}\sigma_{8,0}, \tag{1.28}$$

where $\delta_m(a)$ is the linear growth factor normalized at present ($a = 1$). Measurements of $f\sigma_8$ from redshift-space distortions complement BAO by probing the dynamics of structure formation.

The Sloan Digital Sky Survey (SDSS) was among the pioneering experiments to detect the BAO signal with high precision [12, 166, 61], establishing BAO as a cornerstone cosmological probe. More recently, the Dark Energy Spectroscopic Instrument (DESI) survey has dramatically expanded the reach and precision of BAO measurements by mapping tens of millions of galaxies and quasars over a wide redshift range [28, 20].

Type Ia Supernovae (SNe Ia)

SNe Ia are among the brightest astrophysical objects, serving as standardizable candles for distance measurements. Their well-understood intrinsic luminosity enables determination of luminosity distances from observed apparent magnitudes. The luminosity distance $D_L(z)$ relates to the apparent magnitude m and absolute magnitude M through

$$M = m - 5\log_{10}\left(\frac{D_L}{10\,\mathrm{pc}}\right). \tag{1.29}$$

The luminosity distance itself depends on the cosmological model via

$$D_L(z) = c(1+z)\int_0^z \frac{dz'}{H(z')}. \tag{1.30}$$

Observations of SNe Ia across a range of redshifts provided the first direct evidence for the

accelerated expansion of the Universe and continue to offer powerful constraints on dark energy and cosmological parameters.

Notable recent SNe Ia datasets include the Pantheon+ sample [358, 105], the Union3 compilation [351], and the Dark Energy Survey Year 5 (DES Y5) sample [18], each providing large, well-calibrated supernova samples with careful treatment of systematic uncertainties and selection effects.

1.4 Challenges to ΛCDM from Current Observational Data

The ΛCDM model has achieved remarkable success in describing a vast range of cosmological observations, including the CMB, BBN, and the formation of LSS. Nonetheless, as observational precision has steadily improved, several notable discrepancies—often referred to as *cosmological tensions* or *anomalies*—have persisted and even intensified, calling into question the completeness of the standard cosmological framework.

Among these, the most statistically significant is the so-called *Hubble tension*, referring to the discrepancy between the local Hubble expansion rate (H_0) inferred from early- and late-Universe measurements. Within the context of the ΛCDM model, the *Planck* satellite's high-precision observations of the CMB anisotropies yield an inferred value of $H_0 = 67.4 \pm 0.5$ $\mathrm{km\,s^{-1}\,Mpc^{-1}}$ [42]. This estimate is obtained indirectly by fitting the angular scale of the acoustic peaks in the CMB power spectrum, assuming a spatially flat ΛCDM cosmology with standard radiation content. Consistent results are also reported by ground-based CMB experiments such as the Atacama Cosmology Telescope (ACT) [109] and the South Pole Telescope (SPT) [111], which provide independent high-resolution measurements of the damping tail and lensing-induced smoothing of the CMB power spectra, reinforcing the lower H_0

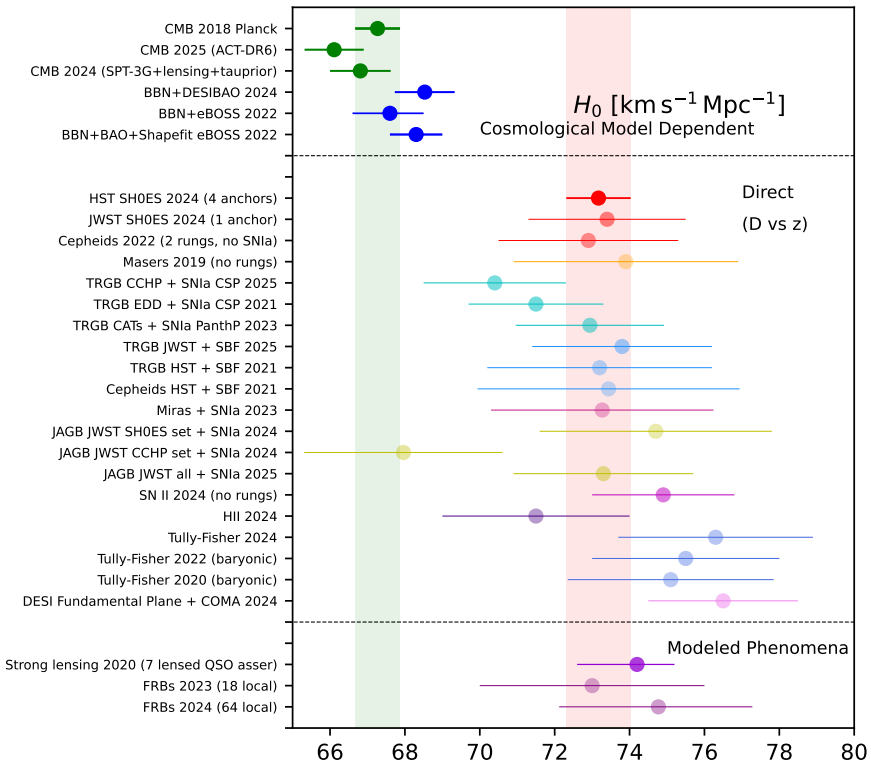


Figure 1.1: Summary of H_0 estimates from different cosmological probes with error bars smaller than 3.5 km s^{-1} Mpc^{-1}. Figure taken from CosmoVerse White Paper [144].

estimate.

In contrast, late-Universe determinations based on the cosmic distance ladder—anchored by Cepheid-calibrated Type Ia supernovae—yield substantially higher values. The SH0ES collaboration reports $H_0 = 73.0 \pm 1.0$ km s^{-1} Mpc^{-1} [344], in $> 5\sigma$ tension with the CMB-inferred value. Since these approaches probe different epochs and rely on distinct physical mechanisms, this discrepancy cannot be trivially attributed to a single measurement bias. Early-Universe constraints depend on model assumptions about the pre-recombination physics and sound horizon scale, while distance-ladder methods are grounded in empirical calibrations of nearby standard candles at $z \lesssim 0.1$. Complementary probes such as

BAO, gravitational lensing time delays, and standard sirens from gravitational waves provide intermediate-redshift constraints, yet the discrepancy remains robust across independent datasets. The current tension in the measurements of the Hubble constant is well illustrated in Figure 1.1, which summarizes recent H_0 estimates from various cosmological probes and illustrates the existing tension.

A second, though milder, tension appears in measurements of the amplitude of matter fluctuations, typically quantified by the parameter $S_8 \equiv \sigma_8 \sqrt{\Omega_m/0.3}$. Weak gravitational lensing and galaxy clustering surveys consistently infer lower values of S_8 than those predicted by the ΛCDM model calibrated to CMB data. Although this discrepancy remains at the $\sim 2\sigma$ level, it may hint at modifications to the growth rate of structure, new dark sector interactions, or a breakdown of the assumption that General Relativity holds unaltered on cosmological scales.

A newly emerged anomaly that has attracted attention in cosmological analyses is the "negative neutrino mass" problem. As cosmological datasets become increasingly precise, some global fits yield best-fit values for the total neutrino mass, Σm_ν, that are slightly negative—an unphysical result—although this deviation remains below the 2σ level. We study this anomaly in detail using state-of-the-art cosmological likelihoods in Chapter 5.

To address these tensions, several extensions to the ΛCDM model have been proposed, including dynamical dark energy with $w \neq -1$, non-zero spatial curvature, additional relativistic species parameterized by $N_{\rm eff}$, and Early Dark Energy (EDE) models that introduce a subdominant component before recombination to help alleviate the H_0 tension. A detailed discussion of these models, their motivations, and performance in solving existing cosmolical tensions is presented in Chapter 2. Subsequent chapters investigate observational constraints and the connection between neutrino physics and cosmological tensions using the latest CMB, BAO, SNe, and LSS data.

Sterile Neutrinos in Cosmology

Among the many proposed extensions, sterile neutrinos have garnered significant attention due to their potential to impact both the radiation and matter content of the Universe. Sterile neutrinos are hypothetical neutral fermions that do not interact via Standard Model gauge forces but can mix with active neutrinos. Light, eV-scale sterile neutrino states are suggested by anomalies in short-baseline oscillation experiments [151]. If produced in the early Universe through oscillations or other mechanisms, sterile neutrinos contribute to $N_{\rm eff}$, altering the expansion rate and the evolution of primordial perturbations [8, 135]. Depending on their mass and production mechanism, sterile neutrinos can also contribute to the total matter density at late times, affecting the growth of structure and the matter power spectrum in ways analogous to active neutrinos [214].

Sterile neutrinos are hypothetical neutral fermions that do not participate in Standard Model gauge interactions but can mix with the active neutrino flavors. Their existence would have profound implications for both the radiation and matter content of the Universe. In the early Universe, sterile neutrinos can be produced through oscillations or other mechanisms, contributing to the effective number of relativistic species, $N_{\rm eff}$, which affects the expansion rate and the evolution of primordial density fluctuations. Depending on their mass and production history, sterile neutrinos can also contribute to the total matter density at late times, influencing the growth of LSS in a manner analogous to active neutrinos.

On the one hand, light sterile neutrinos with masses on the order of eV are particularly significant in the context of current cosmological tensions. Their contribution to $N_{\rm eff}$ can increase the early-Universe expansion rate, potentially raising the inferred value of the Hubble constant, H_0, and thereby partially alleviating the well-known Hubble tension. Sterile neutrinos with masses in eV scale, may also impact the matter power spectrum and the clustering amplitude parameter S_8. Detailed analysis of these neutrinos and their role in addressing cosmological tensions is provided in Chapter 5.

On the other hand, sterile neutrinos with masses in the keV range represent compelling warm dark matter candidates, offering unique windows into the physics of the early Universe prior to BBN. Their production mechanisms depend sensitively on the thermal history and possible dark-sector interactions, which may allow them to evade standard cosmological bounds. These neutrinos influence structure formation at small scales, providing potentially observable signatures distinct from cold dark matter. A comprehensive discussion of keV-scale sterile neutrinos and their cosmological impact is given in Chapter 3.

Together, these sterile neutrino scenarios illustrate the rich phenomenology beyond the Standard Model neutrino sector and demonstrate how cosmological observations serve as powerful probes of new physics. For further details on the theoretical frameworks, observational constraints, and their interplay with cosmological tensions, the reader is referred to Chapters 3, 4, and 5.

These candidate models and extensions to the standard cosmological model open multiple avenues to address current tensions and anomalies, enriching the landscape of possible physics beyond ΛCDM. In the following chapters, we explore their phenomenology, confront them with the latest datasets from CMB measurements, baryon acoustic oscillations, supernovae, and LSS surveys, and assess their viability in the light of upcoming precision cosmology missions.

1.5 Bayesian Analysis Framework

The interpretation of cosmological data often relies on Bayesian statistical inference, which provides a coherent framework for parameter estimation and model comparison [382]. In

this formalism, all inferences are derived from Bayes' theorem,

$$P(\boldsymbol{\theta}|D, M) = \frac{P(D|\boldsymbol{\theta}, M)P(\boldsymbol{\theta}|M)}{P(D|M)}, \tag{1.31}$$

where $P(\boldsymbol{\theta}|D, M)$ is the posterior probability distribution of the model parameters $\boldsymbol{\theta}$ given the data D and model M. The term $P(D|\boldsymbol{\theta}, M)$ denotes the likelihood, which quantifies how well a given parameter set reproduces the observed data, while $P(\boldsymbol{\theta}|M)$ represents the prior, encapsulating our knowledge (or assumptions) about the parameters before considering the data. The denominator, $P(D|M)$, also known as the Bayesian evidence, serves as a normalization factor and plays a key role in model selection.

In cosmology, the high dimensionality and complexity of parameter spaces render analytical evaluation of the posterior distribution intractable. Instead, numerical methods such as Markov Chain Monte Carlo (MCMC) are employed to efficiently sample from the posterior distribution [382]. MCMC algorithms generate correlated random samples that asymptotically trace the shape of the target distribution, allowing one to compute expectation values, confidence intervals, and marginalized constraints. Among the most widely used implementations are the Metropolis–Hastings algorithm [303, 221] that relies on a random-walk proposal distribution that explores parameter space by accepting or rejecting trial steps according to the Metropolis criterion, ensuring convergence to the final posterior.

The parameter inference in this work is performed using the `Cobaya` software package [380], a flexible and modern framework for Bayesian inference in cosmology. `Cobaya` interfaces with state-of-the-art Boltzmann solvers such as `CAMB` and `CLASS`, as well as external likelihoods from CMB, LSS, SNe, and other cosmological probes. It employs MCMC algorithms to generate statistically converged chains that represent the posterior distribution of cosmological parameters. Additionally, the internal `minimizer` sampler was used to locate best-fit points and evaluate χ^2 values, providing a reliable method for likelihood maximization and model

comparison.

Ensuring convergence of the Markov chains is crucial for obtaining robust and unbiased parameter estimates. A widely adopted diagnostic for assessing convergence is the Gelman–Rubin statistic R, which compares the variance between multiple chains to the variance within each chain:

$$R = \sqrt{\frac{\hat{V}}{W}}, \tag{1.32}$$

where W denotes the average within-chain variance and $\hat{V}$ represents the total variance. Convergence is typically considered satisfactory when the statistic approaches unity, within a tolerance of $|R - 1| < 0.01$, indicating that all chains are sampling consistently from the same posterior distribution [197].

The resulting chains were analyzed with `GetDist` [279], a Python package designed to process MCMC outputs from `Cobaya`, enabling comprehensive posterior visualization and the computation of marginalized parameter constraints. Throughout the course of my PhD, I developed extensive expertise with both `Cobaya` and `GetDist`, applying these tools to perform cosmological parameter inference, evaluate the performance of extended models beyond the standard ΛCDM paradigm, and explore degeneracies among key cosmological parameters. This analysis framework, implemented through `Cobaya`, `GetDist`, and modern Boltzmann solvers, provides a statistically rigorous and computationally efficient approach for constraining cosmological parameters and testing extensions to the standard cosmological model.

1.6 Scope and Structure of this Thesis

This dissertation is organized to provide a comprehensive exploration of current challenges and extensions to the standard cosmological model, with a focus on neutrino physics and

early-Universe dynamics.

Chapter 2 reviews the theoretical foundations of modern cosmology, including the ΛCDM model, linear perturbation theory, and key cosmological observables. It also investigates prominent cosmological tensions, such as the discrepancies in the Hubble constant and the amplitude of matter clustering, assessing various extensions to ΛCDM and highlighting early dark energy as a promising partial resolution.

Chapter 3 explores scenarios of low-reheating cosmologies and the role of keV-scale sterile neutrinos as probes of the pre–Big Bang Nucleosynthesis era. This chapter demonstrates how such models can potentially ease the H_0 tension by modifying early-Universe physics.

Building on this, Chapter 4 focuses on neutrino properties within extended cosmological frameworks, analyzing recent datasets from the CMB, baryon acoustic oscillations, and supernovae. It finds indications favoring partially thermalized sterile neutrinos when local measurements of H_0 are included.

Chapter 5 incorporates the latest data from the DESI DR2 BAO measurements to refine constraints on sterile neutrinos and other extensions, confirming that sub-eV sterile neutrinos remain consistent with current cosmological observations while alleviating the Hubble tension.

Chapter 6 presents a sound-horizon-independent determination of the Hubble constant by combining BAO, CMB lensing, galaxy clustering, and supernova data. This chapter offers a robust, model-agnostic framework to assess the necessity of new physics at recombination.

Finally, Chapter 7 summarizes the key findings of this work and outlines future prospects for advancing our understanding of physics beyond the standard cosmological paradigm.

Together, these chapters provide a coherent investigation into how extensions to ΛCDM, especially those involving neutrino physics and early-Universe phenomena, can shed light on

the tensions currently shaping modern cosmology.

Chapter 2

Early or Phantom Dark Energy, Self-Interacting, Extra, or Massive Neutrinos, Primordial Magnetic Fields, or a Curved Universe: An Exploration of Possible Solutions to the H_0 and σ_8 Problems

This chapter is a reprint of material published in Physical Review D 106, 103517(2022).
Reprinted with permission © 2022 American Physical Society.

2.1 Introduction

So far, the best-fitting scenario for describing our Universe on large scales is the standard model of cosmology, also known as ΛCDM. Its success in simultaneously explaining cosmological observables at low and high redshift is undeniable [107]; nevertheless, in this framework several tensions in different data sets, *e.g.*, between the cosmic microwave background (CMB) and observations at low redshift including the distance ladder and large-scale structure (LSS), have emerged. One of these discrepancies is the "H_0 tension", which is a mismatch between the present expansion rate of the Universe, *i.e.*, the Hubble constant H_0, inferred from the distance ladder built from Cepheid variables and Type Ia supernovae (SN Ia), and H_0 inferred from the angular power spectra of the CMB, given a Friedmann ΛCDM cosmology evolution to today.

Recently, this conflict has grown to a level of approximately $\sim 5\sigma$ provided that $H_0 = 67.36 \pm 0.54\,\mathrm{km/s/Mpc}$ from Planck CMB data, within the ΛCDM model [42], largely deviates from $H_0 = 73.04 \pm 1.04\,\mathrm{km/s/Mpc}$, reported by the SH0ES collaboration using the Cepheid-based distance ladder [344]. Another anomaly arises when measuring σ_8, which is the value of the root-mean-square fluctuation of density perturbations calculated with a top-hat window function of $k = 8\,h^{-1}\,\mathrm{Mpc}$. The value σ_8 is often combined with the parameter it is most degenerate with in the combination $S_8 \equiv \sigma_8\sqrt{\Omega_\mathrm{m}/0.3}$, with Ω_m being the matter density parameter. The value of S_8 inferred from Planck CMB data within the ΛCDM framework, $S_8 = 0.832 \pm 0.013$ [42], and low-redshift probes such as weak gravitational lensing and galaxy clustering [59, 386, 35, 120, 356, 228, 67, 140, 333] do not agree with the value inferred from the CMB at a statistical level from approximately 2σ to 4σ [156].

These cosmological inconsistencies may originate from unaccounted systematic errors in the the local distance ladder measurements and/or in the Planck observations. Extended experimental work has been carried out to determine if unknown systematics are the main reason

for this mismatch. For instance, errors in SN Ia dust extinction modelling and intrinsic variations [310, 309, 393], Cepheid metallicity correction [160] and different types of SN Ia populations are potential candidates for these systematic effects; see [149] for a complete review. Additional methods of calibrating the distance ladder, such as using the J-region asymptotic giant branch [273], or calibration via gravitational-wave "standard siren" [121] may provide an independent measure and test of the tension present in local to high-redshift determinations of H_0. In the meantime, it is of value to explore in detail the nature of new physics beyond ΛCDM that can be a robust solution to the H_0 tension, as well as models that aim to solve the S_8 tension, independently or in concert with H_0. That is what we explore here.

Depending on the cosmic period that the new physics takes effect, proposed models can be categorized into late-time and early-time solutions. The first category changes expansion history of the Universe at low redshift, while the latter modifies the physics of the early Universe before recombination; see [357] for a recent review. Late-time solutions include, for example, wCDM [42], w_0w_aCDM [42] or an interacting dark energy model [288, 208]. However, given tight constraints on cosmic expansion history at low redshift, late-time solutions are in general highly disfavored as solutions to H_0 tension [150, 258]. On the other hand, early-time solutions, *e.g.*, early dark energy (EDE) [334, 335, 370], a modified neutrino sector [97, 339, 119, 73, 89, 355, 184, 82, 245, 320, 267, 325, 100, 222, 134, 176, 385, 93, 8], baryon inhomogeneity sourced from primordial magnetic fields [243] and extra dark radiation before recombination (*e.g.*, Ref. [383]), are seen as better candidates in alleviating the tension by keeping ΛCDM's successes in the late Universe intact. We also consider nonzero neutrino mass as the solution to the S_8 tension [311, 84, 396, 95, 300], both on its own and in tandem with other new physics related to both tensions.

Based on established statistical methods for model rejection, we explore a collection of new physics models proposed to alleviate the tensions. Many existing and new theoretical pro-

posals in the literature only judge a new model relative to standard ΛCDM, and sometimes by only comparing the inferred central values of H_0 or S_8 between ΛCDM and the new model. Furthermore, the effects of new models on several other robust cosmological data sets go unaddressed, including the baryon acoustic oscillation (BAO) feature and detailed accelerated expansion history at low redshifts, measured by SN Ia. Meanwhile, new results in observational cosmology often explore only one or two example excursions from ΛCDM. In our work we combine a large set of proposed tension-reduction models with the latest robust observational cosmological data in order to assess which models may successfully resolve the tension while being consistent with the available hallmark data. Along these lines, we consider and evaluate, in detail, the specific statistical significance of any remaining H_0 and S_8 tensions in proposed models, separately and in concert. In summary, the objective of this work is finding the best model, or models, proposed so far that agree with measurements that indicate these anomalies.

This paper is organized as follows: in Sec. 4.5, we list the beyond ΛCDM models studied in this work and discuss the way that they reduce cosmic tensions. In Sec. 2.3, we give details of and motivations for the data sets included in our calculations and the statistical strategies and computational tools employed for deriving statistical significance. We present and discuss the results of the tests made in Sec. 2.4. In Sec. 5.5, we analyse the results and discuss the physics of cosmological parameters' shift for different models and tension data sets, relative to the ΛCDM fit to the CMB. Finally, we summarize the main conclusions of this work in Sec. 2.6.

2.2 Beyond ΛCDM models

In this section, we discuss the beyond ΛCDM models considered in this work. We briefly sketch the physics of each model that alleviate the cosmic tensions and we refer readers to

Appendix 2.7 for details of the models.

- w**CDM**: In the dark energy domination era, phantom dark energy with equation of state $w < -1$ can further accelerate the expansion of the Universe compared to the standard $w = -1$ case. Therefore, the H_0 inferred from CMB experiments can be reconciled with the H_0 measured from local measurements [147, 289, 383, 55]; see also [146, 398] for different parameterizations of w. The evolution of dark energy density via a non-standard equation of state w also alters the growth of structure [10, 250, 257], which can alleviate or exacerbate the S_8 tension.

- **Non-trivial neutrino mass**, $\Sigma m_\nu > 0.06\,\mathrm{eV}$: a lower amplitude of clustering at smaller scales, and therefore smaller σ_8 or S_8, can be achieved by increasing the neutrino mass and its contribution to the total matter density [234]. Several papers have suggested an indication of non-zero active neutrino masses, or combinations of extra mass eigenstates and neutrino masses because of low-σ_8 measurements, *e.g.*, Refs. [248, 84, 396, 159, 95].

- Λ**CDM+**$N_{\rm eff}$: A correlation exists between the Hubble parameter inferred from CMB measurements and the radiation energy budget in the early Universe. The latter can be parameterized by the effective number of relativistic degrees of freedom $N_{\rm eff}$. Therefore, extra relativistic species beyond the standard model neutrinos, such as dark radiation, can effectively reduce the sound horizon, *i.e.*, increase H_0. Additional relativistic energy density affects the position of the acoustic peaks of the CMB relative to the photon damping scale, both of which are well constrained by measurements of the CMB. Extra (sterile) neutrino mass eigenstates can mimic relativistic degrees of freedom at early times and contribute to Σm_ν at late times, and therefore may combine the effects of Σm_ν and $N_{\rm eff}$. See, *e.g.*, a review in Ref. [8].

- **Non-zero curvature**: The size of angular diameter distance, which is measured in

low-redshift measurements such as BAO and SNe, is closely related to the curvature of Universe. Therefore, allowing a non-flat Universe, *i.e.*, making the density parameter of curvature Ω_k a free parameter, offers an additional degree of freedom to modify the low-redshift spacetime geometry. Non-zero curvature also alters the growth of structure, potentially alleviating the S_8 tension. A non-zero curvature can be integrated into models that modify the early Universe to better fit low-redshift measurements; see Refs. [353, 212, 148] for example. Models that modify the electron mass [361] along with added curvature are highly constrained by primordial nucleosynthesis [363], so we do not consider them here.

- **Early dark energy**: A potential solution of H_0-tension is early dark energy (EDE) [334, 335, 370], which behaves like a cosmological constant with an equation of state -1 and makes up a non-negligible fraction of the energy budget before a critical redshift z_c. At $z < z_c$, the energy density of EDE dilutes faster than radiation. By requiring z_c being larger than the redshift of recombination, the expansion rate is boosted at $z > z_c$ while leaving the cosmology at $z < z_c$ intact. Therefore, the sound horizon is reduced such that the inferred value of H_0 is larger which reconciles the result from early- and late-time observations. In our work, we adopt the EDE model of Smith et al. [370] as it can provide a better fit to the high-ℓ C_ℓ of Planck 2018.

- **Self-interacting neutrinos (SIν)**: In the standard cosmology, it is well-known that neutrinos free-stream after the decoupling from the Standard Model (SM) thermal bath, damping the perturbations below the corresponding free-streaming scale. It has been proposed that increasing the relativistic degrees of freedom and/or introducing a non-zero neutrino mass can help in alleviating the Hubble tension; however, these kinds of scenarios also result in a stronger suppression on perturbations due to the free-streaming of neutrinos and relativistic particles. To counteract the damping effect, one can consider including non-standard interactions of the relativistic species, which delay

the self-decoupling and the ensuing free-streaming [97, 339, 119, 73, 89, 355, 184, 82, 245, 320, 267, 325, 100, 222, 134, 176, 385, 93]. In this model, alleviation comes from self-interaction of the neutrinos plus extra relativistic neutrinos that are introduced by the self-interacting mechanism itself, *e.g.*, with seclusion of the mediating particle, its becoming nonrelativistic, and its recoupling by transfer of its energy density to the neutrinos [119]. Specifically, the moderate interaction level has been shown to be preferred by the data [320, 267, 325, 134], which we confirmed in our analysis. Therefore, our baseline model for SIν is enhanced neutrino self-interactions at the moderate level, plus $N_{\rm eff}$.

- **Primordial magnetic fields (PMF) & baryon inhomogeneity**: The existence of primordial magnetic fields can introduce baryon inhomogeneities in the early Universe, which enhances the hydrogen recombination rate compared to the standard scenario [243]. As a result, CMB photon decoupling happens earlier and the sound horizon is reduced. Assuming the late-time evolution of the Universe is unchanged, the inferred value of H_0 from CMB becomes closer to that of late-universe measurements [240].

2.3 Methodology

2.3.1 Data sets

Here, we briefly describe the cosmological data sets included in this work, and our motivation for their inclusion. The first three observational data sets compose our baseline case for testing new physics. We choose these three as they are robust and broad: first, they are large data sets that have small to minimum-possible statistical errors; second, they have been tested extensively for systematic errors, as summarized below; and, third, are measures of cosmological parameters across the broadest possible range of cosmological history, from

the last scattering surface to low-redshift:

- **Planck 2018 CMB data (P18)**: for all of the calculations in this work, we use the CMB temperature and polarization angular power spectra *TT,TE,EE+lowl+lowE* from the Planck 2018 legacy final release release [42]. The tension between the Planck mission's measurement of the amount of lensing existing in the temperature power spectra data have been widely studied in the last years [34, 39, 312]. In order to isolate the effect of low-redshift clustering measurements and their corresponding potential tension, we decided not to include the Planck CMB lensing measurements in our analysis.

- **BAO DR16 (BAO16)**: we include BAO data from the Sloan Digital Sky Survey (SDSS) lineage of experiments in large-scale structure, composed of data from SDSS, SDSS-II, BOSS, and eBOSS [54] (combining data from BOSS DR12 [52] and eBOSS DR16). These cosmological measurements of the positions and redshifts of galaxies provide their correlation function, which gives a tight constraint on the product of the sound-horizon scale and H_0. The sample consists of galaxies, quasars and Lyman-α forest samples' measurement of the BAO sound-horizon scale, making this combination the largest and most constraining of its kind. We included the first 2 redshift bins of the BOSS DR12 luminous red galaxy (LRG) likelihoods in the redshift range $0.2 < z < 0.6$, as well as the eBOSS DR16 LRG, quasar, Lyman-α forest, and Lyman-α forest-quasar cross correlation likelihoods in the redshift range $0.6 < z < 2.2$. These BAO data sets have been extensively tested with mock catalogs in their determination of the correlation function measurement of the BAO scale with respect to systematic theoretical uncertainties, including fiducial cosmology, satellite galaxy kinematics, dynamics, associated redshift space distortions, and methodological uncertainties, including clustering estimators, random catalogues, fitting templates, and covariance matrices [53, 75, 384, 349, 368].

- **Pantheon Sample (SN)**: we include the Pantheon 2018 SN Ia sample from Ref. [359], which combines SDSS, SNLS, and low-redshift and Hubble Space Telescope samples to form the largest sample of SN Ia. In total, the sample consists of 1048 SN Ia in the redshift interval $0.01 \leq z \leq 2.3$. Moreover, this sample includes improvements, such as corrections for expected biases in light-curve fit parameters and their errors, which have substantially reduced the systematic uncertainties related to photometric calibration.

Next, we use the latest SH0ES measurement of the local Hubble constant:

- **SHOES H0 measurement (R21)**: we include a Gaussian likelihood of the Hubble constant inferred by the measurements obtained by the SH0ES collaboration in [344], $H_0 = 73.04 \pm 1.04\,\mathrm{km/s/Mpc}$.

For the possible tension with clustering on small scales, we explore a range of cluster and lensing data:

- **X-ray Clusters (V09)**: we include constraints on the cosmological parameters from the Viklinin (2009) [386] measurement on the galaxy cluster mass function in the redshift interval $z = [0, 0.9]$. The observations of 86 X-ray clusters led to a determination of stringent constraints on the cosmological parameters, thanks to the higher statistical accuracy and smaller systematic errors than these data sets had ever reached. We use the constraints presented in Table I in Ref. [386], $\Omega_{\rm m}h = 0.184 \pm 0.024$, $\sigma_8(\Omega_{\rm m}/0.25)^{0.47} = 0.813 \pm 0.013$ and $\Omega_{\rm m} = 0.34 \pm 0.08$. This data set constraint is a high-precision determination of these parameters, and sets into place one of the biggest tensions on the cosmological parameter σ_8. Due to its high precision, tension, and use in previous studies to indicate new physics, as well as our desire test if any candidate

model can alleviate both inconsistencies simultaneously, we include this data set as a key determinant of the S_8 problem.

- **SZ Clusters (SZ21)**: we include results from the 2021 release of the SPT-SZ survey which show that within ΛCDM, the SPT-SZ cluster sample prefers $\sigma_8\sqrt{\Omega_{\rm m}/0.3} = 0.794\pm0.049$, without the Planck power spectrum measurement considered in Ref. [120], as we consider P18 separately. The sample of 513 clusters from an SPT SZ sample combined with other analysed X-ray and weak lensing samples have made this catalog one of the largest, with several methods of determining the cluster observable-mass relation.

- **Dark Energy Survey Year 3 results (DES)**: we include results from the most recent DES Y3 survey. The photometric redshift calibration methodology they use is the first of its kind, able to recover the true cosmology in simulated surveys, encompassing information from photometry, spectroscopy, clustering cross-correlations and galaxy–galaxy lensing ratios. It employed a combination of 18 synthetic galaxy catalogs designed for the validation of combined clustering and lensing analyses. We use the cosmological constraints $S_8 = 0.813^{+0.023}_{-0.025}$ and $\Omega_{\rm m} = 0.290^{+0.039}_{-0.063}$ obtained from their analysis [140].

We note that not all of these data sets are used for all of the statistical tests and cosmological parameters space analyses demonstrated in Sec. 2.4. Therefore, to avoid confusion we will denote the data sets used for each figure and for more extensive model studies presented later.

2.3.2 Statistical and cosmological software

In our analysis, we use two different statistical tests in order, first, to quantify the success of each ΛCDM extension, and second, to measure the tension with respect to the S_8 and H_0

measurements. The two aforementioned strategies are explained in the following. For the data sets P18, P18+BAO16 and P18+BAO16+SN, alone and also adding the H_0 and S_8 (V09, DES, SZ21) constraints, we compute the change in the effective minimal chi-square $\chi^2_{\rm min} = -2\ln\mathcal{L}$ where $\mathcal{L}$ represents the maximum likelihood for the considered model $\mathcal{M}$. The $\Delta\chi^2_{\mathcal{M}}$ relative to ΛCDM is then derived as

$$\Delta\chi^2_{\mathcal{M}} \equiv \chi^2_{\rm min,\mathcal{M}} - \chi^2_{\rm min,\Lambda CDM}\,. \tag{2.1}$$

The χ^2 value of a data set can be used determine if a trend in the data is happening due to chance or due to a new model component, and can also be used to test a model's "goodness of fit" [330]. However, the $\Delta\chi^2_{\mathcal{M}}$ test does not take into account the complexity of each model, *i.e.*, number of parameters it has. Thus, we also adopt the Akaike information criterion (AIC) that allows fair comparison between models with a different number of parameters. In order to assess the extent to which the fit is improved, for each model we compute the AIC value [48] defined as $\mathrm{AIC} = -2\ln\mathcal{L} + 2k$, with k being the number of parameters of the model. A model is more preferred, relative to a different model, if it decreases the AIC. To compare with ΛCDM, we calculate the AIC of $\mathcal{M}$ relative to that of ΛCDM, defined as

$$\Delta\mathrm{AIC} \equiv \Delta\chi^2_{\mathcal{M}} + 2(N_{\mathcal{M}} - N_{\Lambda\rm CDM})\,, \tag{2.2}$$

where $N_{\mathcal{M}}$ and $N_{\Lambda\rm CDM}$ represent the number of free parameters of $\mathcal{M}$ and ΛCDM, respectively. It is worth highlighting that this method penalizes models which introduce new parameters that do not improve the fit; therefore, a model with a lower AIC value is more successful theoretically and statistically than one with a higher AIC value. To judge the success of each model, we interpret our AIC values against the Jeffreys' scale [244]. This is an empirically calibrated scale with variation in adjectival description of the evidence limits. We choose a categorically "strong" threshold of $p^{-1} = 10^{3/2}$, or 30:1 odds. This is the same criteria used in other recent works found in the literature, *e.g.*, [357]. Our choice for a pre-

ferred model $\mathcal{M}$ over ΛCDM places it "strong" on the Jeffreys' scale, *i.e.*, $\Delta\text{AIC} < -6.91$, with a more negative AIC being a more successful model.

Moreover, we want to quantify the tension when adding H_0 or S_8 measurements to our data sets. We calculate

$$\sqrt{\Delta\chi^2_{\mathcal{D}}} \equiv \sqrt{\chi^2_{\text{min},\mathcal{D}+\mathcal{T}} - \chi^2_{\text{min},\mathcal{D}}}\,, \tag{2.3}$$

where the subindex $\mathcal{D}$ represents the baseline data sets considered and $\mathcal{T}$ represents the tension constraints added in the minimization calculation. The value of $\chi^2_{\text{min},\mathcal{T}}$ is zero in our case. It is important to highlight that this particular test does not compare the goodness of a particular model in describing the data, it just quantifies the tension of a certain model when adding additional data. Therefore, using this strategy one can measure the tension level in units of standard deviation, σ.

We explore the posterior distributions of cosmological and derived parameters of the preferred models using the publicly available Bayesian analysis framework `cobaya` [380], with the Markov chain Monte Carlo (MCMC) sampler [280, 278] and fastdragging [316]. For the best-fit likelihood and parameter calculation we use the minimizer sampler available in `cobaya` [116, 117, 336]. We choose flat priors with cutoffs well outside where likelihoods are significant.

2.4 Results

2.4.1 Alleviation of the H_0 tension

The results from the AIC test, including the R21 Gaussian prior for the Hubble constant [344], are presented in Fig. 2.1. The AIC values of all candidate models are nega-

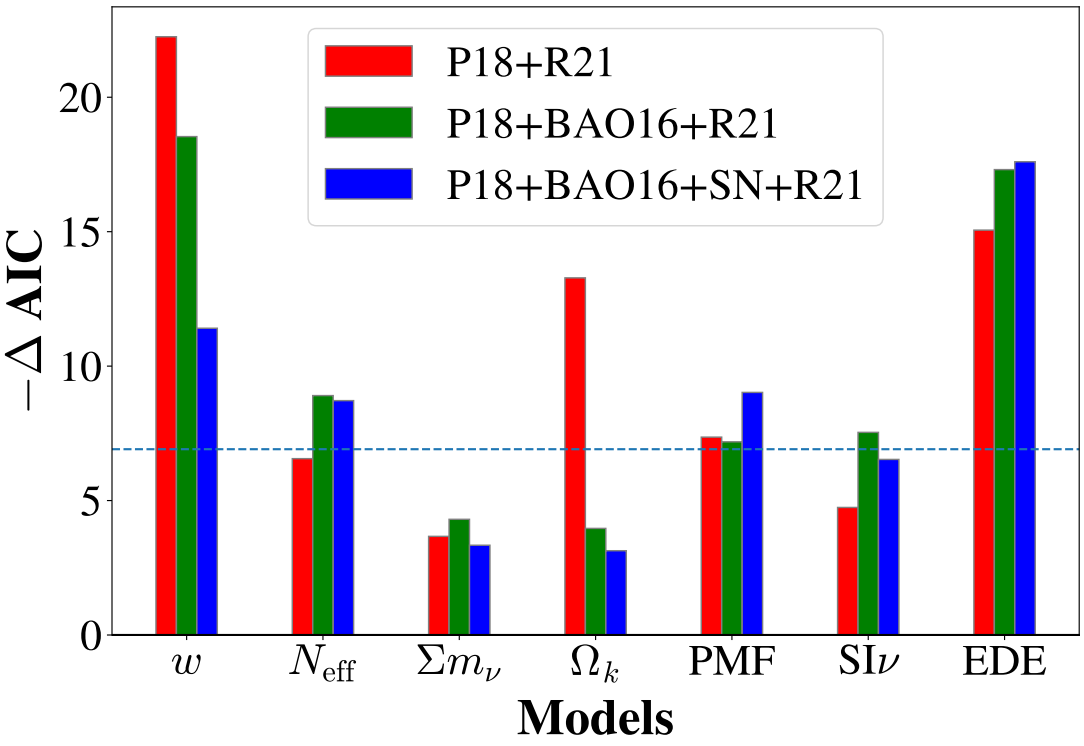


Figure 2.1: Shown here are the $-\Delta$AIC values of considered models (from left to right: wCDM, ΛCDM+$N_{\rm eff}$, non-trivial neutrino mass, non-zero curvature, primordial magnetic fields, self-interacting neutrinos and early dark energy) for relieving the H_0 tension for our baseline CMB, BAO and SNe data sets: P18+R21 (red), P18+BAO16+R21 (green) and P18+BAO16+SN+R21 (blue). The horizontal line is the threshold of stronger than "weak preference" on the Jeffreys' scale.

tive, which means all models do fit the considered data sets better. Nevertheless, when considering the full data sets P18+BAO16+SN (blue), there are only four models which cross the "strong" threshold of -6.91 on the Jeffreys' scale. The most preferred model is EDE with ΔAIC $= -17.6$ with respect to ΛCDM (or roughly 6600:1 odds). Evolving dark energy, wCDM, comes in next, followed by PMF, and then CDM+$N_{\rm eff}$. The use of the supernova absolute magnitude prior (M_b) instead of the H_0 prior for models that behave very differently from ΛCDM at or very near redshift zero has been recently discussed in the literature [161, 110]. The only model that could have been affected by this bias from the ones we analysed in our work is wCDM. We tested this model using both priors and found

that our conclusions are not affected by the use of either of them. The overall fit of both ΛCDM and wCDM to SH0ES is poorer when using an M_b prior, but AIC preference for wCDM is enhanced by 0.5 with the M_b prior. Therefore, from this analysis we select EDE, wCDM, PMF and CDM+$N_{\rm eff}$ as the most successful candidates with respect to ΛCDM. Nearly the same hierarchy is obtained when SN is not included in our calculations (green), with wCDM having a slight preference over EDE. When only P18 is taken into account (red), the preferred models change, wCDM becomes the preferred with $\Delta\text{AIC} = -22.2$, followed by EDE and a non-zero curvature, significantly surpassing the reference strong threshold regime, with this ΔAIC corresponding to roughly 66,000:1 odds. No other models cross the "strong" threshold in this case. The first column of Table 2.1 shows the number of σ value of the residual tension of each model given our full baseline data set P18, BAO16, and SN, when including the SHOES collaboration (R21) H_0 measurement. The residual is calculated using Eq. (2.3). In addition, in Fig. 2.2 we show the 1D posterior distributions of H_0 in our preferred models relative to the R21 measurement.

2.4.2 Alleviation of S_8 tension

The results of our AIC tests for the S_8 tension are presented in Fig. 2.3. In order to force the strongest test for new physics, we choose the most constraining and highest-tension data set, the V09 measurements, on their combination of the $\Omega_{\rm m}$ and σ_8 parameters. None of the models have a negative AIC value when BAO16 alone or BAO16+SN data sets are included in the minimization. When reducing to only P18 and V09, two models are preferred: wCDM and a non-zero curvature, with wCDM being the only one crossing over the "strong" threshold in this case.

There has been significant interest in the S_8 tension indicating a preference for non-minimal neutrino masses (*i.e.*, not-hierarchical, but degenerate neutrino masses). Therefore, in

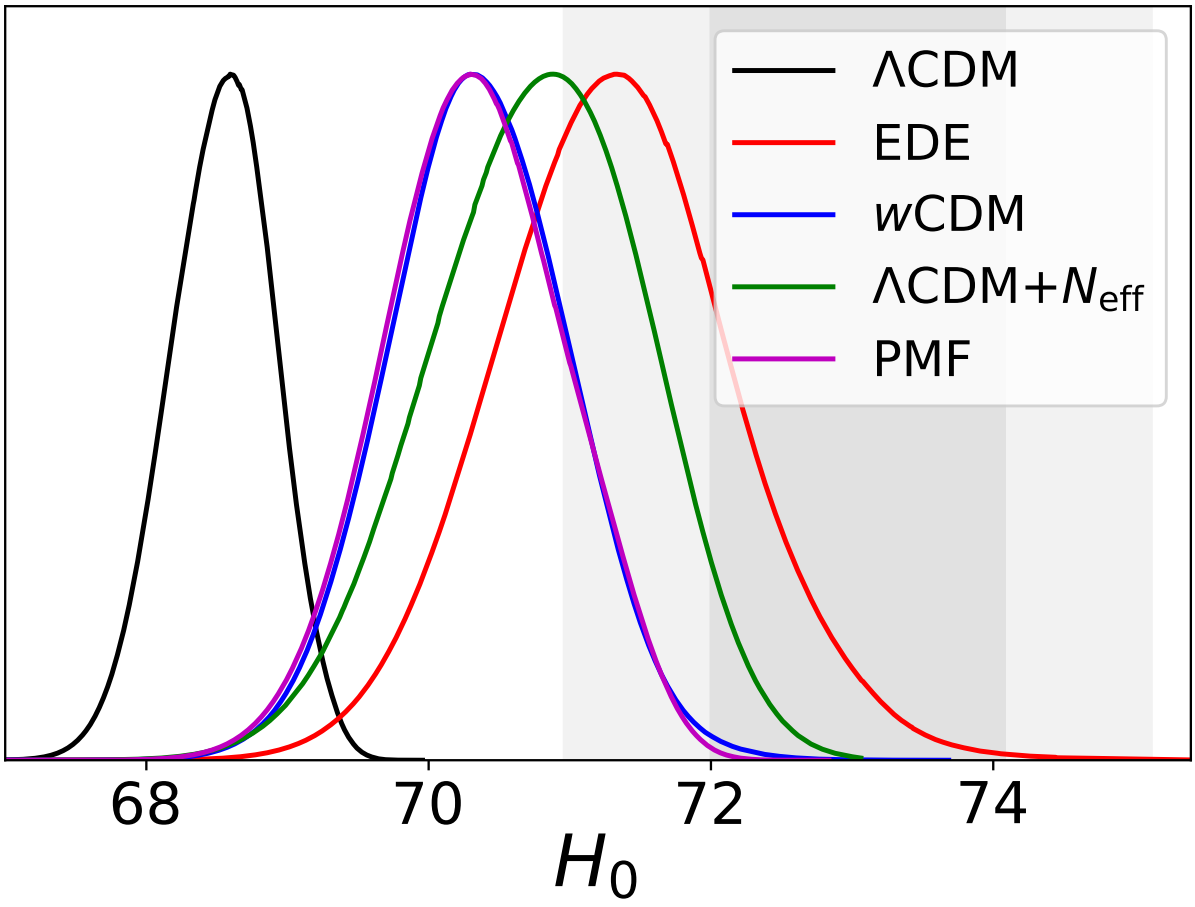


Figure 2.2: Comparison of H_0 posterior distributions from early dark energy (red), wCDM (blue), ΛCDM+$N_{\rm eff}$ (green) and primordial magnetic fields (purple) to ΛCDM (black) being tested against P18+BAO16+SN+R21. The grey shaded regions are 68% and 95% CL limits on H_0 from R21.

Fig. 2.4, we show contours of σ_8 v.s. Σm_ν, comparing V09 (blue), SZ13 (grey) and SZ21 (red). The first two data sets are in the strongest tension with P18 in terms of σ_8, while SZ21 is more consistent with P18. Importantly, even with the strongest tension combination, P18+V09, which prefers a slightly lower $\sigma_8 \sim 0.78$, there is no preference for a non-zero neutrino mass. On the other hand, P18+SZ13 gives a much lower $\sigma_8 \sim 0.75$, and the likelihood peaks at a non-zero neutrino mass. The value of the neutrino mass is inferred in this data set combination to be $\Sigma m_\nu = 0.28 \pm 0.14\,\mathrm{eV}$, and still consistent with a minimal sum of neutrino masses of $\Sigma m_\nu = 0.06\,\mathrm{eV}$ at 2σ.

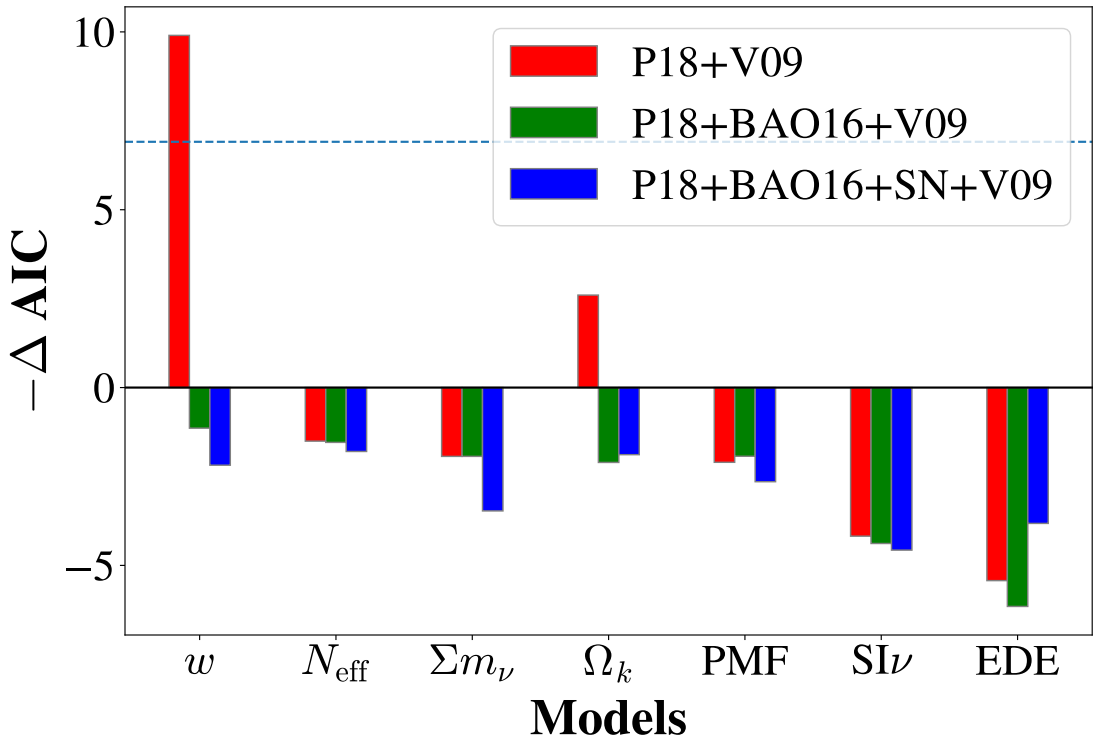


Figure 2.3: Shown here are the $-\Delta$AIC values of considered models (from left to right: wCDM, ΛCDM+$N_{\rm eff}$, non-trivial neutrino mass, non-zero curvature, primordial magnetic fields, self-interacting neutrinos and early dark energy) for relieving the S_8 tension for our baseline CMB, BAO and SNe data sets: P18+V09 (red), P18+BAO16+V09 (green) and P18+BAO16+SN+V09 (blue). The horizontal line is the "strong" threshold on the Jeffreys' scale.

We also ran model minimizations for SZ21, DES, and SZ13 with our baseline data sets (P18+BAO16+SN) and their subsets. None of those tension data sets had greater preference for any of the models than V09, as given by their ΔAIC. Following Eq. (2.3) again, we quantify the existing number of σ tension from the S_8 measurement alone of V09 and DES for each model. These results are presented in the second and third columns of Table 2.1.

2.4.3 Combined alleviation of the H_0 and S_8 tension

The results for models' ΔAIC that take both H_0 (R21) and σ_8 (V09) measurements into account are shown in Fig. 2.5. Based on the resulting ΔAIC values, we find that the models that successfully alleviate the H_0 tension, discussed in Sec. 2.4.1, do not also alleviate the S_8 tension of V09 at the same time. We also tested the models' ΔAIC values for other S_8 tensions, SZ21, DES, and SZ13 with our baseline data sets (P18+BAO16+SN) and their subsets. Again, none of those tension data sets had greater preference for any of the models than V09, as given by their ΔAIC. In the case of P18+R21+V09, wCDM and a non-zero curvature are the preferred models with ΔAIC values crossing the "strong" threshold. When considering P18+BAO16+R21+V09, wCDM maintains the first position with $\Delta\text{AIC} = -10.3$ (equivalent to 170:1 odds). EDE and PMF are next, followed by ΛCDM+$N_{\rm eff}$ and a non-zero curvature; however, their ΔAIC values are below the threshold. Finally, when testing against P18+BAO16+SN+R21+V09, no model has a ΔAIC value above the "strong" threshold of -6.91 on the Jeffreys' scale or 30:1 odds, and the case of a non-minimal neutrino mass has a positive ΔAIC value, *i.e.*, it is certainly less preferred than ΛCDM. We find 4 models with the lowest ΔAIC value as our preferred models, which includes wCDM ($\Delta\text{AIC} = -5.1$), EDE ($\Delta\text{AIC} = -4.8$), ΛCDM+$N_{\rm eff}$ ($\Delta\text{AIC} = -3.5$), and PMF ($\Delta\text{AIC} = -2.2$). Note that a non-zero curvature also has a small negative ΔAIC; however, we do not select it as the preferred model as its $\Delta\text{AIC} \sim 0$.

As with the S_8 tension alone, we also ran model minimizations for R21 plus SZ21, DES, and SZ13. None of those combined H_0 plus S_8 tension data sets had greater preference for any of the models than R21+V09 given, as by their ΔAIC.

2.5 Discussion

2.5.1 Cosmologies and Cosmological Parameters

We further study the four preferred models selected in the previous section by running MCMC chains with the joint data set P18+BAO16+SN+R21. In Fig. 2.7–Fig. 2.10, we present the contours and posterior distributions of cosmological parameters for each preferred model $\mathcal{M}$ with purple (green) contours corresponding to the result of $\mathcal{M}$ (ΛCDM). The baseline cosmological parameters are the baryon density $\Omega_b h^2$, the CDM density $\Omega_c h^2$, the scalar spectral index n_s, the optical depth to reionization $\tau_{\rm reio}$, the `CosmoMC` approximation to the angular size of the sound horizon $100\theta_{\rm MC}$, and the amplitude of primordial scalar perturbations $\log(10^{10}A_s)$. We also show the derived parameters of interest, H_0 and σ_8, and the summary of their mean values and 68% C.L. intervals is given in Table 2.3. For the wCDM model, the optical depth slightly decreases with respect to ΛCDM, as well as the scalar spectral index, the angular acoustic scale and the baryon density. The physical dark matter density increases noticeably, as well as the two derived parameters σ_8 and H_0.

In the case of the ΛCDM+$N_{\rm eff}$ model, $\log(10^{10}A_S)$, the scalar spectral index, physical baryon density and physical dark matter density shift towards higher values than the ones of the standard ΛCDM. The values of σ_8 and H_0 are also greater. The optical depth to the epoch of reionization does not vary significantly. The angular acoustic scale is reduced with respect to ΛCDM.

For EDE we observe similar shifts as the one just described for the $N_{\rm eff}$ model. Moreover, we highlight that these two models have a higher σ_8 and higher n_s, which gives more early halo evolution. In Ref. [262], they used a large suite of cosmological N-body simulations to explore the implications of the different cosmology implied by the EDE model of Ref. [370]. Given that the cosmological parameters are similar for EDE and $N_{\rm eff}$ cosmologies, the implications

for structure formation may be similar. Namely, the increase in σ_8, n_s and decrease in $\Omega_{\rm m}$, all enhance early galaxy formation, which may be indicated by the large number of massive galaxies being detected by JWST [118, 179].

For the existence of PMF, and commensurate baryonic inhomogeneity in the early Universe, the shifts in some of the parameters are noticeable, in which the most significant one is the increased angular acoustic scale in `CosmoMC` approximation $\theta_{\rm MC}$. However, we note that since the redshift of CMB photon decoupling is changed in PMF paradigm, $\theta_{\rm MC}$ is no longer a good approximation to the actual angular scale of the sound horizon θ_*. We check that the value of θ_* derived from the best-fit value of parameters in Table 2.3 is consistent with P18. The dark matter density is also higher in this model, as well as the two derived parameters σ_8 and H_0. The spectral index is reduced as well as the optical depth to the epoch of reionization. $\log(10^{10}A_s)$ and the baryon density do not suffer important changes from the standard values.

Even though the existence of a non-zero curvature is not part of our preferred models, we want to highlight that it is a successful model when only considering P18 data sets as well as the H_0 prior or σ_8 constraint. Nevertheless, when the additional data sets of BAO16 and SN are included, this model is no longer preferred due to the enhanced constraints on curvature from these data.

For SIν (*i.e.*, ΛCDM+$N_{\rm eff}$+$G_{\rm eff}$), we retrieve the result shown in previous literature that the likelihood peaks at moderate and strong interaction levels and moderate interaction levels are preferred by the baseline data sets. We further show that moderate interaction level can effectively alleviate the H_0 tension when being tested against the baseline data sets with R21. However, as a result of an extra free parameter and no significant improvement in the fit, the AIC value of SIν is in general poorer than the ΛCDM+$N_{\rm eff}$ case, thus SIν is not selected as a preferred model.

Models	H_0 (R21)	σ_8 (V09)	σ_8 (DES)
ΛCDM	4.63	3.59	2.44
EDE	1.83	4.21	2.93
wCDM	3.16	3.94	2.36
ΛCDM+$N_{\rm eff}$	3.33	3.61	2.43
PMF	3.63	4.01	2.90

Table 2.1: We show the σ value of the residual tension of each model given our full baseline data set P18, BAO16, and SN, when including the SHOES collaboration (R21) H_0 measurement, X-ray clusters measurement of $\sigma_8(\Omega_{\rm m}/0.25)^{0.47}$ in V09, and the DES measurement of S_8. Though we use more data from V09 and DES in our full analysis, here we use only the tension data point for the residual, which is calculated using Eq. (2.3).

Models	P18	P18+BAO16	P18+BAO16+SN
ΛCDM	0.8055	0.8062	0.8034
EDE	0.8648	0.8570	0.8391
wCDM	0.8164	0.8235	0.8268
ΛCDM+$N_{\rm eff}$	0.8177	0.8202	0.8252
ΛCDM+Σm_ν	0.8191	0.8140	0.8153
ΛCDM+Ω_k	0.8164	0.8193	0.8168
PMF	0.8231	0.8147	0.8253
SIν	0.8189	0.8301	0.8254

Table 2.2: Best-fit values of the parameter σ_8 for the three combinations of our baseline data sets P18, P18+BAO16, and P18+BAO16+SN, when including the SHOES collaboration (R21) H_0 measurement for each of the analysed models. The conclusions from the values S_8 are the same.

2.5.2 The Level of the S_8 Tension

As described above, there is a variety of levels of tension in S_8 (σ_8) given by different data sets. Here we review the implications of adopting the various data sets, which provide a range of results, from no tension to appreciable tension, up to 4σ. As we describe in this section, the most recent analyses of X-ray, SZ, and optically-selected clusters have no tension with the inferred amplitude of matter clustering from Planck 2018. Recent weak lensing data sets remain in tension with Planck 2018 at the level of $\sim 2\sigma$. In order to understand the nature of the S_8 (σ_8) tension further, we show σ_8 v.s. $\Omega_{\rm m}$ contours in Fig. 2.6, comparing Planck 2015 (P15) [36] and P18 with data sets that constrain S_8 including X-

ray clusters (left panel), Sunyaev-Zel'dovich (SZ) clusters (middle panel) and weak lensing measurements (right panel). For X-ray clusters, we show V09 [386] introduced in Sec. 2.3.1 and HIFLUGCS (SR17) [356] which is a cluster sample measurement of the brightest 64 X-ray galaxy clusters that has individually determined, robust total mass estimates, and compares with Planck-SZ determined mass estimates. Their ensuing S_8 constraint is $\sigma_8\sqrt{\Omega_{\rm m}/0.3} = 0.792 \pm 0.049$. As can be seen in this figure, the tension is relaxed both by P18 shifting lower than P15 and by the updated X-ray cluster constraints shifting higher.[1] For SZ clusters, we show the constraint derived from the sample of 189 galaxy clusters from the Planck SZ catalog (SZ13) [35]. We compare SZ13 with recent results from the SPT-SZ collaboration (SZ21) [120]. Similar to X-ray clusters, the tension in SZ cluster samples is relaxed both by P18 shifting lower than P15 and by the newer SZ cluster constraints shifting higher in this parameter space. Optically-selected cluster samples also determine a higher value for σ_8, consistent with non-cluster probes [21].

For lensing measurements, we compare results from the tomographic weak lensing analysis of the Canada-France-Hawaii Telescope Lensing Survey (CFHTLenS) [228], cosmic shear analysis of the fourth data release of the Kilo-Degree Survey (KiDS-1000) [67] and the most recent results from the combined galaxy clustering and lensing measurement of DES Year 3 [140]. As discussed in Sec. 2.3.1, DES has robust photometric redshift calibration methods able to recover results obtained from simulated surveys. Due to the size of the data set, the errors on the cosmological parameters are also reduced relative to previous data sets.

The tension from V09 is clear, with an approximately 3.59σ deviation with Planck, cf. Table 2.1. Recall we adopted this as a benchmark data set in order to introduce a large tension and therefore potentially infer the most likely ΛCDM model extension. However, updated measurements such as SR17 and SZ21 yield a larger value of σ_8 which is consistent with P18. On the other hand, lensing measurements largely agree with each other.

[1] P18 shifts in this parameter space with respect to P15 due to the change in the determination of the optical depth given the updated CMB polarization measurements of P18 [42].

The lack of a preference for a non-zero neutrino mass when including low-S_8/σ_8 data sets with P18 is due to the shift in the CMB optical depth and scalar amplitude parameters to be significantly lower with P18's updated polarization anisotropy measurements, relative to earlier Planck data, along with slight shifts in the other parameters. Overall, as discussed in Sec. 2.4, the S_8 tension is no longer indicative of a possible non-minimal neutrino mass. As we have seen in the evolution of the X-ray and SZ cluster data, the tension with those data sets has been alleviated. This leaves the weak-lensing based inferences of S_8. For the case of DES, the tension with ΛCDM is mild, at $\sim 2.44\sigma$ (see Table 2.1).

Most importantly, we find that none of the new models considered alleviate the S_8/σ_8 tension at the same time as the H_0 tension (c.f. Table 2.2). When including R21, the value of S_8/σ_8 is reduced even in the case of ΛCDM. All of the models considered drive σ_8 higher, as shown in Table 2.2, a feature prevalent in many models trying to alleviate both tensions [242]. The values for S_8 are also higher for all models, except for the ΛCDM+Ω_k model, and only for the case of considering P18 data plus R21 alone. None of these new models alleviate the S_8/σ_8 tension better than ΛCDM when including our full data set. Therefore, when considering if a new model does better than ΛCDM in alleviating the S_8 problem simultaneously with the H_0 problem, one should compare to ΛCDM+R21's own alleviation of S_8, and not ΛCDM without H_0 information.

2.6 Conclusion

In this paper, we have investigated how well seven models—wCDM, ΛCDM+$N_{\rm eff}$, ΛCDM+$\sum m_\nu$, ΛCDM+Ω_k, PMF, SIν and EDE— explain or fail to explain the H_0 and S_8 tensions. We do this by calculating both the change in the AIC and the change in the total χ^2 for the models and data sets. We find that EDE, wCDM, PMF, and ΛCDM+$N_{\rm eff}$ pass the threshold of the "strong" preference criterion of $\Delta{\rm AIC} < -6.91$. However, each of these models still has a

residual tension with the R21 H_0 constraint of greater than 3σ except for EDE, which has a residual tension of less than 2σ. The inclusion of more model parameters corresponding to greater details of the SIν, EDE and PMF models could lead to a poorer preference by ΔAIC, but an exploration of those extensions is beyond the scope of this work [340, 378]. Therefore, of the seven models, EDE satisfies both in having an overall better fit to all the data, including H_0 as well as having almost no remaining tension with the single measurement of H_0. The better fit of EDE largely comes from its consistency with periodic features the high-ℓ C_ℓ measurements of Planck 2018 [370], which will probed well by upcoming CMB experiments [373, 379, 13].

For the case of the S_8/σ_8 tension, we adopted a strong-tension data set (V09), but our conclusions do not change with other S_8 data sets. Only in the case of Planck 2018 CMB data plus V09, are evolving dark energy $w > -1$ and Ω_k not disfavored relative to ΛCDM. However, with the BAO16+SN data, no model alleviates the S_8 tension, due to those constraints on the expansion history. We discussed how the S_8 tension has been alleviated to the $\sim 2\sigma$ level both by shifts in the Planck 2015 to 2018 analyses, as well as shifts in structure formation measures of S_8/σ_8, whether by X-ray clusters, SZ clusters, or weak lensing. Importantly, we show that a non-trivial neutrino mass ($\Sigma m_\nu > 0.06\,\mathrm{eV}$), does not alleviate the S_8/σ_8 tension.

Significantly, we showed that adding the H_0 measurement of R21 to all of the data sets we considered substantially lowers S_8/σ_8 for ΛCDM due to a shift to a larger Ω_Λ, and therefore a commensurate suppression in the growth of large scale structure. Importantly, *no model considered here* lowers the best-fit value of S_8/σ_8 better than ΛCDM when including the H_0 (R21) tension. Therefore, claims in other work of models alleviating both H_0 and S_8 tensions should be sure to compare with ΛCDM's own S_8 alleviation when including H_0, and not compare to ΛCDM without the H_0 constraint.

In the context of Bayesian model selection, via the AIC, the observation of the H_0 tension updates our belief such that the EDE model is best. Given the fact that the values of the

Parameters	w**CDM**	**EDE**	Λ**CDM+**$N_{\rm eff}$	**PMF**
$\Omega_b h^2$	0.02242 ± 0.00014	0.02284 ± 0.00027	$0.02282^{+0.00013}_{-0.00014}$	0.02261 ± 0.00015
$\Omega_c h^2$	0.1197 ± 0.0011	0.1298 ± 0.0034	0.1252 ± 0.0023	$0.1226^{+0.0017}_{-0.0015}$
$100\theta_{\rm MC}$	1.04098 ± 0.00030	1.04057 ± 0.00033	1.04042 ± 0.00037	$1.0518^{+0.0030}_{-0.0024}$
τ	0.0553 ± 0.0078	$0.0587^{+0.0084}_{-0.010}$	0.0621 ± 0.0081	$0.0550^{+0.0069}_{-0.0078}$
$\ln(10^{10} A_s)$	3.046 ± 0.016	$3.072^{+0.017}_{-0.021}$	3.074 ± 0.018	3.074 ± 0.015
n_s	0.9660 ± 0.0039	0.9848 ± 0.0056	0.9843 ± 0.0057	0.9602 ± 0.0039
H_0 [km/s/Mpc]	70.36 ± 0.64	71.31 ± 0.83	$70.77^{+0.82}_{-0.72}$	70.33 ± 0.64
Ω_m	0.2886 ± 0.0057	0.3014 ± 0.0062	0.2969 ± 0.0048	0.2950 ± 0.0052
σ_8	0.838 ± 0.011	$0.840^{+0.011}_{-0.012}$	0.831 ± 0.011	0.8294 ± 0.0098
Extra parameters	$w = -1.094 \pm 0.026$	$f_{z_c} = 0.096^{+0.023}_{-0.027}$, $z_c = 3090 \pm 38$, $\Theta_i = 1.9^{+1.0}_{-1.8}$	$N_{\rm eff} = 3.48 \pm 0.12$	$b = 0.57 \pm 0.19$

Table 2.3: Best-fit values and 68% intervals of parameters for the preferred candidate models from P18+BAO16+SN+R21. The first nine rows are baseline ΛCDM parameters, and the last row shows model-specific extra parameters.

S_8/σ_8 parameters become higher for all models when the R21 observation is included, the observation of the S_8/σ_8 tension does not update the data's preference for the EDE model. For the kinds of models still allowed by the joint P18+BAO16+SN+R21 data sets, the H_0 and S_8/σ_8 tensions will pull the models in different directions.

Future tests of an EDE epoch could come from high-ℓ CMB measurements, as discussed earlier, or from the turn over in the matter power spectrum at very large scales, which should constrain $\theta_{\rm eq}$, the angular size of the sound horizon at matter-radiation equality that could be constrained by large-scale structure surveys. And, maybe most importantly, future independent determinations of the local expansion history H_0 may reaffirm its tension or relax it.

2.7 APPENDIX: Details of considered models

2.7.1 Early dark energy

The phenomenology of EDE can be realized by, *e.g.*, a scalar field ϕ with a potential $V(\phi) \propto [1-\cos(\phi/f)]^n$ such that ϕ is frozen at $z < z_c$ with $w_\phi = -1$ and starts to oscillate at $z = z_c$ and can be effectively described as a fluid with $w_\phi = w_n = (n-1)/(n+1)$, or, slow-roll of ϕ down a potential that $V(\phi) \propto \phi$ at $z < z_c$ and $V(\phi) \to 0$ at late time; see [252, 254, 334, 335, 370] for further details. Note that whether EDE works does not depend much on the details of potential, as long as the typical evolution of energy density is fulfilled.

Taking the scalar potential $V(\phi) \propto [1-\cos(\phi/f)]^n$ as the benchmark model, in the fluid approximation the evolution of density parameter of ϕ reads [334]

$$\Omega_\phi(a) = \frac{2\Omega_\phi(a_c)}{(a/a_c)^{3(w_n+1)}+1}\,, \tag{2.4}$$

where a is the scale factor of the Universe and $a_c = (1+z_c)^{-1}$. The equation of state is

$$w_\phi(a) = \frac{1+w_n}{1+(a_c/a)^{3(1+w_n)}} - 1\,, \tag{2.5}$$

such that the energy density of ϕ can dilutes faster than radiation at $z < z_c$ for $n \geq 3$; in this work, we focus on the case that $n = 3$. Following the literature [370], we define $f_{z_c} \equiv \Omega_\phi(a_c)/\Omega_{\rm tot}(a_c)$ with $\Omega_{\rm tot}(a_c)$ being the density parameter of the total energy density at $z = z_c$ and $\Theta \equiv \phi/f$ being the renormalized field variable which determines the effective sound speed. In our analysis, we set z_c, f_{z_c} and the initial value of the renormalized field variable Θ_i as free parameters.

2.7.2 Self-interacting neutrinos

We focus on the particle model where the self-interaction of neutrinos is mediated by a massive scalar ϕ with mass m_ϕ; the coupling strength of $\phi\nu\nu$ is g_ν. When the neutrino temperature $T_\nu \ll m_\phi$, the scalar particle can be integrated out and the interaction can be described by the effective field theory (EFT). In the EFT framework, the self-interaction $\nu\nu \to \nu\nu$ is analogous to the 4-Fermi interaction with a constant $G_{\rm eff} \equiv g_\nu^2/m_\phi^2$. [2] In the limit that neutrinos are relativistic, *i.e.*, $T_\nu \gg m_\nu$, the thermal-averaged cross section of self-interaction reads

$$\langle \sigma v \rangle \sim G_{\rm eff}^2 T_\nu^2 \,. \tag{2.6}$$

The interaction rate can be written as $\Gamma = n_\nu \langle \sigma v \rangle \sim G_{\rm eff}^2 T_\nu^5$ as $n_\nu \propto T_\nu^3$. We focus on the strongly-interacting regime $G_{\rm eff} \gg G_F \simeq 1.2 \times 10^{-5}\,{\rm GeV}^{-2}$ with G_F being the Fermi constant, such that the self-interaction can drastically delay the SM neutrino decoupling and affect the CMB angular power spectra.

To consistently solve for the CMB angular power spectra in the SIν scenario, when evolving the perturbations, we need to augment the usual Boltzmann hierarchy of neutrinos in the cosmological perturbation theory with additional damping terms. The phase-space distribution function of neutrinos reads $f = f_0(1+\Psi)$ with f_0 being the unperturbed one. The perturbation Ψ can be expanded into a Legendre series; for each multipole ℓ, the corresponding amplitude is Ψ_ℓ. Therefore, instead of solving the Boltzmann equation in terms of Ψ, we can evolve the Boltzmann hierarchy in Ψ_ℓ. Following the convention in **(author?)** [292], in

[2] Note that $G_{\rm eff}$ defined here is equivalent to G_ν defined in Ref. [133, 271].

the Synchronous gauge the Boltzmann hierarchy of massive neutrino can be written as

$$\dot{\Psi}_0 = -\frac{qk}{\epsilon}\Psi_1 + \frac{\dot{h}}{6}\frac{d\ln f_0}{d\ln q}\,, \tag{2.7}$$

$$\dot{\Psi}_1 = \frac{qk}{3\epsilon}\Psi_0 - 2\Psi_2\,, \tag{2.8}$$

$$\dot{\Psi}_2 = \frac{qk}{5\epsilon}(2\Psi_1 - 3\Psi_3) - \left(\frac{\dot{h}}{15} + \frac{2\dot{\eta}}{5}\right)\frac{d\ln f_0}{d\ln q} + C_2^{\rm damp}\,, \tag{2.9}$$

$$\dot{\Psi}_{\ell\geq 3} = \frac{qk}{(2\ell+1)\epsilon}(\ell\Psi_{\ell-1} - (\ell+1)\Psi_{\ell+1}) + C_{\ell\geq 3}^{\rm damp}\,, \tag{2.10}$$

where overdot stands for derivative with respect to the conformal time, k is the comoving wavenumber, q and ϵ are the comoving momentum and energy, h and η are fields describing the metric perturbation. Note that collision terms stemmed from the self-interaction does not affect $\ell = 0$ and $\ell = 1$ since number density and energy density are conserved.

The complete formulas of damping terms $C_\ell^{\rm damp}$ derived from the integral of collision terms can be found in [319, 320]. In this work we adopt the relaxation time approximation [96, 215] or the separable ansatz [133] which gives

$$C_\ell^{\rm damp} = \alpha_\ell \dot{\tau_\nu}\Psi_\ell\,, \tag{2.11}$$

where α_ℓ is the numerical factor from the integration over momentum and $\dot{\tau_\nu} = -a\Gamma$ is the rate of change of the neutrino opacity with a being the cosmological scale factor. This approximation is shown to be an adequate description of a system without dissipative process [87] and numerically agree with the full treatment of self-interaction if the correct α_ℓ is taken for each ℓ [320].[3]

We modify `CAMB` to include the effect of SIν; see [134] for existing codes. At the early time, we approximate neutrinos as a perfect fluid to avoid a numerically stiff problem. A perfect fluid has no stress; therefore, if $\Gamma \gg H$ is met, we set $\Psi_{\ell\geq 2} = 0$ in the initial condition and

[3]To avoid confusion, we note that in [133, 271], $G_{\rm eff} \equiv \sqrt{\alpha_\ell}G_\nu = \sqrt{\alpha_\ell}g_\nu^2/m_\phi^2$.

only evolve $\Psi_{\ell=0,1}$. As the Universe expands, eventually Γ drops below H and we start to solve for the full Boltzmann hierarchy once it is numerically solvable.

The non-standard interaction of SM neutrinos faces constraints in aspects of particle model, cosmology, astrophysics and laboratory experiments. Theoretically, the validity of perturbative calculations requires $g_\nu \leq 4\pi$. The thermal population of neutrinos and ϕ can be probed by $N_{\rm eff}$ at Big-Bang Nucleosynthesis (BBN) and CMB epochs, resulting in constraints on the underlying particle nature; especially, for the case where ϕ is a real scalar $m_\phi > 1.3\,\text{MeV}$ and the Dirac nature of neutrinos is strongly constrained [99]. Modification of the neutrino free-streaming leads to deviations from the standard cosmology in the CMB angular power spectrum, giving us a leverage to constrain the self-interaction strength [64, 133, 271, 350, 104]. Furthermore, the propagation of energetic neutrinos is affected by the self-interaction; for example, detection of ultra-high energy neutrinos from supernovae [298, 152, 264] or as cosmic ray [260, 231, 317, 236, 122] can place a limit on $G_{\rm eff}$. Finally, upon imposing a UV model for the effective interaction, strong bounds can also arise from SM precision observables, *e.g.*, the T-parameter and decay of SM particles [270, 99, 291]. In this work, we remain agnostic about the UV-origin of such effective interactions and consider the flavor-universal case for simplicity, which leaves us the only free parameter $G_{\rm eff}$. Recasting the result of $G_{\rm eff}$ into that of the (g_ν, m_ϕ) parameter space is straightforward as long as proper UV models are applied.

2.7.3 Primordial Magnetic Fields & Baryon Inhomogeneity

By enhancing the hydrogen recombination rate, baryon inhomogeneity before recombination can change the process of CMB photon decoupling. The degree of inhomogeneity is parameterized by the clumping factor

$$b \equiv \frac{\langle n_b^2 \rangle}{\langle n_b \rangle^2} - 1\,, \tag{2.12}$$

where n_b is the baryon number density. The baryon inhomogeneity can be due to, *e.g.*, the existence of primordial magnetic fields [243].

The generation of primordial magnetic fields can happen in the early Universe such as during phase transitions and during inflation; see [158] for detailed review. By solving the evolution of the primordial magnetic field $\vec{B}$ [239], Ref. [240] found that $|\vec{B}| \sim \mathcal{O}(0.1\,\mathrm{nG})$ at Mpc scale to alleviate the Hubble tension by sourcing a baryon inhomogeneity $b \sim \mathcal{O}(0.1)$ that makes recombination happen earlier and thus reduces the sound horizon. In addition, such primordial magnetic fields can be the origin of the cluster magnetic fields observed today [154, 77, 78].

We utilize a modified version of `CAMB`, which includes the computation of the ionization fraction in three zones to account for a non-zero b, to evaluate the significance of baryon inhomogeneity in solving both the H_0 and σ_8 tensions. We adopt M1 in [240] as a benchmark model for the three-zone calculation; see the mentioned reference for details of methodology and relevant parameters.

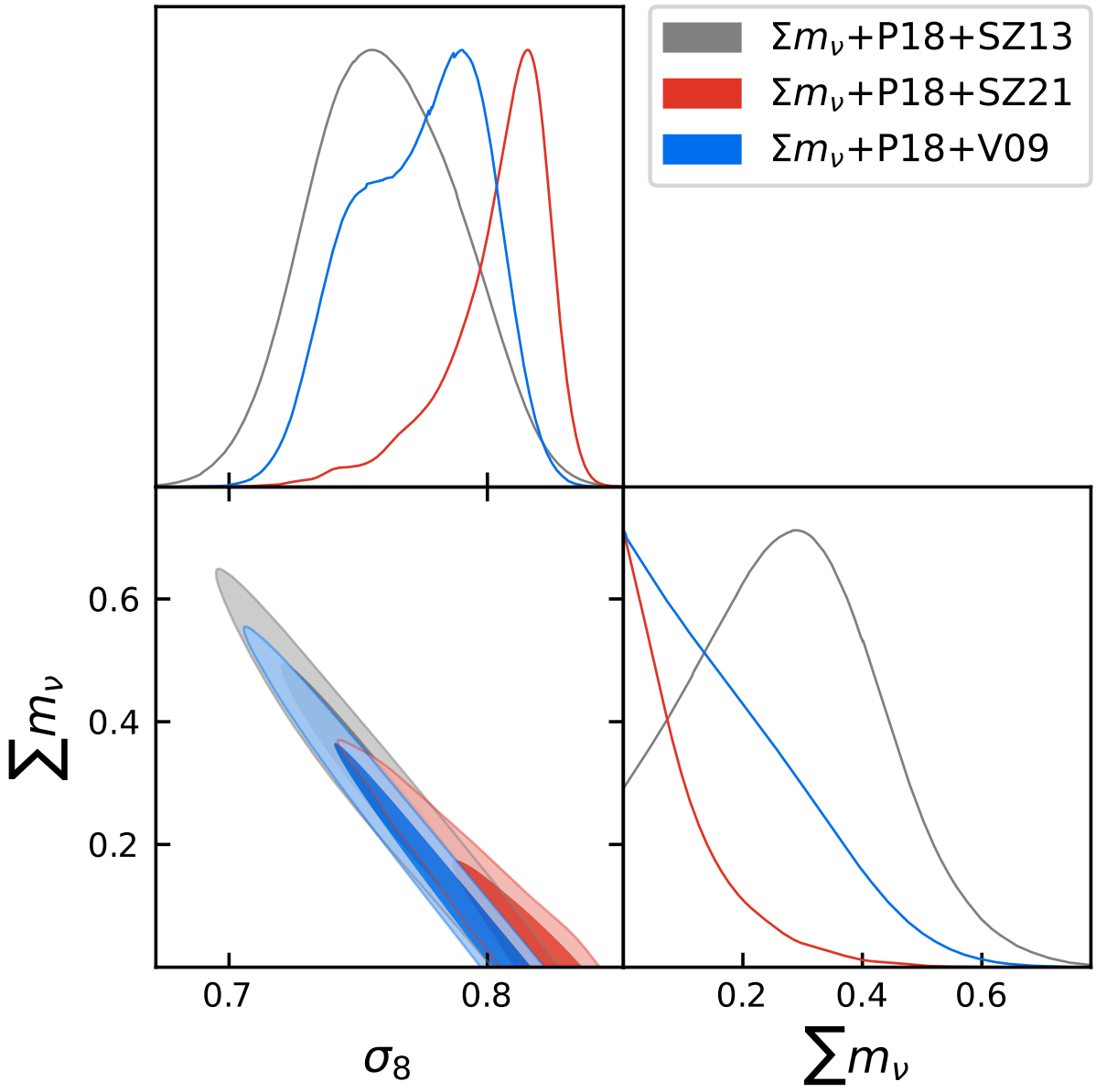


Figure 2.4: We show 68% and 95% CL contours of (Σm_ν, σ_8) and their posterior distribution for the combination of P18 with our three cluster data sets: SZ13 (grey), SZ21 (red) and V09 (blue). Only P18+SZ13 has a likelihood that peaks at nonzero neutrino mass, with $\Sigma m_\nu = 0.28 \pm 0.14\,\mathrm{eV}$.

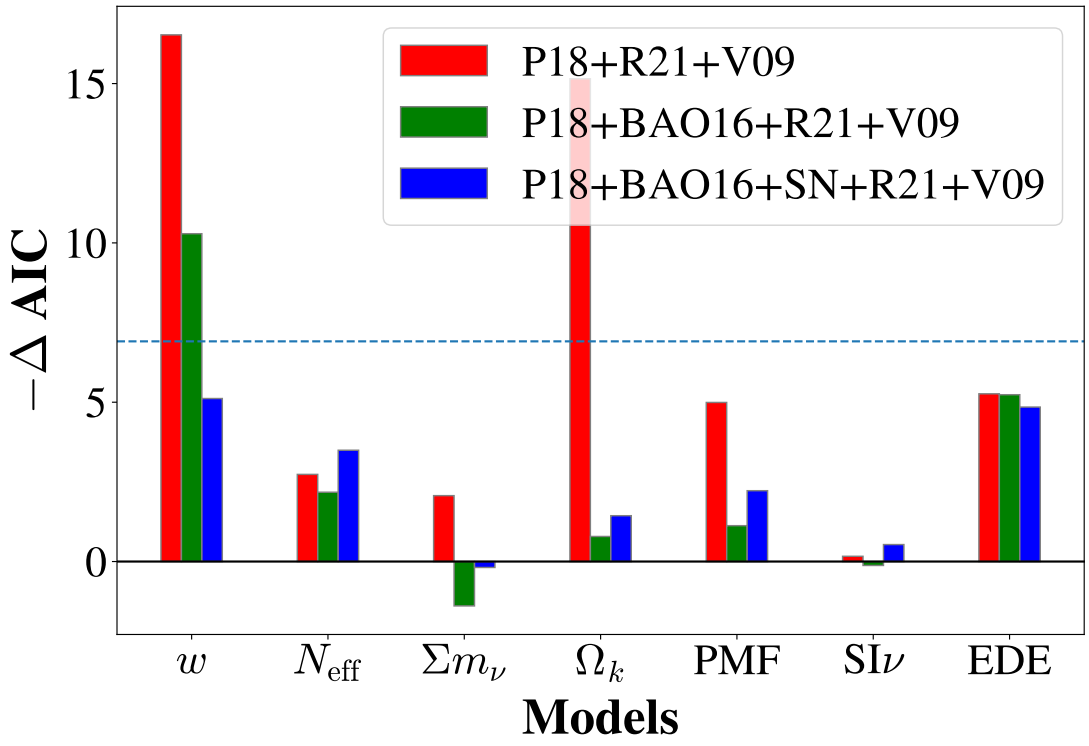


Figure 2.5: Shown here are the $-\Delta$AIC values of considered models (from left to right: wCDM, ΛCDM+$N_{\rm eff}$, non-trivial neutrino mass, non-zero curvature, primordial magnetic fields, self-interacting neutrinos and early dark energy) for relieving the H_0 and S_8 tensions simultaneously for our baseline CMB, BAO and SNe data sets: P18+R21+V09 (red), P18+BAO16+R21+V09 (green) and P18+BAO16+SN+R21+V09 (blue). The horizontal line crosses the threshold of "strong" on the Jeffreys' scale.

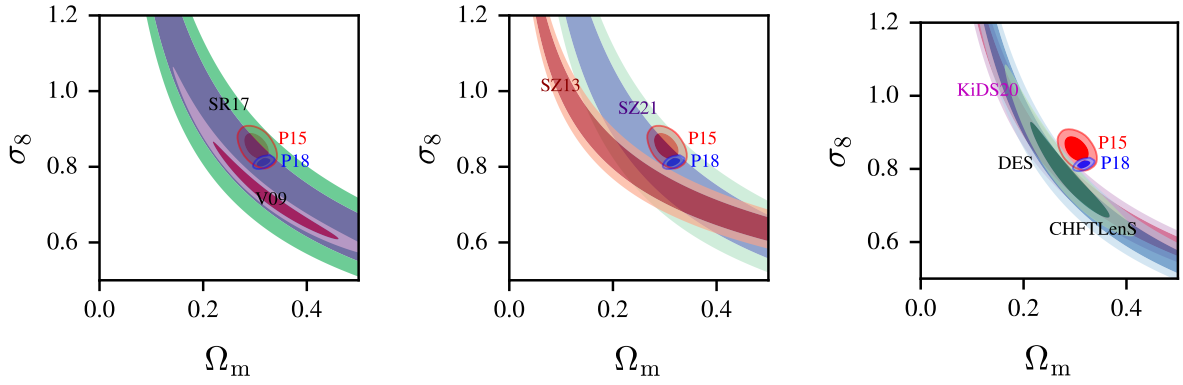


Figure 2.6: Comparison of 1σ and 2σ contours of ($\Omega_{\rm m}$, σ_8) from Planck (2015 and 2018) and measurements including X-ray clusters V09/SR17 (left panel), SZ clusters SZ13/SZ21 (middle panel) and lensing KiDS20/CHFTLenS/DES (pink/olive/light blue, right panel).

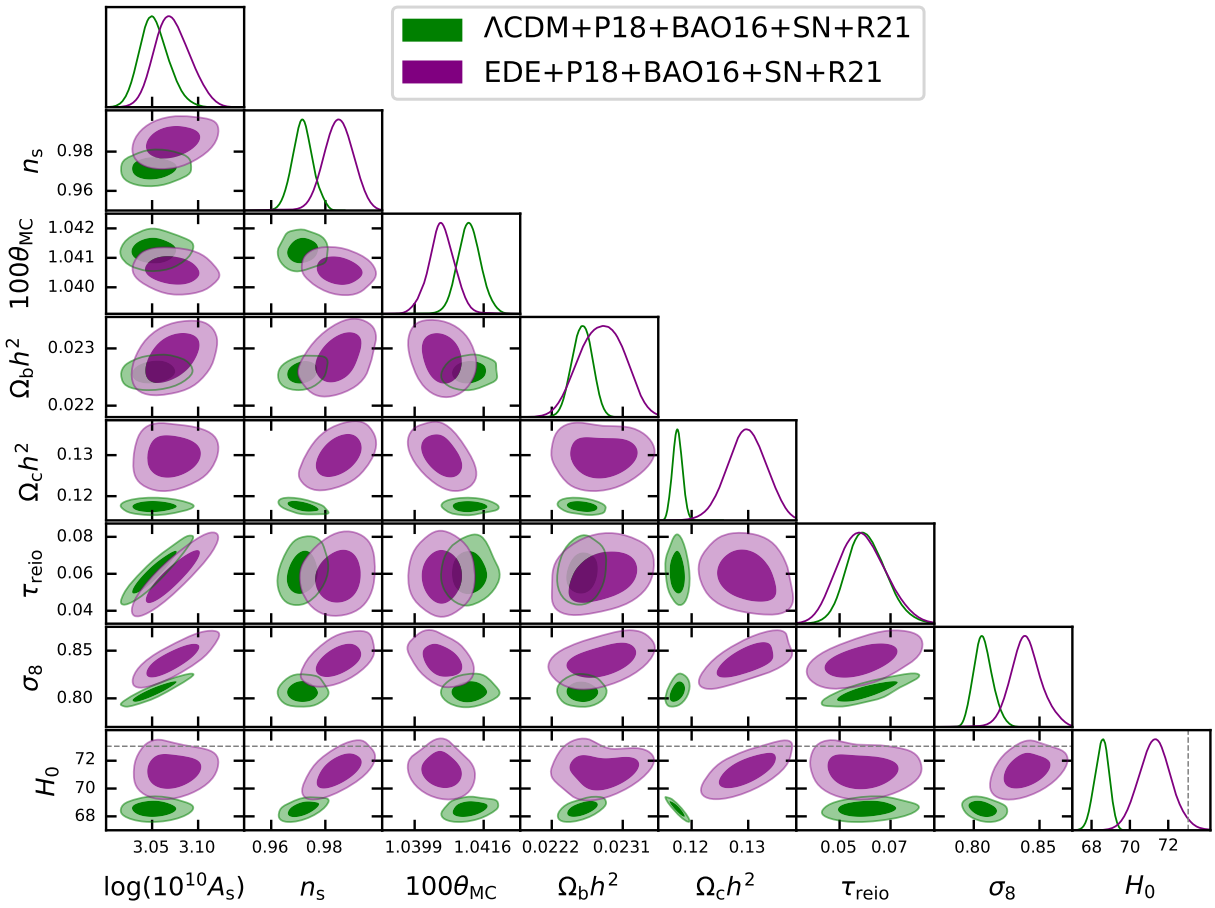


Figure 2.7: EDE v.s. ΛCDM: 68% and 95% CL contours of $\{\log(10^{10}A_s)$, n_s, $100\theta_{\rm MC}$, $\Omega_b h^2$, $\Omega_c h^2$, $\tau_{\rm reio}$, σ_8, $H_0\}$ of EDE (purple) v.s. ΛCDM (green) for our baseline cosmological data sets plus H_0, P18+BAO16+SN+R21. The grey dashed line denotes the best-fit value of $H_0 = 73.04\,{\rm km/s/Mpc}$ reported by R21.

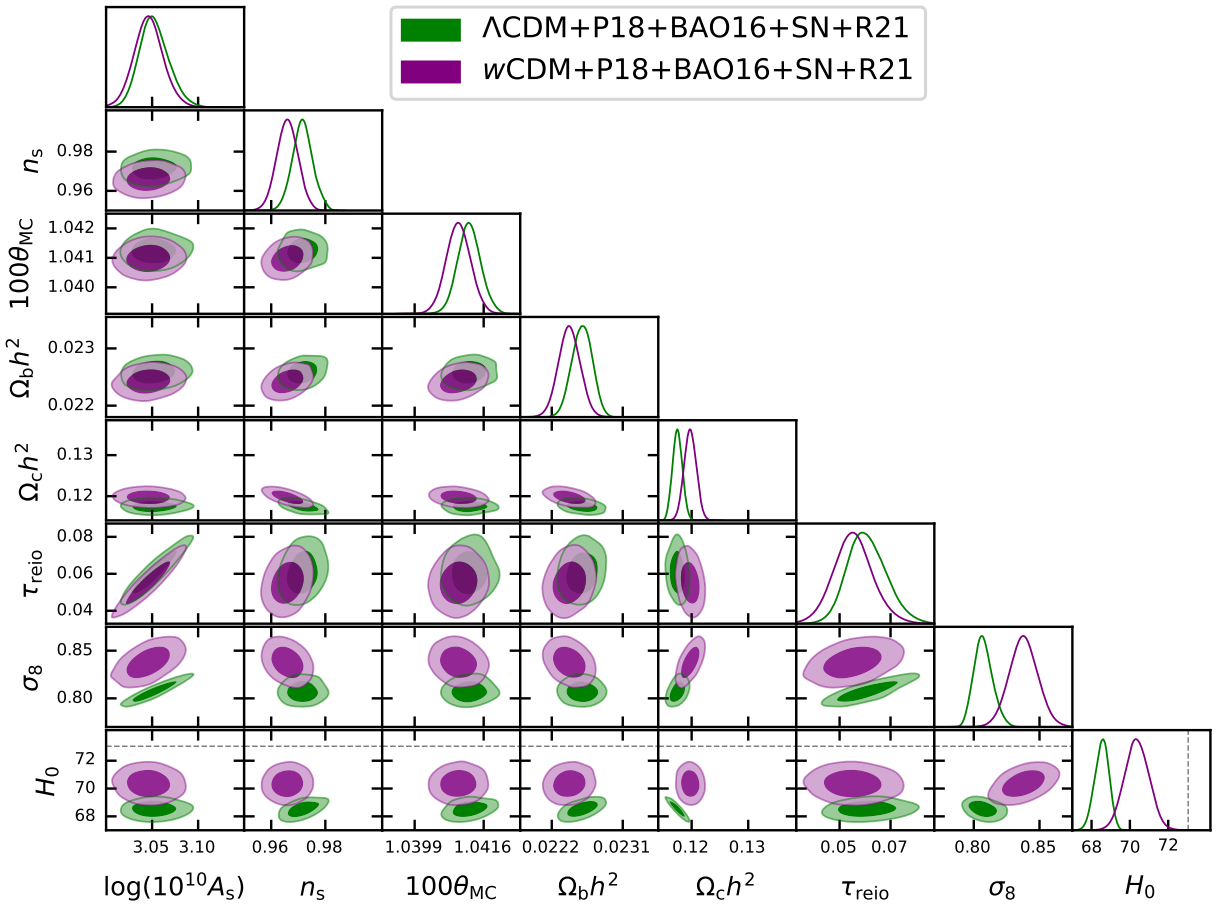


Figure 2.8: wCDM v.s. ΛCDM: 68% and 95% CL contours of $\{\log(10^{10}A_s)$, n_s, $100\theta_{\rm MC}$, $\Omega_b h^2$, $\Omega_c h^2$, $\tau_{\rm reio}$, σ_8, $H_0\}$ of wCDM v.s. ΛCDM for our baseline cosmological data sets plus H_0, P18+BAO16+SN+R21. The grey dashed line denotes the best-fit value of $H_0 = 73.04\,{\rm km/s/Mpc}$ reported by R21.

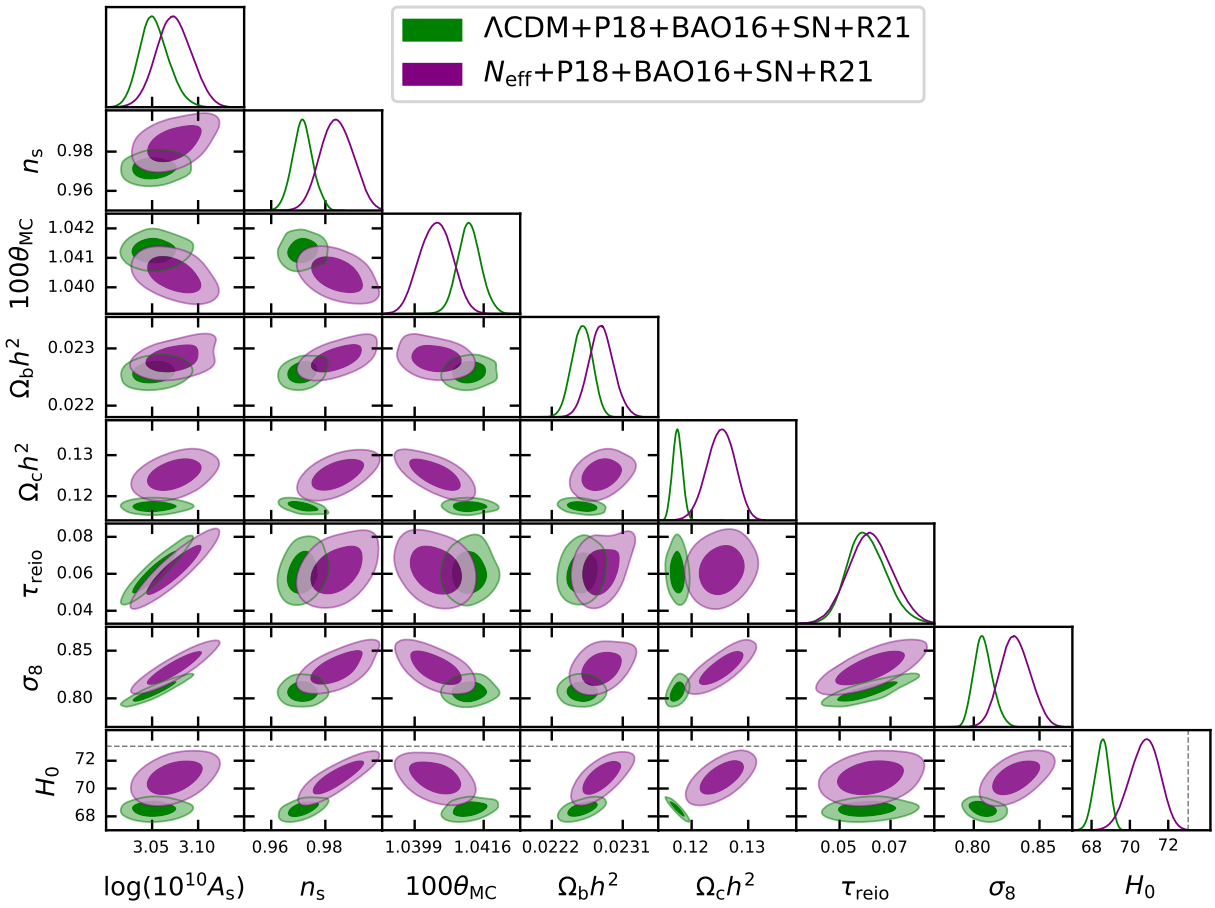


Figure 2.9: ΛCDM+$N_{\rm eff}$ v.s. ΛCDM: 68% and 95% CL contours of $\{\log(10^{10}A_s)$, n_s, $100\theta_{\rm MC}$, $\Omega_b h^2$, $\Omega_c h^2$, $\tau_{\rm reio}$, σ_8, $H_0\}$ of ΛCDM+$N_{\rm eff}$ model (purple) v.s. ΛCDM (green) for our baseline cosmological data sets plus H_0, P18+BAO16+SN+R21. The grey dashed line denotes the best-fit value of $H_0 = 73.04\,$km/s/Mpc reported by R21.

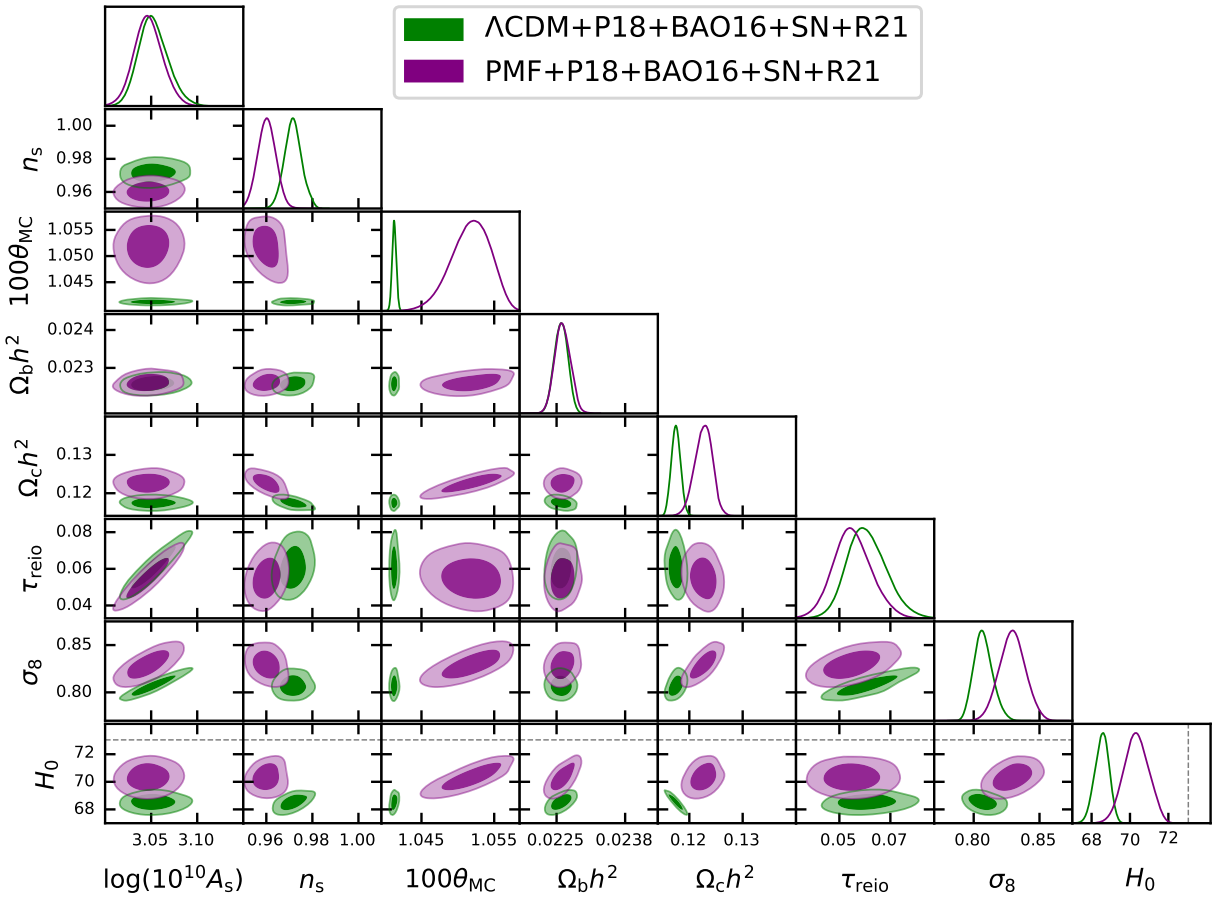


Figure 2.10: PMF v.s. ΛCDM: 68% and 95% CL contours of $\{\log(10^{10}A_s)$, n_s, $100\theta_{\rm MC}$, $\Omega_b h^2$, $\Omega_c h^2$, $\tau_{\rm reio}$, σ_8, $H_0\}$ of PMF (purple) v.s. ΛCDM (green) for our baseline cosmological data sets plus H_0, P18+BAO16+SN+R21. The grey dashed line denotes the best-fit value of $H_0 = 73.04\,{\rm km/s/Mpc}$ reported by R21.

Chapter 3

Visible in the laboratory and invisible in cosmology: decaying sterile neutrinos

This chapter is a reprint of material published in Physical Review D 108, 123036(2023).
Reprinted with permission © 2023 American Physical Society.

3.1 Introduction

Neutrino oscillations provide strong evidence for non-zero neutrino masses and are one of the most clear pieces of evidence of physics beyond the Standard Model (SM) [137]. By measuring the fluxes and energy spectra of neutrinos coming from various sources, such as the Sun, nuclear reactors, and cosmic rays interacting with the Earth's atmosphere, numerous experiments have provided compelling evidence for neutrino oscillations and, by extension, non-zero neutrino masses [394].

In near unanimity, models for neutrino mass generation require the presence of new sterile neutrino states through either Majorana or Dirac neutrino mass mechanisms [137]. Specifically, the addition of two sterile neutrinos can explain both solar and atmospheric neutrino oscillations, while a third massive sterile neutrino has considerable freedom as to its mass and mixing properties [136, 66, 284], and can be a natural dark matter candidate [153]. In this scenario, the sterile neutrino would be a neutral particle that does not participate in the Weak interactions, but could be produced by neutrino oscillations or other mechanisms, and could survive from the early Universe to the present day as a dark matter candidate [8]. The mass scale of the sterile neutrino would need to be in the range of a few to tens of keV in order to be consistent with the observed properties of dark matter [400]. Sterile neutrinos can also affect neutrino oscillation experiments by introducing additional oscillation channels and modifying the observed oscillation patterns. Although these particles have not been definitively detected, on-going experiments have reported anomalies that could potentially be explained by these particles [70, 71, 43, 44, 46, 45]. Further experimental investigations are ongoing to explore the possibility of sterile neutrinos and their role in neutrino physics [25].

The predominant model for the early Universe postulates that it underwent inflation, which diluted any prior constituents to cosmological irrelevance, assured cosmological flatness, and created the primordial density perturbations. When inflation comes to an end, its potential steepens, violating the slow roll, leading to the beginning of the reheating. During this phase, all particles that are kinematically permitted are directly created or generated through the thermal bath that the inflaton decay creates. The reheating temperature, T_{RH}, refers to the temperature of the Universe after the period of inflation when particle decays transfer their energy into SM thermalized particles, establishing the initial hot and dense state. Radiation

domination evolution leading into the required era of big bang nucleosynthesis (BBN) places the lower limit of the cosmological reheating temperature to be as low as $T_{\rm RH} = 1.8\,{\rm MeV}$ and be consistent with primordial nucleosynthesis, and with new physics that adds relativistic energy density, can be consistent with all observations [213, 219]. There are a variety of histories prior to reheating (e.g., kination and scalar-tensor cosmologies) [342, 204, 56], and even the lowest $T_{\rm RH}$ models can accommodate other key important components required of the early Universe, *viz.* baryogenesis and dark matter production [207].

Cosmology, therefore, permits $T_{\rm RH}$ to be anywhere from above the Grand Unified Theory scale $T_{\rm RH} \gtrsim 10^{15}$ GeV and the weak freezeout or BBN scale of $T_{\rm RH} \sim 2\,{\rm MeV}$, so that $T_{\rm RH}$ remains a frontier for cosmology. In the case of a high scale, the long period of weak scattering at high T allows for the thermalization of sterile neutrinos that oscillate with the active neutrinos for much of the parameter space of interest for neutrino oscillations at the eV to sub-eV sterile neutrino mass scale [272]. For high $T_{\rm RH}$, $\sin^2(2\theta)$ is tightly constrained, typically $\sin^2(2\theta) < 10^{-7}$, to ensure that the production of sterile neutrinos in the early Universe is suppressed. However, for sufficiently low $T_{\rm RH}$ universes, the scattering epoch is significantly reduced, so that even short-baseline-motivated eV-scale sterile neutrinos are allowed [220].

In such low reheating temperature (LRT) universes, keV-scale sterile neutrinos with larger mixing angles are also allowed for much of their parameter space [200, 342, 204]. Importantly, sterile neutrinos at the keV-scale in LRT models cannot be the dark matter (see discussion in Sec. 3.3). However, sterile neutrinos in LRT universes still undergo radiative decay, which can be detected by astronomical X-ray telescopes, as in the case of high reheating temperature (HRT) universes [5, 6], and could even be responsible for the unidentified X-ray line at ∼3.5 keV [106, 103]. In Ref. [91], the authors consider several mechanisms to decouple astrophysical and cosmological constraints on large-mixing angle keV-scale sterile neutrinos, including cancellation of the ν_s decay rate with new particles, new particles that

mediate β-decay differently than ν_s decay, CPT violation, lepton number suppression, as well as suppression of production of sterile neutrinos in LRT universes with an additional reduction of their contribution to the dark matter density with no specified mechanism (that paper's "cocktail" model). However, if they are not associated with any other new beyond the Standard Model (BSM) physics, sterile neutrinos in LRT universes remain significantly constrained from radiative decay and structure formation, which we show in Fig. 3.1.

Sterile neutrinos are a BSM extension that may be embedded in a richer phenomenology of their dark sector. It is known that cosmological constraints on active neutrino masses can be alleviated if the active neutrinos annihilate [88] or decay [182]. Similarly, sterile neutrinos that are partially or fully thermalized in the early Universe may decay into lighter states through a new Z', $\nu_s \to \nu_{s'} + \bar{\nu}_{s'} + \nu_{s'}$, or through a new scalar $\nu_s \to \nu_{s'} + \phi$ [155], altering their cosmological impact and related constraints.

In this paper, we study the decay of keV-scale sterile neutrinos to a dark sector, which can allow for their presence at larger mixing angles. Interestingly, the disparate redshifting of sterile neutrinos when they are relativistic vs. non-relativistic can augment low cosmological relativistic energy density, $N_{\rm eff}$, resulting from LRT models to match that inferred from cosmic microwave background (CMB) and large-scale structure observations. ($N_{\rm eff}$ is defined in Sec. 3.4.) In addition, this mechanism can provide a higher $N_{\rm eff}$ to match that preferred by the Hubble tension (e.g., see [202, 173]). Further, we show how dark decay of the sterile neutrino, when combined with LRT, opens up all of the parameter space of interest for nuclear decay searches for keV-scale sterile neutrinos, including HUNTER [369, 299], TRISTAN [302], MAGNETO-ν [401, 261], and PTOLEMY [94, 124]. If a keV-scale sterile neutrino is detected in the parameter space in which these experiments are sensitive, it would be a new probe of the pre-BBN epoch and indicate new physics in the early Universe. In Sec. 3.3, we briefly review LRT models and the constraints on keV-scale sterile neutrinos that mix with

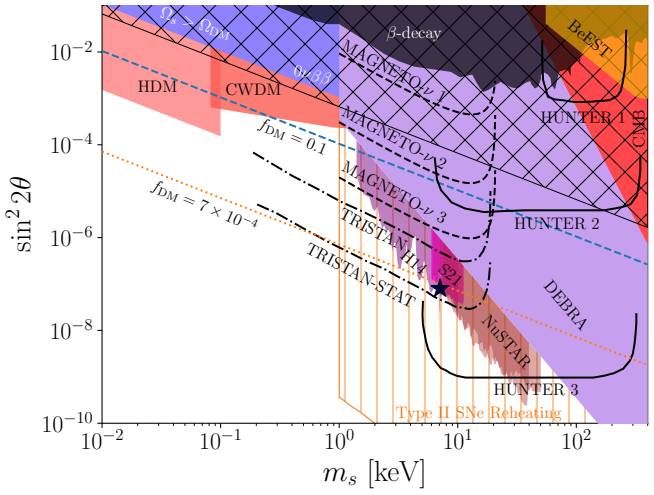


Figure 3.1: Shown here is the parameter space for a possible low reheating temperature universe with $T_{\rm RH} = 5\,\text{MeV}$, for the case of $\nu_s \leftrightarrow \nu_e$ mixing. The regions of this figure are described in the beginning of Sect. 3.3.

the active neutrinos. We introduce two dark decay models and show how dark decay can enhance the cosmological consistency of LRT models in Sec. 3.4 as well as provide a solution to the Hubble tension. We conclude in Sec. 3.5.

3.2 Neutrinos in a Low-Reheating Temperature Universe

The active neutrinos remain in contact with the plasma through weak interactions until temperatures of ~ 2 to 5 MeV—the so-called temperature of weak decoupling. For a standard lepton-number symmetric background, sterile neutrinos are produced through oscillation-based scattering production at the highest rates at $T \approx 130\,\text{MeV}(m_s/1\,\text{keV})^{1/3}$ [153]. However, sterile neutrinos can still be produced in the epoch of weak decoupling when their mixing is sufficiently large. Therefore, keV-scale sterile neutrinos are still subject to cosmological constraints at the largest mixing angles [200, 204]. In LRT cases, the cosmological relativistic energy density, $N_{\rm eff}$, in active neutrinos is reduced. Even though LRT universes

of $T_{\rm RH} = 1.8\,{\rm MeV}$ are consistent with BBN [219], they produce $N_{\rm eff} = 1.0$, which is highly discrepant with $N_{\rm eff}$ determined from Planck's observations of the CMB and galaxy surveys' baryon acoustic oscillations, which find $N_{\rm eff} = 2.99^{+0.34}_{-0.33}$ (95% CL) [42]. For reheating temperatures close to $T_{\rm RH} = 5$ MeV, $N_{\rm eff}$ can be within 10% of its canonical value, so that it remains consistent with current constraints from the CMB and large scale structure. LRT universes with $T_{\rm RH} = 1.8\,{\rm MeV}$ are still possible when there is another source for relativistic energy density. In this and other scenarios we explore below, extra relativistic energy density contributing to $N_{\rm eff}$ is from the decay of massive sterile neutrinos.

For the case of LRT universes, the production of sterile neutrinos proceeds via partial thermalization due to low temperatures, which accommodates larger mixing angles than in HRT universes. Following the notation of Ref. [200], the ν_s distribution function produced in the early Universe turns out to be

$$f_s(E,T) \approx 3.2\, d_\alpha \left(\frac{T_{\rm RH}}{5\,{\rm MeV}}\right)^3 \sin^2 2\theta \left(\frac{E}{T}\right) f_\alpha(E,T)\,, \tag{3.1}$$

where $\sin^2 2\theta$ is the mixing angle between active and sterile neutrino states, $d_\alpha = 1.13$ for $\nu_\alpha = \nu_e$, and $d_\alpha = 0.79$ for $\nu_\alpha = \nu_{\mu,\tau}$. The fraction of the sterile neutrino distribution produced is then

$$f \equiv \frac{n_{\nu_s}}{n_{\nu_\alpha}} \approx 10\, d_\alpha \sin^2 2\theta \left(\frac{T_{\rm RH}}{5\,{\rm MeV}}\right)^3 . \tag{3.2}$$

This scattering-based non-resonant production mechanism for the sterile neutrinos is the minimal case we consider in this work, and represents the conservative level of sterile neutrinos in LRT universes.

3.3 Current Constraints

In this section, we discuss constraints, regions of interest in the mass-mixing plane, and potential signals for sterile neutrinos in the case of a LRT universe. At very high mixing angles, $\sin^2 2\theta \sim 0.1$, BBN is affected due to thermalization of the sterile neutrinos and their contribution to the relativistic energy density through BBN [200, 203]. These constraints are above (weaker) than the other constraints we consider. A fundamental cosmological constraint comes from the exclusion of $\Omega_s > \Omega_{\rm DM}$[1] at large mixing angles that overproduces the sterile neutrinos to be above the dark matter density, and this is shown in the blue region in Fig. 3.1. The edge of this region represents where $\Omega_s = \Omega_{\rm DM}$. However, this line is excluded by hot dark matter (HDM) constraints [37], up to masses at which the sterile neutrinos act as warm dark matter (WDM) ($m_s \sim 0.1\,{\rm keV}$). Above the 0.1 keV mass scale, pure WDM constraints exclude the possibility of sterile neutrinos as the totality of dark matter: WDM constraints on Dodelson-Widrow nonresonantly-produced sterile neutrino dark matter are at the level of $\gtrsim$80 keV, from combined lensing plus galaxy counts constraints [313, 400]. Since LRT scattering-produced sterile neutrinos are kinematically more energetic (i.e., "hotter") [203], then constraints on LRT sterile neutrinos are more stringent than 80 keV, and well into the diffuse extragalactic background limit at 1 keV along the $\Omega_s = \Omega_{\rm DM}$ line. This exclusion is independent of $T_{\rm RH}$ within LRT models ($T_{\rm RH} \lesssim 7\,{\rm MeV}$). The combined HDM and WDM constraints therefore exclude LRT models from producing sterile neutrinos as all of the dark matter, when combined with the diffuse extragalactic background radiation constraints (discussed below) [203]. When $\Omega_s < \Omega_{\rm DM}$, mixed cold plus warm dark matter (CWDM) constraints are relevant [60]. Sterile neutrinos as fractions of the dark matter are therefore constrained by HDM and CWDM considerations, and these are shown in Fig. 3.1. Note that sometimes the HDM constraint is extended to masses $m_s > 0.1\,{\rm keV}$, up to even 10 keV [220], but that is inaccurate as the sterile neutrinos are considered to be WDM above

[1]Here, $\Omega_i \equiv \rho_i/\rho_{\rm crit}$, where $\rho_{\rm crit}$ is the critical density of the Universe

approximately $m_s \sim 0.1\,\mathrm{keV}$, and either WDM or mixed CWDM limits become appropriate.

Below the edge where $\Omega_s = \Omega_{\rm DM}$, sterile neutrinos comprise a fraction of the dark matter such that $f_{\rm DM} \equiv \Omega_s/\Omega_{\rm DM}$. We show two representative cases of $f_{\rm DM} = 0.1$ and $f_{\rm DM} = 7 \times 10^{-4}$ in Fig. 3.1. The lower fraction is commensurate with central values of the candidate signals of an X-ray line at approximately 3.55 keV, seen in the Perseus galaxy cluster, stacked galaxy clusters [106], and M31 [103].

We calculate X-ray limits in the LRT parameter space using the fraction of dark matter as ν_s at each point in the parameter space. In Fig. 3.1, we show five X-ray constraints using the commensurate fractional dark matter in the parameter space:

1. An analysis of 51 Msec of *Chandra X-ray Space Telescope* deep sky observations across the entirety of the sky, sensitive to the Milky Way halo signal, by Sicilian et al. [366], are shown in magenta and labeled S21;

2. M31 *Chandra* observations analyzed by Horiuchi et al. [232] are shown in purple and labeled H14, which we adopt because of their wider energy range than the first *Chandra* constriants;

3. NuSTAR observations toward the Milky Way Galactic Bulge for higher masses [345], are shown in brown and labeled NuSTAR;

4. NuSTAR observations of the full sky, sensitive to the Milky Way halo, are complementary to the prior NuSTAR constraints [346], and are also shown in brown and labeled NuSTAR; and,

5. The conservative but broad-band constraints on excess electromagnetic diffuse emission is labeled as the diffuse extragalactic background radiation (DEBRA) limit [102].

We do not show constraints from Ref. [141] as the limits are a factor of ∼20 weaker than

claimed, which was acknowledged within Ref. [141], and in subsequent comments [9, 101]. And, we do not show limits from Ref. [181] as that work does not include instrumental and on-sky lines present at 3.3 and 3.7 keV in their stated limits. Another astrophysical consideration comes into play in the orange vertically hatched region, where sterile neutrinos deplete energy in the core of a Type II supernova [5, 229, 65, 341], though portions of this region may also be responsible for supernova shock enhancement [229] or the origination of pulsar kicks [268].

We also show regions that are constrained by laboratory experiments, independent of any astrophysical or cosmological models, in Fig. 3.1. Constraints exist from neutrinoless double-beta decay searches in the hatched region labeled $0\nu\beta\beta$ [189], though a cancellation may exist that alleviates this constraint [347, 282, 2]. We also show the constraints from a collection of nuclear beta decay kink searches in the solid black region labeled β-decay [326]. Results from the β-decay search by BeEST are also shown in golden yellow [185].

When photons are produced in the decay of sterile neutrinos before recombination, and when these photons are produced after the thermalization time $t_{\rm th} \simeq 10^6$ sec, then this can distort the thermal nature of the CMB spectrum [171, 235] (see e.g. the discussion in Ref. [199]). The COBE FIRAS limit [180] on distortions of the thermal CMB rejects lifetimes $t_{\rm rec} > \tau > t_{\rm th}$, where $t_{\rm rec}$ is the recombination time. The red region in the upper right corner of Fig. 3.1 shows the CMB distortion limits.

Several current and upcoming laboratory experiments are sensitive to the parameter space of sterile neutrinos we are considering here. In Fig. 3.1, the black dot-dashed line is the forecast 1σ sensitivity of time-of-flight measures from the TRISTAN detector on the KATRIN β-decay experiment, with the lower line showing their statistical limit [302]. The three dashed black lines show the sensitivity of the three stages of MAGNETO-ν [401, 261] The solid lines are the forecast sensitivity for the upcoming K-capture experiment HUNTER (Heavy Unseen Neutrinos by Total Energy-Momentum Reconstruction), in its three stages

[369, 299]. PTOLEMY is a tritium β-decay experiment aimed at detecting the cosmological relic neutrino background which is expected to start collecting data within few years, and may have sensitivity to this parameter space [94, 124]. Ref. [124] provides event rates for this parameter space, but not sensitivity curve is available, so we do not show one for PTOLEMY.

We presented constraints at $T_{\rm RH} = 5\,{\rm MeV}$ in this section. Other values for $T_{\rm RH}$ would change the constraint considerations to some degree. For lower $T_{\rm RH}$, the constraint regions shift upward in $\sin^2 2\theta$, as less thermalization occurs at a given $\sin^2 2\theta$. Conversely for higher $T_{\rm RH}$, as $T_{\rm RH}$ approaches the peak of production of sterile neutrinos at $T \approx 130\,{\rm MeV}(m_s/1\,{\rm keV})^{1/3}$, the constraints of an HRT universe apply. As discussed in the introduction, LRT universes with $T_{\rm RH} = 1.8\,{\rm MeV}$ are allowed when there is a new source for relativistic energy density, such as sterile neutrinos with a dark decay mode, which we now explore.

3.4 Dark Decay Model

The population of partially to fully thermalized sterile neutrinos may not be cosmologically long-lived. In the cases of relatively large mixing that we consider, the sterile neutrinos may decay more rapidly into another sterile neutrino, ν_s', plus other dark sector particles [155, 193]. Such decays are known to alleviate constraints when they occur to the active neutrinos (e.g. [182]), and they will also alleviate constraints on sterile neutrinos. In one class of such models, a generic scalar, ϕ, is introduced with an interaction Lagrangian associated with the decay of the keV-scale ν_s to an arbitrarily lighter ν_s', $\nu_s \to \nu_s'\phi$:

$$\mathcal{L} \supset \frac{g_{i,j}}{2}\bar{\nu_j}\nu_i\phi + \frac{g'_{i,j}}{2}\bar{\nu_j}i\gamma_5\nu_i\phi + {\rm h.c.} \tag{3.3}$$

where ν_i and ν_j are the largely-sterile neutrino mass eigenstates, and $g^{(\prime)}_{i,j}$ are the scalar (pseudoscalar) couplings. Decays of keV-scale sterile neutrinos induced by this coupling are

unconstrained except for the cosmological considerations we present below.

Another possible channel for sterile neutrino decay is $\nu_s \to \nu_s' \bar{\nu}_s' \nu_s'$, mediated by a new Z' boson:

$$\mathcal{L}^{\nu}_{Z'} = g \sum_{\alpha} (\bar{\nu}_{\alpha,L} \gamma^{\mu} \nu_{\alpha,L}) Z'_{\mu} \,, \tag{3.4}$$

where g is the coupling constant associated with the new SU(2) interaction, and α goes over the sterile neutrino states, which in our case is the minimal case of two.

Both of these models in Eq. (3.3) & Eq. (3.4) introduce a new mechanism of sterile neutrino decay within a dark sector. For our interests in this work, only the lifetime of the decay associated with these new interactions, τ, is important, as well as the requirement that the decay products are arbitrarily light, so as to act as dark radiation for all of cosmological history. The decay products of ϕ, ν_s' therefore act as pure dark radiation in contribution to $N_{\rm eff}$, which we define generally as a combination of the radiation energy density in the active neutrinos $N_{\rm eff,act}$, plus the sterile neutrinos $N_{\rm eff,ster}$, plus any relativistic decay products of the sterile neutrinos, $N_{\rm eff,*}$,

$$N_{\rm eff} = N_{\rm eff,act} + N_{\rm eff,ster} + N_{\rm eff,*} \,, \tag{3.5}$$

where

$$N_{\rm eff,act} \equiv \frac{1}{\rho_{\nu}} \sum_{i} \frac{1}{4\pi^3} \int E(p) f_i(p) \mathrm{d}^3 p \,, \tag{3.6}$$

$$N_{\rm eff,ster} \equiv \frac{1}{\rho_{\nu}} \sum_{j} \frac{1}{4\pi^3} \int E(p) f_j(p) \mathrm{d}^3 p \,. \tag{3.7}$$

Here, ρ_{ν} is the relativistic energy density in a thermal single neutrino species, i sums over the partial or fully thermalized active neutrino species with energy distributions f_i, and j sums over the energy densities of the relic stable ν_s' and ϕ. In general, only one of $N_{\rm eff,ster}$ and

$N_{\rm eff,*}$ will be nonzero as the sterile neutrinos become nonrelativistic and then decay into dark radiation. In the case of the lowest LRT models, e.g. $T_{\rm RH} \approx 1.8\,{\rm MeV}$, $N_{\rm eff,act} \approx 1$[219], so that $N_{\rm eff}$ is predominantly dark radiation, while in higher LRT models, e.g. $T_{\rm RH} \approx 7\,{\rm MeV}$, $N_{\rm eff}$ is predominantly active neutrinos ($N_{\rm eff,act}$), with dark sector particles ($N_{\rm eff,*}$) contributing a small perturbation.

3.4.1 Evolution of the Abundance of Decaying Sterile Neutrinos in an LRT universe

In the case of sterile neutrinos with appreciably mixing, their abundance in an LRT universe is initially set by their approach to equilibrium after $T_{\rm RH}$. This process is described by the Boltzmann equation. Their subsequent evolution is set by their redshifting as radiation and, when $T \lesssim m_s$, as matter components, followed by their subsequent decay.

With no direct coupling to the reheating mechanism, sterile neutrinos are not present at $T_{\rm RH}$, and are never in thermal equilibrium in the early Universe [397, 269]. Nevertheless, there are different mechanisms by which the relic population of sterile neutrinos could have been produced subsequent to reheating [153, 364, 268, 327]. In this paper, we focus on the minimal model in which the production of sterile neutrinos requires no new physics other than neutrino mass and mixing, and production arises from non-resonant flavor oscillations between the active neutrinos ν_α of the SM and the sterile neutrino ν_s, as originally proposed by Dodelson and Widrow (DW) [153].

In the LRT model, prior $T_{\rm RH}$, the entropy in radiation and matter is not conserved and consequently, the T dependence on the scale factor a is different than the usual $T \propto a^{-1}$. In this scenario, prior to the radiation dominated standard epoch, a scalar field oscillates coherently around its true minimum and dominates the energy density of the Universe. The decay of this scalar leads to nonthermal decay products that subsequently thermalize to a $T =$

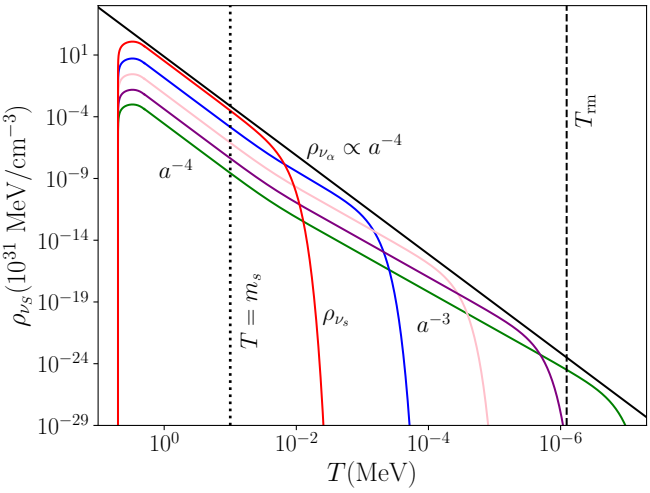


Figure 3.2: Shown here is the calculated production and energy density evolution for massless standard neutrinos (black line) and an example of $m_s = 100\,\mathrm{keV}$ sterile neutrinos. We show five different $\sin^2 2\theta$ cases of sterile neutrino energy density evolution, ρ_{ν_s}. The sterile neutrinos decay at different times (temperatures) ranging from a case that matches the neutrino's mass $T_{\mathrm{decay}} = 0.1\,\mathrm{MeV}$ (red line) down to the temperature of matter radiation equality (green line). Note that sterile neutrinos with very different initial production densities can all match the same density relative to the active neutrinos at their decay. Therefore, a wide range of sterile neutrino masses and $\sin^2 2\theta$ can match a designated N_{eff}, when combined with either a nearly fully thermalized or non-thermalized ρ_{ν_α} in LRT cosmologies. The reheating temperature in this example is chosen to be 5 MeV. The moments of $T = m_s$ and T_{rm} are shown with the dotted and dashed vertical lines, respectively.

T_{RH}, followed by standard radiation domination and evolution (see e.g. Refs. [255, 201, 198]).

Interactions of active neutrinos with the surrounding plasma during the oscillations act as measurements and force the propagating neutrino energy eigenstates into determinate flavor states, which with some probability results in a sterile neutrino. For the parameter space of interest here, the production rate is usually not fast enough for sterile neutrinos to thermally equilibrate, and the process is a freeze-in of the final abundance.

Assuming that only two neutrinos mix, ν_s and one active neutrino ν_α (ν_e in all of the figures we present in this paper), the time evolution of the phase-space density distribution function of sterile neutrinos $f_{\nu_s}(p,t)$ with respect to the density function of active neutrinos $f_{\nu_\alpha}(p,t)$

is given by the following Boltzmann equation [265, 5]

$$\begin{aligned}\frac{d}{dt}f_{\nu_s}(p,t) &= \frac{\partial}{\partial t}f_{\nu_s}(p,t) - Hp\frac{\partial}{\partial p}f_{\nu_s}(p,t) \\ &= \Gamma(p,t)\Big[f_{\nu_\alpha}(1-f_{\nu_s}) - f_{\nu_s}(1-f_{\nu_\alpha})\Big] \ . \end{aligned} \tag{3.8}$$

Here H is the expansion rate of the Universe, p is the magnitude of the neutrino momentum and $\Gamma(p,t)$ is the conversion rate of active to sterile neutrinos. The active neutrinos are assumed to have a suppressed to full Fermi-Dirac distribution, depending on their thermalization state determined by $T_{\rm RH}$.

Since $f_{\nu_s} \ll 1$ and $f_{\nu_s} \ll f_{\nu_\alpha}$, we take $(1-f_{\nu_s}) = 1$, and the second term in brackets on the right-hand side of Eq. (3.8) can be neglected. Thus, changing variables, Eq. (3.8) can be rewritten as [342, 5]

$$-HT\left(\frac{\partial f_{\nu_s}(E,T)}{\partial T}\right)_{E/T} \simeq \ \Gamma(E,T) f_{\nu_\alpha}(E,T) \ , \tag{3.9}$$

where the derivative on the left-hand side is computed at constant E/T.

The conversion rate Γ is the total interaction rate $\Gamma_\alpha = d_\alpha G_F^2 \epsilon T^5$ of the active neutrinos with the surrounding plasma weighted by the average active-sterile oscillation probability $\langle P_m \rangle$ in matter (see Eq. (6.5) of Ref. [5]).

We obtain the sterile neutrino density distributions by integrating the Boltzmann Eq. (3.9). We show the resulting production of sterile neutrino density evolution at the far left of Fig. 3.2, where the density rises from zero. Here, we recover the results of Ref. [204]. Following production, the ν_s energy density dilutes as radiation, $\rho_{\nu_s} \propto a^{-4}$, as long as $T \gg m_s$. As the Universe cools to $T \sim m_s$, there is a transition of the decrease of the ν_s energy density to redshifting as matter, $\rho_{\nu_s} \propto a^{-3}$. For the example shown in Fig. 3.2, $m_s = 100\,\text{keV}$, but onset of pure matter-like redshifting occurs somewhat later than $T \approx m_s$, as LRT-produced

sterile neutrinos are slightly "hotter" than thermal, with $\langle p \rangle \approx 4.11T$ [204].

The presence of sterile neutrinos with masses between the epoch of BBN and the photon last-scattering time allows the ν_s to augment their energy density with respect to the active neutrinos' by becoming nonrelativistic and redshifting more slowly. They then deposit their energy density back into relativistic dark decay products ($\nu_{s'}$ and/or ϕ) denominated as $N_{\rm eff,*}$. Therefore, the massive ν_s can boost $N_{\rm eff}$ above $N_{\rm eff,act}$ produced by reheating alone in an LRT model, Eq. (3.5). The amount of relativistic energy deposited can be approximated by matching the density of the nonrelativistic sterile neutrinos with the targeted boost in dark radiation,

$$m_s n_{\nu_s} = N_{\rm eff,*} \rho_{\nu_\alpha} \,. \tag{3.10}$$

Using Eq. 3.2, we solve for the fraction of sterile neutrino production for a given $N_{\rm eff,*}$ as

$$f = \frac{N_{\rm eff,*} \rho_{\nu_\alpha}}{m_s n_{\nu_\alpha}} \,. \tag{3.11}$$

This relation then stipulates what production of ν_s is needed to hit the target $N_{\rm eff,*}$. The energy density boost needed for smaller levels of production at smaller mixing angles requires longer matter-like redshifting before decay. We take the maximum decay time to be that corresponding to matter radiation equality, $T_{\rm rm}$, so that the decays do not directly affect the photon decoupling epoch.

The relativistic energy density contribution of sterile neutrino decays can range from a majority of $N_{\rm eff}$ ($N_{\rm eff,*} \gtrsim N_{\rm eff,act}$) to a small perturbation onto $N_{\rm eff}$ ($N_{\rm eff,*} < N_{\rm eff,act}$), depending on the $T_{\rm RH}$, m_s, $\sin^2 2\theta$, and τ. Since $N_{\rm eff}$ can be augmented by this mechanism, it may be responsible for any potential evidence for $N_{\rm eff}$ above its standard value. For higher $T_{\rm RH}$, more production occurs for a given $\sin^2 2\theta$ and m_s, so that higher $T_{\rm RH}$ models probe smaller mixing angles (see Fig. 3.3). We go through several examples in the following section.

In summary, the sterile neutrinos can decay at a wide range of time scales, as shown in Fig. 3.2. As an example, we illustrate five decay timescale scenarios. The most rapid decay time is commensurate with $T = m_s$ (this case's outcome would be similar to any decay timescale at $T < m_s$, as the relativistic energy density in ν_s is simply transferred to the dark states). The slowest decay we consider occurs at the time of radiation-matter equality $T_{\rm rm}$. We also show three intermediate cases. In addition, we plot the energy density evolution of the massless active neutrinos (black line).

3.4.2 Decaying Sterile Neutrino Parameter Space in LRT Cosmologies

In an LRT cosmology, sterile neutrinos are produced just after $T_{\rm RH}$, then redshift as radiation, and potentially as matter, before ultimately decaying to dark radiation species. The amount of decay products' contribution to $N_{\rm eff}$ varies with several parameters, as determined by Eq. (3.11). We consider three potential final values for $N_{\rm eff}$ (Eq. (3.5)):

- $N_{\rm eff,Std} = 3.044$, the standard value with a standard enhancement from electron-positron annihilation [90, 50];
- $N_{\rm eff,Upper} = 3.33$, the 95% CL upper bound from Planck 2018 [Eq. (67b)] in Ref. [42]];
- $N_{\rm eff,H0} = 3.48$, the central value preferred by solutions to the Hubble, H_0, tension [344, 173].

The precise value of $N_{\rm eff,act}$ in LRT models depends on $T_{\rm RH}$. We use the bottom panel of Fig. 1 in Ref. [219], for the relation between $T_{\rm RH}$ and $N_{\rm eff,act}$. For the highest temperature LRT cosmology we consider, $T_{\rm RH} = 7\,{\rm MeV}$, the active neutrinos are almost fully thermalized, and $N_{\rm eff,act} = 3.0$. Therefore, to match the standard $N_{\rm eff}$, we require $N_{\rm eff,*} = 0.044$, while

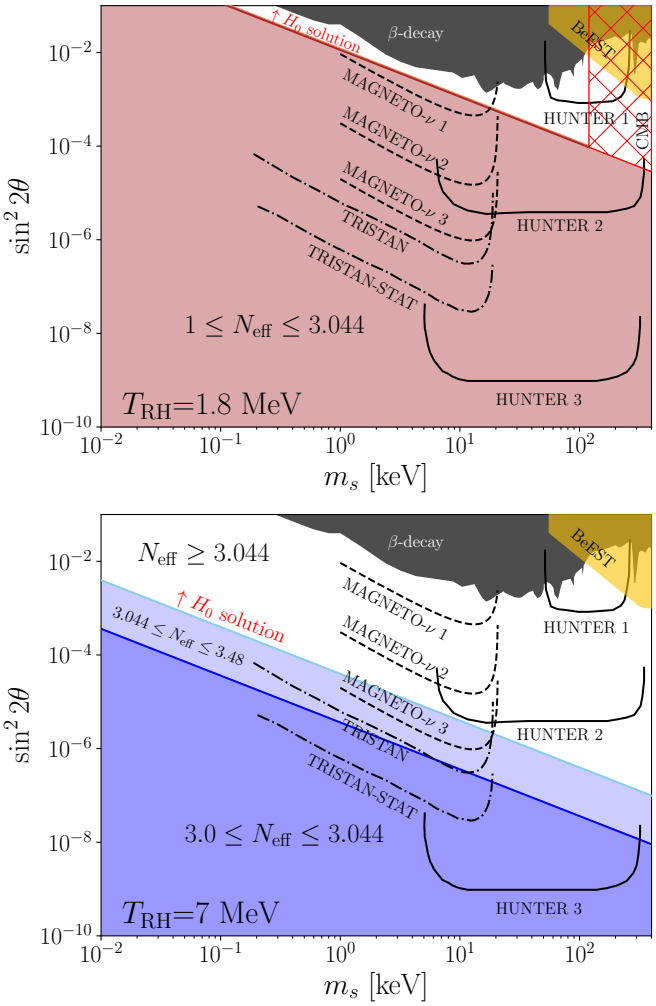


Figure 3.3: Shown are the updated parameter spaces of dark decay in an LRT Universe for two cases, $T_{\rm RH} = 1.8\,{\rm MeV}$ and $7\,{\rm MeV}$, left and right, respectively. The diagonal reddish and blueish lines correspond to the cases when the decay happens at the temperature of matter-radiation equality, and match different $N_{\rm eff}$ values. For each pair, the darker color (lower) is associated with a value of $N_{\rm eff,Std} = 3.044$, and the lighter color one $N_{\rm eff,H0} = 3.48$ [173]. For the darker shaded region, $N_{\rm eff}$ ranges from the minimal provided by $N_{\rm eff,act}$ to the standard value with a contribution from sterile neutrino decay. In the lighter shaded region on the right panel, $N_{\rm eff}$ ranges from the standard value to that preferred to alleviate the Hubble tension, $N_{\rm eff,H0}$. Above the lighter diagonal, the parameter space can accommodate an alleviation of the Hubble tension with $N_{\rm eff,H0}$, or provide the standard density, $N_{\rm eff,Std}$. For the case of $T_{\rm RH} = 1.8\,{\rm MeV}$, the thermal nature of the CMB [235] constrains the red hatched portion. This constraint does not apply for $T_{\rm RH} = 7\,{\rm MeV}$ in this parameter space.

matching the H_0 tension requires $N_{\rm eff,*} = 0.48$, respectively. For a $T_{\rm RH} = 1.8\,{\rm MeV}$, $N_{\rm eff,act} = 1.0$, therefore, the standard density requires $N_{\rm eff,*} = 2.044$ and solving the H_0 tension requires $N_{\rm eff,*} = 2.48$, respectively.

For the case where there is no matter-dominated evolution of the sterile neutrino before it

decays, there is no energy boost from differential redshifting of active and sterile neutrinos, and all density must come from oscillation production. Using Eqs. (3.2) & (3.11), this corresponds to a value of $\sin^2 2\theta > 0.1$, above the parameter space we consider in Fig. 3.3. Another limiting case is when the decay occurs at radiation-matter equality $T_{\rm rm}$. We calculate $T_{\rm rm}$ decay contours and plot them in Fig. 3.3, for the reheating temperatures of 1.8 MeV (left panel) and 7 MeV (right panel). We show two lines: one where the active neutrino and sterile neutrino decay products' density matches the standard $N_{\rm eff,Std} = 3.044$ (darker, lower line)[42] and where the active neutrino and sterile neutrino decay products' density matches the H_0 tension alleviating value of $N_{\rm eff,H0} = 3.48$ (lighter, upper line)[173, 344]. In the right panel's lighter shaded area, $N_{\rm eff}$ spans from its standard value to the value favoring the mitigation of the Hubble tension, denoted as $N_{\rm eff,H0}$. Above the lighter diagonal line, the parameter space is capable of supporting either a resolution to the Hubble tension with $N_{\rm eff,H0}$, or maintaining the standard density, $N_{\rm eff,Std}$. That is, sterile neutrinos with mass and mixing above the the lighter curves are consistent with cosmology at the specified $N_{\rm eff}$ values. This is achieved because there is a cancellation between enhanced production at higher $\sin^2 2\theta$ and earlier decay providing less matter-redshift boost (see Fig. 3.2).

Because the sterile neutrinos mix with active neutrinos, they have a loop radiative decay to a lighter predominantly-active neutrino mass eigenstate and a photon [365, 323]. Since the decays take place necessarily during the photon-coupled era, the effects of the decay photon is on distorting the thermal nature of the CMB photons. Hu & Silk [235] calculated spectral distortions to the CMB radiation originated by the decay of unstable relic particles during the thermalization epoch. The appropriate constraints are from Fig. 1 in Ref. [235], where these limits constraints are most stringent for the largest masses in late-decay scenarios (maximizing the coefficient of the y-axis in Fig. 1 of Ref. [235]). For the models plotted in Fig. 3.3, the decay happens at $T_{\rm rm}$, or an age of the Universe of $t_{\rm rm} \approx 1.6\times10^{12}$ sec. The limits in Ref. [235] are presented in $y \equiv m_X(bn_X/n_\gamma)$, where m_X is the decaying particle mass, n_X/n_γ is its abundance relative to the photons, and b is the branching ratio to photons for

the decay. For the highest mass of our parameter space, $m_s = 400\,\mathrm{keV}$, $y = 4.6 \times 10^{-15}\,\mathrm{GeV}$ for $T_{\mathrm{RH}} = 7\,\mathrm{MeV}$. However, for $T_{\mathrm{RH}} = 1.8\,\mathrm{MeV}$, the abundance of ν_s is much greater at late times, and $y = 1.3 \times 10^{-11}\,\mathrm{GeV}$. So, no radiative decay constraint exists for the case of $T_{\mathrm{RH}} = 7\,\mathrm{MeV}$. We find the highest m_s compatible with the $T_{\mathrm{RH}} = 1.8\,\mathrm{MeV}$ curve, and that is 120 keV, and the constraint is independent of $\sin^2 2\theta$. We show the CMB thermal constraint in Fig. 3.3, and it applies to $T_{\mathrm{RH}} = 1.8\,\mathrm{MeV}$ cosmologies, and is non-existent in our parameter space for cases approaching $T_{\mathrm{RH}} = 7\,\mathrm{MeV}$.

The only other constraints that are present in the parameter space in this scenario are the $\beta-$decay (black contour) [326] and BeEST (yellow contour) [185]. As shown in Fig. 3.3, laboratory experiments such as HUNTER, TRISTAN, or MAGNETO-ν can detect the signal of sterile neutrinos in much of the allowed regions of this parameter space.

3.5 Discussion & Conclusions

The reheating temperature of the Universe is unknown beyond the requirement that it is $T_{\mathrm{RH}} > 1.8\,\mathrm{MeV}$, as long as there is a new source of relativistic energy density in addition to the active neutrinos, and $T_{\mathrm{RH}} \gtrsim 5\,\mathrm{MeV}$, in the case of no new physics [219]. Therefore, T_{RH} is a free parameter in studies of the energy content arising from the hot big bang. Baryogenesis and dark matter production can be accommodated in the reheating process [207, 126]. In LRT cosmologies, the weak-coupling epoch is significantly reduced, suppressing active-sterile neutrino oscillations. As a result, regions of keV-scale sterile neutrinos' parameter space that were previously forbidden by cosmological or astrophysical constraints can become viable [200]. If the dark sector in which the sterile neutrino participates includes dark decay channels, we have shown here that the parameter space in LRT cosmologies is even more significantly alleviated. The energy density described by N_{eff} in such dark-decay LRT cosmologies can have both pure, decay-produced, non-thermal, radiation components, as

well as massive active neutrino components. High sensitivity to $N_{\rm eff}$ will be provided by current and upcoming CMB experiments such as CMB-S4 [4]. The discovery of a sterile neutrino with parameters in this region could indicate a rich LRT thermal history.

Several current and upcoming laboratory experiments are sensitive to keV-scale sterile neutrino parameter space, including HUNTER [369, 299], TRISTAN [302], MAGNETO-ν [401, 261], and PTOLEMY [94, 124]. Laboratory direct dark matter detection experiments employing xenon, including LZ [1] and XENONnT [62], could be sensitive to our considered parameter space [112]. However, only the case of all of the dark matter being sterile neutrinos has been considered, and the constraints proportionately alleviate for fractional dark matter models, with all cases lying above the DEBRA constraints in Fig. 3.1, but they could considerably improve. The appreciable mixing between active and sterile neutrinos we consider here may also arise from non-standard interaction (NSI) searches. Currently, the constraints in this NSI parameter space are largely the ones we have shown: β-decay and $0\nu\beta\beta$-decay [93].

The next few years could provide the potential discovery of laboratory-accessible sterile neutrinos, whose existence is in conflict with HRT cosmologies, with the aforementioned β-decay, K-capture, and neutrino capture experiments. In this work, we showed that the presence of decaying keV-scale sterile neutrinos could also be indicated by the H_0 tension. The discovery of keV-scale sterile neutrinos with appreciable mixing would be an important finding for particle physics, astrophysics, and cosmology, not only for its own discovery, but it would alter the usual assumptions of the early Universe and provide a new paradigm.

Chapter 4

Status of neutrino cosmology: Standard ΛCDM, extensions, and tensions

This chapter is a reprint of material published in Physical Review D 111, 043520 (2025).
Reprinted with permission © 2025 American Physical Society.

4.1 Introduction

Neutrinos are among the most enigmatic particles in the Standard Model (SM) of elementary particle physics. However, they are vital in cosmology, as they impact the Universe's evolution and contribute to the formation of the large-scale structures we see today. Their properties and nature can be studied by the detectable imprints they leave on cosmological data. When neutrinos were definitively measured to oscillate and have mass over 25 years ago, their impact on cosmology was understood to be significant (for reviews, see

Refs. [276, 214, 14]). The 6-parameter cosmological standard model has been exceedingly successful in its consistency with observational data from the last-scattering surface of the cosmic microwave background (CMB) to galactic scales today [42]. The principle constituents of this model are cold dark matter and dark energy in the form of a cosmological constant, so it is referred to as ΛCDM. Neutrinos with arbitrary mass are an extension of ΛCDM, since their oscillations measure the difference of the squares of the neutrinos' mass, and not their absolute mass scale. In addition, if neutrinos are non-thermal or have extra states, this adds another measurable unknown to minimal ΛCDM.

Currently, cosmological data are already offering constraints on neutrino properties that are not only complementary to terrestrial experiments but also competitive with them. For example, leading cosmological results on neutrino mass are approximately a factor of 20 more stringent [28], as cosmology measures the sum of neutrino mass eigenstates, Σm_ν, while direct kinematic laboratory measurements via nuclear β-decay are sensitive to the effective electron antineutrino mass [49]. Cosmological constraints on neutrino properties are model-dependent in that they require the minimalist assumption of a single-parameter extension to ΛCDM, Σm_ν. The existence of a thermal relic cosmic neutrino background is a fundamental prediction of the standard hot Big Bang model and ΛCDM. Though it has not been directly detected, indirect evidence supports its presence through the primordial abundance of light elements produced during Big Bang Nucleosynthesis (BBN), the power spectrum of CMB anisotropies, and cosmological large-scale structure [132]. These observations would be significantly inconsistent without a relativistic cosmological component that closely matches the properties predicted by the standard neutrino decoupling process, involving only weak interactions. As a result, cosmology is attuned to specific neutrino properties: their density, linked to the number of active neutrino species, and their masses. ΛCDM assumes that the only light, relativistic relic particles since BBN are photons and active neutrinos. Extended models propose additional light particles, such as sterile neutrinos or thermal axions, which can mimic the effects of active neutrinos and complicate the interpretation of the inferred

relic neutrino density, since new relativistic components can both add to the relativistic energy density, or replace that of the active neutrinos. These models have been explored to address anomalies like the Hubble tension, the discrepancy between inferred and direct measurements of the Universe's expansion rate.

In the ΛCDM model, three active neutrinos thermalize in the early Universe, decoupling gradually around temperatures of 2 MeV. The effective number of neutrino species, $N_{\rm eff}$, is defined via

$$\frac{\rho_{\rm rad}}{\rho_\gamma} = \frac{7}{8} N_{\rm eff} \left(\frac{4}{11}\right)^{4/3} . \tag{4.1}$$

Here, $\rho_{\rm rad}$ and ρ_γ represent the energy density of non-photon radiation and photons respectively. $N_{\rm eff}$ quantifies the relativistic energy density beyond photons, which could be any relativistic relic component. In the standard cosmology, $N_{\rm eff}$ is composed solely by the active neutrino density contribution, i.e., $N_{\rm eff} = N_\nu^{\rm SM}$, with precise calculations predicting $N_\nu^{\rm SM} = 3.044$ when accounting for neutrino oscillations, incomplete neutrino decoupling through $e^\pm$ annihilation, and QED corrections [50, 90, 186]. Cosmological observations' confirmation of this value is a crucial test of the standard ΛCDM model, and observations that definitively infer a value deviating from N_ν would be a major breakthrough. In concert, the adoption of $N_{\rm eff} = 3.044$ for interpreting the effects of the standard active neutrinos is an essential standard model assumption to place neutrino mass limits with cosmology.

An increased $N_{\rm eff}$ influences the observable power spectrum of CMB anisotropies and matter clustering through changes in the background cosmological expansion through matter-radiation equality, and changes in the growth of perturbations. If the densities of other components are held constant, a higher $N_{\rm eff}$ delays radiation-to-matter equality, leading to significant alterations in the CMB anisotropies, specifically suppressing the high-ℓ multipole peaks relative to their position in ℓ. To better isolate the effect of $N_{\rm eff}$, it is useful to increase

the densities of total radiation and matter uniformly, keeping the redshift of matter-radiation equality fixed. This adjustment reveals that a higher $N_{\rm eff}$ increases the diffusion (Silk damping) scale at decoupling, resulting in decreased CMB temperature power at high multipoles relative to the sound horizon, which determines the acoustic peak positions [14]. The free-streaming radiation parameterized by $N_{\rm eff}$ also produces a phase-shift in the acoustic peaks that is unique [83], and has been detected [85].

Additionally, neutrino's dual behavior, acting as radiation at early times and transitioning to dark matter-like evolution during later structure formation, places them in an unique position in cosmology. As neutrinos transition from relativistic to non-relativistic states, they initially travel at nearly the speed of light, which affects their diffusion scale and has important consequences for gravitational clustering and the growth of large-scale structures. Once they become non-relativistic, the energy density of neutrinos is primarily determined by their total mass:

$$\Omega_\nu = \frac{\rho_\nu^0}{\rho_{\rm crit}^0} = \frac{\Sigma m_\nu}{93.13\ h^2\ {\rm eV}}\,, \tag{4.2}$$

where ρ_ν^0 and $\rho_{\rm crit}^0$ are respectively the total neutrino and critical density of the Universe today and h is the Hubble constant in units of $100\,{\rm km\,s^1\,Mpc^1}$. In this expression, we use the temperature of neutrinos that provides $N_\nu = 3.044$. The absolute neutrino mass scale has been probed using beta decay, with the KATRIN experiment currently providing the best bound on the beta-decay effective neutrino mass of $m_{\nu,\beta} < 0.45\,{\rm eV}$ at 90% confidence [49].

The presence of massive neutrinos has varied effects on CMB observables. An increase in neutrino mass impacts the late-time non-relativistic matter density, altering the angular diameter distance to recombination and the late integrated Sachs Wolfe (ISW) effect. The transition of neutrinos to a non-relativistic state also induces variations in the Universe's

pressure-to-density ratio, observable through the early ISW effect, and reduces the overall signal of weak lensing of CMB anisotropies because of free-streaming suppression of the large scale structure that produces the lensing of the CMB. It is this last observable, lensing of the CMB, that makes high angular resolution CMB observations highly sensitive to neutrino mass [253]. Because the suppression of the matter power spectrum of large-scale structure (LSS) by neutrinos occurs below the horizon scale of matter-radiation equality, an increase in the dark matter density, $\Omega_{\rm cdm}$, can compensate the presence of matter neutrinos in LSS clustering observations, making neutrino mass positively correlated with increases in $\Omega_{\rm cdm}$.

The baryon acoustic oscillation (BAO) signature has become a standard cosmological signal measurable by several cosmological surveys [392]. The BAO peak in real space, measured through the correlation function of matter tracers such as galaxies and gas, is imprinted by the expansion of overdensities moving at the sound speed of the plasma at the time, until the moment of photon decoupling. The length of this motion is the sound horizon. The sound horizon, r_s at the decoupling redshift, z_d, is approximately given by

$$r_{\rm s}(z_{\rm d}) = \int_{\infty}^{z_{\rm d}} \frac{c_s\, dz}{H(z)} \tag{4.3}$$

where c_s is the sound speed, and $H(z) = H_0\sqrt{\Omega_m(1+z)^3 + \Omega_r(1+z)^4}$ is the Hubble rate through the early to decoupling epoch. Here, Ω_m and Ω_r are the critical densities in matter and radiation, respectively. Increases in both Ω_m and $N_{\rm eff}$ (via Ω_r) both increase their contribution to $H(z)$, and decrease the sound horizon and the BAO scale, which makes BAO observations very sensitive to the matter and radiation content of the early Universe. The cosmological evolution of the BAO scale provides it as a powerful standard ruler for measurements of dark energy and its evolution [362]. Neutrino mass affects the BAO length-scale when neutrino mass is sufficiently large as to become non-relativistic during the drag epoch, before photon decoupling. In linear theory, the BAO scale diminishes with increasing neutrino mass because, though the neutrinos free stream and redshift as radiation in early

times, they augment Ω_m during the BAO drag epoch, reducing r_s as an increase in Ω_m would. Therefore, the BAO scale generally makes Σm_ν anti-correlated with $\Omega_{\rm cdm}$, complementary to their degeneracy with LSS clustering [377]. Because the geometrical information in the BAO scale comes in the form of a ratio of r_s to the angular diameter and line-of-sight distances, the geometry measured by the BAO scale is both sensitive to the neutrino mass, and can also change the relation of Σm_ν and $\Omega_{\rm cdm}$ from anti-correlation to correlation as distances' dependencies dominate over r_s dependencies [74]. As detailed in Ref. [287], geometric information from the BAO scale and its ratio to distances can be as sensitive—or even more-so—than growth of structure probes of neutrino mass.

Supernovae (SNe) observations measure the relationship between the luminosity distance and redshift in the local Universe. This is dependent on the late-time cosmological energy density, and therefore, SNe are not directly sensitive to neutrino mass or radiation energy density. However, SNe do constrain parameters degenerate with neutrino mass in CMB and BAO observables, primarily Ω_m and the dark energy equation of state (EoS), w. We include SNe because of their complementary sensitivity to CMB and BAO determinations of cosmological growth and expansion history. In Ref. [287], it was shown that middle to low-redshift geometrical measures from BAO and SNe are highly sensitive to the total cosmological matter content as a *fraction* of the critical density, as opposed to the *physical* density, and therefore are highly sensitive to the neutrino mass contribution to this fractional density. The sensitivity is such that fixing the angular sound horizon from the CMB gives low-redshift measures a scaling of $\Omega_m \propto (1 + f_\nu)^5$, where $f_\nu \equiv \Omega_\nu/\Omega_m$.

Much of our work studies the constraints on neutrinos as minimal extensions beyond the 6-parameter framework of ΛCDM, which successfully describes nearly all cosmological observables with the amplitude of scalar perturbations, A_s, the spectral index of these perturbations, n_s, the optical depth to the last-scattering surface of the CMB, τ, an angular scale corresponding to the sound horizon of the last scattering surface, $\theta_{\rm MC}$, as well as the

density of cold dark matter and baryons relative to the critical density, $\Omega_{\rm cdm}$ and $\Omega_{\rm b}$. We also study an 11-parameter extension of ΛCDM which allows variation of the evolution of the dark energy density through w_0 & w_a, the curvature of the Universe, Ω_k, as well as the neutrino-related parameters, Σm_ν & $N_{\rm eff}$.

The structure of this paper is as follows: Section 6.3.1 details the datasets and likelihoods adopted in our analysis. Section 4.3 explains the statistical methods we employed. Section 4.4 presents our findings within ΛCDM, including constraints on Σm_ν and neutrino mass ordering, as well as $N_{\rm eff}$. In Section 4.5, we discuss tension datasets, including H_0 and S_8, and the neutrino-related extensions of ΛCDM that the tensions motivate, including massive neutrinos and extra (sterile) neutrinos. Finally, we conclude and discuss the future outlook in Section 6.5.

4.2 Cosmological Datasets

We present here the cosmological datasets and methodology adopted in our work. We selected those datasets that are among the most robust measures of cosmological growth and expansion history for their epochs, and which span a wide range of cosmological history. That is, they are those observations that have the minimum statistical errors for their measurements. In addition, these datasets have undergone thorough testing for systematic effects, as we discuss below. Lastly, these observations provide strong leverage for tests of cosmology with measurements of expansion and growth history over the widest possible observational range, from the surface of last scattering to low redshifts.

Datasets			
CMB Planck	CMB Lensing	BAO	SNe
P18 CamSpec P20	Lensing PR4 + ACT DR6	DESI DR1	PP U3 DES Y5

Table 4.1: Summary of the cosmological datasets we considered in this work, as introduced in Section 6.3.1.

4.2.1 Planck CMB

The Planck survey of CMB has precisely measured the CMB anisotropies via their temperature and polarization angular power spectra, with five out of six ΛCDM parameters determined to better than 1% with Planck data alone, with the most accurately known parameter, the angular sound horizon, now measured to 0.03%. Over the years, Planck data and its analysis has advanced considerably, starting with the initial data release in 2013, followed by the incorporation of polarization data in 2015, and culminating in significant enhancements to systematic corrections in the ultimate 2018 data release. Since that final data release, there have been two independent reanalyses of the Planck data products. We consider all three:

Planck 2018 (P18): we use CMB temperature and polarization anisotropy power spectra (and their cross-spectra) from the Planck 2018 legacy data release (PR3) [42, 41]. Specifically, we use: the high-ℓ `Plik`; the low-ℓ `commander` likelihood for the TT spectrum in the multipole range $2 \leq \ell \leq 29$; likelihood or the TT spectrum in the multipole range $30 \leq \ell \leq 2508$ and for the TE and EE spectra in the range $30 \leq \ell \leq 1996$, and the low-ℓ `SimAll` likelihood for the EE spectrum in the range $2 \leq \ell \leq 29$. It is worth mentioning that the lensing anomaly for this analysis is at a 2.8σ level and significantly reduced in the two reanalysis we introduce next [314].

CamSpec: CamSpec project reanalyzed the Planck temperature and polarization maps of the CMB of each Planck data release. The motivation for creating this new revised likelihood was to provide a single-source detailed description of the construction of likelihoods for the Planck collaboration as well as testing the consistency and fidelity of the Planck data. CamSpec included additional methods for improved subtraction of Galactic dust emission, extending sky coverage and improving accuracy in temperature and polarization power spectra, compared to previous Planck analyses [163]. The lensing anomaly in this analysis is reduced when compared to P18 and it is at a 1.7σ level [314].

Planck NPIPE (P20): the Planck Collaboration released a new processing pipeline in 2020 for generating calibrated frequency maps from the final Planck data. This latest reprocessing of data from both the low-frequency (LFI) and high-frequency (HFI) instruments, using the integrated NPIPE pipeline, resulted in more data, reduced noise, and improved consistency across frequency channels [51]. HiLLiPop and LoLLiPoP are the new likelihoods of the CMB temperature and E-mode polarization power spectra from this pipeline, covering both large scales (low-ℓ) and small scales (high-ℓ). These reanalysis uses a higher sky fraction (75%), as well as a wider range of multipoles and a negligible modeling dependence on cosmological ΛCDM parameters. As a result, the constraints derived have 10% to 20% smaller uncertainties on ΛCDM parameters compared to previous pipelines. We employ the HiLLiPop and LoLLiPoP likelihoods obtained from this reanalysis of the CMB temperature and polarization power spectra for the high-ℓ ($30 < \ell < 2500$) TT, TE, and EE data [381]. For the low-ℓ ($\ell < 30$) EE spectra, we utilize the LoLLiPoP likelihoods [381]. This analysis has the smallest level of the lensing anomaly of all the CMB analysis we include, it is at a 0.75σ level [314]. We term the combination of these likelihoods as "**P20.**"

4.2.2 CMB lensing

CMB surveys also capture the power spectrum of the gravitational lensing potential, $C_l^{\phi\phi}$, via 4-point correlation functions. The Planck PR4 lensing map utilizes a quadratic estimator pipeline on CMB maps derived from the enhanced NPIPE reprocessing of data from the Planck HFI. This version incorporates approximately 8% more CMB data compared to Planck PR3, which includes information obtained during satellite re-pointing maneuvers, along with several enhancements in data processing [51]. We additionally consider the new measurements of CMB lensing from the Atacama Cosmology Telescope (ACT) Data Release 6 (DR6) covering over 9,400 square degrees of the sky. These lensing measurements, based on five seasons of CMB observations from ACT, achieve a precision of 2.3% for the CMB lensing power spectrum. This analysis pipeline was developed to reduce sensitivity to foreground contamination and noise characteristics, and included a number of systematic error assessments [294]. We utilize the latest NPIPE PR4 Planck CMB lensing reconstruction [115] alongside DR6 from the ACT [337]. For brevity, this dataset combination is referred to as "**CMB lensing**."

4.2.3 BAO

Dark Energy Spectroscopic Instrument's (DESI) BAO measurements provide robust data on the transverse comoving distance and the Hubble rate, or their combination relative to the sound horizon, across seven redshift bins derived from over 6 million extragalactic objects in the redshift range of $0.1 < z < 4.2$. We employ the latest BAO scale measurements from the DESI Data Release 1 [28]. This dataset includes the Bright Galaxy Sample (BGS: $0.1 < z < 0.4$), Luminous Red Galaxy Sample (LRG: $0.4 < z < 0.6$ and $0.6 < z < 0.8$), Emission Line Galaxy Sample (ELG: $1.1 < z < 1.6$), the combined LRG and ELG Sample (LRG+ELG: $0.8 < z < 1.1$), Quasar Sample (QSO: $0.8 < z < 2.1$), and the Lyman-α Forest

Sample (Lyα: $1.77 < z < 4.16$). We refer to the full DESI dataset is referred to as "**DESI**."

DESI offers several advancements over previous BAO analyses, including more physically-motivated enhancements to BAO fitting and reconstruction methods. DESI implements blind analysis techniques to reduce confirmation bias. Furthermore, DESI has a factor of two to three improvement in survey volume and number of tracers relative to SDSS-IV [54, 368]. It also applies a unified BAO analysis approach across different tracers and allows for a combination of these tracers' measure of the BAO scale [27].

4.2.4 Type Ia SNe

Type Ia SNe (SNe Ia) are crucial standardizable candles that offer an alternative approach to measuring the Universe's expansion history. While SNe measurements have lower statistical power on the expansion history compared to modern BAO measurements within the ΛCDM model, they provide essential information on dark energy, particularly when examining less restricted cosmological models. In our analysis, we include the following three SNe datasets:

Pantheon+ (PP): We utilize the updated SNe Ia luminosity distance measurements from the Pantheon+ (PP) sample [358, 105], comprising 1550 spectroscopically-confirmed SNe Ia in the redshift range $0.001 < z < 2.26$. The PP sample consists of light curves from these verified SNe Ia, which are analyzed to derive cosmological parameters. The different datasets, with all relevant data, references, and their respective redshift ranges outlined in Table 1 of [358]. Compared to the previous Pantheon dataset [359], the PP catalog includes improved photometric calibration and systematic uncertainties. The PP catalog shows the most significant increase in SNe Ia data at lower redshifts, largely due to the addition of the LOSS1, LOSS2, SOUSA, and CNIa0.2 SNes. The PP likelihood includes statistical covariance and models systematic uncertainties as covariances.

Union3 (U3): The Union3 Supernova compilation is an extensive dataset of 2,087 spectroscopically-confirmed SNe Ia, with 1,363 in common with the PP dataset [351], standardized on a consistent distance scale through SALT3 light-curve fitting. It aims to manage systematic uncertainties that arise as the number of usable supernovae increases. The dataset addresses outliers and selection biases. They incorporate a Bayesian framework, called UNITY1.5 (Unified Nonlinear Inference for Type-Ia cosmologY), that improves modeling of selection effects, standardization, and systematic uncertainties compared to traditional simulation-based methods.

Dark Energy Survey Year 5 (DES Y5): The DES Y5 sample is the largest and most comprehensive single-campaign SNe Ia survey to date, totaling 1,829 SNe: 1,635 from DES measurements and 194 from local SNe Ia Ne measurements from the CfA/CSP foundation sample [18]. This dataset represents observations gathered during the first five years of the DES Supernova Program. The SNe cover a redshift range of $0.01 < z < 1.3$, yielding a substantial dataset for cosmological studies. The DES Y5 sample offers improved high-redshift statistics compared to the PP or U3 datasets.

It is important to note that the PP, U3 and DES Y5 datasets contain supernovae that overlap between the samples. To avoid any double counting, these datasets are never utilized together. Table 4.1 summarizes all the datasets that we have just defined. For conciseness, we use the term "**benchmark**" to refer to the combination of the likelihoods from P18, CMB lensing, DESI DR1, and PP described above.

4.2.5 Tension Datasets

We also consider two measurements of the late Universe that are internally robust but are in strong tension with the cosmology inferred from our datasets above. Specifically, these are: the local Hubble expansion rate, H_0 and the amplitude of matter fluctuations, σ_8, at

the scale of $8, \mathrm{Mpc}/h$, sometimes parameterized as S_8 ($S_8 = \sigma_8 \sqrt{\Omega_m/0.3}$). For the latter, S_8, we adopt a recent well-tested measurement. These data are:

SH0ES (H_0): the Gaussian likelihood of the Hubble constant calculated by the measurements of the SH0ES collaboration in [344], $H_0 = 73.04 \pm 1.04\,\mathrm{km/s/Mpc}$. The selection of this result is motivated by the reduced error bars obtained by the collaboration to calculate this value compared to the one obtained following other analysis. We employ the explicit value of H_0, and its error, in our likelihood analysis, and not the absolute magnitude, M_b, as the latter is only important for models that differ from ΛCDM in their expansion history near $z = 0$, e.g., wCDM. Since these models do not appreciably change our conclusions with respect to the neutrino physics of interest to this work, we use H_0 itself.

Dark Energy Survey Year 3 (S_8): The Dark Energy Survey (DES) uses a novel photometric redshift calibration technique for its survey of galaxies. The DES photometric calibration method successfully recovers the input cosmological parameters in simulated surveys by using several statistical quantities derived from the survey data. The cosmic shear measurements are based on an analysis of over 100 million source galaxies, and they constraint the clustering amplitude to be $S_8 = 0.759^{+0.025}_{-0.023}$ [59]. Our choice of this value of the S_8 parameter is motivated by the several verification tests for potential systematics performed by the DES collaboration.

4.3 Methodology

In our work, we will be testing neutrino physics scenarios that can be considered to fit within the ΛCDM framework (such as non-trivial neutrino mass), as well as tests of models beyond ΛCDM. We fit the cosmological models we study by using the publicly available Bayesian analysis framework `cobaya` [380], with the Markov chain Monte Carlo (MCMC)

Parameter	**Prior**
$\Omega_{\rm b}h^2$	$[0.005, 0.1]$
$\Omega_{\rm c}h^2$	$[0.01, 0.99]$
$\log(10^{10}A_{\rm s})$	$[1.61, 3.91]$
$n_{\rm s}$	$[0.8, 1.2]$
$\tau_{\rm reio}$	$[0.01, 0.8]$
$100\theta_{\rm MC}$	$[0.5, 10]$
Σm_ν [eV]	$[0, 10]$
$N_{\rm eff}$	$[0, 100]$
Ω_k	$[-0.3, 0.3]$
w_0	$[-3, 0.1]$
w_a	$[-3, 3]$

Table 4.2: We list our adopted ranges for the flat prior distributions imposed on the 6 ΛCDM, as well as the 5 additional extended-model cosmological parameters.

sampler [280, 278] and fastdragging [316]. We employ the `CAMB` cosmological Boltzmann solver [281, 233]. We run 4 parallel MCMC chains, and use the Gelman-Rubin convergence test, $R - 1 < 0.01$, to verify their convergence for all parameters. In all the runs we choose flat priors with cutoffs well outside where likelihoods are significant. The flat prior ranges within which the parameters are varied are given in Tab. 4.2. We use GetDist [279] to calculate Bayesian posteriors, means, and confidence intervals.

For finding the best-fit likelihood points and their χ^2 values we use the minimizer sampler available in `cobaya` [116, 117, 336]. For all of the scenarios we consider we maximize the likelihood, $\mathcal{L}$, via minimizing its $-2\ln\mathcal{L}$, as we are interested in performing a likelihood ratio for our model-preference test statistic. To identify the true minimum best-fit within an acceptable tolerance, we perform multiple minimizations of $-2\ln\mathcal{L}$, until at least six results yield a minimum value within 0.2 of the minimum determined by the sampler. The motivation for these specific choices are statistically motivated. We model the evaluation

of the minimum value within 0.2 of its true value as a Poisson process. To have a 99.5% confidence that the minimal bin includes an evaluation within 0.2 of the true minimum, one needs at least 5 evaluations within the bin (e.g., see Table II of Ref. [196]). Following this method, we expect to have found the $-2\ln\mathcal{L}$ within 0.2 of its minimum at roughly 99.5% confidence. The likelihood combinations discussed in this section involve over 20 nuisance and free parameters, making the minimization process quite complex. For some datasets and models, the minimum can be found with approximately 200 evaluations. However, the HiLLiPoP likelihood requires significantly more evaluations, $\gtrsim$2000, to achieve our criteria compared to other likelihoods. This is likely because, as noted by others, HiLLiPoP is the only unbinned CMB likelihood, resulting in higher noise in the likelihood function [314]. We decided not to include this likelihood for the results that involved minimizing χ^2 since it did not fulfill our tolerance requirements without the calculation of an excessive number of minimizations. Our statistical approach follows that of Ref. [173]. We employ the minimal chi-square $\chi^2_{\rm min}$ to quantify the success of each scenario with respect to a baseline model, *i.e.*, a $\Delta\chi^2$ test.

We compute the change in the effective minimal chi-square $\chi^2_{\rm min} = -2\ln\mathcal{L}$, where $\mathcal{L}$ represents the maximum likelihood for the considered model $\mathcal{M}$. The $\Delta\chi^2_{\mathcal{M}}$ relative to the baseline model $\mathcal{M}_0$ is then derived as

$$\Delta\chi^2_{\mathcal{M}} \equiv \chi^2_{\rm min,\mathcal{M}} - \chi^2_{\rm min,\mathcal{M}_0}\,. \tag{4.4}$$

The χ^2 value of a dataset can be used to determine if a trend in the data is happening due to chance or due to a new model component, and can also be used to test a model's "goodness of fit" [330].

The $\Delta\chi^2_{\mathcal{M}}$ test does not consider each model's complexity, specifically the number of parameters involved. To account for model complexity, we also use the Akaike information criterion

(AIC) within a Bayesian framework, which enables a fair comparison among models with varying parameter counts. To evaluate the improvement in fit quality, we calculate the AIC for each model, defined as $\mathrm{AIC} = -2\ln\mathcal{L} + 2k$, where k represents the number of parameters in the model [48]. A model is favored over another if it results in a lower AIC. To make a comparison with ΛCDM, we compute the AIC of $\mathcal{M}$ relative to that of ΛCDM, defined as

$$\Delta\mathrm{AIC} \equiv -2(\ln\mathcal{L}_{\mathcal{M}} - \ln\mathcal{L}_{\Lambda\mathrm{CDM}}) + 2(N_{\mathcal{M}} - N_{\Lambda\mathrm{CDM}})\,.$$

Here, $N_{\mathcal{M}}$ and $N_{\Lambda\mathrm{CDM}}$ denote the number of free parameters in models $\mathcal{M}$ and ΛCDM, respectively. The AIC penalizes models that add extra parameters without sufficiently enhancing the fit; consequently, a model with a lower AIC value is theoretically and statistically more favorable than one with a higher value. To evaluate the performance of each model, we interpret AIC values using Jeffreys' scale [244]. This scale, empirically calibrated, offers descriptive terms for varying levels of evidence. Our criterion for favoring model $\mathcal{M}$ over ΛCDM is when it falls in the "strong" category on Jeffreys' scale, meaning $\Delta\mathrm{AIC} < -6.91$.

In addition, we want to quantify the tension when adding H_0 or S_8 measurements to our datasets. We calculate

$$\sqrt{\Delta\chi^2_{\mathcal{D}}} \equiv \sqrt{\chi^2_{\mathrm{min},\mathcal{D}+\mathcal{T}} - \chi^2_{\mathrm{min},\mathcal{D}}}\,. \tag{4.5}$$

In this equation the subscript $\mathcal{D}$ denotes the baseline datasets considered, while $\mathcal{T}$ indicates the tension constraints incorporated into the minimization calculation. This test does not evaluate a model's effectiveness in describing the data; instead, it quantifies the level of tension within a given model when additional data is included.

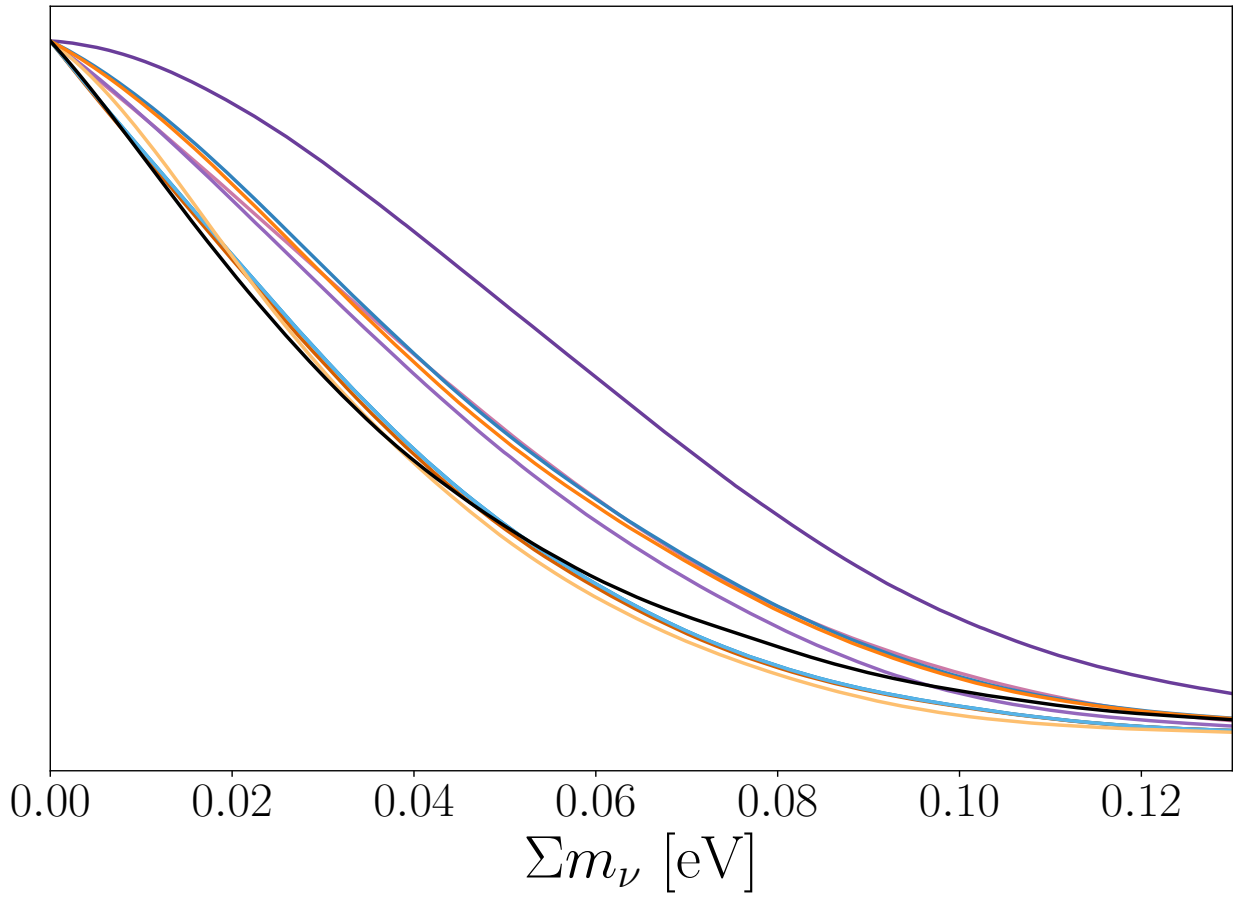


Figure 4.1: Comparison of 1D marginalized posterior distributions for Σm_ν [eV] for different data combinations. As seen above, there are three clusters of likelihoods that are stringent, moderate, and weakest. The stringent combination includes five likelihoods, with P18, DESI, & U3 being orange, P18, DESI, & PP being green, with CamSpec, DESI, & U3 being red, CamSpec, DESI, & PP being grey and the 11 parameter chain with our benchmark data in black. The moderate cluster combination includes four datasets' likelihoods, with P18, DESI, & DES Y5 being red, CamSpec, DESI, & DES Y5 being light blue, with P20, DESI, & U3 being dark blue, and P20, DESI, & PP being green. The weakest likelihood contour, in purple, is for P20, DESI, & DES Y5. All datasets include CMB lensing.

4.4 ΛCDM and Neutrino cosmology

From an experimental standpoint, cosmology can no longer be sufficiently described by the six-parameter ΛCDM model assuming massless neutrinos. Solar, atmospheric, accelerator, and neutrino oscillation experiments, such as those conducted by the Super-Kamiokande [188, 187, 68] , SNO [47], MINOS [47]and NOvA [76], and KamLAND [164], have provided clear evidence for neutrino mass through observed flavor conversion. These laboratory findings confirm that neutrinos have mass and current cosmological data is sensitive to the gravitational effects of their non-relativistic nature.

However, the observable effects of neutrino oscillations are sensitive only to mass-squared splittings among eigenstates, thus constraining only the neutrino mass-squared differences. Matter effects in the solar neutrino problem's solution, however, have allowed determination of the sign of the small mass splitting, leaving two possible mass orderings that leave the second mass splitting undetermined: normal (NO) and inverted ordering (IO). Measuring the exact values of the three mass states and their ordering remains an open challenge in cosmology and particle physics. A related question is whether the mass values of the neutrinos are hierarchical (strongly distinct) or whether they are degenerate (nearly identical) in mass. As discussed in the introduction, cosmological observations are very competitive to experimental bounds on neutrino mass as massive neutrinos influence both the expansion history and the growth of structure in the Universe. Recent years have witnessed increasingly stringent cosmological constraints on the sum of neutrino masses, (Σm_ν), approaching the lower bound permitted by the inverted hierarchy, ($\sim 100\,\mathrm{meV}$) [28, 390]. This implies that the parameter space available for IO is becoming restricted. In this section, we will present the results of the analysis we developed to address these questions.

4.4.1 Hierarchical Neutrino Mass Ordering

Neutrino oscillation experiments have determined that the neutrino mass-squared differences for the solar and atmospheric oscillations are separated by about two orders of magnitude. Specifically, $\Delta m^2_{\rm solar} = (7.53 \pm 0.18) \times 10^{-5}\,{\rm eV}^2$ and $\Delta m^2_{\rm atm} = (2.455 \pm 0.028) \times 10^{-3}\,{\rm eV}^2$ [$\Delta m^2_{\rm atm} = (-2.529 \pm 0.029) \times 10^{-3}\,{\rm eV}^2$] for the NO [IO] atmospheric case [315]. Consequently, there is also a minimum limit on the combined masses of the three active neutrinos ($\Sigma m_\nu = m_1 + m_2 + m_3$):

$$\begin{aligned}
\Sigma m_\nu^{\rm NO} &= m_1 + \sqrt{m_1^2 + \Delta m^2_{\rm solar}} + \sqrt{m_1^2 + |\Delta m^2_{\rm atm}|}\,, \\
\Sigma m_\nu^{\rm IO} &= m_3 + \sqrt{m_3^2 + |\Delta m^2_{\rm atm}|} \\
&\quad + \sqrt{m_3^2 + |\Delta m^2_{\rm atm}| + \Delta m^2_{\rm solar}}\,,
\end{aligned}$$

where the lightest neutrino mass eigenstate is m_1 for NO and m_3 for IO. A key question from cosmology is whether NO or IO is preferred by the data in the case of a hierarchical neutrino mass spectrum. That is, hierarchy is where $m_1 \ll m_{2,3}$ (NO), or $m_3 \ll m_{1,2}$ (IO). Assuming the minimal mass case for both orderings, i.e. $m_1 = 0$ for NO and $m_3 = 0$ for IO, we obtain the minimal Σm_ν for NO and IO by using the observed mass-splittings. This defines our two massive neutrino cases as: **NO** with $\Sigma m_\nu = 58\,{\rm meV}$ and **IO** with $\Sigma m_\nu = 101\,{\rm meV}$.

At the hierarchical scale of interest for cosmological neutrino mass constraints, *i.e.*, $m_1 = 0$ or $m_3 = 0$, it is inappropriate to model Σm_ν as three degenerate mass states ($m_i = \Sigma m_\nu/3$, for $i = 1, 2, 3$). Therefore, we model the massive neutrinos as one massive eigenstate ($m = \Sigma m_\nu$) and two massless eigenstates. Though it has been shown that this introduces some inaccuracies in the effects of massive neutrinos [277, 227], we show below that these effects do not affect our quantitative results appreciably, nor our conclusions.

In the context of the ΛCDM model combined with the established determination of minimal neutrino masses from neutrino oscillation experiments, neutrinos have a minimum mass sum ($\Sigma m_\nu = 58\,\mathrm{meV}$) that contribute to the matter density as in Eq. 4.2, which is determined by the standard thermal history. If cosmological results find $\Sigma m_\nu < 58\,\mathrm{meV}$ with high significance, this would indicate physics beyond standard ΛCDM, its thermal history, or new physics in the neutrino sector. Given this minimum mass, cosmology tests NO versus IO as a binary choice in determining the neutrino's total mass scale.

To infer the cosmological data's preference for NO versus IO, we use the $\Delta\chi^2$ test, which is simply determined as the models have the same number of parameters with fixed neutrino masses (Eq. 4.4). We calculate the preference of these scenarios including the benchmark likelihoods we defined in Section 6.3.1. We find preference for NO over IO of

$$\Delta\chi^2(\text{NO over IO}) = 2.16\,, \tag{4.6}$$

indicating a very weak preference, approximately 1.47σ, for NO over IO. Considering the preference of the value inconsistent with neutrino physics of $\Sigma m_\nu = 0$, and we find *non-standard* massless neutrinos preferred over NO by

$$\Delta\chi^2(\Sigma m_\nu = 0\,\text{over NO}) = 1.85\,, \tag{4.7}$$

indicating very weak preference, approximately 1.36σ, of $\Sigma m_\nu = 0$ over NO. Importantly, the information on the matter content of the Universe from the supernovae surveys, which we adopt in our baseline cosmological dataset, slightly alleviates the cosmological constraint on neutrino mass. Without the PP SNe, we obtain $\Delta\chi^2(\text{NO over IO}) = 3.46\,(1.86\sigma)$ and $\Delta\chi^2(\Sigma m_\nu = 0\,\text{over NO}) = 2.36\,(1.54\sigma)$. We find that the preference tests for the neutrino mass ordering are not substantially changed when adopting the CamSpec or Planck 2020 CMB data. To test the dependence on our default choice for modeling Σm_ν as a single mass

eigenstate, or as three degenerate states, we perform these χ^2-tests with three degenerate neutrino masses, and find that the $\Delta\chi^2$ changes by less than 0.002 for both NO over IO and $\Sigma m_\nu = 0$ over NO. Therefore, our results on evidence for mass ordering are not affected by our choice of modeling the hierarchy. Importantly, we find the sensitivity to neutrino mass ordering from P18+DESI+PP is about as strong as P18+Lensing+PP, showing that geometry is about as sensitive to neutrino mass as structure growth [287].

4.4.2 Free Neutrino Mass

We use the several cosmological datasets available to infer the value Σm_ν when it is allowed to vary freely. Our priors in the MCMC are shown in Table 4.2. We choose different combinations of cosmological likelihoods that we have presented in the introduction §6.3.1 to test the effects of each cosmological epoch in our analysis. We use three sets of CMB data (P18, CamSpec and P20), CMB lensing, BAO DESI DR1, as well as the three SNe samples (PP, U3 and DES Y5). In Fig. 4.1, we present the 1D likelihood profiles of Σm_ν for these cases via MCMC analysis. The respective choices of blue, yellow, and purple colored lines correspond to the posteriors resulting from adding PP, U3, and DES Y5 SNe samples.

The nine different dataset combinations provide limits on the sum of the neutrino masses of

$$\begin{aligned}
&\Sigma m_\nu(\text{P18, DESI, \& PP}) < 82.1\,\text{meV}\,,\\
&\Sigma m_\nu(\text{P18, DESI, \& U3}) < 82.1\,\text{meV}\,,\\
&\Sigma m_\nu(\text{P18, DESI, \& DES Y5}) < 98.0\,\text{meV}\,,\\
&\Sigma m_\nu(\text{CamSpec, DESI, \& PP}) < 76.9\,\text{meV}\,,\\
&\Sigma m_\nu(\text{CamSpec, DESI, \& U3}) < 77.0\,\text{meV}\,,\\
&\Sigma m_\nu(\text{CamSpec, DESI, \& DES Y5}) < 86.6\,\text{meV}\,,\\
&\Sigma m_\nu(\text{P20, DESI, \& PP }) < 94.1\,\text{meV}\,,\\
&\Sigma m_\nu(\text{P20, DESI, \& U3 }) < 93.8\,\text{meV}\,,\\
&\Sigma m_\nu(\text{P20, DESI, \& DES Y5 }) < 108\,\text{meV}\,,
\end{aligned} \tag{4.8}$$

all at 95% CL. We also test the effect of relaxing assumptions of the underlying cosmology from minimal ΛCDM's 6 parameters (plus neutrino mass) to include variation of curvature Ω_k, evolving dark energy EoS, parameterized using w_0 and w_a, and extra radiation $N_{\rm eff}$, which is, in total, an 11 parameter model. In this case, the neutrino mass limit is only mildly relaxed, with

$$\Sigma m_\nu(\text{benchmark, 11 param.}) < 97.0\,\text{meV}\,. \tag{4.9}$$

In Fig. 4.1, the black line corresponds to the 1D posterior distribution of the sum of the neutrino masses of an extended 11-parameter model with our benchmark dataset, P18, DESI, & PP. We show the full inferred extended parameter values and errors in Table 4.2.

We observe three "clusters" of likelihoods in the Σm_ν posteriors that we obtain and resulting limits, as shown in Fig. 4.1. The most stringent cluster of datasets includes five likelihoods: P18, CMB lensing, DESI, & U3; P18, CMB lensing, DESI, & PP; CamSpec, CMB lensing,

DESI, & U3; CamSpec, CMB lensing, DESI, & PP; and, lastly, the 11 parameter chain with P18, CMB lensing, DESI, & PP. The moderate likelihood limit cluster includes four datasets: P18, CMB lensing, DESI, & DES Y5; CamSpec, CMB lensing DESI, & DES Y5; with P20, CMB lensing, DESI, & U3; and P20, CMB lensing, DESI, & PP. The weakest likelihood contour, in purple, is for P20, CMB lensing, DESI, & DES Y5.

The constraints on mass are primarily influenced by two factors. First, variations in cosmological parameters arise from different primary CMB analyses. Among the three Planck CMB analyses, P20 demonstrates the highest consistency between the primary CMB data and Planck PR4 lensing, showing the smallest lensing anomaly. Consequently, the P20 CMB lensing signal is not significantly elevated, resulting in the weakest constraint on neutrino masses, consistent with what has been identified by other authors [57, 314]. CamSpec finds the most stringent constraints on Σm_ν, which occurs due to this analysis preferring a lower scalar spectral index, n_s, and lower optical depth to the last scattering surface, τ, which both lower the amplitude of clustering on small scales, and are therefore positively correlated with Σm_ν (see Fig. 4.2). As a result, their lower values drive a more stringent bound on Σm_ν.

Second, the neutrino mass limits are also sensitive to the adoption of which SNe dataset considered. As discussed in the introduction, neutrino mass is affected by CMB, BAO and SNe constraints in multiple ways. Of these 3 SNe samples, DES Y5 has the highest Ω_m which has two main impacts in cosmological observables: First, a higher Ω_m enhances growth, which can be offset by a higher Σm_ν. Secondly, the BAO scale is kept fixed when increasing Ω_m and decreasing Σm_ν, which goes in the opposite direction [377]. DES Y5 SNe sample differs greatly in its inference of cosmological parameters relative to the other two SNe samples, primarily with a much larger inferred Ω_m than the other SNe datasets [1]. Combining all these effects, the main impact that drives the limit on Σm_ν is the overall raise in Ω_m resulting on a relaxation on neutrino mass bounds when DES Y5 SNe sample is

[1] This may originate from a $\sim$0.04 mag calibration offset between high and low redshifts [162, 142]

included. See Fig. 4.3 for the parameter likelihood correlations for the three SNe datasets. Interestingly, the differences in the Planck CMB analyses are more significant in changes to cosmological parameters, including Σm_ν, than the SNe datasets.

There has been considerable interest recently on the tighter-than expected constraints on Σm_ν to potentially indicate new physics, which could even be parameterized as "negative" neutrino mass by parameterizing the suppression of the growth of structure with massive neutrinos as enhanced growth when extending the growth of structure to be enhanced by the same linear suppression to linear enhancement of growth [131, 210, 314, 170, 57]. To test the strength of the preference for "negative" neutrino mass, we fit Gaussian functions to the one-dimensional likelihoods of the chains for each dataset. We fit to all values of $[\Delta 2 \ln(\mathcal{L})] = 2.5$ with respect to the likelihood maximum, as the MCMC process does not accurately sample the tails of the likelihood distributions. We recover the mean and standard deviation characteristic parameters of the associated Gaussian functions for the different datasets and calculate the deviation in σ from the central value of the Gaussian to the neutrino physics minimal-mass NO case, i.e. $\Sigma m_\nu = 58\,\mathrm{meV}$. For all of the datasets we have analyzed where Σm_ν is free, we find the deviation of the NO from the mean of the inferred likelihood to be between 1.13σ and 1.97σ, always remaining below 2σ.

The 11-parameter scenario, which offers the most model freedom of all the cases we study, finds a preference for the most negative value of inferred Σm_ν, with a tension level with respect NO of about 2.4σ. We infer that this result is due to the much larger parameter space explored in the 11-parameter model, where neutrino masses are degenerate not only with Ω_m, A_s, and τ, but also with w_0, w_a, and Ω_k. We present the 1D marginalized posterior distribution for Σm_ν in this 11-parameter model in Fig.4.4.

4.5 Exploring Beyond ΛCDM Models

Despite ΛCDM's remarkable success in describing nearly everything about our Universe, there are some notable discrepancies that arise between observations and this theoretical framework that could indicate the presence of new physics beyond the standard model. Two of the most striking and long-lasting ones are the Hubble and S_8 tension. The Hubble tension is a significant, $\gtrsim 5\sigma$, mismatch between the value of the expansion rate of the Universe today, which arises from a higher value based on the local expansion rate measured via a classic distance ladder, including Cepheid variables and Type Ia SNe, compared to a lower model-dependent value inferred using CMB observations and assuming ΛCDM. Another notable discrepancy involves the amplitude of matter fluctuations, σ_8, or the related parameter $S_8 = \sigma_8\sqrt{\Omega_m/0.3}$, which is inferred from large-scale structure surveys. The value derived assuming ΛCDM and using Planck CMB observations [42] is higher than those obtained through low-redshift probes such as weak lensing and galaxy clustering [249, 376, 59, 360, 17, 308, 286].

In this section, we present our study of candidate extensions to the ΛCDM paradigm. We perform minimization of the models we introduce in this section using the benchmark likelihoods we presented in Sec. 6.3.1. We evaluate preference for extensions to ΛCDM with the Bayesian evidence provided by the AIC, discussed in §6.1, and level of tension in σ with respect to ΛCDM. We test extensions by comparing the cosmological datasets described above, on their own, and with the addition of external H_0 and S_8 constraint likelihoods, both separately and together.

4.5.1 ΛCDM+$N_{\rm eff}$

Standard ΛCDM and the particle content of the Standard Model of particle physics predicts the relativistic energy density of the early Universe to be consistent with $N_{\rm eff} = N_\nu^{\rm SM} = 3.044$.

The calculations of $N_\nu^{\rm SM}$ take into account neutrino oscillations, incomplete neutrino decoupling through $e^\pm$ annihilation, and QED corrections [50, 90, 186]. The possibility of extra radiation density is prevalent in Beyond the Standard Model (BSM) extensions of particle physics [143]. This has gained extra attention as additional relativistic energy density has also been shown to alleviate the Hubble tension [149]. The possibility of lower relativistic energy density than $N_\nu^{\rm SM}$ is also possible in low-reheating temperature universes or other nonstandard thermal histories. A high-$N_{\rm eff}$ model exemplifies scenarios where the energy density of additional components, like Early Dark Energy or the presence of BSM particles, plays a significant role in the drag epoch early Universe. Adding extra relativistic particles beyond standard model neutrinos, such as dark radiation, reduces the sound horizon, resulting in the sound horizon's greater compatibility with a higher H_0. This additional energy density influences the positions of CMB acoustic peaks relative to the photon damping scale, which are precisely measured by CMB observations. Therefore, the alteration of the sound horizon by an increased $N_{\rm eff}$ to allow for compatibility with the local H_0 limit comes into tension with the independent constraints on $N_{\rm eff}$ from the CMB acoustic peaks and damping scale.

We concretely specify the cosmology of a varying $N_{\rm eff}$ as one where the active neutrinos are exactly one species with relativistic energy density of $N_\nu = 1$, and $\Sigma m_\nu = 58\,{\rm meV}$. The remainder of $N_{\rm eff}$ is pure relativistic energy density (modeled in `CAMB` as `num_nu_massless`). An interesting nonstandard scenario that can be parameterized with an additional contribution of massless ultra-relativistic species is a low reheating temperature cosmology [255]. Our results can be interpreted in that framework (for all values of $N_{\rm eff}$), or as an effective early extra relativistic energy density from any BSM relativistic component (for cases where $N_{\rm eff} > N_\nu^{\rm SM}$).

We first determine a preferred $N_{\rm eff}$ with our baseline datasets. We run a 7-parameter extended model allowing $N_{\rm eff}$ to vary freely between the priors reported on Table 4.2, using

MCMC chains including P18+CMB lensing+DESI BAO DR1 and the three different SNe samples. We find that the inferred relativistic energy density is identical for both the PP and Union3 datasets,

$$N_{\rm eff} = 3.05 \pm 0.17\,, \tag{4.10}$$

shown as the red line and light blue lines in Fig. 4.5. For DES Y5 SNe, we find

$$N_{\rm eff} = 2.99 \pm 0.17\,, \tag{4.11}$$

shown as the black line in Fig. 4.5.

When adding the SH0ES H_0 measurement, we find

$$N_{\rm eff} = 3.45 \pm 0.12\,. \tag{4.12}$$

Significantly, we find that this non-standard $N_{\rm eff}$ model is strongly favored over ΛCDM on the Jeffreys' scale, with a ΔAIC $= -10.9$. The 1D marginalized posterior distributions for $N_{\rm eff}$ when the SHOES H_0 measurement's likelihood is added to our benchmark likelihood set is shown by the green curve in Fig. 4.5. This increased energy density in $N_{\rm eff}$ would be in tension with with (BBN) constraints [132]. However, several mechanisms exist for making this $N_{\rm eff}$ compatible with BBN [7]. For example, if a considerable lepton asymmetry is present in the Universe, $N_{\rm eff} \approx 3.5$ is compatible with the light element abundances [108].

When only the DES Y3 S_8 measurement is included, a free $N_{\rm eff}$ model does not provide a better fit with respect to ΛCDM, with a ΔAIC $= 2.3$ therefore indicating $N_{\rm eff}$ is not the driving physics for a solution to both H_0 and S_8 tensions, a result found previously. When we include the measurements of DES Y3 S_8 and SH0ES H_0, $N_{\rm eff}$+ΛCDM remains strongly favored over ΛCDM, with ΔAIC $= -8.0$. However, this result is driven by the H_0

measurement and is not indicative of a preference for non-standard $N_{\rm eff}$ from S_8.

4.5.2 Sterile Neutrinos

Anomalies in short-baseline neutrino experiments may be due to the existence of one or more sterile neutrinos, e.g., the LSND, MiniBooNE, reactor, and gallium anomalies [128, 135, 318]. Sterile neutrinos are significantly constrained by cosmology [211, 42] and other neutrino experiments [296, 30]. However, there remains much interest on sterile neutrinos' impact on cosmology and their potential signals [220, 192, 63, 8]. Reconciling eV sterile neutrinos with cosmology often involves new mechanisms that suppress their full thermalization [220, 238].

The possibility of $N_{\rm eff} \approx 3.5$ indicated by the Hubble tension could be due to partially thermalized sterile neutrinos. In addition, massive sterile neutrinos could be responsible for the suppression of S_8 [396], though massive sterile neutrinos are constrained by the same physics as the active neutrinos in §4.4.2. Therefore, we examine here how eV-scale sterile neutrinos affect cosmological tensions like H_0 and S_8.

In this model, we consider the following relativistic species: photons, 3 active and one additional sterile neutrino. In our work, we have fixed the active neutrino sector to give a contribution of $N_\nu^{\rm SM} = 3.044$ to $N_{\rm eff}$, with two massless and one massive neutrino with a mass of 58 meV. Therefore, the contribution to $N_{\rm eff}$ from the sterile species is simply $\Delta N_{\rm eff} = N_\nu^{\rm SM} - 3.044$. When the sterile neutrino is relativistic at early times, assuming the only radiation species are photons and neutrinos, the contribution of a light sterile neutrino to $N_{\rm eff}$ is given by [26],

$$\Delta N_{\rm eff} = \left[\frac{7}{8}\frac{\pi^2}{15}T_\nu^4\right]^{-1} \frac{1}{\pi^2}\int dp\ p^3\ f_s(p), \tag{4.13}$$

where T_ν is active neutrino temperature, p is the neutrino momentum, and $f_s(p)$ is mo-

mentum distribution function of the sterile neutrino. At late times its energy density is parametrized as an effective mass [26, 33]:

$$\omega_s \equiv \Omega_s h^2 = \frac{m_s^{\rm eff}}{94.1{\rm eV}} = \frac{h^2 m_s^{\rm ph}}{\pi^2 \rho_c} \int dp\ p^2\ f_s(p), \tag{4.14}$$

where ρ_c is the critical density, $\Omega_s h^2$ is the sterile neutrino energy density. Since sterile neutrinos do not have electroweak interactions and mix, through oscillations, with the active neutrinos, they are not necessarily ever in thermal equilibrium. Active neutrinos decouple at a temperature $T \sim 1$ MeV, they are relativistic. Hence $f_s(p)$ does not depend on the physical mass of the sterile neutrino, $m_{\rm s}^{\rm ph}$. However, $f_s(p)$ depends on the production mechanism of the light sterile neutrino.

We consider non-thermal production of sterile neutrinos. One such mechanism is the Dodelson-Widrow (DW) process [153], for which $f_s(p) = \beta(e^{p/T_\nu} + 1)^{-1}$, where β is a normalization factor. We investigate the possibility that the massive sterile neutrinos are either partially or fully thermalized.

Partially Thermalized

A partially thermalized sterile neutrino model requires two additional free parameters to the six ΛCDM ones:

$$m_{\rm s}^{\rm eff} = \Delta N_{\rm eff}\ m_{\rm s}^{\rm ph}; \qquad \Delta N_{\rm eff} = \beta. \tag{4.15}$$

Here, $m_{\rm s}^{\rm eff}$ is *not the physical mass*. When this parameter and β are allowed to vary freely one encounters the regime where $\beta \sim 0.01$ and the physical mass $m_{\rm s}^{\rm ph} \sim 1\,{\rm keV}$, *i.e.* the warm dark matter regime. To focus on the eV scale, we specified cases where $m_{\rm s}^{\rm eff}$ and β are plausible in short-baseline-motivated eV-scale models. We focus on three thermalization scenarios

for each of either a 1 eV or 0.1 eV sterile neutrino, from partial thermalization cases from Ref. [220] (their Fig. 5). The three scenarios have values of $\Delta N_{\rm eff} = 0.45, 0.074, \& 0.0086$, corresponding to $N_{\rm eff} = 3.49, 3.12, \& 3.05$. These values are for low reheating temperature models where $T_{\rm RH} = 4$MeV for mixing angles of $\sin^2 2\theta = 0.001, 0.01, 0.1$ respectively, but can be achieved in other partial-thermalization cases [238]. As discussed in §4.5.1, a high $N_{\rm eff}$ can be consistent with BBN and the light element abundances with a number of physical mechanisms, including a nontrivial chemical potential in the electron neutrinos [321, 7, 108], which can also suppress or enhance sterile neutrino thermalization [3, 304].

We study the three cases of partial thermalization of neutrinos, using our benchmark datasets of P18, CMB lensing, DESI DR1, PP, plus SH0ES H_0. Interestingly, our results find the existence of a thermalization threshold preference. For a 1 eV partially thermalized sterile neutrino with $N_{\rm eff} = 3.49, 3.12, \& 3.05$, adding the H_0 measurement likelihood, we find ΔAIC $= 25.9, 0.8, 1.1$, respectively, showing that below a certain thermalization limit, between the first and second cases, this model transitions from being strongly disfavored by cosmological data to being at a similar tension level when compared to ΛCDM. Note the ΔAIC values for all the partially thermalized neutrino models we analyze are identical with the models' $\Delta\chi^2$ preferences since no additional free parameters are introduced.

Even more significantly, our results find that a 0.1 eV partially-thermalized sterile neutrino is *more favored* than ΛCDM, when adopting the SH0ES H_0 measurement. In the three thermalization scenarios we considered, *i.e.* with $N_{\rm eff} = 3.49, 3.12, \& 3.05$, when including the SH0ES H_0 measurement, we find ΔAIC $= -11.0, -3.7, \& -2.1$. All of these cases are preferentially fit by our baseline data, alleviating the Hubble tension more effectively than ΛCDM. Note that the model with and 0.1 eV partially-thermalized sterile neutrino with $N_{\rm eff} = 3.49$ is strongly preferred over ΛCDM by its AIC, as well as its $\Delta\chi^2$, at $> 3\sigma$. Its preference is comparable to and very slightly better than the pure relativistic energy $N_{\rm eff}$ studied in §4.5.1. This preference is in part due to the degenerate correlation between $N_{\rm eff}$

and Σm_ν in the BAO scale, which allows for both to increase without changing the BAO scale [74].

Fully Thermalized

We explore the possibility of a fully thermalized sterile neutrino in addition to the three active neutrinos setting $\beta = 1$ and $\Delta N_{\rm eff} = 1$, so $N_{\rm eff} = 4.044$. This model introduces only one additional parameter $m_{\rm s}^{\rm eff}$ which is the physical mass. In this model, we fix $N_{\rm eff} = 4.044$ and vary $m_{\rm s}^{\rm eff}$ together with the other 6 ΛCDM parameters. With our benchmark data, of P18, CMB lensing, DESI DR1, & PP, a fully thermalized sterile neutrino, with free particle mass, is strongly disfavored compared to ΛCDM with ΔAIC > 20. In addition, despite a thermalized sterile neutrino possibly lowering clustering amplitudes and accommodating the DES Y3 S_8, this is strongly disfavored by the baseline data, at the level of ΔAIC > 20.

Interestingly, when including our baseline datasets with the SH0ES H_0 measurement, we find ΔAIC $= 4.5$, not strongly disfavored with respect to ΛCDM. Remarkably, this means that a fully-thermalized eV-scale short-baseline sterile neutrino is roughly as consistent with the H_0 tension as ΛCDM is. Fig. 4.6 shows the 1D marginalized posterior distribution resulting from running the MCMC associated with this fully thermalized model for the *physical mass* $m_{\nu_{\rm s}}$ for the benchmark data alone (black), and with the SH0ES H_0 measurement (red).

4.5.3 The S_8 Tension and Massive Active or Sterile Neutrinos

A reduction in the clustering amplitude on smaller scales, leading to lower values of σ_8 or S_8 within ΛCDM, can be achieved by increasing the neutrino mass and its contribution to the overall density of matter [234]. Several papers have interpreted low S_8 measurements as possible evidence for nonzero active neutrino masses or combinations involving additional

Parameters	**Benchmark**	**Benchmark**	$+ H_0$ **Posterior**	$+ S_8$ **Posterior**	$+ H_0$ **&** S_8 **Posteriors**
$\Omega_{\rm b}h^2$	0.02247 ± 0.00013	0.02236 ± 0.00022	$0.02274^{+0.00017}_{-0.00020}$	0.02237 ± 0.00022	$0.02273^{+0.00018}_{-0.00021}$
$\Omega_{\rm c}h^2$	0.1185 ± 0.0083	0.1184 ± 0.0028	$0.1251^{+0.0028}_{-0.0025}$	0.11756 ± 0.0027	$0.1241^{+0.0029}_{-0.0025}$
$\log(10^{10}A_{\rm s})$	3.049 ± 0.013	3.053 ± 0.016	3.073 ± 0.018	3.049 ± 0.016	3.072 ± 0.015
$n_{\rm s}$	0.9683 ± 0.0036	0.9639 ± 0.0084	$0.9808^{+0.0076}_{-0.0069}$	0.9636 ± 0.0084	$0.9804^{+0.0076}_{-0.0068}$
$\tau_{\rm reio}$	0.0586 ± 0.0071	$0.0586^{+0.0069}_{-0.0077}$	0.0616 ± 0.0089	0.0581 ± 0.0074	$0.0619^{+0.0074}_{-0.0060}$
$100\theta_{\rm MC}$	1.04108 ± 0.00029	1.04107 ± 0.00043	1.04044 ± 0.00036	1.04119 ± 0.00043	$1.04048^{+0.0038}_{-0.0043}$
Σm_ν $(95\%\, CL)$	$< 82.1\,{\rm meV}$	$< 97.0\,{\rm meV}$	$< 125\,{\rm meV}$	$< 112\,{\rm meV}$	$< 130\,{\rm meV}$
$N_{\rm eff}$		2.98 ± 0.18	3.43 ± 0.15	2.94 ± 0.18	$3.39^{+0.18}_{-0.13}$
Ω_k		0.0029 ± 0.0019	0.0023 ± 0.0017	$0.0029^{+0.0017}_{-0.0020}$	0.0027 ± 0.0017
w_0		$-0.961^{+0.012}_{-0.037}$	$-0.975^{+0.012}_{-0.024}$	$-0.962^{+0.012}_{-0.036}$	$-0.978^{+0.018}_{-0.031}$
w_a		$0.013^{+0.039}_{-0.066}$	$0.016^{+0.027}_{-0.045}$	$0.015^{+0.039}_{-0.060}$	$0.019^{+0.028}_{-0.043}$

Table 4.3: Best-fit values and 68% confidence intervals for the parameters are presented for the 7- and 11-parameter extended models are shown. Our benchmark data includes P18, CMB lensing, DESI, and PP likelihoods, both without external data and with the addition of H_0 and S_8 posteriors, considered individually and in combination.

mass eigenstates [84, 396, 95]. However, the strong constraints from the baseline datasets disfavor massive neutrinos at or above the 0.1 eV scale, as discussed in §4.4.2. In addition, massive neutrinos do not alter the physics of the local expansion rate relative to the CMB-epoch sound horizon. In our $\Delta\chi^2$ and AIC tests, including both the H_0 and S_8 tension measurements disfavors massive active neutrinos, as well as either partially or fully thermalized massive sterile neutrinos, relative to ΛCDM, though at a level lower than the strong threshold.

4.5.4 Evolving Dark Energy, Massive Neutrinos, Extra Relativistic Energy Density, and Curvature

Single-parameter modifications studied in the Planck 2018 analysis [42] often fail to reconcile the H_0 and S_8 tensions. For example, introducing changes in parameters such as the sum of neutrino masses Σm_ν, spatial curvature Ω_k, or the effective number of neutrino species $N_{\rm eff}$ affects H_0 and S_8 in similar directions, limiting their ability to resolve both tensions simultaneously [173]. To test whether multi-parameter simultaneous modifications of dark energy, neutrino physics, relativistic energy density and/or geometry may be responsible for the observed H_0 and S_8 tensions, we vary all of these model components in our 11-parameter model. We relax the standard ΛCDM assumptions and use a model which allows the six parameters of the standard ΛCDM model to vary freely, along with five additional parameters: $N_{\rm eff}, \Sigma m_\nu, \Omega_k, w_0$ and w_a.

Dynamical Dark Energy (DDE) — A time-dependent EoS for dark energy would be a major discovery, and is indicated at almost 4σ by the DESI BAO data, when combined with SNe data [28]. This evolution may also affect other cosmological tensions. While simple variations in dark energy EoS alone might not fully resolve the Hubble tension, they could improve model fits when combined with sterile neutrinos or other parameters [257]. During

the era where dark energy prevails, phantom dark energy with an EoS $w < -1$ induces an accelerated expansion of the Universe more pronounced than in ΛCDM with $w = -1$. This allows for the H_0 determined from CMB experiments to align better with the H_0 derived from local Universe measurements [147, 289, 383, 55]. There are several parameterizations for w that can be examined to study this model [146, 398]. In this work we will use the Chevallier-Polarski-Linder (CPL) parameterization [123, 283], where the dark energy EoS is given by $w(a) = w_0 + w_a(1-a)$. This parameterization is advantageous due to its simplicity [283]; however, interpreting constraints in the w_0 & w_a space in terms of transitions to phantom-like behavior (where the EoS $w < -1$) requires caution, since observational data only constrain the EoS over a limited range of redshifts, restricting the ability to fully capture high and low redshift dependencies. The behavior of $w(z)$ outside this constrained redshift range stems from the parameterization itself rather than from the data, indicating that this parameterization should be regarded as purely phenomenological. Recent findings from the DESI collaboration have used this parameterization and have been interpreted to suggest the existence of evolving dark energy [28]. Particularly, the data show a preference for a present-day quintessence-like EoS ($w_0 > -1$) that crossed the phantom barrier ($w_a < 0$). However, this interpretation is sensitive to the Type Ia SNe sample used in conjunction with DESI's measurements of BAO, when combined with CMB observations [162]. Their results find a preference that reaches a significance level of about 3.5σ and 3.9σ when combining P18, DESI BAO with Union3 and DES Y5, respectively, while it is reduced to around 2.5σ with PP [28, 206].

Nonzero Curvature — The angular diameter distance, measured through low-redshift observations such as BAO and SNe, is directly related to the Universe's curvature. Permitting a non-flat Universe by treating the curvature density parameter, Ω_k, as a variable introduces an additional degree of freedom, which influences the geometry of spacetime. Nonzero curvature also has implications for structure formation, offering a potential approach to alleviate the S_8 tension. Such models with nonzero curvature can be consistent with low-redshift

observations, as explored in Refs. [353, 212, 148, 113].

The best-fit values of this 11 parameter model, when we include the benchmark data, P18, CMB Lensing, BAO and PP likelihoods, are shown in Table 4.3. The parameters for this extended model, in the first column of Table 4.3, are remarkably consistent with ΛCDM, with the exception of $w = -0.961^{+0.012}_{-0.037}$, which is more positive than Λ by over 3σ. The curvature $\Omega_k = 0.0029 \pm 0.0019$ is less than 2σ away from flat. Notably, evidence for a nontrivial w_a is not present, which is likely due to the less significant changes away from ΛCDM in the other nonstandard parameters, $N_{\rm eff}$ and Ω_k, shown in the green contours in Fig. 4.7.

Tension Data — We test to see if there is indication of new physics in the extended model when including the H_0 and S_8 tension data. We show the changes in the extension parameters when the H_0 and S_8 measurement likelihoods are included in Fig. 4.7. The primary change observed with the addition of the Hubble constant measurement is a slightly more negative central value for $w_0 = 0.975^{+0.012}_{-0.024}$, with a smaller lower bound error. Additionally, as with the 7 parameter ΛCDM plus $N_{\rm eff}$ model, there is a significant increase in the relativistic energy density, $N_{\rm eff} = 3.43 \pm 0.15$. There is a relaxation of the neutrino mass bound, with $\Sigma m_\nu < 125\,{\rm meV}$ (95% C.L.). Importantly, when adding curvature, neutrino mass, and $N_{\rm eff}$, there is no evidence for evolution of the dark energy equation of state, $w_a = 0.016^{+0.027}_{-0.045}$. Curvature does not significantly shift, with $\Omega_k = 0.0023 \pm 0.0017$.

When the S_8 measurement is included, the main difference is a relaxation of the neutrino mass upper bound to $\Sigma m_\nu < 112\,{\rm meV}$ (95% C.L.). The relativistic energy density is consistent with the standard value, $N_{\rm eff} = 2.94 \pm 0.18$. The remaining parameters w_0, w_a and Ω_k do not suffer notable deviations.

4.6 Discussion & Conclusions

Our analysis studies several current cosmological survey datasets with respect to a minimal ΛCDM model, with specific attention to the inferred sum of neutrino masses, effective neutrino number, and sterile neutrino models. One of the fundamental questions hoped to be answered by cosmology is whether a normal or inverted ordering is preferred in the hierarchical neutrino mass case, where the lightest neutrino mass is negligible relative to the other two mass eigenstates. We include SNe survey data to complement constraints on cosmological parameters, using a suite of nine sets of CMB (P18, CamSpec, P20) and SNe (PP, Union3, DES Y5) data, along with the DESI DR1 BAO data. We propose and use the robust $\Delta\chi^2$-test in determining the cosmological evidence for NO or IO. In this hierarchical case, using our benchmark data, we find that the preference for NO over IO remains weak, 1.47σ, with similar preferences for all 9 dataset contributions that we explored. When we exclude SNe data, the preference for NO over IO becomes very slightly stronger, at 1.86σ. Similarly, the cosmological data slightly favor massless neutrinos, at 1.36σ, in our benchmark data, with similar preferences in all 9 datasets. Though matter clustering modeling can be affected [277, 227] by the choice of a single or three degenerate neutrino mass eigenstates—which are both incorrect at the minimal mass hierarchy, when two neutrinos are massive—we find our conclusions do not change when altering the selection of the number of nonzero neutrino masses.

Exploring neutrino masses as free, we find limits on their sum in a range between $\Sigma m_\nu < 76.9\,\mathrm{meV}$ up to $\Sigma m_\nu < 108\,\mathrm{meV}$ (95% CL). As pointed out in other work, the strong constraints on Σm_ν arise in large part to the lensing anomaly, which indicates stronger amplitude CMB lensing power than expected [131, 210]. The variation in the limits on Σm_ν arise from the separate groups' analyses of the Planck CMB data and the separate SNe datasets. As has been known for some time, Ω_m is positively correlated with Σm_ν in the amplitude of clustering of matter, as measured by CMB lensing. Conversely, Ω_m and Σm_ν are

largely negatively correlated in the BAO scale. As discussed in Ref. [287], the measurements of the BAO scale distance ratios, as well as distances from SNe, are as sensitive of a probe of neutrino mass as the growth of structure, and sometimes more so.

The range of mass limits are affected by two primary factors: First, the cosmological parameters vary as inferred by the separate primary CMB analyses. Between the three CMB analyses, P18, CamSpec, and P20, P20 has the most consistency between the primary CMB and Planck PR4 lensing, and therefore the least lensing anomaly. Therefore, the P20 CMB lensing signal is not significantly anomalously high, and therefore the P20 inferred limit on neutrino masses is the weakest. Second, the matter density inferred by the SNe samples differs, as parameterized by Ω_m or $\Omega_c h^2$, with DES Y5 data preferring higher Ω_m than either PP or U3. This higher value of Ω_m required by DES Y5 shifts the likelihood in the direction of the positive correlation of Ω_m with the CMB lensing amplitude. The commensurate positive correlation of Ω_m with Σm_ν results in a higher inferred Σm_ν, for the DES Y5 case. These effects are illustrated in the triangle plots in Fig. 4.2 and Fig. 4.3, which show the correlations between Σm_ν, A_s, n_s, $\Omega_b h^2$, $\Omega_c h^2$, τ and H_0 cosmological parameters across the different datasets.

As more cosmological survey data have become available, the constraints on the sum of neutrino masses generally have become progressively tighter, with current 95% CL upper limits crossing below the minimum value permitted by the inverted mass hierarchy, $\Sigma m_\nu = 101\,\text{meV}$. However, as we discuss above, the preference for NO over IO remains weak. We analyze the shape of the likelihoods for Σm_ν, and we find a shape that has a peak to the inferred likelihood be at a negative sum of neutrino masses, as reported in previous work [131, 210, 314, 170, 247]. In our results, the extrapolated negative central value of the inferred Σm_ν relative to the minimum required by NO remains below 2σ significance. The preference for "negative" neutrino mass is primarily from the same physics that is responsible for very tight Σm_ν limits discussed above, namely, the high amplitude of the CMB lensing signal

disfavoring any suppression of the matter power spectrum due to neutrino mass.

We explore the H_0 and S_8 tension datasets. As found in previous work, extra relativistic energy density, $N_{\rm eff} = 3.45 \pm 0.12$ significantly alleviates the H_0 tension. Note, a high $N_{\rm eff}$ can be accommodated by BBN and the light element abundances by a number of physical mechanisms, including a nontrivial chemical potential in the electron neutrinos [321, 7, 3, 108, 304].

Anomalies in short-baseline neutrino experiments have indicated the possible existence of light sterile neutrinos [135]. Very significantly, our results indicate a preference for a 0.1 eV partially-thermalized sterile neutrino at 3.3σ relative to standard ΛCDM when including the H_0 measurement. This preference is particularly strong for scenarios with approximately $N_{\rm eff} \approx 3.5$, suggesting that partially thermalized sterile neutrinos consistent with the short-baseline signals could provide a viable explanation for the Hubble tension. Fully thermalized sterile neutrinos are comparable to ΛCDM in fitting the benchmark cosmological data when the H_0 measurement is included. Excluding the H_0 data, fully or partially thermalized sterile neutrinos remain disfavored. No extended model we test alleviates the S_8 tension.

We also studied an extended 11-parameter model that includes nontrivial curvature, $N_{\rm eff}$, and evolving dark energy via $w_0 \,\&\, w_a$. The cosmology inferred by the extended model does not significantly differ in its parameters from those in the ΛCDM framework, except for $w_0 = 0.975^{+0.012}_{-0.024}$, which has about 2σ preference for being non-Λ. In this extended model, the neutrino mass limit is not very significantly weakened, with $\Sigma m_\nu < 97.0\,{\rm meV}$ (95% CL).

Cosmology is forecast to achieve high-sensitivity to neutrino mass and number, with upcoming data from ongoing CMB analyses from the ACT [125] and SPT [120] experiments, as well as cosmological structure surveys DESI and Euclid. The CMB-S4 experiment, combined with current and ongoing experiment datasets, should achieve 5σ sensitivity to NO, and a sensitivity to extra relativistic degrees of freedom of $\sigma(N_{\rm eff}) \approx 0.03$ [13, 104]. These new

data will set the stage for unprecedented precision in cosmology that could lead to the long-anticipated cosmological detection of neutrino mass or, if undetected, signal new physics beyond the standard model for cosmology or particle physics [13, 301].

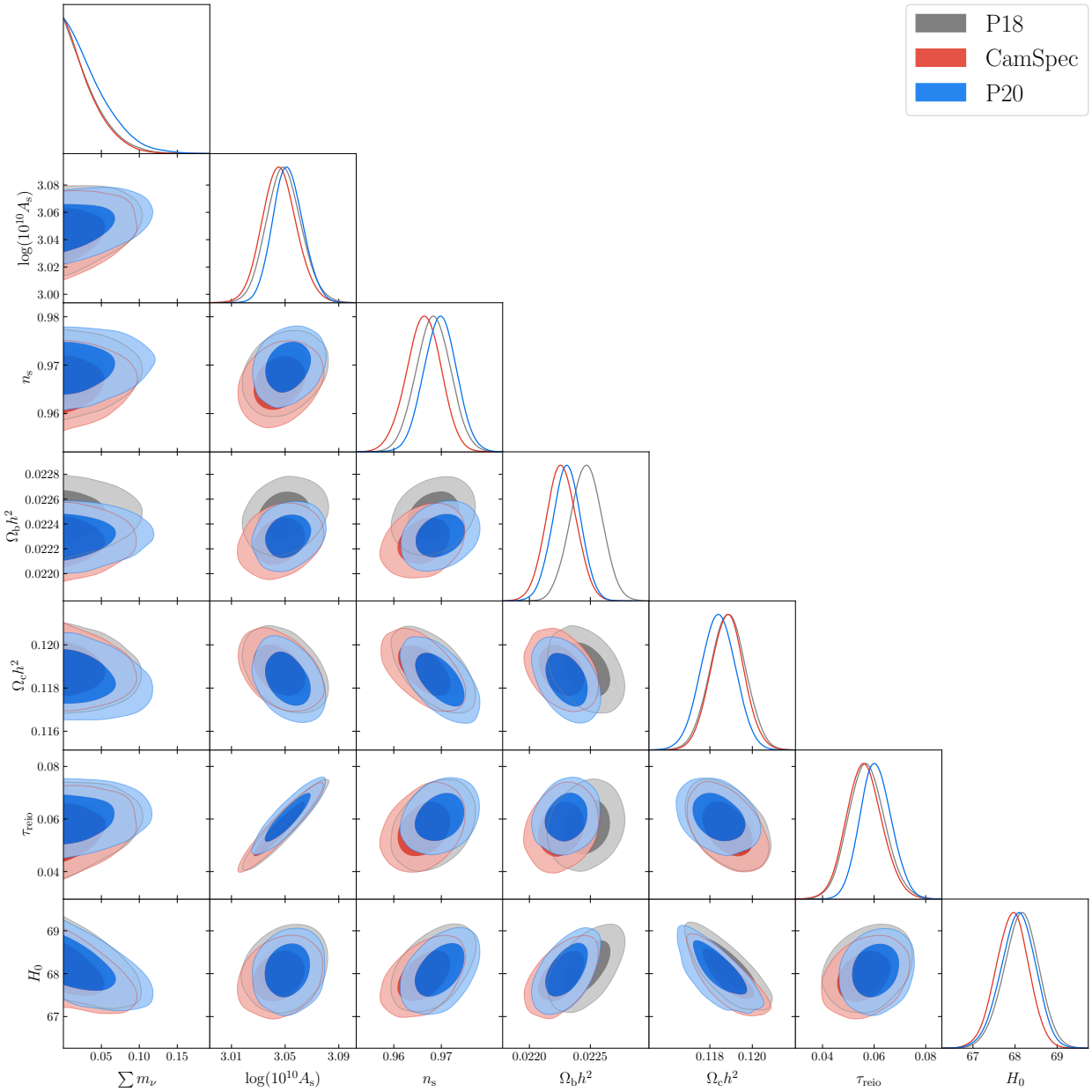


Figure 4.2: Shown is the comparison of our benchmark datasets, but with different choices of the CMB analyses (P18, CamSpec, P20), with their 68% and 95% CL likelihoods of ΛCDM parameters plus Σm_ν. Σm_ν is in units of eV and H_0 in units of $\mathrm{km\,s^1\,Mpc^1}$.

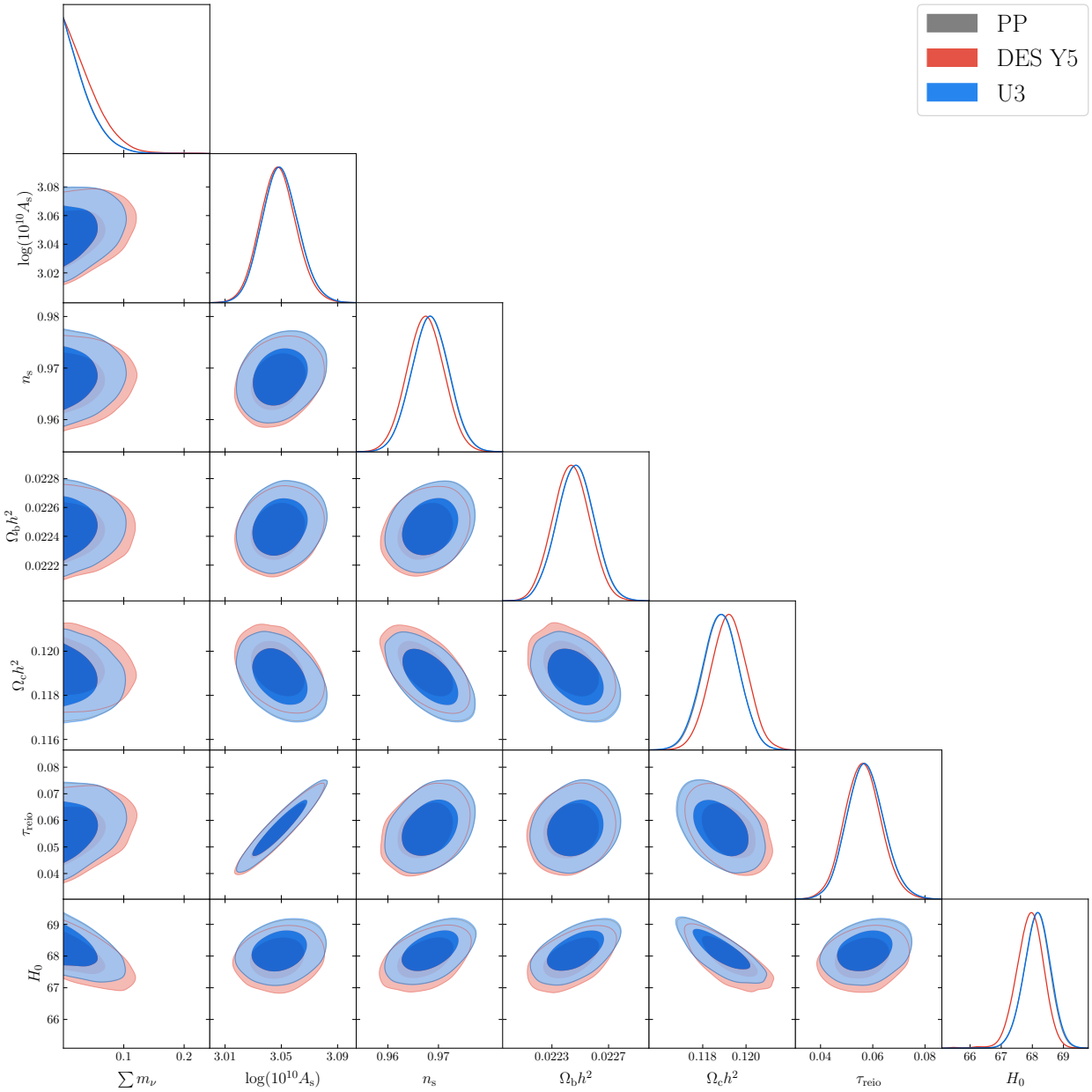


Figure 4.3: Shown is the comparison of our benchmark datasets, but with different choices of the SNe samples (PP, DES Y5, and U3), with their 68% and 95% CL likelihoods of ΛCDM parameters plus Σm_ν. Here, Σm_ν is in units of eV and H_0 in units of $\mathrm{km\,s^1\,Mpc^1}$.

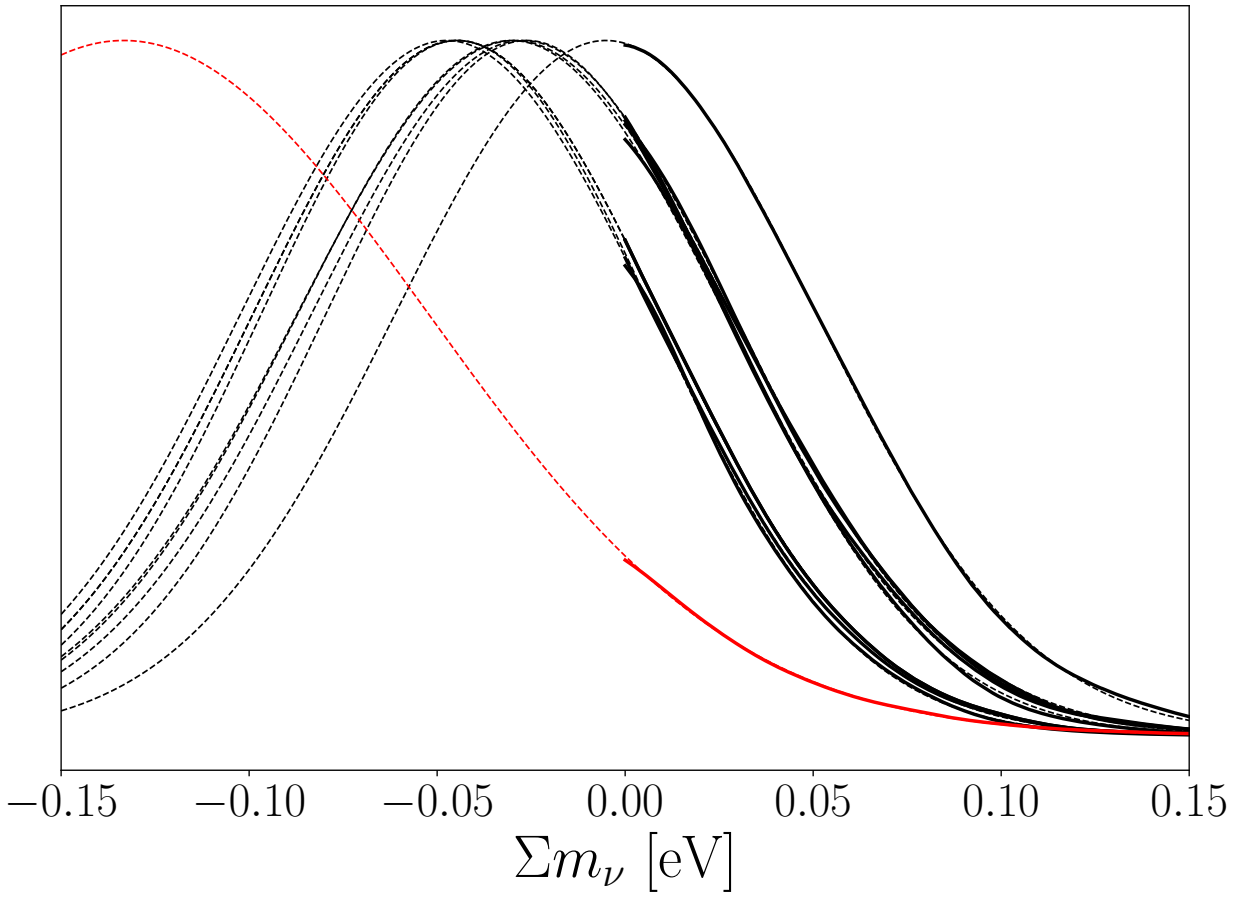


Figure 4.4: Shown here are the same 1D marginalized posterior distributions for Σm_ν shown in Fig. 4.1 (dashed lines), together with their Gaussian fits (solid lines). The black colored lines represent the different cosmological dataset combinations for the 7-parameter model where Σm_ν can vary freely. The red lines correspond to the 11-parameter chain. Going from left to right in the peak of the black-colored likelihoods, the curves correspond to the cosmological likelihood combinations P18+DESI+U3; P18+DESI+PP; CamSpec+DESI+U3; CamSpec+DESI+PP; P20+DESI+U3; P18+DESI+DES Y5, P20+DESI+PP; CamSpec+CMB lensing+DESI+DES Y5; and lastly the P20+DESI+DES Y5. The centroid for each combination, respectively, is below 2σ from the normal-ordering minimal neutrino mass, for all of the cases. The centroid for the red 11 parameter chain likelihood of the benchmark data is at the 2.31σ level. All datasets include CMB lensing.

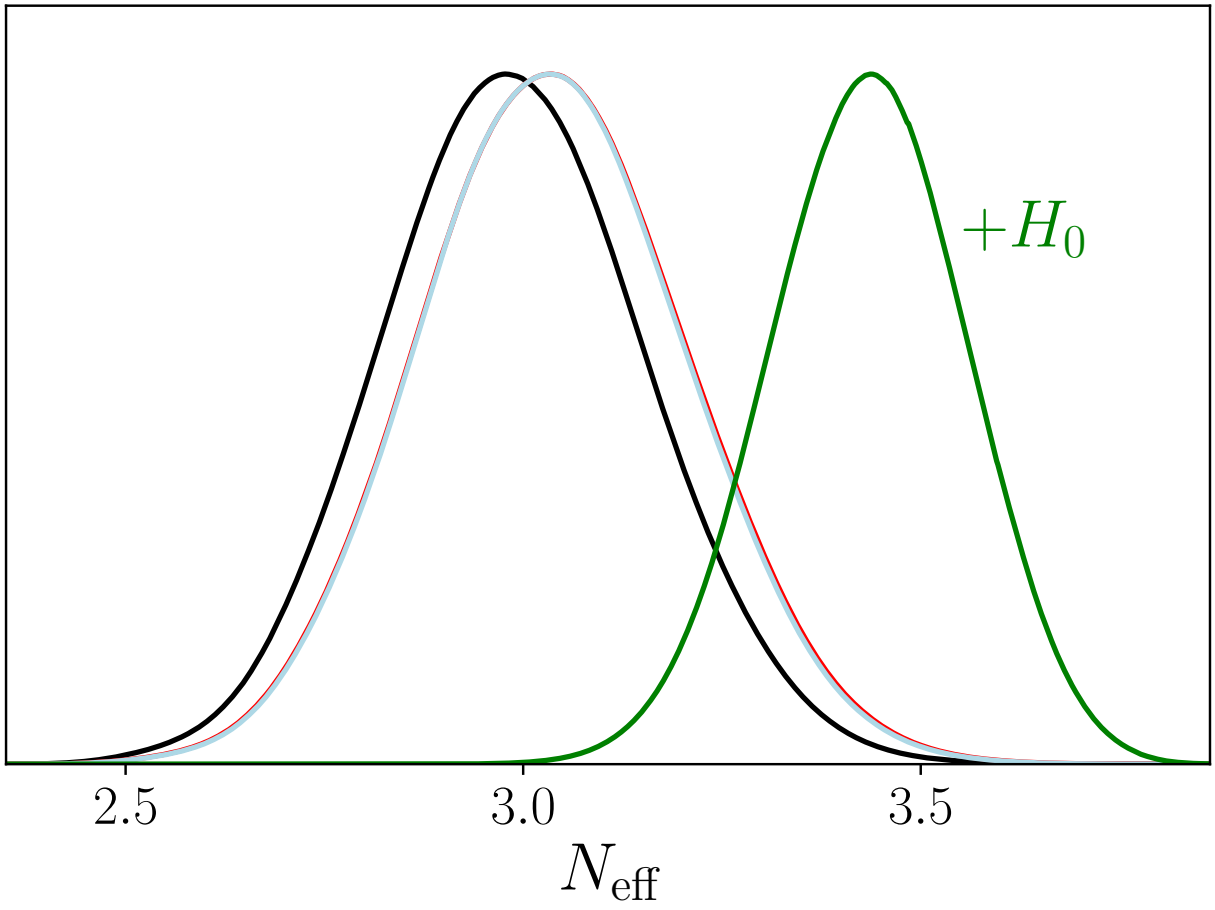


Figure 4.5: Shown here is a comparison of 1D marginalized posterior distributions for $N_{\rm eff}$ for different SNe data combinations when added to the P18, CMB lensing and DESI likelihoods. The solid dark blue, dashed light-blue, and black lines correspond to the PP, U3, DES Y5 SNe samples respectively, with all consistent with $N_\nu^{\rm SM}$. The green line is the resulting posterior distribution when the SH0ES H_0 measurement likelihood is added to the PP chain. finding $N_{\rm eff} = 3.45 \pm 0.12$.

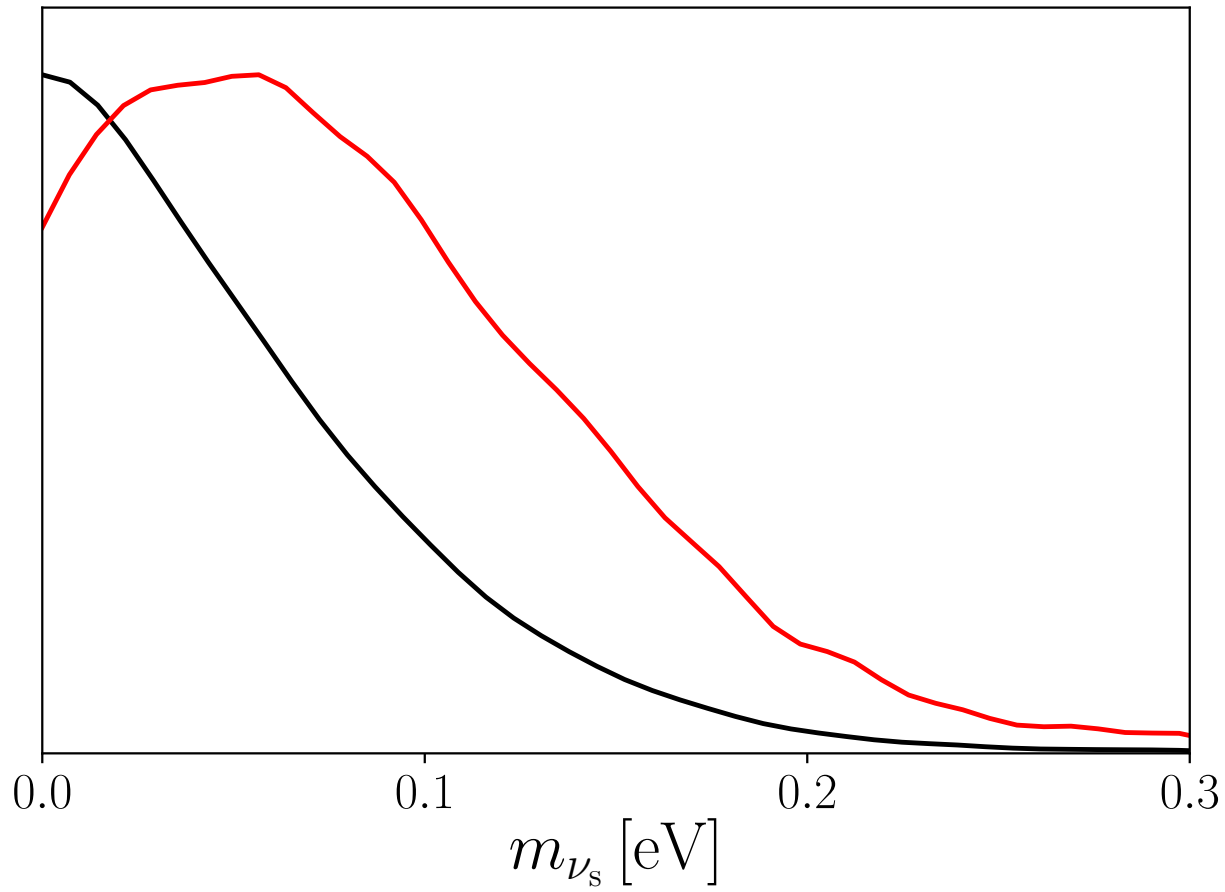


Figure 4.6: Comparison of the one-dimensional marginalized posterior distributions for m_{ν_s} is shown, for the case of a fully thermalized sterile neutrino ($N_{\rm eff} = 4.044$). The black curve represents the benchmark data alone, while the red curve includes the SH0ES H_0 measurement.

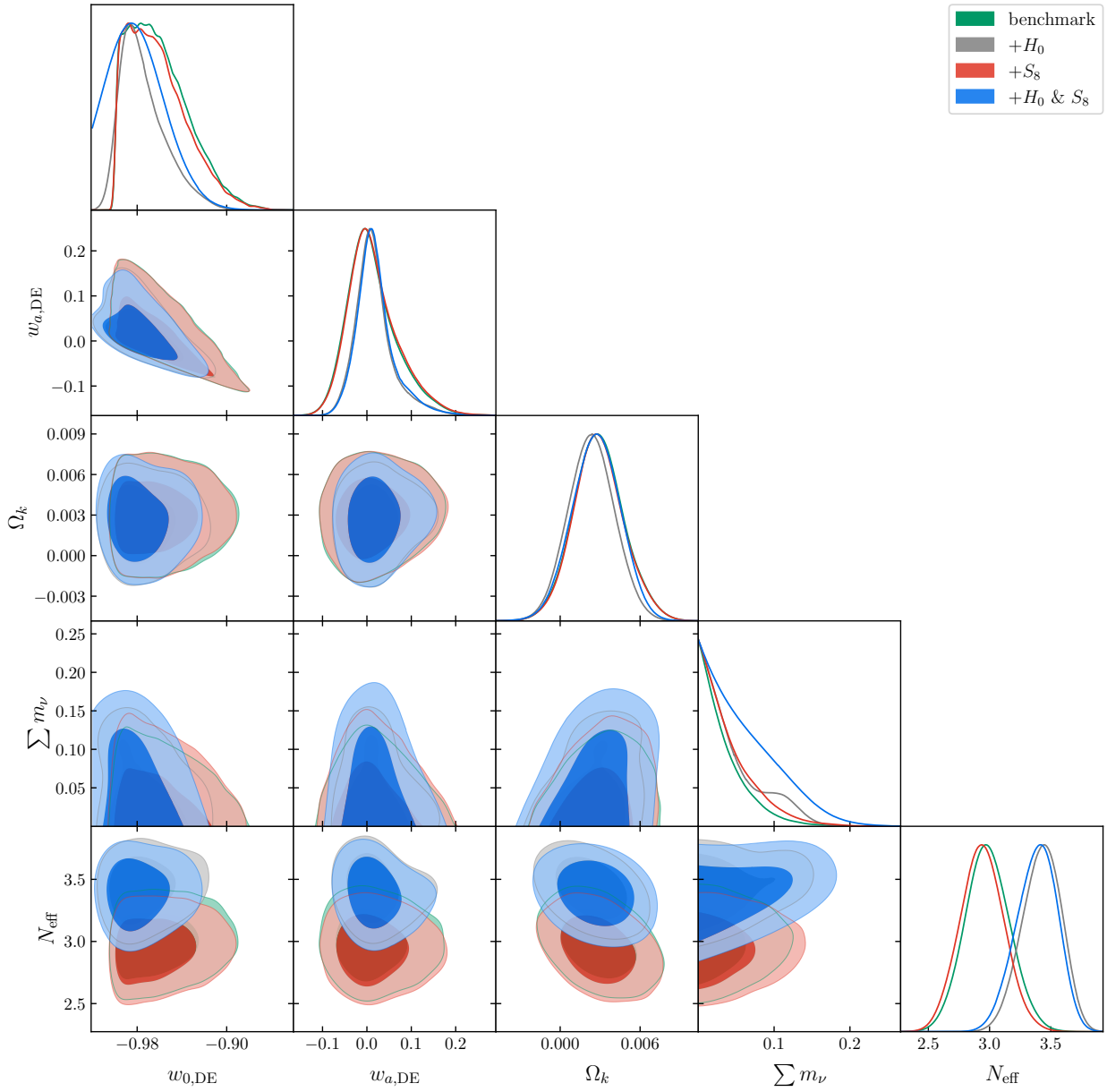


Figure 4.7: Shown are the 68% and 95% CL likelihood contours of the extension parameters in our 11-parameter case, using our benchmark data. Without the tension data, no significant shifts are seen in any extended parameters, except for $w_0 = 0.975^{+0.012}_{-0.024}$. As with more economical models, only N_{eff} deviates strongly from its standard value when including H_0. Here, Σm_ν is in units of eV and H_0 is in units of km s^1 Mpc^1.

Chapter 5

Extra Radiation Cosmologies: Implications of the Hubble Tension for eV-scale Neutrinos

This chapter is a reprint of material submitted for publication in Physical Review D. Reprinted with permission © 2025 American Physical Society.

5.1 Introduction

Neutrinos play a fundamental role in cosmology, influencing several epochs, including but not limited to: the early Universe at weak freeze-out and primordial Big Bang nucleosynthesis (BBN), the growth of large-scale structure (LSS), as well as the anisotropies of the cosmic microwave background (CMB). Their small but nonzero masses, inferred from oscillation experiments [188, 164, 47], and their relativistic behavior in the early Universe leave measurable imprints on both the CMB and LSS. In the early Universe, neutrinos were

all relativistic and contributed to the total radiation density, parameterized by the effective number of relativistic species, $N_{\rm eff}$. The standard thermal history predicts a value of $N_{\rm eff} = 3.044$, slightly greater than the integer value due to heating of the plasma during e^+/e^- annihilation [275, 139]. Deviations from this prediction would provide evidence of new physics such as additional light relics, non-standard neutrino interactions, or the presence of sterile neutrinos (ν_s), in the case of $N_{\rm eff} > 3.044$ [205, 8, 155], or new early-Universe dynamics such as massive particle decay or low reheating temperature scenarios in the case of $N_{\rm eff} < 3.044$ [255, 256, 207, 219, 220, 11, 109].

It has been known for some time that finite neutrino masses suppress the growth of cosmic structures on scales smaller than the horizon at matter-radiation equality, due to a combination of free streaming of neutrinos below that scale and the scale-dependence of the linear growth of structure [276, 14]. This characteristic suppression of clustering at smaller scales with increasing sum of neutrino masses was the pioneering method proposed for high sensitivity of cosmological LSS observables to the value of the total neutrino mass. The sum of neutrino masses here is $\Sigma m_\nu \equiv \Sigma_i m_i$, where i sums over all thermalized mass eigenstates. Recently, the constraints on Σm_ν have become so strong as to entertain the possibility of extra growth on smaller scales due to a fifth force in the dark matter sector, or other new physics, dubbed the "negative neutrino mass" problem [131]. More complicated models of reionization, altering the optical depth to the CMB, may also be responsible for this tension [246], as well as evolving dark energy models [170], which can alleviate constraints on Σm_ν from LSS. Additional potential solutions are discussed in Ref. [290].

The presence of extra relativistic energy density, whether in extra neutrino species or other relativistic species, produces a similar suppression of LSS below the horizon at matter-radiation equality due to the delay of this equality with increasing $N_{\rm eff}$ [276, 14]. This makes Σm_ν and $N_{\rm eff}$ positively correlated in their effects on LSS, with measurements of both being key goals of cosmological surveys [205].

Altering $N_{\rm eff}$ modifies key observable features of the CMB. An increase in $N_{\rm eff}$ reduces the angular size of the sound horizon through its effect on the expansion rate, scaling as $H(z)^{-1}$, and also alters Silk photon damping, which scales as $H(z)^{-1/2}$ as a scattering phenomenon. In early data from high multipole measures of the CMB found evidence for high $N_{\rm eff}$ via this physics, with the Atacama Cosmology Telescope (ACT) finding approximately 2σ evidence for high $N_{\rm eff} = 4.56 \pm 0.75$ [157] and the South Pole Telescope finding $N_{\rm eff} = 3.86 \pm 0.42$ [259]. This spurred interest in the possible evidence of light sterile neutrinos from cosmology, where it was found that the late time measure of the critical density in matter, Ω_m, from Type Ia supernovae surveys was critical in inferring the preference or lack thereof of light sterile neutrinos in cosmology [248]. Subsequently, measurements of low amplitude of fluctuations at small scales, parameterized as σ_8 by their amplitude at $8h\,{\rm Mpc}^{-1}$, renewed interest in cosmological preference for light sterile neutrinos [84, 396, 159]. Then, with the results from Planck 2018, massive neutrinos were very constrained by a combination of a low measurement of the optical depth to the CMB and high CMB lensing amplitude in that dataset, leaving extra sterile neutrinos highly constrained [40].

The interplay between $N_{\rm eff}$ and Σm_ν is particularly important in the context of current cosmological tensions, most notably the discrepancy between local distance-ladder measurements of the Hubble expansion rate, H_0, and the lower values inferred from the CMB under the ΛCDM model [149, 144, 145]. BAO data alone does not directly determine H_0, but when combined with other datasets such as BBN or CMB lensing, it generally prefers a slightly higher H_0 compared to the baseline Planck ΛCDM value, though still significantly lower than the local distance-ladder measurements [20]. Increasing $N_{\rm eff}$ reconciles the CMB and BAO's inferred lower H_0 with the higher, locally measured, values of H_0 [92]. Increasing $N_{\rm eff}$ reconciles the CMB inferred H_0 by decreasing the sound horizon at recombination by increasing the contribution to the expansion rate $H(z)$ through the radiation-dominated

epoch into the era of matter-radiation equality:

$$r_{\rm s}(z_{\rm rec}) = \int_{\infty}^{z_{\rm rec}} \frac{c_s\, dz}{H(z)}\,, \tag{5.1}$$

where $r_{\rm s}$ is the sound horizon at recombination, $z_{\rm rec}$ is the redshift of recombination, and c_s is the sound speed of the plasma. It has been established that $N_{\rm eff}$ is as robust of a solution to the Hubble tension as other new physics, including early dark energy, given statistical tests of the data sets [173], with a preference for a high value of $N_{\rm eff} \approx 3.5$ [172].

Extra neutrino density from cosmology begs the question as to its relation with hints from short-baseline neutrino oscillation experiments that suggest the possible existence of additional neutrino species beyond the three active flavors [43, 45]. Fits to short baseline oscillation anomalies prefer ν_s, with masses (m_s) at the eV scale [135, 318]. Unlike active neutrinos, sterile neutrinos do not participate in weak interactions, but, if partially or completely thermalized in the early Universe, they can contribute to both Σm_ν and $N_{\rm eff}$ [8]. The partial or full thermalized presence of ν_s alters cosmological observables similar to massive active neutrinos and extra relativistic energy density, which are typically tested individually as deviations from minimal ΛCDM. The presence of an extra ν_s is not identical to the individual parameters, as the extra species carries relativistic energy density and neutrino mass as a distinct, massive neutrino state that affects cosmological observables uniquely.

In exploring these scenarios, we found in Ref. [172] that cosmologies with a partially-thermalized sterile neutrino component are strongly favored when incorporating the SH0ES measurement of the Hubble constant, when compared to standard ΛCDM. This preference arises because a sterile neutrino increases $N_{\rm eff}$, thereby reducing the sound horizon and reconciling the CMB-inferred expansion rate with SH0ES. Because of the relative insensitivity of BAO observables to increasing Σm_ν when increasing $N_{\rm eff}$, we found that even massive, partially thermalized sterile neutrinos with $m_s = 0.1\,\text{eV}$ are preferred at 3.3σ relative to

standard ΛCDM. The fact that such models are preferred by the data provides the strong motivation for our present work, where we systematically investigate the nature of BAO, LSS, and CMB sensitivity to massive sterile neutrinos in light of current observational constraints. Our work aims to test the status of current cosmological data on the presence of partially to fully thermalized sterile neutrinos, as the presence of massive neutrinos is constrained by LSS, while the Hubble tension prefers extra relativistic energy density.

The structure of this manuscript is as follows. In the next section, §5.2, we review the effects on cosmological observables by massive neutrinos and extra relativistic energy density, both of which can be provided by ν_s. We connect this with the implications of the Hubble tension's shift on $N_{\rm eff}$ and inferred limits on m_s. In §5.3, we present tests of sterile neutrino scenarios with recent cosmological data sets. Our results are presented and analyzed in §6.4. We conclude with a discussion of future prospects in Section 5.5.

5.2 Neutrino Cosmology: $N_{\rm eff}$ & Σm_ν from CMB, LSS, and BAO

Massive neutrinos and their related relativistic energy density play a fundamental role in cosmology, leaving distinctive imprints on the CMB, LSS, and BAO observables. We review these signatures and emphasize how they complement each other in the presence of additional massive neutrinos. The effects of extra, massive neutrinos are well known in the case of their impact on LSS, which we review for completeness. Their effects on BAO observables is less well known, which we expand on more as a result.

5.2.1 Suppression of LSS by Σm_ν & $N_{\rm eff}$

A well-established effect in cosmology is the suppression of LSS power at relatively smaller scales induced by the free-streaming of massive neutrinos. The amplitude of this suppression is related to the total neutrino mass, Σm_ν, and arises because massive neutrinos, becoming non-relativistic at late times, do not cluster efficiently when they are relativistic, and also suppress growth below their free streaming scale [168, 234]. The fractional suppression in the matter power spectrum can be approximated as

$$\frac{\Delta P}{P} \simeq -8 f_\nu \simeq -8 \frac{\Omega_\nu}{\Omega_m} \simeq -\frac{1}{\Omega_m h^2} \frac{\Sigma m_\nu}{11.6\,\mathrm{eV}}\,, \tag{5.2}$$

where $f_\nu = \Omega_\nu/\Omega_m$ is the neutrino fraction of the matter density [234]. The neutrino density is related to the total mass by $\Omega_\nu = \Sigma m_\nu / 93.13\, h^2\,\mathrm{eV}$, with h the Hubble parameter in units of $100\,\mathrm{km\,s^{-1}\,Mpc^{-1}}$. As can be readily seen from Eq. (5.2), a sensitivity of 1% in change in power, $\Delta P/P$, will result in a sensitivity to Σm_ν of 10 meV, given $\Omega_m h^2 \approx 0.1$. This suppression is most significant on scales that enter the horizon prior to neutrinos becoming non-relativistic, which coincides with their free-streaming scale, suppressing growth of structure, leading to a reduced amplitude of matter clustering at below the horizon size at matter-radiation equality. The often used metric of fluctuation amplitudes at the $8h\mathrm{Mpc}^{-1}$ scale is σ_8, which is below that horizon size is the amplitude of fluctuation. Therefore, σ_8 is a useful measure of the effects of neutrino mass suppression at these cosmologically smaller scales.

The effective number of relativistic species, $N_{\rm eff}$, alters structure growth through a different mechanism. Increasing $N_{\rm eff}$ raises the radiation energy density, increasing the expansion rate during radiation domination, and delaying matter–radiation equality. When fixing the amplitude of scalar perturbations from inflation, this delay enhances the decay of perturbations in the radiation domination era, and shifts the horizon size of matter radiation equality to

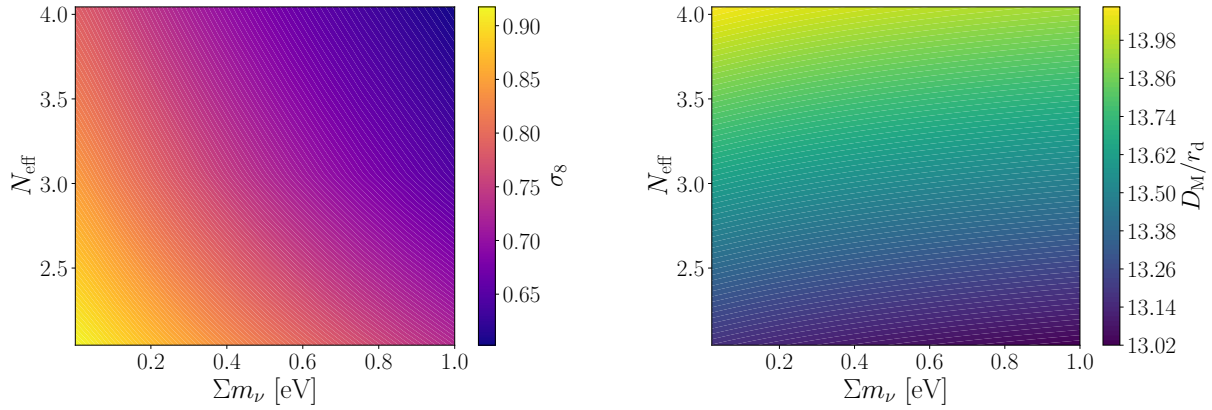


Figure 5.1: **Left panel:** contours of the clustering amplitude σ_8 as a function of the total neutrino mass Σm_ν and the effective number of relativistic species $N_{\rm eff}$, computed while keeping the remaining ΛCDM parameters fixed at their standard values. Lowering Σm_ν and $N_{\rm eff}$ increases σ_8, while raising them decreases it. **Right panel:** contours of the BAO distance ratio $D_{\rm M}/r_{\rm d}$ at $z = 0.51$ for different Σm_ν and $N_{\rm eff}$ values when the total matter density is fixed. An increase in neutrino mass is compensated by a reduction in the cold dark matter fraction. These contours reveal the anticorrelated response of Σm_ν and $N_{\rm eff}$ through their opposite effects on the $D_{\rm M}/r_{\rm d}$ BAO observable. Together, these panels highlight the complementary ways in which neutrino properties imprint on growth and geometry.

larger scales. This results, as in the case of increasing the mass of neutrinos, as a decrease in σ_8.

Increases in both Σm_ν and $N_{\rm eff}$ lower σ_8, suppressing the amount of structure. Therefore, they are correlated parameters when analyzing their effects in LSS observables, including galaxy power spectra and CMB lensing. The left panel in Figure 5.1 shows this correlation between Σm_ν and $N_{\rm eff}$ where the contours of constant σ_8 trace diagonal directions in the $\Sigma m_\nu - N_{\rm eff}$ plane. While the physical origins differ, neutrino free-streaming versus delayed matter-radiation equality, the net imprint on late-time clustering is similar.

5.2.2 BAO: Geometry and Anticorrelation

BAO arise from pressure waves in the photon–baryon plasma of the early Universe. Measurements of the BAO feature were first evidenced in the Sloan Digital Sky Survey (SDSS)

[167] & the Two-Degree Field Galaxy Redshift Survey [127], and more accurately measured in the Baryon Oscillation Spectroscopic Survey [52], and the Extended Baryon Oscillation Spectroscopic Survey [54], with the Dark Energy Spectroscopic Instrument (DESI) providing the most recent measurements [20]. BAO observations enable precise determinations of cosmological distances and the expansion history. In a spatially flat cosmological model with matter, radiation, and a cosmological constant, the Hubble parameter at redshift z is given by the Friedmann Equation as $H(z) = H_0\sqrt{\Omega_m(1+z)^3 + \Omega_r(1+z)^4 + 1 - \Omega_m}$, where H_0 is the present-day Hubble constant, Ω_m the matter density relative to the critical density today, and Ω_r the commensurate radiation density. BAO observations do not measure distances directly, but angles and comoving distance ratios. The relevant distance measures are the comoving angular diameter distance $D_{\rm M}(z)$ and comoving line-of-sight distance $D_{\rm H}(z)$, given by

$$D_{\rm M}(z) = \int_0^z \frac{c\,dz'}{H(z')}, \tag{5.3}$$

$$D_{\rm H}(z) = \frac{c}{H(z)}. \tag{5.4}$$

BAO observations constrain the ratio of these distances to the sound horizon at the drag epoch $r_{\rm d}$, which corresponds to the comoving distance traveled by acoustic waves in the photon–baryon fluid before baryon decoupling. Evaluating the sound-horizon integral in Eq. (5.1) at the drag epoch, $z_{\rm d}$, rather than at recombination, provides $r_{\rm d}$. The transverse BAO scale measures the angular size of $r_{\rm d}$ and is given by $D_{\rm M}(z)/r_{\rm d}$, while the radial BAO scale probes the distance along the line of sight through $D_{\rm H}(z)/r_{\rm d}$. Together, these measurements provide powerful probes of the expansion history.

The geometric observables of angular diameter distance and comoving distance provide an additional channel for sensitivity to neutrino properties. The effect of increasing Σm_ν and $N_{\rm eff}$ not only suppresses the growth of structure at smaller scales, but also alters the background expansion rate, effectively changing the cosmic distances inferred from BAO.

To delve into the effects of neutrino properties, we consider two well-separated redshifts in cosmic history: $z = 0.51$, corresponding to the mean first bin redshift of luminous red galaxies (LRG) in DESI Second Data Release (DR2), and $z = 2.33$, corresponding to the DESI DR2 mean redshift for Lyα forest. Considering $z = 0.51$ first, there is an anticorrelation that can be understood in terms of how neutrino properties shift the BAO peak in the power spectrum. Neutrinos with combined masses of at least 58 meV affect the BAO feature in non-trivial ways. As described by Thepsuriya and Lewis [377], increasing Σm_ν alone tends to shift the BAO peak down and to smaller spatial scales because the sound horizon shrinks as more neutrino mass augments Ω_m, during and after matter–radiation equality, increasing $H(z)$ in the drag epoch, and therefore reducing the integrand in Eq. (5.1). However, if the total matter density is held fixed, then a larger neutrino mass requires a reduction in the cold dark matter fraction, which instead shifts the BAO peak to larger spatial scales, because neutrinos are just starting to act as matter (becoming nonrelativistic) around matter-radiation equality. In contrast, increasing $N_{\rm eff}$ raises the radiation energy density, delays matter–radiation equality, and shifts the BAO scale to smaller spatial scales by also reducing the integrand in Eq. (5.1). As we describe below, $D_{\rm M}$ at a low redshift of $z = 0.51$ is not significantly affected when Σm_ν is varied, and it is $r_{\rm d}$ that largely determines the behavior of the BAO measurable, $D_{\rm M}/r_{\rm d}$. Therefore, the opposite response of the ratio to Σm_ν and $N_{\rm eff}$ are directly reflected in the anticorrelation pattern shown in the right panel of Fig. 5.1.

BAO measurements are predicated on the high amount of cosmological information from the CMB. Therefore, we analyze the distribution of Markov Chain Monte Carlo (MCMC) chain points preferred by the CMB data in the space of the BAO observables, as shown in Fig. 5.2, which plots a subset of the MCMC chain points from the *Planck* 2018 only likelihoods. We choose cosmologies with one extra parameter—either $N_{\rm eff}$ or Σm_ν, to show their individual effects on BAO observables. There, one can see that increasing $N_{\rm eff}$ leads to a *decrease* in $D_{\rm H}/r_{\rm d}$ at redshift $z = 0.51$ and an *increase* in that ratio at redshift $z = 2.33$. The opposite happens when Σm_ν is increased: $D_{\rm H}/r_{\rm d}$ *increases* at redshift $z = 0.51$ and

decreases at redshift $z = 2.33$. For $D_{\rm M}/r_{\rm d}$, larger $N_{\rm eff}$ results in an *decrease* of this ratio at both redshifts $z = 0.51$ and $z = 2.33$ and larger Σm_ν results in an *increase* of this ratio at both redshifts $z = 0.51$ and $z = 2.33$, as shown in Fig. 5.2. The end result of these trends is an *anticorrelation* between $N_{\rm eff}$ and Σm_ν when we look at BAO observables. This was previously described in the more constrained parameter space in Fig. 5.1. In short, a simultaneous increase in both $N_{\rm eff}$ and Σm_ν shifts $D_{\rm M}/r_{\rm d}$ and $D_{\rm H}/r_{\rm d}$ in opposite directions, allowing for the predicted BAO measurement to stay constant, and consistent with the observed values. That is, in the case if partially or fully thermalized massive sterile neutrinos, BAO measurements can accommodate the simultaneous presence of increased $N_{\rm eff}$ and Σm_ν.

The change in slope of the CMB-derived points between the left and right panels of Fig. 5.2 is driven by the opposite responses of $D_{\rm H}/r_{\rm d}$ to variations in Σm_ν and $N_{\rm eff}$. For increasing neutrino mass, $D_{\rm H}/r_{\rm d}$ increases at $z = 0.51$ but decreases at $z = 2.33$, while for increasing $N_{\rm eff}$ the trend is reversed: $D_{\rm H}/r_{\rm d}$ decreases at $z = 0.51$ and increases at $z = 2.33$. In the case of neutrino mass, this behavior arises from the degeneracy with Ω_m, enforced by the CMB data: as Σm_ν increases, the degeneracy with Ω_m requires it to rapidly increase to preserve the angular size of the sound horizon on the sky, as discussed in Ref. [287]. We fit the degeneracy between Ω_m and H_0 in the full likelihood to find the linear relation between the degeneracy of these parameters. Given this combination of effects, an increase in Ω_m drives a reduction of $D_{\rm H}$ at high redshift (the dashed red line in left panel of Fig. 5.3), while driving an increase in $D_{\rm M}$ at high redshift. For the low redshift case, $D_{\rm H}$ and $D_{\rm M}$ instead both increase with Σm_ν. This is why the contours invert in direction from the left to the right panel of Fig. 5.2, for the case of Σm_ν.

For varying $N_{\rm eff}$, shown in the right panel of Fig. 5.3, $D_{\rm H}$ decreases as $N_{\rm eff}$ increases for both redshifts, which is shown in the bottom panels of Fig. 5.2. As previously discussed, $r_{\rm d}$ also decreases with increasing $N_{\rm eff}$, but the fractional change in $r_{\rm d}$ is larger than that in $D_{\rm H}$. This

dominance of the variation in $r_{\rm d}$ over that in $D_{\rm H}$ is the key factor responsible for the reversal of the slope of the CMB points across the two panels for *that* observable parameter, shown between the panels of Fig. 5.2. Though the contours invert for Σm_ν and $N_{\rm eff}$ at higher z for different reasons, they preserve the anticorrelation between them seen at low z. Therefore, BAO observables accommodate a simultaneous increase in Σm_ν and $N_{\rm eff}$ across a wide range of redshifts.

Many of parts of these effects are explored in previous studies. In **(author?)** [287], they show that BAO observables are sensitive to matter *fractions* rather than absolute densities, and that within ΛCDM, the total matter fraction Ω_m must increase significantly as Σm_ν grows, making geometric measurements a powerful and complementary probe of neutrino mass alongside structure growth suppression. The effects of neutrino physics on the drag scale were also studied in **(author?)** [377]. The relation between the BAO scale at different redshifts and its dependence on neutrino mass and number as constrained by the CMB was also explored in **(author?)** [74], where the anticorrelation we discuss was also shown. In this work, we have gone beyond and shown explicitly where these relations in BAO observables arise in their sensitivities to Σm_ν and $N_{\rm eff}$.

5.3 Cosmological datasets & Methodology

5.3.1 Baseline cosmological dataset

For our baseline data, we use a combination of cosmological datasets to constrain our models. The datasets are similar to our previous work [172], but here we include the more newly available DESI DR2 data.

CMB Planck Final Data Release (P18)

The Planck 2018 (PR3) legacy data release [42, 41] provides highly precise measurements of the CMB temperature and polarization power spectra, with five out of six ΛCDM parameters determined to better than 1% and the angular sound horizon measured to 0.03%. We include high-ℓ `Plik` likelihoods, low-ℓ `commander` likelihoods for TT in $2 \leq \ell \leq 29$, `SimAll` for EE in the same range, and TE and EE spectra at $30 \leq \ell \leq 1996$.

CMB Lensing

We incorporate CMB lensing measurements from the Planck NPIPE PR4 reconstruction [115], which includes roughly 8% more data than PR3 with improved processing, as well as ACT DR6 lensing data covering over 9,400 deg^2 of the sky [337, 294], achieving 2.3% precision on the lensing power spectrum.

BAO: DESI DR2

We use BAO measurements from over 14 million galaxies and quasars in DESI DR2. We adopt the DESI DR2 BAO likelihood [20], which updates the previous DR1 measurements and includes the volume-averaged distance D_V/r_d from the Bright Galaxy Survey sample ($0.1 < z < 0.4$), $D_\mathrm{M}/r_\mathrm{d}$ and $D_\mathrm{H}/r_\mathrm{d}$ for LRG samples ($0.4 < z < 0.6$ and $0.6 < z < 0.8$), a combined LRG plus Emission Line Galaxies (ELG) tracers ($0.8 < z < 1.1$), ELG measurements ($1.1 < z < 1.6$), quasar clustering ($0.8 < z < 2.1$), and Lyα BAO constraints ($1.8 < z < 4.2$). We refer to this combination as "DESI2."

Type Ia Supernovae

Type Ia supernovae (SNe) provide an independent probe of the expansion history. We adopt the Pantheon+ sample [358, 105], containing 1550 spectroscopically confirmed SNe Ia over $0.001 < z < 2.26$ with improved calibration and systematics relative to the previous Pan-

theon release [359].

Local Expansion Rate: H_0 (SH0ES)

We adopt the Supernovae and H_0 for the Equation of State of dark energy (SH0ES) measurement of H_0 for the local Hubble expansion rate. We use the Gaussian likelihood for the Hubble constant from the SH0ES collaboration [344], $H_0 = 73.04 \pm 1.04\,\mathrm{km\,s^{-1}\,Mpc^{-1}}$. We introduce a H_0 prior directly in the likelihood rather than the absolute magnitude M_b since using the latter only substantially affects models with non-standard late-time expansion histories, which are not considered in this work.

5.3.2 Complementary Data: SDSS DR12 BAO & Full-Shape

Since the LSS information from the full-shape power spectrum of DESI DR2 is not publicly available, we consider constraints from the latest BAO and full-shape analysis of SDSS DR12, which we dub SDSSBAOFS [52]. Unlike BAO-only analyses, the full-shape likelihood is sensitive not only to the position of the acoustic feature but also to the broadband shape of the LSS clustering spectrum, which carries information about the underlying matter content and growth of structure as a function of scale. This makes it valuable for constraining the effects of massive neutrinos and extra N_{eff}, which both induce the characteristic suppression of the full-shape power at smaller scales.

5.3.3 Methodology

As we performed our analyses of these models given the cosmological data, we found a dependence on the final result for signals of massive, extra neutrinos that depend on whether

one adopts Bayesian or frequentist statistics. Bayesian inference offers a systematic framework for model comparison through the evaluation of the Bayesian evidence [382], whereas frequentist approaches such as profile likelihoods provide complementary, prior-independent assessments of the parameter space [130]. Frequentist techniques for parameter inference that employ profile likelihoods have historically been used less often in cosmology, largely because of their computational expense. However, they have recently gained traction due to their ability to yield results that complement Bayesian analyses. In the Bayesian framework, credible intervals depend on the specification of priors for all parameters and incorporate nuisance parameters through integration (i.e., marginalization). In contrast, frequentist confidence intervals do not inherently require priors and instead address nuisance parameters by maximizing the likelihood. These methodological differences, involving both prior dependence and the treatment of nuisance parameters, are especially relevant in scenarios where the data weakly constrain the model and/or when parameters are near physical boundaries. In Bayesian studies, this situation can give rise to effects driven by the choice or volume of the prior (see, e.g., [190, 371, 226, 224, 230] for applications in cosmology). Importantly, both Bayesian and frequentist approaches converge in the limit of sufficiently large datasets.

Since we are interested in extra, massive sterile neutrino models, we implement the extra relativistic energy density above the standard energy content in the active neutrinos, which we adopt to be $N_\nu \equiv 3.044$. We model such a cosmology as a partially thermalized sterile neutrino model with Σm_ν and $\Delta N_{\rm eff} \equiv N_{\rm eff} - N_\nu$ as additional parameters to the six ΛCDM ones [172], which is the formulation required by `CAMB` [281]:

$$m_{\rm s}^{\rm eff} = \Delta N_{\rm eff}\; m_{\rm s}^{\rm ph}; \qquad \Delta N_{\rm eff} = \beta. \tag{5.5}$$

Importantly, $m_{\rm s}^{\rm eff}$ is not to be mistaken to be the physical mass. `CAMB` requires $m_{\rm s}^{\rm eff}$ and β to be the free parameters describing the sterile neutrino. Here, $m_{\rm s}^{\rm ph}$ denotes the physical mass of the additional sterile neutrino species only, excluding the three active Standard

Model neutrinos. In this case, one encounters the model space where $\beta \sim 0.01$ and the physical mass approaches $m_{\rm s}^{\rm ph} \sim 1\,{\rm keV}$, which is when the sterile neutrino can displace the need for CDM and becomes the (warm) dark matter. Because the sterile neutrino mass can be arbitrarily large and $\Delta N_{\rm eff}$ arbitrarily small for a fixed contribution to the dark matter density, one must map the parameter space to a finite volume in the case of Bayesian statistics. In our results, we found that the often-used parameterization in $1/m_s$ leads to inaccurate results on constraints on massive, extra neutrinos, with the results depending on the statistical approach, as discussed further in the Appendix. Therefore, for our main results, we adopt either frequentist statistics or Bayesian models where only $m_{\rm s}^{\rm eff}$ or β were individually left free.

We employ frequentist approaches based on profile likelihoods, which provide a prior-independent way to assess constraints on cosmological parameters, including those bounded by physical limits. In this method, the likelihood is evaluated at fixed values of the parameter of interest while maximizing over all remaining cosmological and nuisance parameters. We employ 180 extremizations of the likelihood using the extremizing sampler provided in `Cobaya` [380]. in order to best determine the likelihood's true value, due to the considerations we discussed in Ref. [172]. The general construction of confidence intervals for bounded parameters like m_s was formalized in the Feldman–Cousins framework [178], which defines coverage in the "true parameter–measured parameter" space. An equivalent description in terms of the likelihood-ratio test statistic has been outlined in Ref. [225].

We also perform Bayesian inference using the publicly available `Cobaya` package, implementing the MCMC sampler [280, 278] with fast dragging [316], and computing theoretical predictions with the `CAMB` cosmological Boltzmann solver [281, 233]. Each analysis is run with four parallel MCMC chains, and convergence is assessed using the Gelman-Rubin statistic, requiring $R - 1 < 0.01$ for all parameters.

We adopt flat priors for all cosmological parameters, chosen to extend well beyond the region

of significant likelihood support. Specifically, we vary the baryon density $\Omega_{\rm b}h^2$ from 0.005 to 0.1, the cold dark matter density $\Omega_{\rm c}h^2$ from 0.01 to 0.99, the scalar amplitude $\log(10^{10}A_{\rm s})$ from 1.61 to 3.91, the scalar spectral index $n_{\rm s}$ from 0.8 to 1.2, the reionization optical depth $\tau_{\rm reio}$ from 0.01 to 0.8, and the angular scale of the sound horizon $100\theta_{\rm MC}$ from 0.5 to 10. For the neutrino sector, when we conider only active neutrino masses, as in Fig. 5.2, the total neutrino mass is varied as Σm_ν between 0 and 10 eV. For the cases considering sterile neutrinos, we fix the total active neutrino mass to 0.058 eV (modeled as a single mass state), and vary $m_{\rm s}^{\rm eff}$ and β so that the extra contribution to the effective number of relativistic species, $N_{\rm eff}$, is between 0 and 100, and the sterile neutrino mass m_s from 0.0001 to 3 eV.

5.4 Results

Let us first consider our datasets without SH0ES' measurement of H_0. In this case, we can use Bayesian methods to determine the value of $N_{\rm eff}$, with P18, CMB Lensing, DESI2 & SNe PP datasets, assuming any extra relativistic energy density is massless,

$$N_{\rm eff} = 3.10 \pm 0.16\,. \tag{5.6}$$

Including SH0ES' measurement of H_0, with P18, CMB Lensing, DESI2 & SNe PP datasets

$$N_{\rm eff} = 3.43 \pm 0.13\,, \tag{5.7}$$

which gives the best fit local expansion rate of this model to be $H_0 = 70.64\,{\rm km\,s^{-1}\,Mpc^{-1}}$. This reduces the tension between CMB-inferred H_0 and SH0ES's measurement from 5σ in ΛCDM to 2.4σ in a sterile neutrino cosmology, given SH0ES' value $H_0 = 73.04 \pm 1.04\,{\rm km\,s^{-1}\,Mpc^{-1}}$. Although not fully resolved, the Hubble tension is significantly reduced with larger $N_{\rm eff}$ [174, 57]. For the case of $N_{\rm eff}$ being harbored in a massive sterile neutrino,

we adopt $m_s = 0.1\,\mathrm{eV}$ as a representative mass, and we find

$$N_{\mathrm{eff}} = 3.50 \pm 0.13\,, \tag{5.8}$$

where all of these N_{eff} values were determined by Bayesian methods. We tested the result in Eq (5.8) with a frequentist profile likelihood, and found consistent results.

To explore the impact of fixing N_{eff} to a higher value motivated by H_0 data, we perform a profile likelihood analysis on m_s, adopting the massive sterile neutrino inferred best-fit value of $N_{\mathrm{eff}} = 3.50$. The sterile neutrino mass represents a parameter subject to a strict physical boundary, $m_s \geq 0$. In this case, the standard asymptotic assumptions underlying Wilks' theorem are not valid, since the maximum-likelihood estimator and the likelihood ratio test statistic are no longer parabolically related when the unconstrained best fit lies in the unphysical region. Consequently, the naive use of $\Delta\chi^2$ contours can lead to under- or over-coverage near the boundary [225].

To address the physical boundary, we follow the Feldman–Cousins prescription [178], performing the profile likelihood scan in m_s by maximizing over cosmological and nuisance parameters at each fixed $m_s \geq 0$, as shown in Fig. 5.4. The resulting $\Delta\chi^2(m_s)$ profile was then fit with a quadratic function restricted to the physical branch. The 68% and 95% CL intervals were then derived from the intersection of the observed profile with the modified critical values. For more details on this method, see Ref. [225]. For our data, this construction yields an upper limit of

$$m_s < 0.170\,\mathrm{eV}\ (95\%\,\mathrm{CL})\,. \tag{5.9}$$

Since in our ΛCDM model the active neutrino mass is fixed to a single massive state with $m_\nu = 0.058\,\mathrm{eV}$, the upper bound on the total neutrino mass, Σm_ν, including both active and sterile species, is relaxed by a factor of 4.3 compared to the standard constraint of

$\Sigma m_\nu < 0.053\,\mathrm{eV}$ (95% CL) obtained from a similar dataset that does not attribute the extra radiation energy density to a sterile neutrino [169]. The relaxation arises from the physics discussed in §5.2. For a fixed $N_{\rm eff}$, we find that Bayesian methods find a consistent limit for m_s as in Eq. (5.9).

To explore the preference of SH0ES H_0 for sterile neutrinos as a function of exact m_s, as compared to the baseline ΛCDM case with $N_{\rm eff} = 3.044$, where $\Delta N_{\rm eff} = 0$ and $m_{\rm s}$ undefined, as no additional sterile neutrino is present, we find

$$\begin{aligned} m_s &= 0.1\,\mathrm{eV}, \quad \Delta\chi^2 = -10.1 \\ m_s &= 0.2\,\mathrm{eV}, \quad \Delta\chi^2 = -7.0 \\ m_s &= 0.3\,\mathrm{eV}, \quad \Delta\chi^2 = -3.2 \\ m_s &= 1\,\mathrm{eV}, \quad\ \ \Delta\chi^2 = 34.6\,, \end{aligned} \tag{5.10}$$

where negative values of $\Delta\chi^2$ correspond to an improved fit relative to ΛCDM. Since both $N_{\rm eff}$ and m_s are fixed in all minimizations, the compared models have the same number of free parameters. The lightest masses are the most preferred, with even the case of $m_s = 0.1$ eV favored at greater than 3σ.

We also tested whether the inclusion of the full-shape galaxy power spectrum data, together with the BAO feature, affects the constraints on m_s. Using SDSSBAOFS in combination with our baseline dataset in a Bayesian analysis—excluding DESI2 to avoid overlap with SDSS and because the DESI full-shape data is not yet publicly available—we find that the constraints become less stringent. For $N_{\rm eff} = 3.5$, the limit is $m_{\rm s} < 0.238$ eV (95% CL) with the P18+SDSSBAOFS+PP+H_0 dataset, weaker than from BAO alone.

5.5 Discussion & Conclusions

In this work, we show how BAO observables are less sensitive to $N_{\rm eff}$ and Σm_ν together, than when either alone is left free, due to inherent degeneracies in the geometric observables of BAO. Though the Hubble tension may be alleviated from increasing $N_{\rm eff}$ alone [343], we find that evidence for extra relativistic energy density in the combination of CMB and local expansion rate measurements, relaxes the limit on the mass of a partially thermalized sterile neutrino, and is greater than a factor of 4 weaker than standard massive neutrino limits, Eq. (5.9). Moreover, cosmologies with partially thermalized sterile neutrinos ($N_{\rm eff} = 3.5$), for $m_s \ll 1\,{\rm eV}$, are preferred at 3.2σ [Eq. (5.10)] over ΛCDM. Our updated analysis here, with DESI2, reinforces our earlier findings [172] that sub-eV sterile neutrinos are preferred by the tension data. This reflects previous hints for extra $N_{\rm eff}$ and sterile neutrinos, as discussed in the introduction. We have also found that Bayesian methods are problematic for mapping the parameter space for sterile neutrino mass when $N_{\rm eff}$ is free, as the light sterile neutrino mass can increase to the warm dark matter (WDM) keV scale, as discussed in the Appendix. These prior volume effects may have impacts on WDM constraints that use $1/m_s$ mappings [237, 194, 389].

There is also an important connection to hints of light, eV-scale sterile neutrinos as responsible for short-baseline neutrino oscillation experiment results from LSND and MiniBOONE [43, 45], anomalies observed in Gallium experiments SAGE [22], GALLEX [251], and BEST [79, 80], as well as ν_μ disappearance in ICECUBE [15]. These experiments may suggest the presence of sterile neutrinos with mass-squared differences with the active neutrinos of order 1 eV^2. Importantly, recent results from MicroBooNE show no evidence for an anomalous excess of electronlike events and exclude an electronlike interpretation of the MiniBooNE low-energy excess at $> 99\%$ C.L. [24]. In order to accommodate constraints from other short-baseline experiments, models with more than one sterile neutrino have been considered, with the extra neutrino mass eigenstates having even larger mass differences than 1

eV^2 [128], and the effects of statistical methods have been investigated in detail regarding combined experiments [387, 388].

Our results disfavor light sterile neutrinos above the $\sim$0.3 eV scale. Therefore, there is tension with the mass scales preferred by short-baseline oscillation experiments. However, it is well known that cosmological neutrino mass constraints are alleviated in cosmologies with relaxed assumptions on dark energy, curvature, and other often-fixed cosmological parameters (e.g., see Refs. [104, 170]). Relaxation of models of reionization can also alleviate neutrino mass constraints [246]. The subsequent reanalysis of Planck primary CMB and lensing data by Ref. [381] finds slightly weaker bounds on massive neutrinos [172], which could also further accommodate massive sterile neutrinos. Exploring multiple extra-parameter models, dynamical dark energy, and more complex models of reionization are beyond the scope of our present work, but are of interest if the Hubble tension and evidence for short-baseline oscillations persist. Full-shape measurements of cosmological matter clustering may enhance constraints on the presence of massive neutrinos, but our analysis finds they are not yet significantly constraining given the available full-shape dataset from SDSS DR12, as discussed above.

Importantly, we find that a sterile neutrino cosmology should have a contribution to the relativistic energy density at below that of a fully-thermalized sterile neutrino ($\Delta N_{\rm eff} = 1$). Such a scenario is inconsistent with the mixing angles required for the short-baseline results, since they would thermalize the sterile neutrino [272]. However, partial thermalization can arise from models that suppress thermalization, including low-reheating temperature universes and models with lepton asymmetries [7, 238, 220]. These cosmologies can also accommodate constraints from BBN. Interestingly, recent CMB results from ACT DR6 find $N_{\rm eff} = 2.86 \pm 0.13$, which increases the tension between CMB datasets and $N_{\rm eff}$ solutions to the Hubble tension [109].

The H_0 tension has motivated renewed attention to the role of neutrinos as messengers of

possible new physics, especially as current generation surveys such as DESI and Euclid will deliver increasingly precise BAO and LSS measurements across a broad redshift range with a wide variety of statistics [28, 301, 173]. Future CMB surveys will also have increased sensitivity to $N_{\rm eff}$ [13, 209, 23]. We find that cosmological data can be consistent with, and may even prefer, short-baseline-oscillation motivated light sterile neutrinos, though with mass scales that tend to be lighter than that preferred by the oscillation experiments. As further oscillation and cosmological data is available, we will uncover whether the elusive neutrino sector is responsible for both oscillation and cosmological tensions.

5.6 APPENDIX: Prior Dependence and Volume Effects

Bayesian inference is sensitive not only to the likelihood function but also to the choice of priors. When placing constraints on the sterile neutrino mass m_s, it is therefore essential to carefully consider how priors are defined, particularly under non-linear reparametrizations of the mass. A notable bias arises when a uniform prior is imposed not on m_s itself, but on transformed variables such as $1/m_s$. While such choices may be motivated by wanting to map an infinite parameter space where m_s can become a heavy dark matter particle, the inverted parameter does not correspond to a uniform weighting in m_s space. Instead, it redistributes the prior volume in a non-trivial way and can significantly bias the resulting posterior constraints.

One can test the volume dependence by using inverted weighted scalings, $1/m_s$, $1/m_s^2$, or $1/\sqrt{m_s}$, where we use the standard posterior distribution estimation package `getdist` [279]. For example, imposing a flat prior on $1/m_s$ induces an effective prior on m_s proportional to $1/m_s^2$, thereby strongly favoring small values of the mass. Likewise, a flat prior on $1/\sqrt{m_s}$

produces an induced prior scaling as $1/m_s^{3/2}$, and a flat prior on $1/m_s^2$ leads to an even steeper weighting. In all of these cases, the prior volume is disproportionately concentrated at low m_s, independent of the likelihood, artificially driving the posterior distribution toward vanishing masses. This behavior is problematic when interpreting constraints on sterile neutrino masses, as shown in Fig. 5.5. For example, we find that when using a flat prior on $1/\sqrt{m_s}$ in DESI2 analyses, the posterior is biased toward lower masses, even in regions where the likelihood is relatively flat. Our inferred upper limits on the sterile neutrino mass vary widely with the choice of prior. For example, a prior uniform in $1/\sqrt{m_s}$ gives the tightest limit, $1/m_s$ yields a bound roughly five times larger, and $1/m_s^2$ gives the loosest constraint, over twenty times the tightest. This illustrates that the derived limits on m_s can be driven primarily by the prior rather than the data itself.

In general, when you place a flat prior on a transformed parameter, you are not placing a flat prior on m_s itself. Instead, you are reweighting the space of m_s values, giving disproportionate volume to certain ranges—typically the low-mass region. This violates the principle of non-informative priors unless the transformation is physically motivated and explicitly accounted for in interpretation. This issue may be worth considering when assessing cosmological limits on WDM particle masses or light sterile neutrinos, where the physical quantity of interest is m_s itself [237, 194, 389].

Using transformed priors in such contexts can severely misrepresent the viable parameter space and overstate the level of constraint. Flat priors on m_s avoid such distortions when the mass is the physical quantity of interest. This approach ensures that each interval in m_s contributes equally to the prior volume and that the resulting posterior more faithfully reflects the data's constraining power, which can also be achieved by frequentist methods.

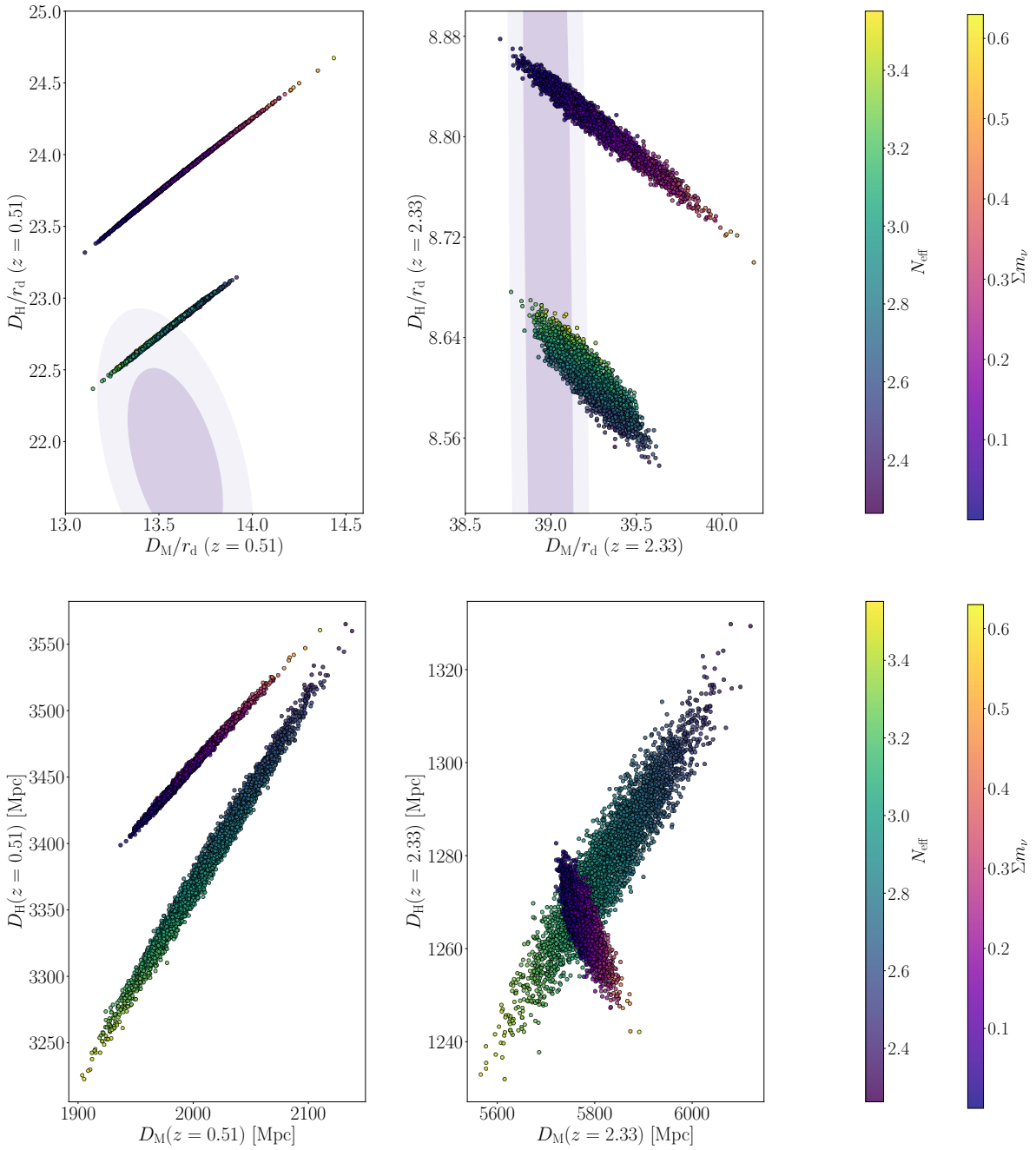


Figure 5.2: **Top Panels:** $D_{\rm M}/r_{\rm d}$ shown along the horizontal axis and $D_{\rm H}/r_{\rm d}$ along the vertical axis, calculated from the parameters of the MCMC chains from the *Planck* 2018 CMB likelihoods alone, for two distinct models with free neutrino mass and $N_{\rm eff}$, separately. The left panel corresponds to a redshift of 0.51 and the right panel to a redshift of 2.33. The colors indicate the values of $N_{\rm eff}$ and Σm_ν specified in the color bar. A positive vertical offset has been applied to the Σm_ν chains in both panels to ensure clarity of the figure ($z = 0.51$ vertical offset of $+1$; $z = 2.33$ vertical offset of $+0.2$). The purple contours denote the 1σ and 2σ DESI DR2 BAO measurements of $D_{\rm M}/r_{\rm d}$ and $D_{\rm H}/r_{\rm d}$. **Bottom Panels:** To show their dependence on the neutrino parameters independent of $r_{\rm d}$, $D_{\rm M}$ is shown along the horizontal axis and $D_{\rm H}$ is along the vertical axis for models with free neutrino mass and $N_{\rm eff}$, including only the *Planck* 2018 CMB likelihoods. A positive vertical offset of $+100$ Mpc has been applied to the Σm_ν chain points at $z = 0.51$ to ensure clarity of the figure.

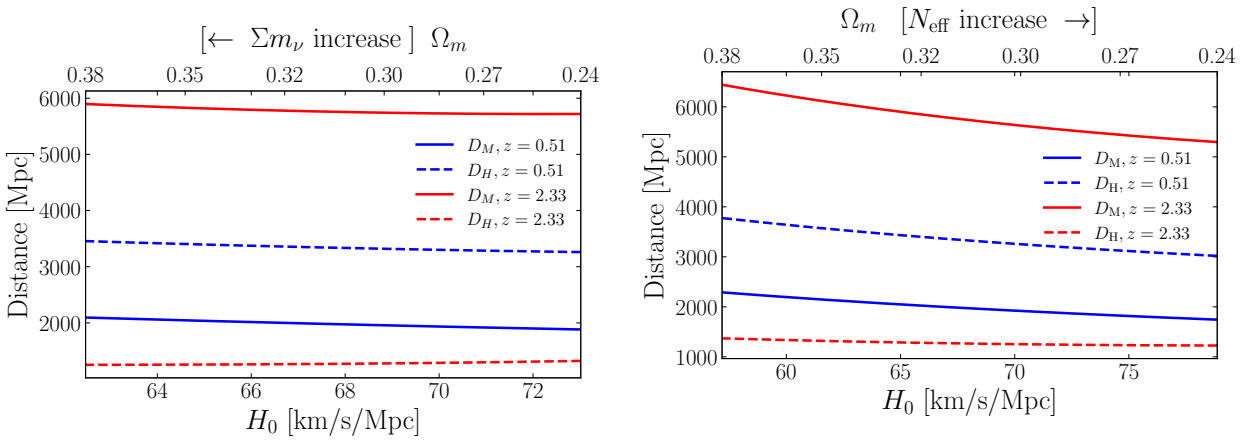


Figure 5.3: Variation of the transverse distance $D_{\rm M}$ (solid lines) and the radial distance $D_{\rm H}$ (dashed lines) is shown at two redshifts: $z = 0.51$ (blue) and $z = 2.33$ (red). These are plotted as the Hubble constant H_0 along the lower horizontal axis and the matter density Ω_m are varied along their linear degeneracy from the *Planck* 2018 CMB likelihoods, as described in the text. The left panel shows models where Σm_ν increases in correlation with Ω_m (to the left) and the right panel shows models where $N_{\rm eff}$ increases in anticorrelation to Ω_m, to the right.

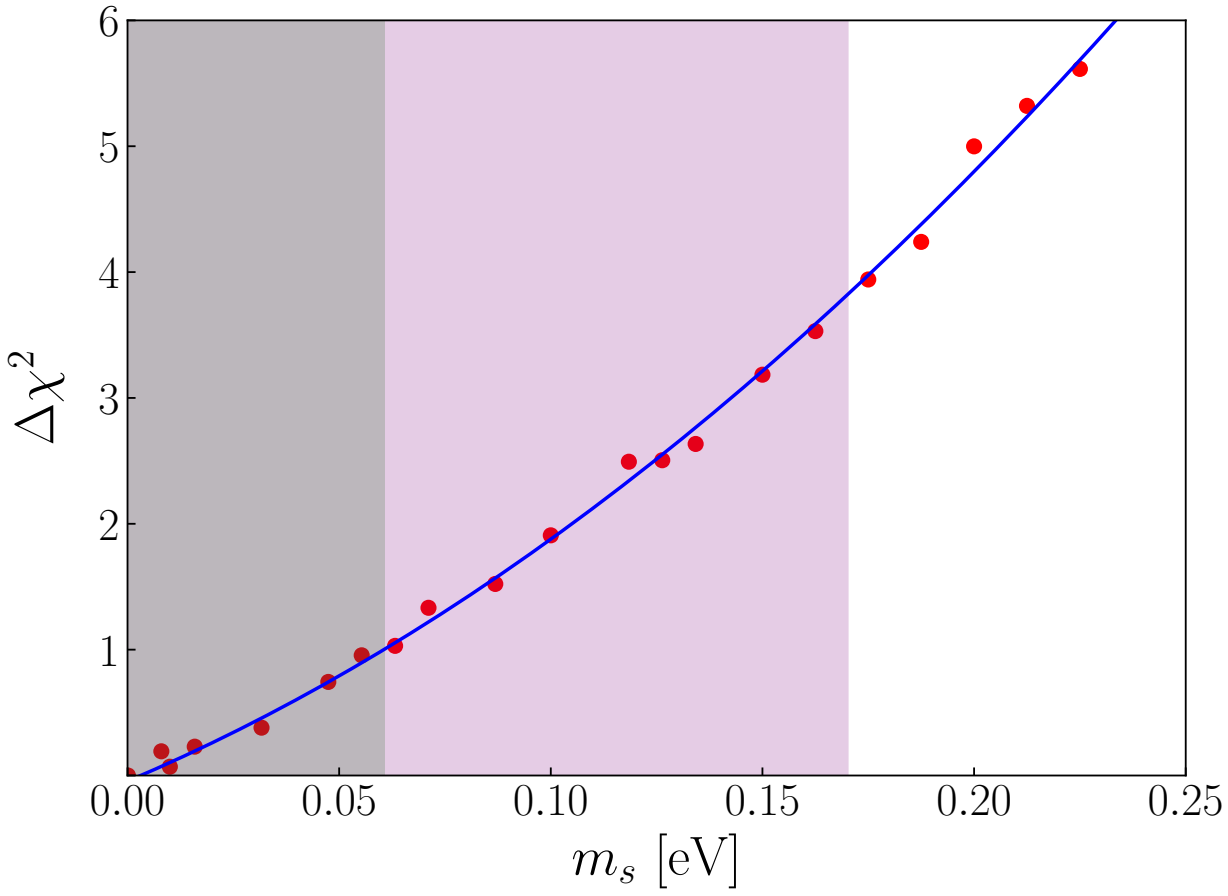


Figure 5.4: We show the profile likelihood for the physical sterile neutrino mass m_s, with the effective number of neutrino species fixed to $N_{\rm eff} = 3.50$. The red points show the computed $\Delta\chi^2$ values at discrete mass points used in the fit, while the blue curve represents a parabolic interpolation through these points. Shaded bands indicate the 68% (black) and 95% (purple) confidence intervals, respectively.

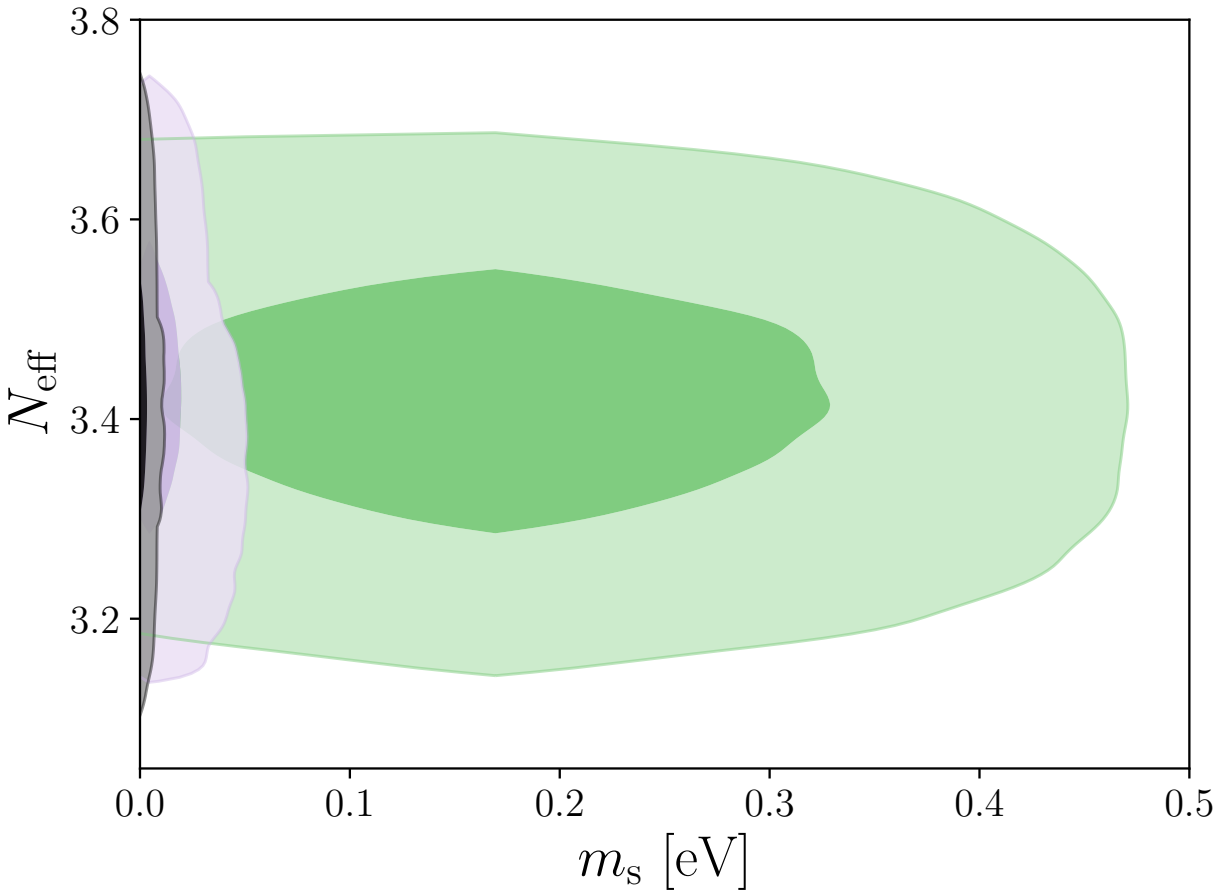


Figure 5.5: Two-dimensional posterior distributions are shown for the physical sterile neutrino mass, $m_{\rm s}$ and the effective number of neutrino species, $N_{\rm eff}$, under three different prior choices using MCMC Bayesian methods and our baseline datasets. The black contours correspond to a prior set as $1/\sqrt{m_s}$, the light purple contours to a prior as $1/m_s$, and the pale green contours, which give the most relaxed bounds, correspond to a prior of $1/m_s^2$. This figure illustrates the impact of prior volume effects in Bayesian analyses of this cosmological model.

Chapter 6

Sound-Horizon-Agnostic Inference of the Hubble Constant and Neutrino Mass from BAO, CMB Lensing, and Galaxy Weak Lensing and Clustering

This chapter is a reprint of material submitted for publication in Astrophysical Journal Letters, 2025.

6.1 Introduction

Determining the Hubble constant, H_0, with high precision is both a fundamental goal and an ongoing challenge in modern cosmology. Despite the success of the standard ΛCDM model in explaining a wide range of cosmological observations, a significant tension persists between the value $H_0 = 67.36 \pm 0.54$ km/s/Mpc inferred from *Planck* measurements of the cosmic

microwave background (CMB), under the assumption of ΛCDM [42], and the value $H_0 = 73.04 \pm 1.04$ km/s/Mpc obtained from Cepheid-based distance ladder measurements [344].

CMB analyses rely on the well-established physics of recombination to determine the sound horizon at photon–baryon decoupling, or the drag epoch, r_d, which is used in the extraction of cosmological parameters. However, the Hubble tension may indicate the need for additional physics during the epoch of recombination, such as primordial magnetic fields [239, 243, 240, 241], early dark energy [254, 335, 370], extra relativistic species [92, 172], neutrino self-interactions [267, 324], or variations of fundamental constants that alter recombination physics [216, 217, 81], among other proposed mechanisms [149, 357, 173]. These scenarios would modify the standard determination of r_d, making it smaller and thereby increasing the CMB-inferred value of H_0.

This motivates the exploration of methods for constraining H_0 that do not rely on modeling r_d. Several recent studies [329, 86, 177, 328, 399, 338] have utilized datasets that probe the scale of matter–radiation equality, $k_{\rm eq}$, and hence the physical matter density $\Omega_m h^2$, in combination with uncalibrated supernova (SN) luminosity distances, which constrain the present-day matter fraction Ω_m, to obtain a sound-horizon-free measurement of H_0. Both the full-shape galaxy power spectrum $P(k)$ and the CMB lensing convergence spectrum $C_\ell^{\kappa\kappa}$ are sensitive to $k_{\rm eq}$. In full-shape analyses, $P(k)$ is decomposed into its smooth (the component that constrains $k_{\rm eq}$) and oscillatory (BAO) parts, and r_d is marginalized over in the oscillatory part to eliminate dependence on the sound horizon. While this method preserves some of the calibration-independent angular diameter distance information encoded in the BAO wiggles, it does not fully exploit the constraining power of the complete set of transverse, radial, and volume-averaged BAO observables.

In this work, we employ an alternative approach introduced in [331], combining uncalibrated transverse, radial, and volume-averaged BAO measurements, which constrain $r_d H_0$ and Ω_m, with CMB and galaxy lensing, which provide a constraint on $\Omega_m h^2$ and break the r_d–H_0

degeneracy. Here, r_d is treated as a free primary parameter and is measured from the data alongside H_0. We use BAO measurements from the DESI DR2 release [20], the combination [338] of CMB lensing convergence spectra $C_\ell^{\kappa\kappa}$ from *Planck* [51], the Atacama Cosmology Telescope (ACT DR6) [337, 293, 294], and the South Pole Telescope (SPT-3G) [195], hereafter referred to as APS, along with the DES Year-3 three two-point galaxy weak lensing and clustering correlation functions (3×2-pt, DESY3) [17, 19]. In addition, we include the CMB acoustic scale angle, $\theta_\star$, treating it as an additional transverse BAO point at redshift $z = 1090$. We also include the Pantheon+ compilation of uncalibrated SN magnitudes [105], which add an additional constraint on Ω_m; however, this contribution is not significant since the uncalibrated BAO data alone already constrain Ω_m well.

In addition to providing an early-Universe-independent constraint on H_0, our approach also enables, in principle, a measurement of the sum of neutrino masses, Σm_ν, through the sensitivity of CMB lensing and galaxy lensing and clustering to the suppression of small-scale structure, especially when combined with a weak external prior on the amplitude of primordial fluctuations A_s. By combining DESI DR2 BAO and $\theta_\star$ with CMB lensing from APS, DESY3 galaxy weak lensing and clustering, and the Pantheon+ SN, we obtain $H_0 = 70.0 \pm 1.7$ km/s/Mpc when Σm_ν is fixed at the minimal value of 0.06 eV. With an additional conservative but informative prior on A_s, we obtain $H_0 = 70.03 \pm 0.97$ km/s/Mpc and $r_d = 144.8 \pm 1.6$ Mpc. Allowing Σm_ν to vary, we find $H_0 = 75.3^{+3.3}_{-4.0}$ km/s/Mpc and $\Sigma m_\nu < 1.11$ eV (95% CL) without an informative prior on A_s, and $H_0 = 73.9 \pm 2.2$ km/s/Mpc with $\Sigma m_\nu = 0.46^{+0.40}_{-0.45}$ eV (95% CL) when the prior on A_s is included. We also perform forecasts showing that future CMB lensing data from a Simons-Observatory-like (SO-L) experiment [23] and future galaxy weak lensing and clustering measurements, when combined with data from the completed DESI BAO program and an expanded SN dataset, can constrain H_0 with a precision of ~ 0.67 km/s/Mpc if Σm_ν is fixed, and ~ 1.1 km/s/Mpc when Σm_ν is varied, with $\Sigma m_\nu < 0.26$ eV (95% CL).

The structure of this paper is as follows: Section 6.2 introduces our approach to using the BAO observables in an r_d-independent way and discusses the sensitivity of the datasets used in this analysis to the parameters of interest. Section 6.3.1 presents the details of the analysis, including the data likelihoods, parameter prior assumptions, and the forecast methodology. In Section 6.4, we present the constraints derived from current data and the forecasts, with and without varying Σm_ν. We summarize our findings in Section 6.5.

6.2 Constraining cosmology with the sound horizon as a free parameter

6.2.1 BAO Observables

BAO provide standard-ruler distance measurements through three types of observables [166]: the transverse BAO scale, the line-of-sight BAO scale, and the isotropic average of the two. The transverse observable measures the angular size of the sound horizon r_d and is defined as

$$\beta_\perp(z) = \frac{D_M(z)}{r_d}, \tag{6.1}$$

where $D_M(z)$ is the comoving distance to redshift z. For illustration, we focus on $\beta_\perp(z)$, though the methodology described below applies equally to the radial and isotropic BAO observables.

Assuming a spatially flat ΛCDM model and neglecting radiation (an acceptable approxima-

tion at the relevant redshifts), $\beta_\perp(z)$ can be written as

$$\begin{aligned}\beta_\perp(z) &= \frac{1}{r_d}\int_0^z \frac{c\,dz'}{H(z')} \\ &= \frac{2998\,\mathrm{Mpc}}{r_d h}\int_0^z \frac{dz'}{\sqrt{\Omega_m(1+z')^3+(1-\Omega_m)}},\end{aligned} \tag{6.2}$$

where $c/H_0 = 2998\,\mathrm{Mpc}/h$, and $h = H_0/(100\,\mathrm{km/s/Mpc})$. This shows that BAO observations at multiple redshifts constrain both the matter density fraction Ω_m and the product $r_d h$. Breaking the degeneracy between r_d and h requires additional information, such as the standard-model prediction for r_d combined with a Big Bang Nucleosynthesis (BBN) prior on the baryon density ω_b [31]. An alternative, explored in [331, 332] and adopted here, is to supplement BAO with a constraint on $\Omega_m h^2$ while treating r_d as a free parameter, thereby avoiding assumptions about the sound horizon.

The additional constraint on $\Omega_m h^2$ can come from CMB lensing measurements, which are sensitive to the matter–radiation equality scale k_{eq} and thus constrain the matter-to-radiation density ratio. As a consistency test, one may also adopt a Gaussian prior on $\Omega_m h^2$ from the Planck best-fit ΛCDM model and check whether the H_0 and r_d values inferred from BAO agree with those in the best-fit model [331, 332].

Unlike full-shape $P(k)$ approaches [329, 328, 399], this method makes use of all three BAO observables at each redshift, maximizing the geometrical information encoded in the data. In particular, it enables a constraint on H_0 that is less dependent on SN-derived values of Ω_m, since BAO alone already provide a strong constraint.

Finally, one can include the CMB acoustic scale angle, $\theta_\star$, treating it as an additional transverse BAO data point at $z = 1100$, as discussed in Sec. 6.3.1.

6.2.2 CMB Lensing, Galaxy Lensing and Clustering

The matter–radiation equality scale is imprinted in the matter power spectrum, which determines the CMB lensing convergence spectrum $C_\ell^{\kappa\kappa}$. As shown in [38, 86], CMB lensing constrains the combination $A_s(\Omega_m h^2)^\alpha$, where $\alpha > 0$. Owing to projection effects, $C_\ell^{\kappa\kappa}$ is nearly insensitive to the acoustic oscillation features in $P(k)$, and hence to the value of r_d, as we demonstrate below. However, CMB lensing does depend on the baryon fraction of the total matter density, since baryons cluster later than dark matter and their abundance affects the growth factor. For this reason, even though we treat r_d as a free parameter, we still apply the BBN prior on ω_b.

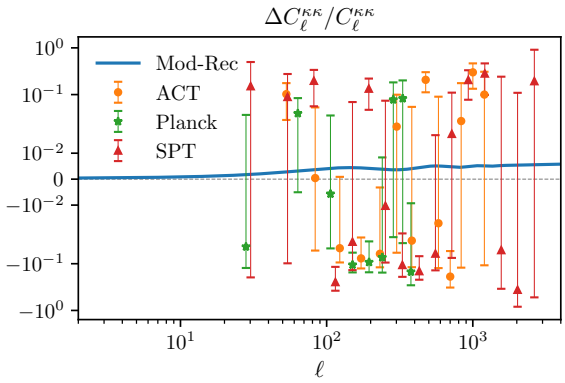


Figure 6.1: Relative difference in the CMB lensing convergence spectrum $C_\ell^{\kappa\kappa}$ for a modified recombination model with an r_d smaller by 2%, relative to the Planck best-fit ΛCDM model. Orange points, green stars, and red triangles with error bars show the $C_\ell^{\kappa\kappa}$ bandpowers from *ACT*, *Planck*, and *SPT-3G*, respectively. The figure illustrates that recombination changes capable of raising H_0 to $\sim$ 72 km/s/Mpc have only a minor effect on the CMB lensing spectrum.

The late-time matter distribution can also be probed through galaxy clustering and galaxy weak lensing, which depend on both the amplitude and scale-dependence of matter fluctuations. These observables provide complementary information to CMB lensing. The three

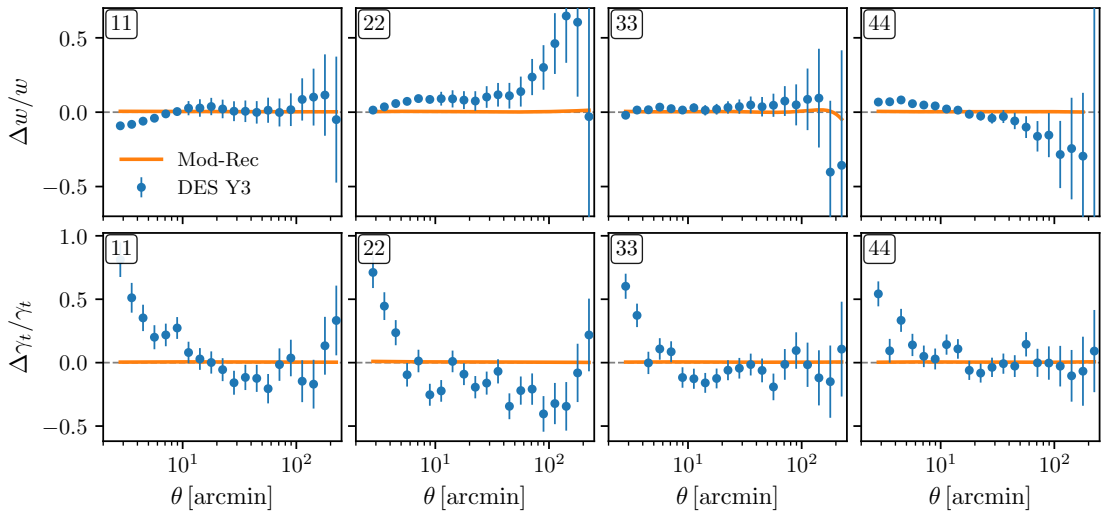


Figure 6.2: Relative difference with respect to the Planck+DES Y3 best-fit ΛCDM prediction for galaxy clustering correlation functions $w_{ij}(\theta)$ and $\gamma_{t,ij}(\theta)$ in four redshift bins ($i = j = 1, \ldots, 4$). Points with error bars show the DES Y3 measurements, while solid lines show the residuals for the same modified recombination model as in Fig. 6.1. The figure shows that recombination changes leave the 3×2-pt observables essentially unaffected.

two-point correlation functions (3×2-pt) are

$$w_{ij}(\theta) = \langle \delta_g^i(\hat{n})\, \delta_g^j(\hat{n} + \theta) \rangle, \tag{6.3}$$

$$\gamma_{t,ij}(\theta) = \langle \delta_g^i(\hat{n})\, \gamma_t^j(\hat{n} + \theta) \rangle, \tag{6.4}$$

$$\xi_{\pm,ij}(\theta) = \langle \gamma^i(\hat{n})\, \gamma^j(\hat{n} + \theta) \rangle, \tag{6.5}$$

where δ_g^i is the galaxy overdensity in redshift bin i, γ_t^j is the tangential shear in bin j, and γ^i is the shear field. In this work, we include all three correlation functions.

To assess the sensitivity of CMB lensing and galaxy 3×2-pt data to the sound horizon, we compared observables computed with the standard ionization history $x_e(z)$ in the Planck best-fit ΛCDM cosmology to those obtained with the same cosmological parameters but a modified $x_e(z)$. Specifically, we used the four-parameter phenomenological model of [306], which yields an r_d smaller by about 2%, corresponding to $H_0 \sim 72$ km/s/Mpc. Figure 6.1

shows the resulting relative difference in $C_\ell^{\kappa\kappa}$, alongside lensing bandpowers from Planck, ACT-DR6, and SPT-3G. The change remains below 1% and well within current measurement uncertainties. Similarly, Fig. 6.2 shows the residuals in $w_{ij}(\theta)$ and $\gamma_{t,ij}(\theta)$, compared to DES Y3 measurements [140, 17]. For brevity, $\xi_{\pm,ij}(\theta)$ is not shown, as it also exhibits no significant difference. These comparisons demonstrate that CMB lensing and galaxy 3×2-pt observables are effectively insensitive to moderate reductions in r_d induced by modified recombination physics.

6.2.3 The effect of massive neutrinos

Massive neutrinos affect both the expansion history and the growth of cosmic structures. Neutrinos with total mass $\Sigma m_\nu \lesssim 1$ eV behave as relativistic species before photon–baryon decoupling, contributing to the radiation energy density at $z \gtrsim 1000$ and delaying matter–radiation equality. This alters the horizon scale at equality, $k_{\rm eq}$, imprinted in the matter power spectrum. On smaller scales, neutrino free-streaming suppresses the growth of density fluctuations below the free-streaming length, producing a scale-dependent suppression of the matter power spectrum. Both effects influence the CMB lensing convergence spectrum, modifying its amplitude and shape, as shown in Fig. 2 of [290]. Combining CMB lensing with other cosmological probes that constrain the present-day matter density fraction therefore provides sensitivity to the neutrino mass (see, e.g., [287, 290, 131]).

The 3×2-pt galaxy weak lensing and clustering data, such as DES measurements, constrain the clustering amplitude and expansion history at low redshift, strengthening joint inference and significantly reducing the allowed parameter space for neutrino masses. Massive neutrinos suppress small-scale power and lower the amplitude of clustering and shear correlations, while the altered growth history modifies their redshift evolution. Because galaxy weak lensing and clustering respond differently to changes in the growth of structure and in Ω_m,

their combination provides complementary sensitivity to Σm_ν through both scale-dependent suppression and changes in Ω_m.

6.2.4 Parameter degeneracies

In ΛCDM, BAO constrain $r_d H_0$ and Ω_m, while the CMB lensing spectrum amplitude constrains approximately (see Eq. (2.10) of **(author?)** [131])

$$C_\ell^{\kappa\kappa} \propto (\Omega_m h^2)^2 A_s \left[1 - 0.003 \frac{\Sigma m_\nu / (58 \text{ meV})}{\Omega_m h^2}\right]. \tag{6.6}$$

This scaling shows that, even if the neutrino fraction is known, external information on A_s is needed to determine $\Omega_m h^2$. With Σm_ν free, the CMB lensing amplitude alone cannot disentangle $\Omega_m h^2$, A_s, and f_ν. An additional constraint on Σm_ν comes from the scale-dependent suppression of $C_\ell^{\kappa\kappa}$, illustrated in Fig. 2 of [290]. The detectability of this suppression depends on the noise in $C_\ell^{\kappa\kappa}$. Including galaxy lensing and clustering extends the mode coverage and enhances the ability to disentangle $\Omega_m h^2$, A_s, and Σm_ν. In addition, A_s is well constrained by large-scale CMB anisotropies, which are independent of r_d, justifying the adoption of a conservative prior on A_s from CMB data (see Sec. 6.3.2).

Allowing for massive neutrinos, which contribute as radiation at equality but as part of Ω_m today, introduces a positive correlation between Σm_ν and H_0 when using CMB lensing and BAO. A larger Σm_ν reduces the effective matter density at equality, requiring a larger $\Omega_m h^2$ to maintain the same $k_{\rm eq}$. With Ω_m constrained by BAO, this in turn requires a larger H_0. These parameter relationships are evident in Fig. 6.3, which shows the joint posteriors for H_0, Σm_ν, and $\Omega_m h^2$ (see also Fig. 2 of [290]).

6.3 Analysis details

6.3.1 Datasets

DESI DR2 BAO

We use the DESI DR2 BAO `Cobaya` likelihood, based on measurements provided in Table III of [20]. The dataset includes the D_V/r_d measurement from the BGS sample at $0.1 < z < 0.4$, D_M/r_d and D_H/r_d for two LRG bins at $0.4 < z < 0.6$ and $0.6 < z < 0.8$, a combined LRG+ELG tracer at $0.8 < z < 1.1$, ELG measurements at $1.1 < z < 1.6$, QSO clustering BAO at $0.8 < z < 2.1$, and the Lyα BAO constraint at $1.8 < z < 4.2$. We refer to this dataset as DESI2.

The CMB acoustic scale $\theta_\star$

The CMB acoustic scale angle, $\theta_\star$, also known as $\theta_{\rm CMB}$, is the angular size of the sound horizon at the epoch of recombination. We use $\theta_\star$ as a transverse BAO measurement, $\beta_\perp^\star = 94.286 \pm 0.217$, at $z_\star = 1090$ [332], derived from $\theta_\star$ measured by Planck under the assumption that the ΛCDM relation between r_d and the sound horizon at the redshift corresponding to the peak of the CMB visibility function, r_*, holds (with $r_\star \approx r_d/1.02$). The authors verified that this relation remains valid in known extensions of ΛCDM that modify r_d.

Adding $\theta_\star$ to our dataset helps tighten the BAO constraints on $r_d H_0$ and Ω_m.

CMB Lensing: *Planck*, ACT, and SPT-3G

We use the combination of CMB lensing bandpowers from *Planck* [51], the Atacama Cosmology Telescope (ACT DR6) [337, 293, 294], and the South Pole Telescope (SPT-3G) [195]

provided in [338]. This combination, subsequently referred to as APS-L, provides the most constraining CMB lensing power spectrum measurement to date with a combined signal-to-noise ratio of 61, offering strong constraints on the amplitude of matter fluctuations S_8 [338].

Dark Energy Survey 3×2-pt

We include the full 3×2-pt correlation functions from the Dark Energy Survey Year 3 (DES Y3) encompassing cosmic shear, galaxy clustering, and galaxy-galaxy lensing as detailed in [17]. This joint analysis over ~ 5000 deg^2 provides competitive constraints on cosmological parameters, yielding $S_8 = 0.776^{+0.017}_{-0.017}$ and $\Omega_m = 0.339^{+0.032}_{-0.031}$, and serves as a powerful low-redshift complement to CMB-based probes. By directly tracing the growth of structure, DES Y3 measurements are particularly sensitive to the suppression effects induced by massive neutrinos, thereby providing valuable information on the sum of neutrino masses. We use the `Cobaya` [380] implementation of the likelihood from [391].

Pantheon+ Supernovae

We use the Pantheon+ (PP) dataset of 1550 spectroscopically-confirmed Type Ia SN spanning $0.001 < z < 2.26$ to probe the late-time expansion history [358, 105]. This updated compilation improves upon the original Pantheon release through enhanced photometric calibration, extended low-redshift coverage, and refined treatment of systematics.

6.3.2 Model Parameters and Priors

We use the Monte-Carlo Markov Chains (MCMC) package `Cobaya` [380] with a version of the Boltzmann code `CAMB` [281] modified to treat r_d as a primary (rather than derived) parameter. The sampled parameters are r_d, H_0, $\Omega_c h^2$, $\Omega_b h^2$, the spectral index n_s, A_s, and

Σm_ν. We also consider the case where Σm_ν is fixed at the minimal value of 0.06 eV. The parameter priors adopted in this work are summarized in Table 6.1. Below, we briefly explain the reasoning behind our choices of priors.

	Current Data Prior	Forecast Fiducial value, Prior
$\ln(10^{10}A_s)$	[2, 4] or $\mathcal{N}(3.04, 0.02)$	3.045, $\mathcal{N}(3.04, 0.02)$
H_0 [km/s/Mpc]	[40, 100]	67.32, [40, 100]
n_s	$\mathcal{N}(0.96, 0.02)$	0.966, $\mathcal{N}(0.96, 0.02)$
100 $\Omega_b h^2$	$\mathcal{N}(2.23, 0.05)$	2.24, $\mathcal{N}(2.23, 0.05)$
$\Omega_c h^2$	[0.001, 0.99]	0.120, [0.001, 0.99]
Σm_ν [eV]	[0, 3.0]	0.06, [0, 3.0]
r_d [Mpc]	[100, 200]	147.1, [100, 200]
τ (fixed)	0.059	0.059

Table 6.1: Priors adopted for the parameters in the analysis of current data, and the fiducial values and priors used in the forecast. Uniform priors are indicated by square brackets, while Gaussian priors with mean μ and standard deviation σ are denoted as $\mathcal{N}(\mu, \sigma)$.

For the H_0 and the cold dark matter density parameter, $\Omega_c h^2$, we use flat uninformative priors with ranges given in Table 6.1.

When analysing the current data, we present results both with a weak flat prior on A_s, $\ln(10^{10}A_s) \in [2, 4]$ (same as in [338]), as well a Gaussian prior, $\mathcal{N}(3.04, 0.02)$, centered on the Planck-ΛCDM preferred value [115] with a standard deviation encompassing the A_s posteriors obtained in a broad range of modified recombination models [306]. Having a stronger prior on A_s helps break the degeneracy between A_s and $\Omega_m h^2$ in CMB lensing, significantly tightening the posterior of H_0.

For the scalar spectral index n_s, we adopt a Gaussian prior $\mathcal{N}(0.96, 0.02)$, same as the prior used in [338], that encompasses a broad range of posteriors in models with modified recombination histories. We found that adopting a more restrictive prior on n_s did not appreciably alter the constraints on the parameters of interest.

Varying the optical depth to reionization, τ, has no impact on our posterior distributions.

We therefore fix this parameter to the Planck + DESI DR2 ΛCDM best-fit value, $\tau = 0.059$ [305]. This choice is also consistent with the value obtained from the `SRoll2` low-ℓ polarization analysis [322]. Given the key role of τ for the parameter constraints derived from the combination of CMB temperature, polarization and lensing spectra, with implications for the apparent tension between the Planck CMB and DESI BAO [354], having a τ-insensitive way of measuring a subset of cosmological parameters offers a valuable cross-check.

We adopt a Gaussian prior on the physical baryon density, $\Omega_b h^2 \sim \mathcal{N}(0.0223, 0.0005)$, obtained from observations of the primordial abundances of light elements, particularly deuterium, and is consistent with the standard BBN scenario combined with updated nuclear reaction rate data [129].

We adopt a wide and minimally informative flat prior on the net neutrino mass, Σm_ν, spanning $[0, 3]$ eV, allowing our constraints to remain largely driven by the data [172]. We also perform separate analyses with Σm_ν fixed at the minimum value of 0.06 eV determined by neutrino oscillation experiments [164, 76, 47, 175, 138]. We note that prior choice for the neutrino mass sum has been shown to significantly affect Bayesian evidence and posterior inferences, especially in the case of signigicant parameter degeneracies. Several works have emphasized the impact of adopting linear versus logarithmic priors, particularly in distinguishing between neutrino mass orderings and assessing constraints on Σm_ν [223, 190, 285, 191, 367]. In light of these findings, our baseline analysis adopts a uniform prior on Σm_ν, consistent with common practice in cosmological analyses. However, we also demonstrate in Fig. 6.4 the impact of using a logarithmic prior. In addition, a number of groups have explored analyses where Σm_ν is allowed to take negative values, which can be informative for isolating parameter degeneracies and quantifying the statistical power of cosmological data [131, 170, 290]. Investigating negative-mass parameterizations lies beyond the scope of this project.

6.3.3 Forecasts

In what follows, we describe the methodology used in our forecasts of the constraints expected from future CMB lensing, galaxy lensing and clustering, BAO and SN datasets. We adopt the Planck best-fit ΛCDM model as our fiducial cosmology with parameters provided in Table 6.1.

CMB Lensing

For the forecast, we construct a lensing likelihood function $\mathcal{L}$ assuming Gaussian errors and covariance for the binned CMB lensing convergence spectrum, $C^{\hat{\kappa}\kappa}_{L_b}$ [337, 294]:

$$-2\ln\mathcal{L} = \Sigma_{bb'}\left[\hat{C}^{\kappa\kappa}_{L_b} - C^{\kappa\kappa}_{L_b}(\theta)\right]\mathbb{C}^{-1}_{bb'}\left[\hat{C}^{\kappa\kappa}_{L'_b} - C^{\kappa\kappa}_{L'_b}(\theta)\right], \tag{6.7}$$

where b denotes a bin centered at multiple L_b, $C^{\kappa\kappa}_{L_b}(\theta)$ is the theory spectrum calculated using a set of cosmological parameters θ, $\hat{C}^{\kappa\kappa}_{L_b}$ is the mock "measured" spectrum and $\mathbb{C}_{bb'}$ is the covariance matrix generated as described below.

We adopt the extended range bin configuration used in the ACT DR6 analysis, with the $N_{\rm bins} = 18$ non-overlapping bins centered at $L = [14, 30, 53, 84, 123, 172, 232, 302, 382, 476, 582, 700, 832, 1001, 1200, 1400, 1600, 1874]$. To evaluate the impact of using a different binning scheme on the forecasted parameter constraints, we also generated mock CMB lensing datasets $N_{\rm bins}$ ranging from 13 to 100, with the bin widths forming an arithmetic progression resulting in progressively wider bins at higher multipoles. We found that the uncertainties in the cosmological parameters converged for the 18-bin case we have adopted.

To generate a single realization of the mock data, we use the additive Gaussian noise approximation by drawing a random sample from a Gaussian distribution centered at the fiducial

cosmology $C_L^{\kappa\kappa}$ and standard deviation given by

$$\Delta C_L^{\kappa\kappa} = \sqrt{\frac{2}{f_{\rm sky}(2L+1)}} \left(C_L^{\kappa\kappa} + N_L^{\kappa\kappa}\right), \tag{6.8}$$

where $N_L^{\kappa\kappa}$ is the noise power spectrum, and $f_{\rm sky}$ is the fraction of sky coverage [263]. Following the methodology described in [337], we obtain the band-power covariance matrix from $N_{\rm mock} = 796$ mock simulations while assuming SO-like sky coverage $f_{\rm sky} = 0.5$. To account for the biased estimate of the covariance matrix from a finite number of realizations, we rescale the estimated inverse covariance matrix by the Hartlap factor [218]:

$$f_{\rm H} = \frac{N_{\rm mock} - N_{\rm bins} - 2}{N_{\rm mock} - 1}, \tag{6.9}$$

where $N_{\rm bins}$ is the number of bandpowers.

As the noise power spectrum $N_L^{\kappa\kappa}$, we use the Simons Observatory minimum variance (MV) noise curve `v3.1.1` with the goal sensitivity for the large aperture telescope (LAT) [32]. The dominant contribution arises from the disconnected Gaussian term, $N^{(0)}$, which originates from random correlations in the primary CMB anisotropies [295]. Additional noise comes from instrumental and atmospheric fluctuations, which introduce anisotropic variance in the maps. Foreground contamination, including the thermal and kinetic Sunyaev–Zel'dovich effects, cosmic infrared background, and unresolved point sources, adds non-Gaussian structure that biases lensing estimators. Furthermore, masking of bright sources and survey geometry effects can induce additional biases if not properly accounted for [72].

3×2-pt galaxy weak lensing and clustering

To model a future galaxy weak lensing and clustering dataset (w_{ij}, $\gamma_{t,ij}$, and $\xi_{\pm,ij}$), we generate mock DES-Year-1-like 3×2-pt data vectors based on our fiducial ΛCDM cosmology.

We then add Gaussian noise drawn from the DES Y1 covariance matrix, rescaled by a factor of 25 to approximate the precision expected from future surveys. Our mock likelihood is based on the publicly available `Cobaya` implementation of the DES Y1 [266, 16] likelihood, with the rescaled covariance and the mock data.

For the MCMC runs with the mock SO-L CMB lensing data, we vary and marginalize over the DES-Y1 likelihood nuisance parameters. For runs combined with the CV-L CMB lensing mock, we fixed the nuisance parameters at their fiducial values. The former setup is meant to represent a combination that can be expected to be available in the relatively near future, while the latter is more representative of the ultimate limit. Throughout the paper, we denote the 3×2-pt mock analysis with fixed nuisance parameters with an asterisk, *i.e.* $3 \times 2\text{-pt}^*$, in both tables and figures.

BAO & SN forecast methodology

To model a future BAO dataset, we generate mock data for the three types of BAO observables $D_M/r_d, D_H/r_d$, and D_V/r_d based on the fiducial model and the DESI DR2 data covariance, reduced by a factor of 2. This is meant to approximate the BAO data from the completed full 14,000 deg^2 DESI program [29], which will cover approximately twice the volume included in the DR2 release. We obtain a covariance matrix from $N_{\rm mock} = 796$ simulations, with the mock BAO estimates given as 13 data points at 7 effective redshifts: $z_{\rm eff} = [0.295, 0.510, 0.706, 0.934, 1.321, 1.484, 2.330]$, that match the redshifts in the native `Cobaya` DESI DR2 BAO likelihood and making it easy to modify it for use with our mock data.

To model a future SN Ia dataset, we adopt the Pantheon+ sample [105] as our template, computing the theoretical distance modulus, $\mu_{\rm th}(z)$, at each redshift using `CAMB` [281] for the Planck ΛCDM best-fit parameters. Mock data are then generated by adding Gaussian

noise with standard deviations given by the Pantheon+ uncertainties reduced by a factor of 2.5, corresponding to an "ultimate" SN sample with roughly six times more objects than the current dataset, as expected from Vera Rubin LSST and Euclid, both of which forecast around 10^4 high-quality SN Ia [297, 69]. The mock SN sample is then binned into $N_{\rm bins} = 40$ redshift bins using an equal-occupancy (quantile) scheme, which ensures that each bin contains a comparable number of SN and thus similar statistical precision on $\mu(z_b)$. For validation, we also tested an alternative "Union3" binning scheme with fixed bin centers matching the Union3 [352] compilation.

We produce $N_{\rm mock} = 796$ independent realizations of the binned data vector $\hat{\mu}(z_b)$ and estimate the covariance matrix $\mathbb{C}_{bb'}$ from these realizations. To correct for the bias in the inverse covariance from a finite number of realizations, we rescale it by the Hartlap factor.

The resulting mock SN likelihood has the form

$$-2\ln\mathcal{L} = \sum_{bb'} \left[\hat{\mu}(z_b) - \mu_{\rm th}(z_b;\theta)\right] \mathbb{C}^{-1}_{bb'} \left[\hat{\mu}(z_{b'}) - \mu_{\rm th}(z_{b'};\theta)\right], \tag{6.10}$$

where θ denotes the set of cosmological parameters.

This approach yields a mock SN likelihood that retains the statistical properties and redshift coverage of Pantheon+, but with the improved constraining power expected from Vera Rubin LSST and Euclid.

6.4 Results

In what follows, we present the r_d-agnostic parameter constraints inferred from the current data, as well as the forecasts. The results for the fixed and the varying Σm_ν analyses are summarized in Tables 6.2 and 6.3, respectively, and the key parameter posteriors are shown

Current Data (fixed Σm_ν)	H_0 [km/s/Mpc]	$100\,\Omega_m h^2$	Ω_m	r_d [Mpc]	$\ln(10^{10}A_s)$	S_8
[1] DESI2+Planck+DESY3+PP	67.69 ± 0.35	14.16 ± 0.07	0.309 ± 0.005	148.6 ± 0.35	3.040 ± 0.014	0.818 ± 0.008
DESI2+$\theta_\star$+APS-L (Base)	70.5 ± 2.0	14.75 ± 0.81	0.297 ± 0.005	144.2 ± 4.0	3.039 ± 0.073	0.831 ± 0.011
Base+A_s	70.42 ± 0.99	14.71 ± 0.30	0.297 ± 0.005	144.3 ± 1.6	3.040 ± 0.019	0.830 ± 0.011
Base+DESY3	70.3 ± 1.7	14.62 ± 0.64	0.295 ± 0.005	144.7 ± 3.2	3.045 ± 0.059	0.826 ± 0.009
Base+DESY3+A_s	70.40 ± 0.98	14.65 ± 0.29	0.296 ± 0.005	144.5 ± 1.6	3.041 ± 0.019	0.826 ± 0.009
Base+DESY3+PP	70.0 ± 1.7	$14.60^{+0.60}_{-0.68}$	0.298 ± 0.005	145.0 ± 3.2	3.044 ± 0.060	0.827 ± 0.009
Base+DESY3+PP+A_s	70.03 ± 0.97	14.62 ± 0.29	0.298 ± 0.005	144.8 ± 1.6	3.041 ± 0.019	0.827 ± 0.009
Forecast (fixed Σm_ν)						
BAO+$\theta_\star$+SO-L+SN+A_s	67.40 ± 0.71	14.33 ± 0.23	0.315 ± 0.004	146.8 ± 1.3	3.037 ± 0.019	0.830 ± 0.004
BAO+$\theta_\star$+SO-L+3 × 2-pt+SN	$67.30^{+1.1}_{-1.2}$	$14.33^{+0.43}_{-0.51}$	0.316 ± 0.003	146.9 ± 2.5	3.037 ± 0.045	0.831 ± 0.003
BAO+$\theta_\star$+SO-L+3 × 2-pt+SN+A_s	67.24 ± 0.67	14.30 ± 0.22	0.316 ± 0.003	147.0 ± 1.2	3.039 ± 0.019	0.831 ± 0.003
BAO+$\theta_\star$+CV-L+SN+A_s	67.30 ± 0.70	14.37 ± 0.22	0.317 ± 0.004	147.2 ± 1.3	3.040 ± 0.019	0.835 ± 0.002
BAO+$\theta_\star$+CV-L+3 × 2-pt*+SN	67.10 ± 1.0	14.27 ± 0.41	0.317 ± 0.002	147.8 ± 2.2	3.051 ± 0.038	0.835 ± 0.002
BAO+$\theta_\star$+CV-L+3 × 2-pt*+SN+A_s	67.30 ± 0.57	14.35 ± 0.21	0.317 ± 0.002	147.3 ± 1.2	3.042 ± 0.018	0.834 ± 0.002

Table 6.2: Constraints on cosmological parameters from current data, assuming fixed $\Sigma m_\nu = 0.06$ eV. The "Base" dataset denotes DESI2+$\theta_\star$+APS-L. Uncertainties are quoted at 68% CL.

Current Data (varying Σm_ν)	H_0 [km/s/Mpc]	$100\,\Omega_m h^2$	Ω_m	Σm_ν [eV]	$\ln(10^{10}A_s)$	S_8
[2] DESI2+Planck+DESY3+PP	$67.82^{+0.47}_{-0.39}$	14.15 ± 0.08	$0.308^{+0.005}_{-0.006}$	< 0.052 (0.112)	3.038 ± 0.014	0.819 ± 0.009
Base+DESY3	$75.7^{+3.1}_{-4.2}$	$17.0^{+1.3}_{-2.0}$	0.297 ± 0.005	$0.54^{+0.23}_{-0.38}$ (1.10)	$3.007^{+0.073}_{-0.065}$	0.821 ± 0.009
Base+DESY3+A_s	74.2 ± 2.2	16.32 ± 0.96	0.297 ± 0.005	$0.45^{+0.20}_{-0.27}$ (0.862)	3.038 ± 0.019	0.821 ± 0.009
Base+DESY3+PP	$75.3^{+3.3}_{-4.0}$	$17.0^{+1.4}_{-1.9}$	0.299 ± 0.005	$0.55^{+0.23}_{-0.37}$ (1.11)	3.006 ± 0.069	0.822 ± 0.009
Base+DESY3+PP+A_s	73.9 ± 2.2	16.36 ± 0.92	0.299 ± 0.005	$0.46^{+0.21}_{-0.25}(0.46^{+0.40}_{-0.45})$	3.038 ± 0.019	0.824 ± 0.010
Forecast (varying Σm_ν)						
BAO+$\theta_\star$+SO-L+SN+A_s	$69.6^{+1.6}_{-2.3}$	$15.32^{+0.64}_{-1.0}$	0.316 ± 0.004	< 0.357 (0.632)	3.037 ± 0.019	0.826 ± 0.005
BAO+$\theta_\star$+SO-L+3 × 2-pt+SN	$67.8^{+1.2}_{-1.5}$	$14.56^{+0.48}_{-0.64}$	0.317 ± 0.003	< 0.135 (0.273)	3.039 ± 0.045	0.830 ± 0.004
BAO+$\theta_\star$+SO-L+3 × 2-pt+SN+A_s	$67.71^{+0.84}_{-1.1}$	$14.52^{+0.31}_{-0.49}$	0.317 ± 0.003	< 0.133 (0.263)	3.040 ± 0.018	0.830 ± 0.004
BAO+$\theta_\star$+CV-L+SN+A_s	$68.40^{+0.98}_{-1.8}$	$14.86^{+0.36}_{-0.76}$	0.317 ± 0.004	< 0.188 (0.403)	3.037 ± 0.019	0.833 ± 0.004
BAO+$\theta_\star$+CV-L+3 × 2-pt*+SN	$67.9^{+1.2}_{-1.4}$	$14.62^{+0.47}_{-0.62}$	0.317 ± 0.002	$0.122^{+0.050}_{-0.081}$ (0.247)	3.046 ± 0.038	0.833 ± 0.003
BAO+$\theta_\star$+CV-L+3 × 2-pt*+SN+A_s	$67.99^{+0.81}_{-0.97}$	$14.67^{+0.33}_{-0.43}$	0.317 ± 0.002	$0.123^{+0.051}_{-0.079}(0.244)$	3.041 ± 0.018	0.833 ± 0.003

Table 6.3: Constraints on cosmological parameters from current data, allowing Σm_ν to vary. The "Base" dataset denotes DESI2+$\theta_\star$+APS-L. For Σm_ν, both 68% CL intervals and 95% CL upper bounds are shown.

in Figures 6.3 and 6.5. The r_d-agnostic tests are compared to the standard ΛCDM fits to the combination of DESI2 BAO, PP SN and DES Year-3 with the full complement of Planck CMB spectra, namely, the NPIPE `CamSpec` high-ℓ likelihood [163, 348], the PR4 CMB lensing [115], and the PR3 low-ℓ TT and EE [42, 41](DESI2+Planck+DESY3+PP), where r_d was a derived parameter computed using the standard recombination routine in `CAMB`. Throughout this section, including in the tables and the figures, we refer to the DESI2+$\theta_\star$+APS-L combination as the "Base" dataset.

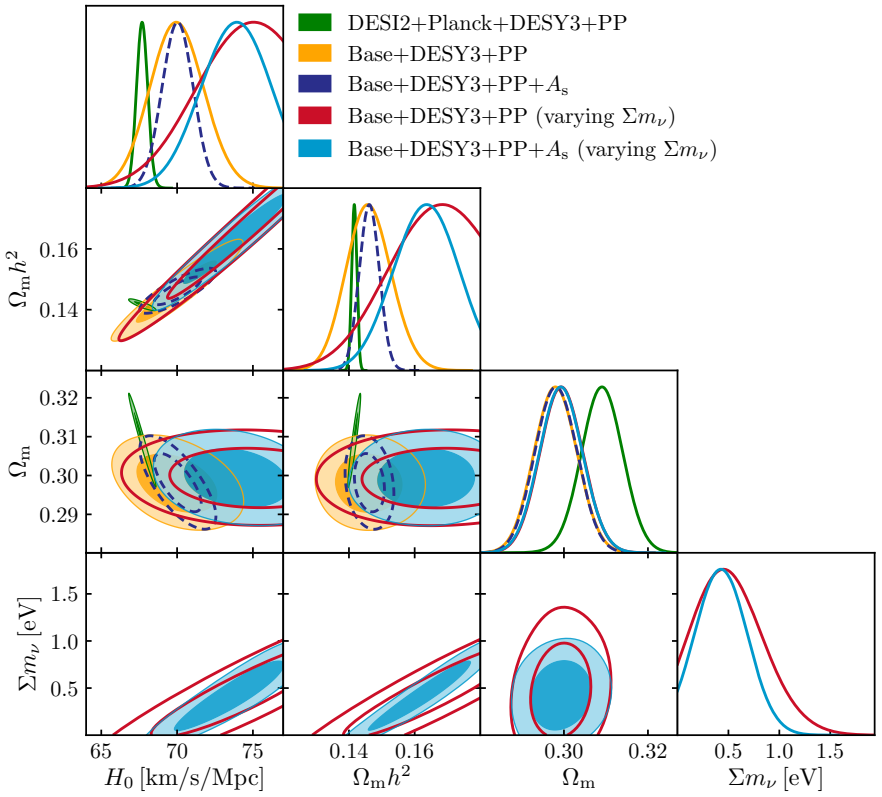


Figure 6.3: The 68% and 95% CL contours and the 1D marginalized posterior distributions for H_0, $\Omega_m h^2$, Ω_m, and Σm_ν from current data. The elongated 2D contours of H_0, $\Omega_m h^2$ and Σm_ν highlight the positive correlations between these parameters discussed in the text. The DESI2+Planck+DESY3+PP analysis uses the full Planck data, with r_d as a derived parameter computed using the standard recombination routine in CAMB. In the analyses of all other data combinations in this figure, r_d is a free parameter.

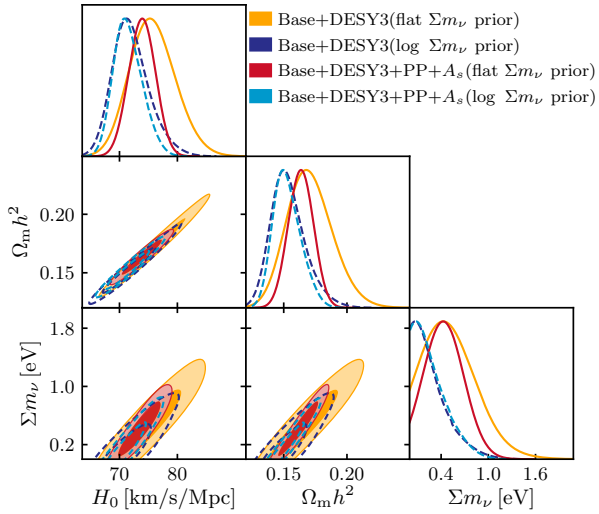


Figure 6.4: The 68% and 95% CL contours, along with the 1D marginalized posterior distributions for H_0, $\Omega_m h^2$, and Σm_ν from current data, comparing the results obtained with a uniform prior and a logarithmic prior on Σm_ν. This figure illustrates how using a logarithmic prior eliminates the apparent bias towards higher values of H_0 and $\Omega_m h^2$.

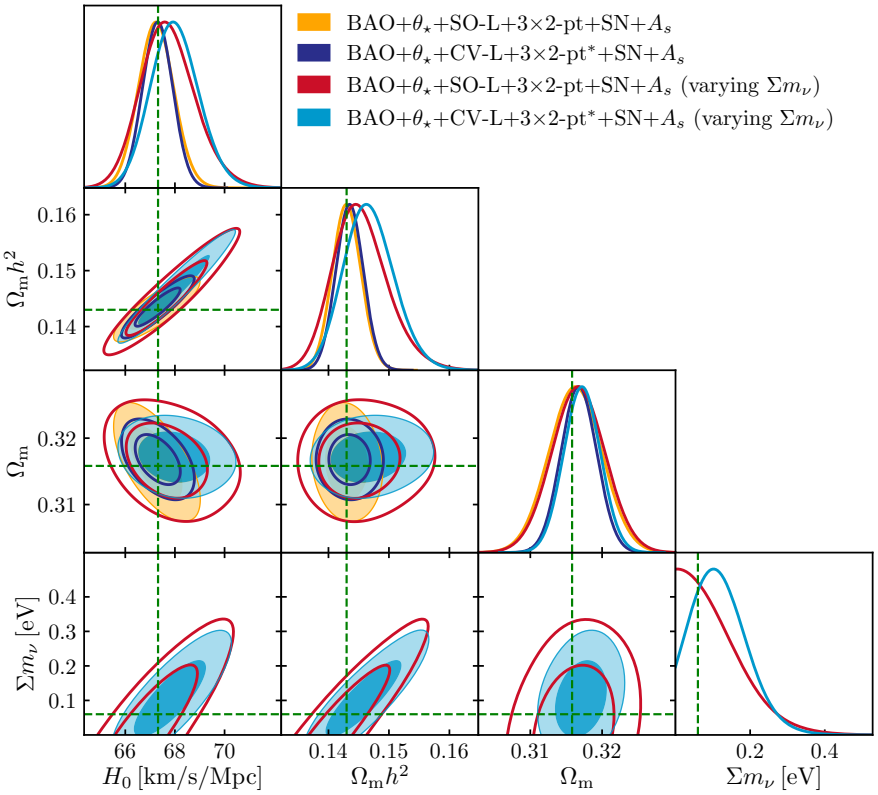


Figure 6.5: The forecasted 68% and 95% CL posterior distributions for H_0, $\Omega_m h^2$, Ω_m, and Σm_ν. For reference, the green dashed lines represent the fiducial values used in the forecast.

6.4.1 Current data constraints with fixed Σm_ν

With r_d as a free parameter, the combination of DESI2, $\theta_\star$ and APS-L (Base) yields $H_0 = 70.5 \pm 2.0$ km/s/Mpc. Adding DESY3 improves the H_0 constraint by about 15%, with $H_0 = 70.3 \pm 1.7$ km/s/Mpc. Supplementing this with the CMB-based Gaussian prior on A_s significantly reduces the uncertainty, resulting in $H_0 = 70.40 \pm 0.98$ km/s/Mpc, while also improving the constraints on r_d and $\Omega_m h^2$.

Adding the PP SN data leads to only minor shifts in the mean values and practically no reduction in parameter uncertainties. This lack of improvement despite SN offering an independent constraint on Ω_m can be explained by the fact that PP prefers a value of Ω_m [105] that is 1.8σ higher than the one preferred by DESI2 [20]. The combination of Base+DESY3+PP+A_s yields $H_0 = 70.03 \pm 0.97$ km/s/Mpc that is 2.3σ above $H_0 = 67.69 \pm 0.35$ km/s/Mpc obtained from the conventional derived-r_d fit to DESI2+Planck+DESY3+PP, 2.4σ above the Planck-only value of $H_0 = 67.36 \pm 0.54$ km/s/Mpc and 2.1σ below the SH0ES Cepheid-based distance ladder measurement of 73.04 ± 1.04 km/s/Mpc.

The Base+DESY3+PP+A_s value of $S_8 = 0.827 \pm 0.009$ is in good agreement with $S_8 = 0.825^{+0.015}_{-0.013}$ obtained in [338] from APS-L alone, and the DESI2+Planck+DESY3+PP value of $S_8 = 0.818 \pm 0.008$.

6.4.2 Current data constraints with varying Σm_ν

Neutrinos with masses in the $[0, 3.0]$ eV range contribute as radiation at matter-radiation equality, and also suppress the growth of cosmic structure on smaller scales. Both effects affect the shape of the matter power spectrum and, consequently, the CMB lensing convergence spectrum and the galaxy lensing and clustering, making the latter a probe of the total neutrino mass.

As discussed in Sec. 6.2.4 and seen in Fig. 6.3, there is a positive correlation between Σm_ν and $\Omega_m h^2$ driven by the need to preserve the value of $k_{\rm eq}$ for larger values of Σm_ν. With Ω_m constrained by BAO (and independently also by SN), this implies that Σm_ν is positively correlated with H_0. We find that allowing Σm_ν to vary considerably dilutes the constraint on H_0, with the combination of Base+DESY3+PP yielding $H_0 = 75.3^{+3.3}_{-4.0}$ km/s/Mpc. Adding a CMB-informed prior on A_s improves this to $H_0 = 73.9 \pm 2.2$ km/s/Mpc, while constraining the neutrino masses to $\Sigma m_\nu = 0.46^{+0.21}_{-0.25}$ eV ($0.46^{+0.40}_{-0.45}$ eV at 95% CL).

Assigning uniform probability for Σm_ν to take any value in the $[0, 3]$ eV range, with the parameter being relatively unconstrained positively correlated with H_0, tends to bias the H_0 and $\Omega_m h^2$ posteriors towards larger values. To demonstrate that this is a prior-related effect, in Figure 6.4 we show posteriors for a few data combinations while using a logarithmic prior on Σm_ν covering the $[0.001, 3]$ eV mass range. With the logarithmic prior, the combination of Base+DESY3+PP+A_s yields $H_0 = 71.5^{+1.4}_{-2.9}$ and $\Sigma m_\nu = 0.205^{+0.097}_{-0.23}$ eV at 68% CL ($0.20^{+0.46}_{-0.24}$ eV at 95% CL). These are statistically consistent with the uniform prior results, but now without the apparent bias.

The r_d-agnostic bounds on Σm_ν presented in this section are substantially weaker than those from the conventional derived-r_d analysis of the DESI DR2+*Planck*+DESY3+PP dataset, $\Sigma m_\nu < 0.052$ eV (0.112 eV at 95% CL), that are getting very close to the limit of 0.06 eV.

Notably, the constraints on S_8 derived while varying Σm_ν are effectively the same as those from the fixed Σm_ν analysis in the previous subsection, and in excellent agreement with $S_8 = 0.815^{+0.016}_{-0.021}$ obtained by the KiDS-Legacy analysis [375, 395] with fixed $\Sigma m_\nu = 0.06$ eV, and $S_8 = 0.811^{+0.022}_{-0.020}$ from the DES Year 3 joint analysis of cluster abundances, weak lensing, and galaxy clustering while varying Σm_ν.

6.4.3 Forecasted parameter constraints

Finally, we present a forecast based on mock CMB lensing data from a Simons-Observatory-like (SO-L) experiment, a future 3×2-pt galaxy weak lensing and clustering dataset, the completed DESI BAO program, the present value of $\theta_\star$, a mock future SN sample with ~ 9000 SN magnitudes, and the same prior on A_s as the one used in the earlier subsections. We also perform the same forecast with a cosmic-variance-limited (CV-L) CMB Lensing mock data. The forecasted parameter constraints for the cases of fixed and varied Σm_ν are summarized in Tables 6.2 and 6.3, and shown in Fig. 6.5. These forecasts are not meant to be an exhaustive study of the promise of the r_d-agnostic method, but rather provide a sense of what improvement one can expect over a reasonable timescale.

With a fixed Σm_ν and without an informative A_s prior, we obtain $H_0 = 67.30^{+1.1}_{-1.2}$ km/s/Mpc from the combination including the SO-L data, and $H_0 = 67.10 \pm 1.0$ km/s/Mpc from the combination with CV-L. It is interesting that eliminating the noise from the CMB lensing dataset, as in the cosmic variance limited case, leads to almost no improvement in the constraints. This is because the uncertainty in H_0 is dominated by the remaining degeneracy between $\Omega_m h^2$ and A_s. The inclusion of the A_s prior significantly reduces the uncertainty, yielding $H_0 = 67.24 \pm 0.67$ from the combination with SO-L, and $H_0 = 67.30 \pm 0.57$ from the combination with CV-L, while also improving the constraints on other cosmological parameters. This demonstrates that the r_d-agnostic method is capable of constraining the Hubble constant at one-percent level with a realistic CMB Lensing dataset when Σm_ν is fixed.

When allowing Σm_ν to vary, we find $H_0 = 67.71^{+0.84}_{-1.1}$ km/s/Mpc and $\Sigma m_\nu < 0.133\,(< 0.263)$ eV at 68% (95%) CL from the BAO+$\theta_\star$+SO-L+3×2-pt+SN+A_s combination, and $H_0 = 67.99^{+0.81}_{-0.97}$ km/s/Mpc and $\Sigma m_\nu = 0.123^{+0.051}_{-0.079}\,(< 0.244)$ eV at 68% (95%) CL from BAO+$\theta_\star$+CV-L+3×2-pt*+SN+A_s combination. As in the fixed Σm_ν case, the added

sensitivity to small-scale suppression at high ℓ offered by the CV-L combination does not lead to a substantial improvement in constraining power, while the prior on A_s makes a notable difference.

In the mock posteriors, we no longer see the shift to higher $\Omega_m h^2$ and H_0 values when sampling Σm_ν with a uniform prior. This is because Σm_ν is much better constrained by the mock data, reducing the dependence on the prior choice.

6.5 Summary

The Hubble tension, and attempts to resolve it through new ingredients in early-Universe physics, motivate efforts to measure H_0 without relying on a model for the sound horizon r_d or calibrating supernovae. In this work, we combined CMB lensing measurements from ACT, *Planck*, and SPT-3G with the DES Year-3 3×2-pt galaxy weak lensing and clustering correlations, DESI DR2 BAO, the CMB acoustic scale angle $\theta_\star$, and PP SN data, while treating r_d as a free parameter.

With a conservative prior on the amplitude of primordial fluctuations A_s, we find $H_0 = 70.03 \pm 0.97$ km/s/Mpc when fixing the neutrino mass sum to its minimal value $\Sigma m_\nu = 0.06$ eV. This is 2.1σ below the SH0ES Cepheid-based distance-ladder measurement [344] and 2.4σ above the *Planck* ΛCDM value [348], consistent with alternative distance-ladder determinations [183]. Allowing Σm_ν to vary increases the uncertainty in H_0, but still yields a sub-3% r_d-agnostic constraint of $H_0 = 73.9 \pm 2.2$ km/s/Mpc.

Forecasts combining future CMB lensing data from a Simons-Observatory-like experiment, a next-generation 3×2-pt dataset, the completed DESI BAO program, $\theta_\star$, a future SN sample, and a conservative A_s prior predict $\sigma(H_0) \simeq 0.67$ km/s/Mpc. This is comparable to the precision of full-*Planck* CMB analyses, demonstrating that the sound-horizon-agnostic

approach can deliver an independent and competitive test of the need for new physics at recombination.

Although our Gaussian prior on A_s was deliberately conservative, encompassing the parameter space allowed by modified recombination models with higher H_0, it will be valuable to explore whether future tomographic clustering and weak-lensing data from Vera Rubin LSST [297] and *Euclid* [58] can remove the need for such a prior. The expanded mode coverage from LSST and *Euclid* should improve sensitivity to the neutrino free-streaming suppression of growth [307] and help disentangle the effects of $\Omega_m h^2$, A_s, and Σm_ν, especially when combined with low-noise CMB lensing. We leave this for future work.

Chapter 7

Conclusions and Future Directions

This thesis has explored the theoretical and phenomenological challenges within the standard cosmological model, ΛCDM, focusing in particular on the role of neutrinos and other extensions beyond the Standard Model of particle physics. Through detailed analyses of cosmological data, we have examined how neutrino properties and early-Universe physics can influence key observables, such as the expansion history, the CMB anisotropies, and LSS formation. The results presented here contribute to a broader understanding of how fundamental particles shape the evolution of the Universe and offer insight into the persistent tensions among cosmological datasets.

In the coming years, cosmology will enter an even more data-rich era. Upcoming surveys such as *Euclid*, the Dark Energy Spectroscopic Instrument (DESI) with its forthcoming data releases, and the Simons Observatory on the CMB front will deliver unprecedented precision on both background and perturbation observables. These datasets will provide powerful opportunities to test extensions to the ΛCDM model, constrain the sum of neutrino masses, and probe potential departures from standard physics in the early Universe.

Looking forward, one of the main directions I plan to pursue in my future research is to build

upon the results of this work by incorporating and analyzing new cosmological probes. In particular, the Lyman-α forest — the dense collection of hydrogen absorption lines first identified by Roger Lynds in 1970 through quasar observations — has become one of the most powerful tracers of small-scale structure in the Universe. The Lyman-α forest now serves as a unique window into the distribution and thermal state of the intergalactic medium, which remains not yet precisely understood. By capturing the imprint of density fluctuations on scales much smaller than those probed by the CMB or galaxy surveys, it provides complementary information on the growth of structure, the sum of neutrino masses, and possible interactions in the dark sector.

The combination of Lyman-α forest data with CMB, BAO, and LSS observations will enable a joint exploration of neutrino effects, dark radiation, and non-standard thermal histories with significantly greater precision. In parallel, the synergy between next-generation cosmological surveys and laboratory neutrino experiments will be transformative, allowing us to probe whether the neutrino sector conceals new physics, whether dark matter interacts with visible particles, and whether cosmic acceleration can be explained by new dynamical components or modifications of gravity.

In summary, this thesis contributes to the ongoing effort to understand the interplay between cosmology and particle physics. While the standard cosmological model remains extraordinarily successful, the emerging discrepancies and unresolved questions signal that our understanding of the Universe is still incomplete. The inclusion of forthcoming high-precision data from *Euclid*, future DESI releases, LiteBIRD, and small-scale probes such as the Lyman-α forest will dramatically enhance our ability to constrain neutrino properties, dark sector interactions, and early-Universe dynamics. The next decade promises to be a defining period for cosmology — one that may reveal the first clear signs of physics beyond the ΛCDM paradigm.

Bibliography

[1] J. Aalbers et al. First Dark Matter Search Results from the LUX-ZEPLIN (LZ) Experiment. *Phys. Rev. Lett.*, 131(4):041002, 2023.

[2] A. Abada, A. Hernández-Cabezudo, and X. Marcano. Beta and Neutrinoless Double Beta Decays with KeV Sterile Fermions. *JHEP*, 01:041, 2019.

[3] K. Abazajian, N. F. Bell, G. M. Fuller, and Y. Y. Y. Wong. Cosmological lepton asymmetry, primordial nucleosynthesis, and sterile neutrinos. *Phys. Rev. D*, 72:063004, 2005.

[4] K. Abazajian et al. CMB-S4 Science Case, Reference Design, and Project Plan. 7 2019.

[5] K. Abazajian, G. M. Fuller, and M. Patel. Sterile neutrino hot, warm, and cold dark matter. *Phys. Rev. D*, 64:023501, 2001.

[6] K. Abazajian, G. M. Fuller, and W. H. Tucker. Direct detection of warm dark matter in the X-ray. *Astrophys. J.*, 562:593–604, 2001.

[7] K. N. Abazajian. Telling Three from Four Neutrinos with Cosmology. *Astropart. Phys.*, 19:303–312, 2003.

[8] K. N. Abazajian. Sterile neutrinos in cosmology. *Phys. Rept.*, 711-712:1–28, 2017.

[9] K. N. Abazajian. Technical Comment on "The dark matter interpretation of the 3.5-keV line is inconsistent with blank-sky observations". 4 2020.

[10] K. N. Abazajian and S. Dodelson. Neutrino Mass and Dark Energy from Weak Lensing. *Phys. Rev. Lett.*, 91:041301, 2003.

[11] K. N. Abazajian and H. G. Escudero. Visible in the laboratory and invisible in cosmology: Decaying sterile neutrinos. *Phys. Rev. D*, 108(12):123036, 2023.

[12] K. N. Abazajian et al. The Seventh Data Release of the Sloan Digital Sky Survey. *Astrophys. J. Suppl.*, 182:543–558, 2009.

[13] K. N. Abazajian et al. CMB-S4 Science Book, First Edition. 10 2016.

[14] K. N. Abazajian and M. Kaplinghat. Neutrino Physics from the Cosmic Microwave Background and Large-Scale Structure. *Ann. Rev. Nucl. Part. Sci.*, 66(1):401–420, 2016.

[15] R. Abbasi et al. Search for an eV-Scale Sterile Neutrino Using Improved High-Energy $\nu\mu$ Event Reconstruction in IceCube. *Phys. Rev. Lett.*, 133(20):201804, 2024.

[16] T. M. C. Abbott et al. Dark Energy Survey Year 1 Results: Constraints on Extended Cosmological Models from Galaxy Clustering and Weak Lensing. *Phys. Rev. D*, 99(12):123505, 2019.

[17] T. M. C. Abbott et al. Dark Energy Survey Year 3 results: Cosmological constraints from galaxy clustering and weak lensing. *Phys. Rev. D*, 105(2):023520, 2022.

[18] T. M. C. Abbott et al. The Dark Energy Survey: Cosmology Results With ˜1500 New High-redshift Type Ia Supernovae Using The Full 5-year Dataset. 1 2024.

[19] T. M. C. Abbott et al. Dark Energy Survey Year 3 Results: Cosmological Constraints from Cluster Abundances, Weak Lensing, and Galaxy Clustering. 3 2025.

[20] M. Abdul Karim et al. DESI DR2 Results II: Measurements of Baryon Acoustic Oscillations and Cosmological Constraints. 3 2025.

[21] M. H. Abdullah, A. Klypin, and G. Wilson. Cosmological Constraints on Ω_m and σ_8 from Cluster Abundances Using the GalWCat19 Optical-spectroscopic SDSS Catalog. *Astrophys. J.*, 901(2):90, 2020.

[22] J. N. Abdurashitov et al. Measurement of the response of a Ga solar neutrino experiment to neutrinos from an Ar-37 source. *Phys. Rev. C*, 73:045805, 2006.

[23] M. Abitbol et al. The Simons Observatory: science goals and forecasts for the enhanced Large Aperture Telescope. *JCAP*, 08:034, 2025.

[24] P. Abratenko et al. Search for an Anomalous Production of Charged-Current νe Interactions without Visible Pions across Multiple Kinematic Observables in MicroBooNE. *Phys. Rev. Lett.*, 135(8):081802, 2025.

[25] M. A. Acero et al. White Paper on Light Sterile Neutrino Searches and Related Phenomenology. 3 2022.

[26] M. A. Acero and J. Lesgourgues. Cosmological constraints on a light non-thermal sterile neutrino. *Phys. Rev. D*, 79:045026, 2009.

[27] A. G. Adame et al. DESI 2024 III: Baryon Acoustic Oscillations from Galaxies and Quasars. 4 2024.

[28] A. G. Adame et al. DESI 2024 VI: Cosmological Constraints from the Measurements of Baryon Acoustic Oscillations. 4 2024.

[29] A. G. Adame et al. Validation of the Scientific Program for the Dark Energy Spectroscopic Instrument. *Astron. J.*, 167(2):62, 2024.

[30] P. Adamson et al. Limits on Active to Sterile Neutrino Oscillations from Disappearance Searches in the MINOS, Daya Bay, and Bugey-3 Experiments. *Phys. Rev. Lett.*, 117(15):151801, 2016. [Addendum: Phys.Rev.Lett. 117, 209901 (2016)].

[31] G. E. Addison, D. J. Watts, C. L. Bennett, M. Halpern, G. Hinshaw, and J. L. Weiland. Elucidating ΛCDM: Impact of Baryon Acoustic Oscillation Measurements on the Hubble Constant Discrepancy. *Astrophys. J.*, 853(2):119, 2018.

[32] P. Ade et al. The Simons Observatory: Science goals and forecasts. *JCAP*, 02:056, 2019.

[33] P. A. R. Ade et al. Planck 2013 results. I. Overview of products and scientific results. *Astron. Astrophys.*, 571:A1, 2014.

[34] P. A. R. Ade et al. Planck 2013 results. XVI. Cosmological parameters. *Astron. Astrophys.*, 571:A16, 2014.

[35] P. A. R. Ade et al. Planck 2013 results. XX. Cosmology from Sunyaev–Zeldovich cluster counts. *Astron. Astrophys.*, 571:A20, 2014.

[36] P. A. R. Ade et al. Planck 2015 results. XIII. Cosmological parameters. *Astron. Astrophys.*, 594:A13, 2016.

[37] P. A. R. Ade et al. Planck 2015 results. XIII. Cosmological parameters. *Astron. Astrophys.*, 594:A13, 2016.

[38] P. A. R. Ade et al. Planck 2015 results. XV. Gravitational lensing. *Astron. Astrophys.*, 594:A15, 2016.

[39] N. Aghanim et al. Planck intermediate results. LI. Features in the cosmic microwave background temperature power spectrum and shifts in cosmological parameters. *Astron. Astrophys.*, 607:A95, 2017.

[40] N. Aghanim et al. Planck 2018 results. I. Overview and the cosmological legacy of Planck. *Astron. Astrophys.*, 641:A1, 2020.

[41] N. Aghanim et al. Planck 2018 results. V. CMB power spectra and likelihoods. *Astron. Astrophys.*, 641:A5, 2020.

[42] N. Aghanim et al. Planck 2018 results. VI. Cosmological parameters. *Astron. Astrophys.*, 641:A6, 2020. [Erratum: Astron.Astrophys. 652, C4 (2021)].

[43] A. Aguilar et al. Evidence for neutrino oscillations from the observation of $\bar{\nu}_e$ appearance in a $\bar{\nu}_\mu$ beam. *Phys. Rev. D*, 64:112007, 2001.

[44] A. A. Aguilar-Arevalo et al. A Search for Electron Neutrino Appearance at the $\Delta m^2 \sim 1eV^2$ Scale. *Phys. Rev. Lett.*, 98:231801, 2007.

[45] A. A. Aguilar-Arevalo et al. Event Excess in the MiniBooNE Search for $\bar{\nu}_\mu \to \bar{\nu}_e$ Oscillations. *Phys. Rev. Lett.*, 105:181801, 2010.

[46] A. A. Aguilar-Arevalo et al. First Measurement of the Muon Neutrino Charged Current Quasielastic Double Differential Cross Section. *Phys. Rev. D*, 81:092005, 2010.

[47] Q. R. Ahmad et al. Direct evidence for neutrino flavor transformation from neutral current interactions in the Sudbury Neutrino Observatory. *Phys. Rev. Lett.*, 89:011301, 2002.

[48] H. Akaike. A new look at the statistical model identification. *IEEE Transactions on Automatic Control*, 19(6):716–723, 1974.

[49] M. Aker et al. Direct neutrino-mass measurement based on 259 days of KATRIN data. 6 2024.

[50] K. Akita and M. Yamaguchi. A precision calculation of relic neutrino decoupling. *JCAP*, 08:012, 2020.

[51] Y. Akrami et al. *Planck* intermediate results. LVII. Joint Planck LFI and HFI data processing. *Astron. Astrophys.*, 643:A42, 2020.

[52] S. Alam et al. The clustering of galaxies in the completed SDSS-III Baryon Oscillation Spectroscopic Survey: cosmological analysis of the DR12 galaxy sample. *Mon. Not. Roy. Astron. Soc.*, 470(3):2617–2652, 2017.

[53] S. Alam et al. The Completed SDSS-IV extended Baryon Oscillation Spectroscopic Survey: N-body Mock Challenge for the eBOSS Emission Line Galaxy Sample. 7 2020.

[54] S. Alam et al. Completed SDSS-IV extended Baryon Oscillation Spectroscopic Survey: Cosmological implications from two decades of spectroscopic surveys at the Apache Point Observatory. *Phys. Rev. D*, 103(8):083533, 2021.

[55] G. Alestas, L. Kazantzidis, and L. Perivolaropoulos. H_0 tension, phantom dark energy, and cosmological parameter degeneracies. *Phys. Rev. D*, 101(12):123516, 2020.

[56] R. Allahverdi, R. Brandenberger, F.-Y. Cyr-Racine, and A. Mazumdar. Reheating in Inflationary Cosmology: Theory and Applications. *Ann. Rev. Nucl. Part. Sci.*, 60:27–51, 2010.

[57] I. J. Allali and A. Notari. Neutrino mass bounds from DESI 2024 are relaxed by Planck PR4 and cosmological supernovae. 6 2024.

[58] L. Amendola et al. Cosmology and fundamental physics with the Euclid satellite. *Living Rev. Rel.*, 21(1):2, 2018.

[59] A. Amon et al. Dark Energy Survey Year 3 results: Cosmology from cosmic shear and robustness to data calibration. *Phys. Rev. D*, 105(2):023514, 2022.

[60] D. Anderhalden, A. Schneider, A. V. Maccio, J. Diemand, and G. Bertone. Hints on the nature of dark matter from the properties of milky way satellites. *Journal of Cosmology and Astroparticle Physics*, 2013(03):014, 2013.

[61] L. Anderson et al. The clustering of galaxies in the SDSS-III Baryon Oscillation Spectroscopic Survey: baryon acoustic oscillations in the Data Releases 10 and 11 Galaxy samples. *Mon. Not. Roy. Astron. Soc.*, 441(1):24–62, 2014.

[62] E. Aprile et al. First Dark Matter Search with Nuclear Recoils from the XENONnT Experiment. *Phys. Rev. Lett.*, 131(4):041003, 2023.

[63] M. Archidiacono, N. Fornengo, S. Gariazzo, C. Giunti, S. Hannestad, and M. Laveder. Light sterile neutrinos after BICEP-2. *JCAP*, 06:031, 2014.

[64] M. Archidiacono and S. Hannestad. Updated constraints on non-standard neutrino interactions from Planck. *JCAP*, 07:046, 2014.

[65] C. A. Argüelles, V. Brdar, and J. Kopp. Production of keV Sterile Neutrinos in Supernovae: New Constraints and Gamma Ray Observables. *Phys. Rev. D*, 99(4):043012, 2019.

[66] T. Asaka, S. Blanchet, and M. Shaposhnikov. The numsm, dark matter and neutrino masses. *Phys. Lett.*, B631:151–156, 2005.

[67] M. Asgari et al. KiDS-1000 Cosmology: Cosmic shear constraints and comparison between two point statistics. *Astron. Astrophys.*, 645:A104, 2021.

[68] Y. Ashie et al. A Measurement of atmospheric neutrino oscillation parameters by SUPER-KAMIOKANDE I. *Phys. Rev. D*, 71:112005, 2005.

[69] P. Astier et al. Extending the supernova Hubble diagram to z $\sim$ 1.5 with the Euclid space mission. *Astron. Astrophys.*, 572:A80, 2014.

[70] C. Athanassopoulos et al. Evidence for anti-muon-neutrino —> anti-electron-neutrino oscillations from the LSND experiment at LAMPF. *Phys. Rev. Lett.*, 77:3082–3085, 1996.

[71] C. Athanassopoulos et al. Evidence for muon-neutrino —> electron-neutrino oscillations from pion decay in flight neutrinos. *Phys. Rev. C*, 58:2489–2511, 1998.

[72] Z. Atkins et al. The Atacama Cosmology Telescope: map-based noise simulations for DR6. *JCAP*, 11:073, 2023.

[73] F. Atrio-Barandela and S. Davidson. Interacting hot dark matter. *Phys. Rev. D*, 55:5886–5894, 1997.

[74] E. Aubourg et al. Cosmological implications of baryon acoustic oscillation measurements. *Phys. Rev. D*, 92(12):123516, 2015.

[75] S. Avila et al. The Completed SDSS-IV extended Baryon Oscillation Spectroscopic Survey: exploring the Halo Occupation Distribution model for Emission Line Galaxies. *Mon. Not. Roy. Astron. Soc.*, 499(4):5486–5507, 2020.

[76] D. S. Ayres et al. NOvA: Proposal to Build a 30 Kiloton Off-Axis Detector to Study $\nu_\mu \to \nu_e$ Oscillations in the NuMI Beamline. 3 2004.

[77] R. Banerjee and K. Jedamzik. Are cluster magnetic fields primordial? *Phys. Rev. Lett.*, 91:251301, 2003. [Erratum: Phys.Rev.Lett. 93, 179901 (2004)].

[78] R. Banerjee and K. Jedamzik. The Evolution of cosmic magnetic fields: From the very early universe, to recombination, to the present. *Phys. Rev. D*, 70:123003, 2004.

[79] V. V. Barinov et al. Results from the Baksan Experiment on Sterile Transitions (BEST). *Phys. Rev. Lett.*, 128(23):232501, 2022.

[80] V. V. Barinov et al. Search for electron-neutrino transitions to sterile states in the BEST experiment. *Phys. Rev. C*, 105(6):065502, 2022.

[81] M. Baryakhtar, O. Simon, and Z. J. Weiner. Cosmology with varying fundamental constants from hyperlight, coupled scalars. *Phys. Rev. D*, 110(8):083505, 2024.

[82] A. Basboll, O. E. Bjaelde, S. Hannestad, and G. G. Raffelt. Are cosmological neutrinos free-streaming? *Phys. Rev. D*, 79:043512, 2009.

[83] S. Bashinsky and U. Seljak. Neutrino perturbations in CMB anisotropy and matter clustering. *Phys. Rev. D*, 69:083002, 2004.

[84] R. A. Battye and A. Moss. Evidence for Massive Neutrinos from Cosmic Microwave Background and Lensing Observations. *Phys. Rev. Lett.*, 112(5):051303, 2014.

[85] D. Baumann, D. Green, J. Meyers, and B. Wallisch. Phases of New Physics in the CMB. *JCAP*, 01:007, 2016.

[86] E. J. Baxter and B. D. Sherwin. Determining the Hubble Constant without the Sound Horizon Scale: Measurements from CMB Lensing. *Mon. Not. Roy. Astron. Soc.*, 501(2):1823–1835, 2021.

[87] D. Bazow, G. S. Denicol, U. Heinz, M. Martinez, and J. Noronha. Nonlinear dynamics from the relativistic Boltzmann equation in the Friedmann-Lemaître-Robertson-Walker spacetime. *Phys. Rev. D*, 94(12):125006, 2016.

[88] J. F. Beacom, N. F. Bell, and S. Dodelson. Neutrinoless universe. *Phys. Rev. Lett.*, 93:121302, 2004.

[89] N. F. Bell, E. Pierpaoli, and K. Sigurdson. Cosmological signatures of interacting neutrinos. *Phys. Rev. D*, 73:063523, 2006.

[90] J. J. Bennett, G. Buldgen, P. F. De Salas, M. Drewes, S. Gariazzo, S. Pastor, and Y. Y. Y. Wong. Towards a precision calculation of $N_{\rm eff}$ in the Standard Model II: Neutrino decoupling in the presence of flavour oscillations and finite-temperature QED. *JCAP*, 04:073, 2021.

[91] C. Benso, V. Brdar, M. Lindner, and W. Rodejohann. Prospects for Finding Sterile Neutrino Dark Matter at KATRIN. *Phys. Rev. D*, 100(11):115035, 2019.

[92] J. L. Bernal, L. Verde, and A. G. Riess. The trouble with H_0. *JCAP*, 10:019, 2016.

[93] J. M. Berryman et al. Neutrino Self-Interactions: A White Paper. In *2022 Snowmass Summer Study*, 3 2022.

[94] M. G. Betti et al. Neutrino physics with the PTOLEMY project: active neutrino properties and the light sterile case. *JCAP*, 07:047, 2019.

[95] F. Beutler et al. The clustering of galaxies in the SDSS-III Baryon Oscillation Spectroscopic Survey: signs of neutrino mass in current cosmological data sets. *Mon. Not. Roy. Astron. Soc.*, 444(4):3501–3516, 2014.

[96] P. L. Bhatnagar, E. P. Gross, and M. Krook. A model for collision processes in gases. i. small amplitude processes in charged and neutral one-component systems. *Phys. Rev.*, 94:511–525, May 1954.

[97] Z. Bialynicka-Birula. Do Neutrinos Interact between Themselves? *Nuovo Cim.*, 33:1484–1487, 1964.

[98] D. Blas, J. Lesgourgues, and T. Tram. The Cosmic Linear Anisotropy Solving System (CLASS). Part II: Approximation schemes. , 2011(7):034, July 2011.

[99] N. Blinov, K. J. Kelly, G. Z. Krnjaic, and S. D. McDermott. Constraining the Self-Interacting Neutrino Interpretation of the Hubble Tension. *Phys. Rev. Lett.*, 123(19):191102, 2019.

[100] N. Blinov and G. Marques-Tavares. Interacting radiation after Planck and its implications for the Hubble Tension. *JCAP*, 09:029, 2020.

[101] A. Boyarsky, D. Malyshev, O. Ruchayskiy, and D. Savchenko. Technical comment on the paper of Dessert et al. "The dark matter interpretation of the 3.5 keV line is inconsistent with blank-sky observations". 4 2020.

[102] A. Boyarsky, A. Neronov, O. Ruchayskiy, and M. Shaposhnikov. Constraints on sterile neutrino as a dark matter candidate from the diffuse x-ray background. *Mon. Not. Roy. Astron. Soc.*, 370:213–218, 2006.

[103] A. Boyarsky, O. Ruchayskiy, D. Iakubovskyi, and J. Franse. Unidentified Line in X-Ray Spectra of the Andromeda Galaxy and Perseus Galaxy Cluster. *Phys. Rev. Lett.*, 113:251301, 2014.

[104] T. Brinckmann, J. H. Chang, and M. LoVerde. Self-interacting neutrinos, the Hubble parameter tension, and the cosmic microwave background. *Phys. Rev. D*, 104(6):063523, 2021.

[105] D. Brout et al. The Pantheon+ Analysis: Cosmological Constraints. *Astrophys. J.*, 938(2):110, 2022.

[106] E. Bulbul, M. Markevitch, A. Foster, R. K. Smith, M. Loewenstein, and S. W. Randall. Detection of An Unidentified Emission Line in the Stacked X-ray spectrum of Galaxy Clusters. *Astrophys. J.*, 789:13, 2014.

[107] P. Bull et al. Beyond ΛCDM: Problems, solutions, and the road ahead. *Phys. Dark Univ.*, 12:56–99, 2016.

[108] A.-K. Burns, T. M. P. Tait, and M. Valli. Indications for a Nonzero Lepton Asymmetry from Extremely Metal-Poor Galaxies. *Phys. Rev. Lett.*, 130(13):131001, 2023.

[109] E. Calabrese et al. The Atacama Cosmology Telescope: DR6 Constraints on Extended Cosmological Models. 3 2025.

[110] D. Camarena and V. Marra. On the use of the local prior on the absolute magnitude of Type Ia supernovae in cosmological inference. *Mon. Not. Roy. Astron. Soc.*, 504:5164–5171, 2021.

[111] E. Camphuis et al. SPT-3G D1: CMB temperature and polarization power spectra and cosmology from 2019 and 2020 observations of the SPT-3G Main field. 6 2025.

[112] M. D. Campos and W. Rodejohann. Testing keV sterile neutrino dark matter in future direct detection experiments. *Phys. Rev. D*, 94(9):095010, 2016.

[113] S. Cao, J. Ryan, and B. Ratra. Using Pantheon and DES supernova, baryon acoustic oscillation, and Hubble parameter data to constrain the Hubble constant, dark energy dynamics, and spatial curvature. *Mon. Not. Roy. Astron. Soc.*, 504(1):300–310, 2021.

[114] S. M. Carroll. The Cosmological constant. *Living Rev. Rel.*, 4:1, 2001.

[115] J. Carron, M. Mirmelstein, and A. Lewis. CMB lensing from Planck PR4 maps. *JCAP*, 09:039, 2022.

[116] C. Cartis, J. Fiala, B. Marteau, and L. Roberts. Improving the Flexibility and Robustness of Model-Based Derivative-Free Optimization Solvers. *arXiv e-prints*, page arXiv:1804.00154, Mar. 2018.

[117] C. Cartis, L. Roberts, and O. Sheridan-Methven. Escaping local minima with derivative-free methods: a numerical investigation. *arXiv e-prints*, page arXiv:1812.11343, Dec. 2018.

[118] M. Castellano et al. Early results from GLASS-JWST. III: Galaxy candidates at z∼9-15. *arXiv e-prints*, page arXiv:2207.09436, July 2022.

[119] Z. Chacko, L. J. Hall, T. Okui, and S. J. Oliver. CMB signals of neutrino mass generation. *Phys. Rev. D*, 70:085008, 2004.

[120] P. S. Chaubal et al. Improving Cosmological Constraints from Galaxy Cluster Number Counts with CMB-cluster-lensing Data: Results from the SPT-SZ Survey and Forecasts for the Future. *Astrophys. J.*, 931(2):139, 2022.

[121] H.-Y. Chen, M. Fishbach, and D. E. Holz. A two per cent Hubble constant measurement from standard sirens within five years. *Nature*, 562(7728):545–547, 2018.

[122] J. F. Cherry, A. Friedland, and I. M. Shoemaker. Neutrino Portal Dark Matter: From Dwarf Galaxies to IceCube. 11 2014.

[123] M. Chevallier and D. Polarski. Accelerating universes with scaling dark matter. *Int. J. Mod. Phys. D*, 10:213–224, 2001.

[124] K.-Y. Choi, E. Lkhagvadorj, and S. M. Yoo. Probing sterile neutrino dark matter in the PTOLEMY-like experiment. *JCAP*, 06:021, 2023.

[125] S. K. Choi et al. The Atacama Cosmology Telescope: a measurement of the Cosmic Microwave Background power spectra at 98 and 150 GHz. *JCAP*, 12:045, 2020.

[126] D. Chowdhury and A. Hait. Thermalization in the presence of a time-dependent dissipation and its impact on dark matter production. *JHEP*, 09:085, 2023.

[127] S. Cole et al. The 2dF Galaxy Redshift Survey: Power-spectrum analysis of the final dataset and cosmological implications. *Mon. Not. Roy. Astron. Soc.*, 362:505–534, 2005.

[128] J. M. Conrad, W. C. Louis, and M. H. Shaevitz. The LSND and MiniBooNE Oscillation Searches at High Δm^2. *Ann. Rev. Nucl. Part. Sci.*, 63:45–67, 2013.

[129] R. J. Cooke, M. Pettini, and C. C. Steidel. One Percent Determination of the Primordial Deuterium Abundance. *Astrophys. J.*, 855(2):102, 2018.

[130] G. Cowan. *Statistical data analysis*. 1998.

[131] N. Craig, D. Green, J. Meyers, and S. Rajendran. No νs is Good News. 5 2024.

[132] R. H. Cyburt, B. D. Fields, K. A. Olive, and T.-H. Yeh. Big Bang Nucleosynthesis: 2015. *Rev. Mod. Phys.*, 88:015004, 2016.

[133] F.-Y. Cyr-Racine and K. Sigurdson. Limits on Neutrino-Neutrino Scattering in the Early Universe. *Phys. Rev. D*, 90(12):123533, 2014.

[134] A. Das and S. Ghosh. Flavor-specific interaction favors strong neutrino self-coupling in the early universe. *JCAP*, 07:038, 2021.

[135] B. Dasgupta and J. Kopp. Sterile Neutrinos. *Phys. Rept.*, 928:1–63, 2021.

[136] A. de Gouvea. See-saw energy scale and the LSND anomaly. *Phys. Rev. D*, 72:033005, 2005.

[137] A. de Gouvêa. Neutrino Mass Models. *Ann. Rev. Nucl. Part. Sci.*, 66:197–217, 2016.

[138] P. F. de Salas, D. V. Forero, S. Gariazzo, P. Martínez-Miravé, O. Mena, C. A. Ternes, M. Tórtola, and J. W. F. Valle. 2020 global reassessment of the neutrino oscillation picture. *JHEP*, 02:071, 2021.

[139] P. F. De Salas, S. Gariazzo, O. Mena, C. A. Ternes, and M. Tórtola. Neutrino Mass Ordering from Oscillations and Beyond: 2018 Status and Future Prospects. *Front. Astron. Space Sci.*, 5:36, 2018.

[140] J. DeRose et al. Dark Energy Survey Year 3 results: Cosmology from combined galaxy clustering and lensing validation on cosmological simulations. *Phys. Rev. D*, 105(12):123520, 2022.

[141] C. Dessert, N. L. Rodd, and B. R. Safdi. The dark matter interpretation of the 3.5-keV line is inconsistent with blank-sky observations. *Science*, 367(6485):1465–1467, 2020.

[142] S. Dhawan, B. Popovic, and A. Goobar. The axis of systematic bias in SN˜Ia cosmology and implications for DESI 2024 results. 9 2024.

[143] E. Di Valentino et al. Snowmass2021 - Letter of interest cosmology intertwined II: The hubble constant tension. *Astropart. Phys.*, 131:102605, 2021.

[144] E. Di Valentino et al. The CosmoVerse White Paper: Addressing observational tensions in cosmology with systematics and fundamental physics. *Phys. Dark Univ.*, 49:101965, 2025.

[145] E. Di Valentino, J. Levi Said, and E. N. Saridakis. Cosmological tensions in the era of precision cosmology: Insights from Tensions in Cosmology 2025. 9 2025.

[146] E. Di Valentino, A. Melchiorri, E. V. Linder, and J. Silk. Constraining Dark Energy Dynamics in Extended Parameter Space. *Phys. Rev. D*, 96(2):023523, 2017.

[147] E. Di Valentino, A. Melchiorri, and J. Silk. Reconciling Planck with the local value of H_0 in extended parameter space. *Phys. Lett. B*, 761:242–246, 2016.

[148] E. Di Valentino, A. Melchiorri, and J. Silk. Planck evidence for a closed Universe and a possible crisis for cosmology. *Nature Astron.*, 4(2):196–203, 2019.

[149] E. Di Valentino, O. Mena, S. Pan, L. Visinelli, W. Yang, A. Melchiorri, D. F. Mota, A. G. Riess, and J. Silk. In the realm of the Hubble tension—a review of solutions. *Class. Quant. Grav.*, 38(15):153001, 2021.

[150] E. Di Valentino, A. Mukherjee, and A. A. Sen. Dark Energy with Phantom Crossing and the H_0 Tension. *Entropy*, 23(4):404, 2021.

[151] A. Diaz, C. A. Argüelles, G. H. Collin, J. M. Conrad, and M. H. Shaevitz. Where Are We With Light Sterile Neutrinos? *Phys. Rept.*, 884:1–59, 2020.

[152] D. A. Dicus, S. Nussinov, P. B. Pal, and V. L. Teplitz. Implications of relativistic gas dynamics for neutrino-neutrino cross sections. *Physics Letters B*, 218(1):84–90, 1989.

[153] S. Dodelson and L. M. Widrow. Sterile-neutrinos as dark matter. *Phys. Rev. Lett.*, 72:17–20, 1994.

[154] K. Dolag, M. Bartelmann, and H. Lesch. Evolution and structure of magnetic fields in simulated galaxy clusters. *Astron. Astrophys.*, 387:386, 1999.

[155] A. D. Dolgov. Neutrinos in cosmology. *Phys. Rept.*, 370:333–535, 2002.

[156] M. Douspis, L. Salvati, and N. Aghanim. On the Tension between Large Scale Structures and Cosmic Microwave Background. *PoS*, EDSU2018:037, 2018.

[157] J. Dunkley et al. The Atacama Cosmology Telescope: Cosmological Parameters from the 2008 Power Spectra. *Astrophys. J.*, 739:52, 2011.

[158] R. Durrer and A. Neronov. Cosmological Magnetic Fields: Their Generation, Evolution and Observation. *Astron. Astrophys. Rev.*, 21:62, 2013.

[159] C. Dvorkin, M. Wyman, D. H. Rudd, and W. Hu. Neutrinos help reconcile Planck measurements with both the early and local Universe. *Phys. Rev. D*, 90(8):083503, 2014.

[160] G. Efstathiou. A Lockdown Perspective on the Hubble Tension (with comments from the SH0ES team). 7 2020.

[161] G. Efstathiou. To H0 or not to H0? *Mon. Not. Roy. Astron. Soc.*, 505(3):3866–3872, 2021.

[162] G. Efstathiou. Evolving Dark Energy or Supernovae Systematics? 8 2024.

[163] G. Efstathiou and S. Gratton. A Detailed Description of the CamSpec Likelihood Pipeline and a Reanalysis of the Planck High Frequency Maps. 4, 10 2019.

[164] K. Eguchi et al. First results from KamLAND: Evidence for reactor anti-neutrino disappearance. *Phys. Rev. Lett.*, 90:021802, 2003.

[165] A. Einstein. The foundation of the general theory of relativity. *Annalen Phys.*, 49(7):769–822, 1916.

[166] D. J. Eisenstein et al. Detection of the Baryon Acoustic Peak in the Large-Scale Correlation Function of SDSS Luminous Red Galaxies. *Astrophys. J.*, 633:560–574, 2005.

[167] D. J. Eisenstein et al. Detection of the Baryon Acoustic Peak in the Large-Scale Correlation Function of SDSS Luminous Red Galaxies. *Astrophys. J.*, 633:560–574, 2005.

[168] D. J. Eisenstein and W. Hu. Baryonic features in the matter transfer function. *Astrophys. J.*, 496:605, 1998.

[169] W. Elbers et al. Constraints on Neutrino Physics from DESI DR2 BAO and DR1 Full Shape. 3 2025.

[170] W. Elbers, C. S. Frenk, A. Jenkins, B. Li, and S. Pascoli. Negative neutrino masses as a mirage of dark energy. 7 2024.

[171] J. Ellis, G. Gelmini, J. L. Lopez, D. Nanopoulos, and S. Sarkar. Astrophysical constraints on massive unstable neutral relic particles. *Nuclear Physics B*, 373(2):399–437, 1992.

[172] H. G. Escudero and K. N. Abazajian. Status of neutrino cosmology: Standard ΛCDM, extensions, and tensions. *Phys. Rev. D*, 111(4):043520, 2025.

[173] H. G. Escudero, J.-L. Kuo, R. E. Keeley, and K. N. Abazajian. Early or phantom dark energy, self-interacting, extra, or massive neutrinos, primordial magnetic fields, or a curved universe: An exploration of possible solutions to the H0 and $\sigma 8$ problems. *Phys. Rev. D*, 106(10):103517, 2022.

[174] M. Escudero, J. Lopez-Pavon, N. Rius, and S. Sandner. Relaxing Cosmological Neutrino Mass Bounds with Unstable Neutrinos. *JHEP*, 12:119, 2020.

[175] I. Esteban, M. C. Gonzalez-Garcia, M. Maltoni, T. Schwetz, and A. Zhou. The fate of hints: updated global analysis of three-flavor neutrino oscillations. *JHEP*, 09:178, 2020.

[176] I. Esteban and J. Salvado. Long Range Interactions in Cosmology: Implications for Neutrinos. *JCAP*, 05:036, 2021.

[177] G. S. Farren, O. H. E. Philcox, and B. D. Sherwin. Determining the Hubble constant without the sound horizon: Perspectives with future galaxy surveys. *Phys. Rev. D*, 105(6):063503, 2022.

[178] G. J. Feldman and R. D. Cousins. A Unified approach to the classical statistical analysis of small signals. *Phys. Rev. D*, 57:3873–3889, 1998.

[179] S. L. Finkelstein et al. A Long Time Ago in a Galaxy Far, Far Away: A Candidate z ~14 Galaxy in Early JWST CEERS Imaging. *arXiv e-prints*, page arXiv:2207.12474, July 2022.

[180] D. J. Fixsen, E. S. Cheng, J. M. Gales, J. C. Mather, R. A. Shafer, and E. L. Wright. The Cosmic Microwave Background Spectrum from the Full COBE FIRAS Data Set. , 473:576, Dec. 1996.

[181] J. W. Foster, M. Kongsore, C. Dessert, Y. Park, N. L. Rodd, K. Cranmer, and B. R. Safdi. Deep Search for Decaying Dark Matter with XMM-Newton Blank-Sky Observations. *Phys. Rev. Lett.*, 127(5):051101, 2021.

[182] G. Franco Abellán, Z. Chacko, A. Dev, P. Du, V. Poulin, and Y. Tsai. Improved cosmological constraints on the neutrino mass and lifetime. *JHEP*, 08:076, 2022.

[183] W. L. Freedman, B. F. Madore, T. J. Hoyt, I. S. Jang, A. J. Lee, and K. A. Owens. Status Report on the Chicago-Carnegie Hubble Program (CCHP): Measurement of the Hubble Constant Using the Hubble and James Webb Space Telescopes. *Astrophys. J.*, 985(2):203, 2025.

[184] A. Friedland, K. M. Zurek, and S. Bashinsky. Constraining Models of Neutrino Mass and Neutrino Interactions with the Planck Satellite. 4 2007.

[185] S. Friedrich et al. Limits on the Existence of sub-MeV Sterile Neutrinos from the Decay of ^{7}Be in Superconducting Quantum Sensors. *Phys. Rev. Lett.*, 126(2):021803, 2021.

[186] J. Froustey, C. Pitrou, and M. C. Volpe. Neutrino decoupling including flavour oscillations and primordial nucleosynthesis. *JCAP*, 12:015, 2020.

[187] S. Fukuda et al. Solar B-8 and hep neutrino measurements from 1258 days of Super-Kamiokande data. *Phys. Rev. Lett.*, 86:5651–5655, 2001.

[188] Y. Fukuda et al. Evidence for oscillation of atmospheric neutrinos. *Phys. Rev. Lett.*, 81:1562–1567, 1998.

[189] A. Gando et al. Search for Majorana Neutrinos near the Inverted Mass Hierarchy Region with KamLAND-Zen. *Phys. Rev. Lett.*, 117(8):082503, 2016. [Addendum: Phys.Rev.Lett. 117, 109903 (2016)].

[190] S. Gariazzo, M. Archidiacono, P. F. de Salas, O. Mena, C. A. Ternes, and M. Tórtola. Neutrino masses and their ordering: Global Data, Priors and Models. *JCAP*, 03:011, 2018.

[191] S. Gariazzo et al. Neutrino mass and mass ordering: no conclusive evidence for normal ordering. *JCAP*, 10:010, 2022.

[192] S. Gariazzo, C. Giunti, and M. Laveder. Light Sterile Neutrinos in Cosmology and Short-Baseline Oscillation Experiments. *JHEP*, 11:211, 2013.

[193] S. Gariazzo, C. Giunti, and M. Laveder. Cosmological Invisible Decay of Light Sterile Neutrinos. 4 2014.

[194] A. Garzilli, A. Magalich, O. Ruchayskiy, and A. Boyarsky. How to constrain warm dark matter with the Lyman-α forest. *Mon. Not. Roy. Astron. Soc.*, 502(2):2356–2363, 2021.

[195] F. Ge et al. Cosmology from CMB lensing and delensed EE power spectra using 2019–2020 SPT-3G polarization data. *Phys. Rev. D*, 111(8):083534, 2025.

[196] N. Gehrels. Confidence Limits for Small Numbers of Events in Astrophysical Data. , 303:336, Apr. 1986.

[197] A. Gelman and D. B. Rubin. Inference from Iterative Simulation Using Multiple Sequences. *Statistical Science*, 7:457–472, Jan. 1992.

[198] G. Gelmini, P. Gondolo, A. Soldatenko, and C. E. Yaguna. The Effect of a late decaying scalar on the neutralino relic density. *Phys. Rev. D*, 74:083514, 2006.

[199] G. Gelmini, E. Osoba, S. Palomares-Ruiz, and S. Pascoli. MeV sterile neutrinos in low reheating temperature cosmological scenarios. *JCAP*, 10:029, 2008.

[200] G. Gelmini, S. Palomares-Ruiz, and S. Pascoli. Low reheating temperature and the visible sterile neutrino. *Phys. Rev. Lett.*, 93:081302, 2004.

[201] G. B. Gelmini and P. Gondolo. Neutralino with the right cold dark matter abundance in (almost) any supersymmetric model. *Phys. Rev. D*, 74:023510, 2006.

[202] G. B. Gelmini, A. Kusenko, and V. Takhistov. Possible Hints of Sterile Neutrinos in Recent Measurements of the Hubble Parameter. *JCAP*, 06:002, 2021.

[203] G. B. Gelmini, P. Lu, and V. Takhistov. Cosmological Dependence of Non-resonantly Produced Sterile Neutrinos. *JCAP*, 12:047, 2019.

[204] G. B. Gelmini, P. Lu, and V. Takhistov. Visible Sterile Neutrinos as the Earliest Relic Probes of Cosmology. *Phys. Lett. B*, 800:135113, 2020.

[205] M. Gerbino et al. Synergy between cosmological and laboratory searches in neutrino physics: a white paper. 3 2022.

[206] W. Giarè. Dynamical Dark Energy Beyond Planck? Constraints from multiple CMB probes, DESI BAO and Type-Ia Supernovae. 9 2024.

[207] G. F. Giudice, E. W. Kolb, and A. Riotto. Largest temperature of the radiation era and its cosmological implications. *Phys. Rev. D*, 64:023508, 2001.

[208] A. Gómez-Valent, V. Pettorino, and L. Amendola. Update on coupled dark energy and the H_0 tension. *Phys. Rev. D*, 101(12):123513, 2020.

[209] D. Green et al. Messengers from the Early Universe: Cosmic Neutrinos and Other Light Relics. *Bull. Am. Astron. Soc.*, 51(3):159, 2019.

[210] D. Green and J. Meyers. The Cosmological Preference for Negative Neutrino Mass. 7 2024.

[211] J. Hamann, S. Hannestad, G. G. Raffelt, and Y. Y. Y. Wong. Sterile neutrinos with eV masses in cosmology: How disfavoured exactly? *JCAP*, 09:034, 2011.

[212] W. Handley. Curvature tension: evidence for a closed universe. *Phys. Rev. D*, 103(4):L041301, 2021.

[213] S. Hannestad. What is the lowest possible reheating temperature? *Phys. Rev. D*, 70:043506, 2004.

[214] S. Hannestad. Neutrino physics from precision cosmology. *Prog. Part. Nucl. Phys.*, 65:185–208, 2010.

[215] S. Hannestad and R. J. Scherrer. Selfinteracting warm dark matter. *Phys. Rev. D*, 62:043522, 2000.

[216] L. Hart and J. Chluba. Updated fundamental constant constraints from Planck 2018 data and possible relations to the Hubble tension. *Mon. Not. Roy. Astron. Soc.*, 493(3):3255–3263, 2020.

[217] L. Hart and J. Chluba. Varying fundamental constants principal component analysis: additional hints about the Hubble tension. *Mon. Not. Roy. Astron. Soc.*, 510(2):2206–2227, 2022.

[218] J. Hartlap, P. Simon, and P. Schneider. Why your model parameter confidences might be too optimistic: Unbiased estimation of the inverse covariance matrix. *Astron. Astrophys.*, 464:399, 2007.

[219] T. Hasegawa, N. Hiroshima, K. Kohri, R. S. L. Hansen, T. Tram, and S. Hannestad. MeV-scale reheating temperature and thermalization of oscillating neutrinos by radiative and hadronic decays of massive particles. *JCAP*, 12:012, 2019.

[220] T. Hasegawa, N. Hiroshima, K. Kohri, R. S. L. Hansen, T. Tram, and S. Hannestad. MeV-scale reheating temperature and cosmological production of light sterile neutrinos. *JCAP*, 08:015, 2020.

[221] W. K. Hastings. Monte Carlo Sampling Methods using Markov Chains and their Applications. *Biometrika*, 57(1):97–109, Apr. 1970.

[222] H.-J. He, Y.-Z. Ma, and J. Zheng. Resolving Hubble Tension by Self-Interacting Neutrinos with Dirac Seesaw. *JCAP*, 11:003, 2020.

[223] L. T. Hergt, W. J. Handley, M. P. Hobson, and A. N. Lasenby. Bayesian evidence for the tensor-to-scalar ratio r and neutrino masses m_ν: Effects of uniform vs logarithmic priors. *Phys. Rev. D*, 103:123511, 2021.

[224] L. Herold and E. G. M. Ferreira. Resolving the Hubble tension with early dark energy. *Phys. Rev. D*, 108(4):043513, 2023.

[225] L. Herold, E. G. M. Ferreira, and L. Heinrich. Profile likelihoods in cosmology: When, why, and how illustrated with ΛCDM, massive neutrinos, and dark energy. *Phys. Rev. D*, 111(8):083504, 2025.

[226] L. Herold, E. G. M. Ferreira, and E. Komatsu. New Constraint on Early Dark Energy from Planck and BOSS Data Using the Profile Likelihood. *Astrophys. J. Lett.*, 929(1):L16, 2022.

[227] L. Herold and M. Kamionkowski. Revisiting the impact of neutrino mass hierarchies on neutrino mass constraints in light of recent DESI data. 12 2024.

[228] C. Heymans et al. CFHTLenS tomographic weak lensing cosmological parameter constraints: Mitigating the impact of intrinsic galaxy alignments. *Mon. Not. Roy. Astron. Soc.*, 432:2433, 2013.

[229] J. Hidaka and G. M. Fuller. Dark matter sterile neutrinos in stellar collapse: Alteration of energy/lepton number transport and a mechanism for supernova explosion enhancement. *Phys. Rev. D*, 74:125015, 2006.

[230] E. B. Holm, L. Herold, T. Simon, E. G. M. Ferreira, S. Hannestad, V. Poulin, and T. Tram. Bayesian and frequentist investigation of prior effects in EFT of LSS analyses of full-shape BOSS and eBOSS data. *Phys. Rev. D*, 108(12):123514, 2023.

[231] D. Hooper. Detecting MeV Gauge Bosons with High-Energy Neutrino Telescopes. *Phys. Rev. D*, 75:123001, 2007.

[232] S. Horiuchi, P. J. Humphrey, J. Onorbe, K. N. Abazajian, M. Kaplinghat, and S. Garrison-Kimmel. Sterile neutrino dark matter bounds from galaxies of the Local Group. *Phys. Rev. D*, 89(2):025017, 2014.

[233] C. Howlett, A. Lewis, A. Hall, and A. Challinor. CMB power spectrum parameter degeneracies in the era of precision cosmology. *JCAP*, 04:027, 2012.

[234] W. Hu, D. J. Eisenstein, and M. Tegmark. Weighing neutrinos with galaxy surveys. *Phys. Rev. Lett.*, 80:5255–5258, 1998.

[235] W. Hu and J. Silk. Thermalization constraints and spectral distortions for massive unstable relic particles. *Phys. Rev. Lett.*, 70:2661–2664, May 1993.

[236] K. Ioka and K. Murase. IceCube PeV–EeV neutrinos and secret interactions of neutrinos. *PTEP*, 2014(6):061E01, 2014.

[237] V. Iršič et al. New Constraints on the free-streaming of warm dark matter from intermediate and small scale Lyman-α forest data. *Phys. Rev. D*, 96(2):023522, 2017.

[238] T. D. Jacques, L. M. Krauss, and C. Lunardini. Additional Light Sterile Neutrinos and Cosmology. *Phys. Rev. D*, 87(8):083515, 2013. [Erratum: Phys.Rev.D 88, 109901 (2013)].

[239] K. Jedamzik and T. Abel. Small-scale primordial magnetic fields and anisotropies in the cosmic microwave background radiation. *JCAP*, 10:050, 2013.

[240] K. Jedamzik and L. Pogosian. Relieving the Hubble tension with primordial magnetic fields. *Phys. Rev. Lett.*, 125(18):181302, 2020.

[241] K. Jedamzik, L. Pogosian, and T. Abel. Hints of Primordial Magnetic Fields at Recombination and Implications for the Hubble Tension. 3 2025.

[242] K. Jedamzik, L. Pogosian, and G.-B. Zhao. Why reducing the cosmic sound horizon alone can not fully resolve the Hubble tension. *Commun. in Phys.*, 4:123, 2021.

[243] K. Jedamzik and A. Saveliev. Stringent Limit on Primordial Magnetic Fields from the Cosmic Microwave Background Radiation. *Phys. Rev. Lett.*, 123(2):021301, 2019.

[244] H. Jeffreys. *The theory of probability*. OUP Oxford, 1998.

[245] K. S. Jeong and F. Takahashi. Self-interacting Dark Radiation. *Phys. Lett. B*, 725:134, 2013.

[246] T. Jhaveri, T. Karwal, and W. Hu. Turning a negative neutrino mass into a positive optical depth. *Phys. Rev. D*, 112(4):043541, 2025.

[247] J.-Q. Jiang, W. Giarè, S. Gariazzo, M. G. Dainotti, E. Di Valentino, O. Mena, D. Pedrotti, S. S. da Costa, and S. Vagnozzi. Neutrino cosmology after DESI: tightest mass upper limits, preference for the normal ordering, and tension with terrestrial observations. 7 2024.

[248] S. Joudaki, K. N. Abazajian, and M. Kaplinghat. Are Light Sterile Neutrinos Preferred or Disfavored by Cosmology? *Phys. Rev. D*, 87(6):065003, 2013.

[249] S. Joudaki et al. KiDS+VIKING-450 and DES-Y1 combined: Cosmology with cosmic shear. *Astron. Astrophys.*, 638:L1, 2020.

[250] S. Joudaki, M. Kaplinghat, R. Keeley, and D. Kirkby. Model independent inference of the expansion history and implications for the growth of structure. *Phys. Rev. D*, 97(12):123501, 2018.

[251] F. Kaether, W. Hampel, G. Heusser, J. Kiko, and T. Kirsten. Reanalysis of the GALLEX solar neutrino flux and source experiments. *Phys. Lett. B*, 685:47–54, 2010.

[252] M. Kamionkowski, J. Pradler, and D. G. E. Walker. Dark energy from the string axiverse. *Phys. Rev. Lett.*, 113(25):251302, 2014.

[253] M. Kaplinghat, L. Knox, and Y.-S. Song. Determining neutrino mass from the CMB alone. *Phys. Rev. Lett.*, 91:241301, 2003.

[254] T. Karwal and M. Kamionkowski. Dark energy at early times, the Hubble parameter, and the string axiverse. *Phys. Rev. D*, 94(10):103523, 2016.

[255] M. Kawasaki, K. Kohri, and N. Sugiyama. Cosmological constraints on late time entropy production. *Phys. Rev. Lett.*, 82:4168, 1999.

[256] M. Kawasaki, K. Kohri, and N. Sugiyama. MeV scale reheating temperature and thermalization of neutrino background. *Phys. Rev. D*, 62:023506, 2000.

[257] R. E. Keeley, S. Joudaki, M. Kaplinghat, and D. Kirkby. Implications of a transition in the dark energy equation of state for the H_0 and σ_8 tensions. *JCAP*, 12:035, 2019.

[258] R. E. Keeley and A. Shafieloo. Ruling Out New Physics at Low Redshift as a solution to the H_0 Tension. 6 2022.

[259] R. Keisler et al. A Measurement of the Damping Tail of the Cosmic Microwave Background Power Spectrum with the South Pole Telescope. *Astrophys. J.*, 743:28, 2011.

[260] P. Keranen. Testing exotic neutrino-neutrino interactions with AGN neutrinos. *Phys. Lett. B*, 417:320–325, 1998.

[261] G.-B. Kim. Magneto-ν: Searching for kev sterile neutrino dark matter in 241pu beta decays. UCLA Dark Matter 2023, 2023.

[262] A. Klypin, V. Poulin, F. Prada, J. Primack, M. Kamionkowski, V. Avila-Reese, A. Rodriguez-Puebla, P. Behroozi, D. Hellinger, and T. L. Smith. Clustering and Halo Abundances in Early Dark Energy Cosmological Models. *Mon. Not. Roy. Astron. Soc.*, 504(1):769–781, 2021.

[263] L. Knox. Determination of inflationary observables by cosmic microwave background anisotropy experiments. *Phys. Rev. D*, 52:4307–4318, 1995.

[264] E. W. Kolb and M. S. Turner. Supernova SN 1987a and the Secret Interactions of Neutrinos. *Phys. Rev. D*, 36:2895, 1987.

[265] E. W. Kolb and M. S. Turner. *The Early Universe*, volume 69. 1990.

[266] E. Krause et al. Dark Energy Survey Year 1 Results: Multi-Probe Methodology and Simulated Likelihood Analyses. 6 2017.

[267] C. D. Kreisch, F.-Y. Cyr-Racine, and O. Doré. Neutrino puzzle: Anomalies, interactions, and cosmological tensions. *Phys. Rev. D*, 101(12):123505, 2020.

[268] A. Kusenko. Sterile neutrinos, dark matter, and the pulsar velocities in models with a Higgs singlet. *Phys. Rev. Lett.*, 97:241301, 2006.

[269] A. Kusenko. Sterile neutrinos: The Dark side of the light fermions. *Phys. Rept.*, 481:1–28, 2009.

[270] R. Laha, B. Dasgupta, and J. F. Beacom. Constraints on New Neutrino Interactions via Light Abelian Vector Bosons. *Phys. Rev. D*, 89(9):093025, 2014.

[271] L. Lancaster, F.-Y. Cyr-Racine, L. Knox, and Z. Pan. A tale of two modes: Neutrino free-streaming in the early universe. *JCAP*, 07:033, 2017.

[272] P. Langacker. ON THE COSMOLOGICAL PRODUCTION OF LIGHT STERILE-NEUTRINOS. 9 1989.

[273] A. J. Lee, L. Rousseau-Nepton, W. L. Freedman, B. F. Madore, M.-R. L. Cioni, T. J. Hoyt, I. S. Jang, A. Javadi, and K. A. Owens. The Astrophysical Distance Scale. V. A 2% Distance to the Local Group Spiral M33 via the JAGB Method, Tip of the Red Giant Branch, and Leavitt Law. *Astrophys. J.*, 933(2):201, 2022.

[274] J. Lesgourgues. The Cosmic Linear Anisotropy Solving System (CLASS) I: Overview. *arXiv e-prints*, page arXiv:1104.2932, Apr. 2011.

[275] J. Lesgourgues, G. Mangano, G. Miele, and S. Pastor. *Neutrino Cosmology*. Cambridge University Press, 2013.

[276] J. Lesgourgues and S. Pastor. Massive neutrinos and cosmology. *Phys. Rept.*, 429:307–379, 2006.

[277] J. Lesgourgues, S. Pastor, and L. Perotto. Probing neutrino masses with future galaxy redshift surveys. *Phys. Rev. D*, 70:045016, 2004.

[278] A. Lewis. Efficient sampling of fast and slow cosmological parameters. *Phys. Rev. D*, 87(10):103529, 2013.

[279] A. Lewis. GetDist: a Python package for analysing Monte Carlo samples. 10 2019.

[280] A. Lewis and S. Bridle. Cosmological parameters from CMB and other data: A Monte Carlo approach. *Phys. Rev. D*, 66:103511, 2002.

[281] A. Lewis, A. Challinor, and A. Lasenby. Efficient computation of CMB anisotropies in closed FRW models. *Astrophys. J.*, 538:473–476, 2000.

[282] Y. F. Li and S.-s. Liu. Vanishing effective mass of the neutrinoless double beta decay including light sterile neutrinos. *Phys. Lett. B*, 706:406–411, 2012.

[283] E. V. Linder. Exploring the expansion history of the universe. *Phys. Rev. Lett.*, 90:091301, 2003.

[284] M. Lindner, A. Merle, and V. Niro. Soft $L_e - L_\mu - L_\tau$ flavour symmetry breaking and sterile neutrino keV Dark Matter. *JCAP*, 01:034, 2011. [Erratum: JCAP 07, E01 (2014)].

[285] A. J. Long, M. Raveri, W. Hu, and S. Dodelson. Neutrino Mass Priors for Cosmology from Random Matrices. *Phys. Rev. D*, 97(4):043510, 2018.

[286] A. Loureiro et al. KiDS and Euclid: Cosmological implications of a pseudo angular power spectrum analysis of KiDS-1000 cosmic shear tomography. *Astron. Astrophys.*, 665:A56, 2022.

[287] M. Loverde and Z. J. Weiner. Massive neutrinos and cosmic composition. 9 2024.

[288] M. Lucca and D. C. Hooper. Shedding light on dark matter-dark energy interactions. *Phys. Rev. D*, 102(12):123502, 2020.

[289] K. J. Ludwick. The viability of phantom dark energy: A review. *Mod. Phys. Lett. A*, 32(28):1730025, 2017.

[290] G. P. Lynch and L. Knox. What's the matter with Σm_ν? 3 2025.

[291] K.-F. Lyu, E. Stamou, and L.-T. Wang. Self-interacting neutrinos: Solution to Hubble tension versus experimental constraints. *Phys. Rev. D*, 103(1):015004, 2021.

[292] C.-P. Ma and E. Bertschinger. Cosmological perturbation theory in the synchronous and conformal Newtonian gauges. *Astrophys. J.*, 455:7–25, 1995.

[293] N. MacCrann et al. The Atacama Cosmology Telescope: Mitigating the Impact of Extragalactic Foregrounds for the DR6 Cosmic Microwave Background Lensing Analysis. *Astrophys. J.*, 966(1):138, 2024.

[294] M. S. Madhavacheril et al. The Atacama Cosmology Telescope: DR6 Gravitational Lensing Map and Cosmological Parameters. *Astrophys. J.*, 962(2):113, 2024.

[295] M. S. Madhavacheril, K. M. Smith, B. D. Sherwin, and S. Naess. CMB lensing power spectrum estimation without instrument noise bias. 11 2020.

[296] M. Maltoni, T. Schwetz, M. A. Tortola, and J. W. F. Valle. Ruling out four neutrino oscillation interpretations of the LSND anomaly? *Nucl. Phys. B*, 643:321–338, 2002.

[297] R. Mandelbaum et al. The LSST Dark Energy Science Collaboration (DESC) Science Requirements Document. 9 2018.

[298] A. Manohar. A Limit on the Neutrino-neutrino Scattering Cross-section From the Supernova. *Phys. Lett. B*, 192:217, 1987.

[299] C. J. Martoff et al. HUNTER: precision massive-neutrino search based on a laser cooled atomic source. *Quantum Sci. Technol.*, 6(2):024008, 2021.

[300] I. G. Mccarthy, S. Bird, J. Schaye, J. Harnois-Deraps, A. S. Font, and L. Van Waerbeke. The BAHAMAS project: the CMB–large-scale structure tension and the roles of massive neutrinos and galaxy formation. *Mon. Not. Roy. Astron. Soc.*, 476(3):2999–3030, 2018.

[301] Y. Mellier et al. Euclid. I. Overview of the Euclid mission. 5 2024.

[302] S. Mertens et al. A novel detector system for KATRIN to search for keV-scale sterile neutrinos. *J. Phys. G*, 46(6):065203, 2019.

[303] N. Metropolis, A. W. Rosenbluth, M. N. Rosenbluth, A. H. Teller, and E. Teller. Equation of State Calculations by Fast Computing Machines. , 21(6):1087–1092, June 1953.

[304] A. Mirizzi, N. Saviano, G. Miele, and P. D. Serpico. Light sterile neutrino production in the early universe with dynamical neutrino asymmetries. *Phys. Rev. D*, 86:053009, 2012.

[305] S. H. Mirpoorian, K. Jedamzik, and L. Pogosian. Is Dynamical Dark Energy Necessary? DESI BAO and Modified Recombination. 4 2025.

[306] S. H. Mirpoorian, K. Jedamzik, and L. Pogosian. Modified recombination and the Hubble tension. *Phys. Rev. D*, 111(8):083519, 2025.

[307] S. Mishra-Sharma, D. Alonso, and J. Dunkley. Neutrino masses and beyond- ΛCDM cosmology with LSST and future CMB experiments. *Phys. Rev. D*, 97(12):123544, 2018.

[308] H. Miyatake et al. Hyper Suprime-Cam Year 3 results: Cosmology from galaxy clustering and weak lensing with HSC and SDSS using the emulator based halo model. *Phys. Rev. D*, 108(12):123517, 2023.

[309] E. Mortsell, A. Goobar, J. Johansson, and S. Dhawan. The Hubble Tension Revisited: Additional Local Distance Ladder Uncertainties. 6 2021.

[310] E. Mortsell, A. Goobar, J. Johansson, and S. Dhawan. Sensitivity of the Hubble Constant Determination to Cepheid Calibration. *Astrophys. J.*, 933(2):212, 2022.

[311] C. Moskowitz. Cosmic mismatch hints at the existence of a 'sterile' neutrino. *Nature*, 02 2014.

[312] P. Motloch and W. Hu. Tensions between direct measurements of the lens power spectrum from Planck data. *Phys. Rev. D*, 97(10):103536, 2018.

[313] E. O. Nadler, S. Birrer, D. Gilman, R. H. Wechsler, X. Du, A. Benson, A. M. Nierenberg, and T. Treu. Dark Matter Constraints from a Unified Analysis of Strong Gravitational Lenses and Milky Way Satellite Galaxies. *Astrophys. J.*, 917(1):7, 2021.

[314] D. Naredo-Tuero, M. Escudero, E. Fernández-Martínez, X. Marcano, and V. Poulin. Living at the Edge: A Critical Look at the Cosmological Neutrino Mass Bound. 7 2024.

[315] S. Navas et al. Review of particle physics. *Phys. Rev. D*, 110(3):030001, 2024.

[316] R. M. Neal. Taking Bigger Metropolis Steps by Dragging Fast Variables. *arXiv Mathematics e-prints*, page math/0502099, Feb. 2005.

[317] K. C. Y. Ng and J. F. Beacom. Cosmic neutrino cascades from secret neutrino interactions. *Phys. Rev. D*, 90(6):065035, 2014. [Erratum: Phys.Rev.D 90, 089904 (2014)].

[318] E. B. Norman, A. Drobizhev, N. Gharibyan, K. E. Gregorich, Y. G. Kolomensky, B. N. Sammis, N. D. Scielzo, J. A. Shusterman, and K. J. Thomas. Half-life of Ge71 and the gallium anomaly. *Phys. Rev. C*, 109(5):055501, 2024.

[319] I. M. Oldengott, C. Rampf, and Y. Y. Y. Wong. Boltzmann hierarchy for interacting neutrinos I: formalism. *JCAP*, 04:016, 2015.

[320] I. M. Oldengott, T. Tram, C. Rampf, and Y. Y. Y. Wong. Interacting neutrinos in cosmology: exact description and constraints. *JCAP*, 11:027, 2017.

[321] M. Orito, T. Kajino, G. J. Mathews, and R. N. Boyd. Neutrino degeneracy and decoupling: New limits from primordial nucleosynthesis and the cosmic microwave background. 5 2000.

[322] L. Pagano, J. M. Delouis, S. Mottet, J. L. Puget, and L. Vibert. Reionization optical depth determination from Planck HFI data with ten percent accuracy. *Astron. Astrophys.*, 635:A99, 2020.

[323] P. B. Pal and L. Wolfenstein. Radiative Decays of Massive Neutrinos. *Phys. Rev. D*, 25:766, 1982.

[324] S. Pan, W. Yang, E. Di Valentino, E. N. Saridakis, and S. Chakraborty. Interacting scenarios with dynamical dark energy: Observational constraints and alleviation of the H_0 tension. *Phys. Rev. D*, 100(10):103520, 2019.

[325] M. Park, C. D. Kreisch, J. Dunkley, B. Hadzhiyska, and F.-Y. Cyr-Racine. ΛCDM or self-interacting neutrinos: How CMB data can tell the two models apart. *Phys. Rev. D*, 100(6):063524, 2019.

[326] C. Patrignani. Review of particle physics. *Chinese Physics C*, 40(10):100001, oct 2016.

[327] K. Petraki and A. Kusenko. Dark-matter sterile neutrinos in models with a gauge singlet in the Higgs sector. *Phys. Rev. D*, 77:065014, 2008.

[328] O. H. E. Philcox, G. S. Farren, B. D. Sherwin, E. J. Baxter, and D. J. Brout. Determining the Hubble constant without the sound horizon: A 3.6% constraint on H0 from galaxy surveys, CMB lensing, and supernovae. *Phys. Rev. D*, 106(6):063530, 2022.

[329] O. H. E. Philcox, B. D. Sherwin, G. S. Farren, and E. J. Baxter. Determining the Hubble Constant without the Sound Horizon: Measurements from Galaxy Surveys. *Phys. Rev. D*, 103(2):023538, 2021.

[330] R. L. Plackett. Karl pearson and the chi-squared test. *International Statistical Review / Revue Internationale de Statistique*, 51(1):59–72, 1983.

[331] L. Pogosian, G.-B. Zhao, and K. Jedamzik. Recombination-independent determination of the sound horizon and the Hubble constant from BAO. *Astrophys. J. Lett.*, 904(2):L17, 2020.

[332] L. Pogosian, G.-B. Zhao, and K. Jedamzik. A Consistency Test of the Cosmological Model at the Epoch of Recombination Using DESI Baryonic Acoustic Oscillation and Planck Measurements. *Astrophys. J. Lett.*, 973(1):L13, 2024.

[333] V. Poulin, K. K. Boddy, S. Bird, and M. Kamionkowski. Implications of an extended dark energy cosmology with massive neutrinos for cosmological tensions. *Phys. Rev. D*, 97(12):123504, 2018.

[334] V. Poulin, T. L. Smith, D. Grin, T. Karwal, and M. Kamionkowski. Cosmological implications of ultralight axionlike fields. *Phys. Rev. D*, 98(8):083525, 2018.

[335] V. Poulin, T. L. Smith, T. Karwal, and M. Kamionkowski. Early Dark Energy Can Resolve The Hubble Tension. *Phys. Rev. Lett.*, 122(22):221301, 2019.

[336] M. Powell. The bobyqa algorithm for bound constrained optimization without derivatives. *Technical Report, Department of Applied Mathematics and Theoretical Physics*, 01 2009.

[337] F. J. Qu et al. The Atacama Cosmology Telescope: A Measurement of the DR6 CMB Lensing Power Spectrum and Its Implications for Structure Growth. *Astrophys. J.*, 962(2):112, 2024.

[338] F. J. Qu et al. Unified and consistent structure growth measurements from joint ACT, SPT and \textitPlanck CMB lensing. 4 2025.

[339] G. Raffelt and J. Silk. LIGHT NEUTRINOS AS COLD DARK MATTER. *Phys. Lett. B*, 192:65–70, 1987.

[340] M. Rashkovetskyi, J. B. Muñoz, D. J. Eisenstein, and C. Dvorkin. Small-scale clumping at recombination and the Hubble tension. *Phys. Rev. D*, 104(10):103517, 2021.

[341] A. Ray and Y.-Z. Qian. Evolution of tau-neutrino lepton number in protoneutron stars due to active-sterile neutrino mixing. *Phys. Rev. D*, 108(6):063025, 2023.

[342] T. Rehagen and G. B. Gelmini. Effects of kination and scalar-tensor cosmologies on sterile neutrinos. *JCAP*, 06:044, 2014.

[343] A. G. Riess et al. A 2.4% Determination of the Local Value of the Hubble Constant. *Astrophys. J.*, 826(1):56, 2016.

[344] A. G. Riess et al. A Comprehensive Measurement of the Local Value of the Hubble Constant with 1 km s^1 Mpc^1 Uncertainty from the Hubble Space Telescope and the SH0ES Team. *Astrophys. J. Lett.*, 934(1):L7, 2022.

[345] B. M. Roach, K. C. Y. Ng, K. Perez, J. F. Beacom, S. Horiuchi, R. Krivonos, and D. R. Wik. NuSTAR Tests of Sterile-Neutrino Dark Matter: New Galactic Bulge Observations and Combined Impact. *Phys. Rev. D*, 101(10):103011, 2020.

[346] B. M. Roach, S. Rossland, K. C. Y. Ng, K. Perez, J. F. Beacom, B. W. Grefenstette, S. Horiuchi, R. Krivonos, and D. R. Wik. Long-exposure NuSTAR constraints on decaying dark matter in the Galactic halo. *Phys. Rev. D*, 107(2):023009, 2023.

[347] W. Rodejohann. On cancellations in neutrinoless double beta decay. *Nucl. Phys. B*, 597:110–126, 2001.

[348] E. Rosenberg, S. Gratton, and G. Efstathiou. CMB power spectra and cosmological parameters from Planck PR4 with CamSpec. *Mon. Not. Roy. Astron. Soc.*, 517(3):4620–4636, 2022.

[349] G. Rossi et al. The completed SDSS-IV extended Baryon Oscillation Spectroscopic Survey: N-body mock challenge for galaxy clustering measurements. *Mon. Not. Roy. Astron. Soc.*, 505(1):377–407, 2021.

[350] S. Roy Choudhury, S. Hannestad, and T. Tram. Updated constraints on massive neutrino self-interactions from cosmology in light of the H_0 tension. *JCAP*, 03:084, 2021.

[351] D. Rubin et al. Union Through UNITY: Cosmology with 2,000 SNe Using a Unified Bayesian Framework. 11 2023.

[352] D. Rubin et al. Union Through UNITY: Cosmology with 2,000 SNe Using a Unified Bayesian Framework. 11 2023.

[353] J. Ryan, S. Doshi, and B. Ratra. Constraints on dark energy dynamics and spatial curvature from Hubble parameter and baryon acoustic oscillation data. *Mon. Not. Roy. Astron. Soc.*, 480(1):759–767, 2018.

[354] N. Sailer, G. S. Farren, S. Ferraro, and M. White. Dispuτable: the high cost of a low optical depth. 4 2025.

[355] R. F. Sawyer. Bulk viscosity of a gas of neutrinos and coupled scalar particles, in the era of recombination. *Phys. Rev. D*, 74:043527, 2006.

[356] G. Schellenberger and T. H. Reiprich. HICOSMO – cosmology with a complete sample of galaxy clusters – I. Data analysis, sample selection and luminosity–mass scaling relation. *Mon. Not. Roy. Astron. Soc.*, 469(3):3738–3761, 2017.

[357] N. Schöneberg, G. Franco Abellán, A. Pérez Sánchez, S. J. Witte, V. Poulin, and J. Lesgourgues. The H_0 Olympics: A fair ranking of proposed models. 7 2021.

[358] D. Scolnic et al. The Pantheon+ Analysis: The Full Data Set and Light-curve Release. *Astrophys. J.*, 938(2):113, 2022.

[359] D. M. Scolnic et al. The Complete Light-curve Sample of Spectroscopically Confirmed SNe Ia from Pan-STARRS1 and Cosmological Constraints from the Combined Pantheon Sample. *Astrophys. J.*, 859(2):101, 2018.

[360] L. F. Secco et al. Dark Energy Survey Year 3 results: Cosmology from cosmic shear and robustness to modeling uncertainty. *Phys. Rev. D*, 105(2):023515, 2022.

[361] T. Sekiguchi and T. Takahashi. Early recombination as a solution to the H_0 tension. *Phys. Rev. D*, 103(8):083507, 2021.

[362] H.-J. Seo and D. J. Eisenstein. Probing dark energy with baryonic acoustic oscillations from future large galaxy redshift surveys. *Astrophys. J.*, 598:720–740, 2003.

[363] O. Seto and Y. Toda. Big Bang Nucleosynthesis constraints on varying electron mass solution to the Hubble tension. 6 2022.

[364] X.-D. Shi and G. M. Fuller. A New dark matter candidate: Nonthermal sterile neutrinos. *Phys. Rev. Lett.*, 82:2832–2835, 1999.

[365] R. Shrock. Decay l0 —> nu(lepton) gamma in gauge theories of weak and electromagnetic interactions. *Phys. Rev. D*, 9:743–748, 1974.

[366] D. Sicilian, N. Cappelluti, E. Bulbul, F. Civano, M. Moscetti, and C. S. Reynolds. Probing the Milky Way's Dark Matter Halo for the 3.5 keV Line. *Astrophys. J.*, 905(2):146, 2020.

[367] F. Simpson, R. Jimenez, C. Pena-Garay, and L. Verde. Strong Bayesian Evidence for the Normal Neutrino Hierarchy. *JCAP*, 06:029, 2017.

[368] A. Smith et al. The Completed SDSS-IV Extended Baryon Oscillation Spectroscopic Survey: N-body Mock Challenge for the Quasar Sample. *Mon. Not. Roy. Astron. Soc.*, 499(1):269–291, 2020.

[369] P. F. Smith. Proposed experiments to detect keV range sterile neutrinos using energy-momentum reconstruction of beta decay or K-capture events. *New J. Phys.*, 21(5):053022, 2019.

[370] T. L. Smith, V. Poulin, and M. A. Amin. Oscillating scalar fields and the Hubble tension: a resolution with novel signatures. *Phys. Rev. D*, 101(6):063523, 2020.

[371] T. L. Smith, V. Poulin, J. L. Bernal, K. K. Boddy, M. Kamionkowski, and R. Murgia. Early dark energy is not excluded by current large-scale structure data. *Phys. Rev. D*, 103(12):123542, 2021.

[372] G. F. Smoot et al. Structure in the COBE differential microwave radiometer first year maps. *Astrophys. J. Lett.*, 396:L1–L5, 1992.

[373] J. A. Sobrin et al. The Design and Integrated Performance of SPT-3G. *Astrophys. J. Supp.*, 258(2):42, 2022.

[374] D. N. Spergel et al. First year Wilkinson Microwave Anisotropy Probe (WMAP) observations: Determination of cosmological parameters. *Astrophys. J. Suppl.*, 148:175–194, 2003.

[375] B. Stölzner et al. KiDS-Legacy: Consistency of cosmic shear measurements and joint cosmological constraints with external probes. 3 2025.

[376] S. Sugiyama et al. Hyper Suprime-Cam Year 3 results: Cosmology from galaxy clustering and weak lensing with HSC and SDSS using the minimal bias model. *Phys. Rev. D*, 108(12):123521, 2023.

[377] K. Thepsuriya and A. Lewis. Accuracy of cosmological parameters using the baryon acoustic scale. *JCAP*, 01:034, 2015.

[378] L. Thiele, Y. Guan, J. C. Hill, A. Kosowsky, and D. N. Spergel. Can small-scale baryon inhomogeneities resolve the Hubble tension? An investigation with ACT DR4. *Phys. Rev. D*, 104(6):063535, 2021.

[379] R. J. Thornton et al. The Atacama Cosmology Telescope: The polarization-sensitive ACTPol instrument. *Astrophys. J. Suppl.*, 227(2):21, 2016.

[380] J. Torrado and A. Lewis. Cobaya: Code for Bayesian Analysis of hierarchical physical models. *JCAP*, 05:057, 2021.

[381] M. Tristram et al. Cosmological parameters derived from the final Planck data release (PR4). *Astron. Astrophys.*, 682:A37, 2024.

[382] R. Trotta. Bayes in the sky: Bayesian inference and model selection in cosmology. *Contemp. Phys.*, 49:71–104, 2008.

[383] S. Vagnozzi. New physics in light of the H_0 tension: An alternative view. *Phys. Rev. D*, 102(2):023518, 2020.

[384] M. Vargas-Magaña et al. The clustering of galaxies in the completed SDSS-III Baryon Oscillation Spectroscopic Survey: theoretical systematics and Baryon Acoustic Oscillations in the galaxy correlation function. *Mon. Not. Roy. Astron. Soc.*, 477(1):1153–1188, 2018.

[385] J. Venzor, G. Garcia-Arroyo, A. Pérez-Lorenzana, and J. De-Santiago. Massive neutrino self-interactions with a light mediator in cosmology. 2 2022.

[386] A. Vikhlinin et al. Chandra Cluster Cosmology Project III: Cosmological Parameter Constraints. *Astrophys. J.*, 692:1060–1074, 2009.

[387] J. Villarreal, J. M. Hardin, and J. M. Conrad. Feldman-Cousins' ML Cousin: Sterile Neutrino Global Fits using Simulation-Based Inference. 1 2025.

[388] J. Villarreal, J. Woodward, J. M. Hardin, and J. M. Conrad. A frequentist simulation-based inference treatment of sterile neutrino global fits. *Mach. Learn. Sci. Tech.*, 6(3):035053, 2025.

[389] B. Villasenor, B. Robertson, P. Madau, and E. Schneider. New constraints on warm dark matter from the Lyman-α forest power spectrum. *Phys. Rev. D*, 108(2):023502, 2023.

[390] D. Wang, O. Mena, E. Di Valentino, and S. Gariazzo. Updating neutrino mass constraints with background measurements. *Phys. Rev. D*, 110(10):103536, 2024.

[391] Z. Wang, D. Saadeh, K. Koyama, L. Pogosian, B. Bose, L. Yi, and G.-B. Zhao. Extending MGCAMB tests of gravity to nonlinear scales. *JCAP*, 11:003, 2024.

[392] D. H. Weinberg, M. J. Mortonson, D. J. Eisenstein, C. Hirata, A. G. Riess, and E. Rozo. Observational Probes of Cosmic Acceleration. *Phys. Rept.*, 530:87–255, 2013.

[393] R. Wojtak and J. Hjorth. Intrinsic tension in the supernova sector of the local Hubble constant measurement and its implications. , 515(2):2790–2799, Sept. 2022.

[394] R. L. Workman and Others. Review of Particle Physics. *PTEP*, 2022:083C01, 2022.

[395] A. H. Wright et al. KiDS-Legacy: Cosmological constraints from cosmic shear with the complete Kilo-Degree Survey. 3 2025.

[396] M. Wyman, D. H. Rudd, R. A. Vanderveld, and W. Hu. Neutrinos Help Reconcile Planck Measurements with the Local Universe. *Phys. Rev. Lett.*, 112(5):051302, 2014.

[397] C. E. Yaguna. Sterile neutrino production in models with low reheating temperatures. *JHEP*, 06:002, 2007.

[398] W. Yang, S. Pan, E. Di Valentino, E. N. Saridakis, and S. Chakraborty. Observational constraints on one-parameter dynamical dark-energy parametrizations and the H_0 tension. *Phys. Rev. D*, 99(4):043543, 2019.

[399] E. A. Zaborowski et al. A Sound Horizon-Free Measurement of H_0 in DESI 2024. *JCAP*, 06:020, 2025.

[400] I. A. Zelko, T. Treu, K. N. Abazajian, D. Gilman, A. J. Benson, S. Birrer, A. M. Nierenberg, and A. Kusenko. Constraints on Sterile Neutrino Models from Strong Gravitational Lensing, Milky Way Satellites, and the Lyman-α Forest. *Phys. Rev. Lett.*, 129(19):191301, 2022.

[401] X. Zhang. Searching for a keV sterile neutrino via 241Pu beta spectrum, July 2022.